APPLICATION OF TIME-FREQUENCY REPRESENTATIONS TO NON-STATIONARY
RADAR CROSS SECTION

THESIS

John McShane, Captain, USAF

AFIT/GE/ENG/09-28

DEPARTMENT OF THE AIR FORCE
AIR UNIVERSITY

AIR FORCE INSTITUTE OF TECHNOLOGY

Wright-Patterson Air Force Base, Ohio

AFIT/GE/ENG/09-28

Application of Time-Frequency Representations To Non-Stationary Radar Cross Section

THESIS

Presented to the Faculty

Department of Electrical and Computer Engineering

Graduate School of Engineering and Management

Air Force Institute of Technology

Air University

Air Education and Training Command

In Partial Fulfillment of the Requirements for the

Degree of Master of Science in Electrical Engineering

John McShane, B.S.E.E.

Captain, USAF

March 2009

AFIT/GE/ENG/09-28

Application of Time-Frequency Representations To Non-Stationary Radar Cross Section

John McShane, B.S.E.E.
Captain, USAF

Approved:

/signed/	21 Mar 2009
Dr. Peter Collins (Chairman)	date
/signed/	21 Mar 2009
Dr. Andrew Terzuoli (Member)	date
/signed/	21 Mar 2009
Maj. Michael Mendenhall (Member)	date

AFIT/GE/ENG/09-28

Abstract

Radar Cross Section (RCS) imaging of a non-wide sense stationary signal poses significant problems in identifying scattering centers in the post processed radar-generated image. A non-wide sense stationary RCS is typically encountered when moving parts on the target impress a phase shift into the backscatter signal that is uncorrelated to the previous return pulse. When the Fourier transform of the phase shifted complex signal is taken, range and cross range information on scattering centers are misplaced. Time Frequency Representations (TFR) must be used to help locate these scattering centers so they can be properly treated to reduce the target's RCS and increase its survivability. This thesis analyzes and compares various TFRs on non-wide sense stationary signals in hope of providing test centers with better methods for locating scattering centers under time variant conditions.

Acknowledgements

Table of Contents

List of Figures

List of Tables

List of Symbols

List of Abbreviations

Application of Time-Frequency Representations To Non-Stationary Radar Cross Section

I. Introduction

Radar Cross Section imaging is used to identify areas of high RCS on military weapon systems. The localization of high RCS "flare spots" allows the weapon system designers to treat the suspected region to reduce its signature. In general, the designers are able to locate these areas through an implementation of the Fourier transform. The radar system used to create the large bandwidth signal needed for high-resolution RCS plots is the coherent pulsed stepped frequency radar. If the target is stationary over the radar's sampling period, the post processed image will properly place the scatters in range. However, if the target moves during the sampling period, either unintentionally or through a reconfiguration, the standard RCS image processing will misplace and/or "smear" a localized feature over the average of apparent localizations. Therefore, for non-stationary targets, Time Frequency Representations must be used to locate areas of high RCS as a function of time and range. The time value produced by the TFR allows the weapon system designer to understand the RCS contributors at a specific target configuration.

In this thesis, a comprehension of multiple Time Frequency Respresentations is desired to fully exploit the useable features from a non-stationary RCS signal in hope of accurately locating RCS flare spots. The correct usage of these TFRs can be used to more accurately detect regions of high RCS scattering on non-stationary weapon systems allowing the weapon system designer to locate and treat these areas to reduce the system's overall RCS and increase its survivability. The aim of this research is to offer the Low Observable (LO) community a better method for detecting scattering features in a non-stationary environment than the standard Short Time Fourier Transform (STFT).

This thesis is structured into five chapters covering current TFR research and usage, the development of four promising TFRs, the implementation of these TFRs on non-stationary RCS data, and finally an analysis and comparison of their RCS flare spot localization abilities. Specifically, Section II reviews the coherent pulsed stepped frequency radar, the development of stationary and non-stationary electromagnetic signals, and Time Frequency Representations. The Time Frequency Representations explored in this section include: the Short Time Fourier Transform, the ambiguity function, the Wigner distribution, the Pseudo Wigner distribution and the Cochleagram. The discussion on these TFRs includes their mathematical roots and how they differ from each other. It is important to mention that a Wavelet Time-Frequency approach is another promising method for analyzing non-stationary RCS. However, as it pertains to the scope of this thesis, Wavelets will not be covered. Section III describes the implementation of four TFRs on non-stationary RCS data. Targets were developed to mimic simple stationary and non-stationary scenarios. The targets are discussed to provide the reader with an understanding of their purpose and expectations. RCS measurements on the targets were accomplished using AFIT's anechoic chamber. Range setup photos not provided in this section can be seen in Appendix A. Section III also discusses the data obtained, and the implementation of four TFRs on this data. The four TFRs implemented include: the standard Short Time Fourier Transform, Gaunaurd's Short Time Fourier Transform, the Wigner distribution and the Scene Match function. Processing of the RCS target data by each of the TFRs was accomplished in Matlab® and can be reviewed in Appendix B. Section IV presents and discusses the RCS flare spot localization plots produced by the implemented TFRs on the non-stationary target data. An in depth analysis of each of the TFRs was accomplished to include their strengths, weaknesses and recommended implementation. TFR plots for the targets not analyzed in this section can be found in Appendix C. Finally, Section V reviews conclusions made throughout the thesis and offers recommendations to the LO community and future research in this area on the usage of TFRs for RCS analysis.

II. The Application of Time Frequency Representations in RCS Imaging

2.1 Introduction

According to E.F. Knott, a renowned Radar Cross Section expert, there are five basic reasons for conducting RCS measurements on a target. The five reasons are [12]:

1. Acquire understanding of basic scattering phenomena;

2. Acquire diagnostic data;

3. Verify system performance;

4. Build a database;

5. Satisfy a contractual requirement.

In this thesis, the acquisition of diagnostic data through radar image processing of a non-wide sense stationary RCS is explored. Radar image processing helps locate areas of high RCS on major weapon systems. The localization and treatment of these "flare spots" is crucial to the low observable characteristics of the weapon system being designed [12]. RCS imaging of a non-wide sense stationary signal poses significant challenges in identifying scattering centers in the post processed radar generated image. A non-wide sense stationary RCS is typically encountered when moving parts on the target impress a relative phase shift into the backscatter signal. When the Fourier transform of the phase shifted complex signal is taken, range and cross range information on scattering centers are misplaced. Time Frequency Representations must be used to locate scattering centers so they can be properly treated in order to reduce the weapon system's RCS and increase its survivability. Currently, the Short Time Fourier Transform is used to determine the localization of flare spots given a time varying signal. However, other TFRs may be better suited for flare spot localization.

In this section, the RCS imaging process is described. The Short Time Fourier Transform is discussed and analyzed. Alternative TFRs to include the ambiguity

3

function, Wigner distribution, pseudo Wigner distribution, and Cochleagram are derived and analyzed as possible techniques for better flare spot localization over the Short Time Fourier Transform. It is important to note that the bold face terms in this section represent the first time the term is used. The symbols page contains a list of the bold faced terms referenced to the page they were first used.

2.2 RCS Image Formation via Step Frequency Radar

RCS flare spots on targets can be located using specialized radar imaging equipment such as the coherent pulsed stepped frequency radar. This system produces a step-frequency waveform that allows high resolution images of the target to be formed.

2.2.1 Step-Frequency Waveform. The step-frequency waveform used in imaging radars consists of a group of **N** coherent pulses whose frequencies are increased by frequency step **Δf**. The frequency of the nth pulse can be expressed by the equation:

$$f_n = f_0 + n\Delta f \tag{2.1}$$

where $\mathbf{f_0}$ is the starting frequency and $\mathbf{f_n}$ is the frequency of the nth pulse [27]. Each pulse is **T** seconds long and the time interval between pulses is designated as $\mathbf{T_r}$. Although the instantaneous bandwidth of each pulse is narrow, a large bandwidth can be realized by processing all N pulses to effectively equal $N\Delta f$. From this, the range resolution of the target using a stepped frequency waveform is computed to be:

$$\Delta R = \frac{c}{2B_{eff}} = \frac{c}{2N\Delta f} \tag{2.2}$$

where $\mathbf{\Delta R}$ is the range resolution and $\mathbf{B_{eff}}$ is the effective bandwidth. It should be noted that N can be increased to produce very high resolution [27].

2.2.2 Coherent Pulsed Stepped Frequency Radar. A coherent pulsed stepped frequency radar system typically has a low power RF source with the voltage-controlled oscillator phase locked to a stable quartz oscillator. The system's coherent receiver contains two oscillators, the coherent oscillator (COHO) and the stabilized local oscillator (STALO). The transmitted signal is the amplified sum of the COHO, STALO and stepped frequency given by the expression [27]:

$$f = f_{stalo} + f_{coho} + n\Delta f \qquad (2.3)$$

where $\mathbf{f_{stalo}}$ and $\mathbf{f_{coho}}$ are the STALO and COHO frequencies respectively.

The radiated RF pulse is reflected off the test target and captured by the receiving antenna. The received signal goes through an amplifier and then a mixer set to the STALO frequency. The output of the mixer is down converted to the COHO's Intermediate Frequency (IF). The receiver's synchronous detector uses the COHO signal as a reference signal to extract phase and amplitude information from the down converted return pulse given that they are now at the same frequency. The synchronous detector produces two complex outputs; one is in-phase and the other quadrature-phase (I and Q). Two phase detectors are required to eliminate blind phases. Using only a single phase detector would risk loosing signal information if the sampling did not occur at the peak positive or negative values of the sinewave [22]. The quadrature signal is generated by mixing the received signal by a 90° phase shift from the COHO. Therefore, if the COHO signal in the I channel is $sin(\ 2\pi f_{IF}\ t)$, then the COHO in the Q channel is $cos\ (2\pi f_{IF}\ t)$, where $\mathbf{f_{IF}}$ is the Intermediate Frequency and $\mathbf{t}$ is time [22]. Having both the I and Q channels eliminates blind phases, ensures a uniform output with no loss, improves the Signal to Noise Ratio (SNR) and discriminates positive and negative Doppler frequencies [27]. This type of receiver is paramount for producing radar imagery due to the necessity of phase information in image processing [12].

In modern coherent pulsed stepped frequency radars, the STALO is programmed to discretely step through a large frequency band. As an example, the AFIT RCS

range system can be programmed to sweep from 6 GHz to 18 GHz with discrete frequency steps of 10 MHz. The return pulses for each frequency are typically integrated before stepping to the next frequency. The radar will sweep through its frequency band and store the computed I and Q data before moving onto the next azimuth test angle θ. The received (I and Q) data over all test azimuth angles, typically $\theta = 0 - 360^o$, is processed using a two dimensional Fourier transformation. The transformed data reveals range and cross range scattering information. Resolution in range depends on the number of frequency samples used over the frequency sweep as described in Equation 2.2, while cross range resolution depends on the angular width used to step through the angular sweep. The resulting data produces a radar image of the target [12].

2.2.3 Modeling the Target Return Using a Step Frequency Radar. In order to understand the TFRs used for non-stationary RCS analysis, it is important to have a firm understanding of the theory and equations used in step-frequency radar processing. The transmitted signal can be represented by the equation:

$$s(t) = A_1 cos2\pi(f_0 + n\Delta f)t \tag{2.4}$$

Where $\mathbf{s(t)}$ is the transmitted signal and $\mathbf{A}$ is the amplitude. The return echo after a round trip delay of $\frac{2R}{c}$ is represented as:

$$r(t) = A_2 cos2\pi(f_0 + n\Delta f)(t - \frac{2R}{c}) \tag{2.5}$$

where $\mathbf{r(t)}$ is the return signal, $\mathbf{R}$ is the distance to the target and $\mathbf{c}$ is the speed of light.

The output of the phase detector, which is used for RCS imaging, is modeled as the product of the received signal and the reference signal. The resulting product is then sent through a low pass filter. For in-phase sampling, the phase detector will

6

output $A \cos(\phi_n)$ for the nth pulse. Likewise, the output for quadrature sampling is represented as $A \, jsin(\phi_n)$ where [27]:

$$\phi_n = 2\pi(f_0 + n\Delta f)\frac{2R}{c} \tag{2.6}$$

and ϕ represents the phase of the signal. Therefore, the combination of the I and Q channels results in $A \cos(\phi_n) \; + \; A \, jsin(\phi_n)$. Through Euler's identity this simplifies to $Ae^{-j\phi_n}$. The magnitude of the return signal is obtained by taking the square root of $I^2 + Q^2$ [22].

2.3 Scattering in RCS Imaging

The coherent pulsed stepped frequency radar is commonly used in the RCS diagnostic community for producing radar images. The National Radar Test Facility (NRTF) range in New Mexico and AFIT's own RCS anechoic chamber use similar systems to produce radar images of test targets. This system works very well at locating areas of high RCS with respect to azimuth angle θ when the target is stationary over the frequency sweep. The return pulses of a stationary target are correlated to a fixed range and phase and can be classified as wide sense stationary (WSS) over the sweep. Post processing of a stationary signal will accurately place the scattering centers in range.

2.3.1 Stationary Target. For a stationary target, Equation 2.6 can be represented as:

$$\phi_n = \frac{4\pi f_0 R}{c} + 2\pi \cdot \underbrace{\frac{\Delta f}{T_r}\frac{2R}{c}}_{f_s} nT_r \tag{2.7}$$

where the braced section represents the frequency shift $\mathbf{f_s}$. Resolving the frequency shift allows one to measure the range by taking the Discrete Fourier transform (DFT) of the received signal from N frequency stepped pulses [27]. The range measurements are dependent on the frequency limitations. If the differential of the frequency shift is taken, we clearly see the dependence through:

7

$$\Delta R = \frac{c}{2} \frac{T_r}{\Delta f} \Delta f_s \tag{2.8}$$

where $\Delta f_s = \frac{1}{NT_r}$ [27]. Substituting the expression for Δf_s into Equation 2.8, range resolution can be simplified to:

$$\Delta R = \frac{c}{2N\Delta f} \tag{2.9}$$

Similarly, the unambiguous range $\mathbf{R_u}$ can be obtained through the equation:

$$R_u = \frac{c}{2\Delta f} \tag{2.10}$$

Therefore, for a stationary target, the unambiguous range R_u is divided into N subdivisions each with width $\frac{c}{2N\Delta f}$ to give the range resolution ΔR [27].

However, if the target moves during the frequency sweep, a Doppler and phase shift will be impressed onto the backscatter signal that is uncorrelated in range and phase to the transmitted pulse from which the matched filter is made. When the DFT of the complex non-stationary signal is taken, pulse to pulse phase and range information are no longer correlated and portions of the resulting target image are misplaced in range. In order to better understand the range inaccuracies, one must understand the theory behind a non-stationary RCS signal.

2.3.2 Moving Target. Non-stationary targets will impose additional effects into the return signal. The radar return from a target of constant velocity $\mathbf{v}$ and range R can be expressed by the equation:

$$R_n = R_0 + vnT_r \tag{2.11}$$

The phase of signal produced by a moving target is represented as:

$$\phi_n = 2\pi(f_0 + n\Delta f)\frac{2}{c}(R_0 + vnT_r) \tag{2.12}$$

8

This equation can be expanded to reveal contributing frequency components as [27]:

$$\phi_n = \frac{4\pi f_0 R_0}{c} + 2\pi \underbrace{\frac{\Delta f}{T_r}\frac{2R_0}{c}}_{f_s} nT_r + 2\pi \underbrace{\frac{2vf_0}{c}}_{f_d} nT_r + 2\pi \underbrace{\frac{2vn\Delta f}{c}}_{f_{spread}} nT_r \qquad (2.13)$$

where $\mathbf{f_d}$ is the Doppler frequency and $\mathbf{f_{spread}}$ is the frequency spread [27]. Equation 2.13 implies that some of the returned signal has accurate phase information from the range of the target, but is obscured by the Doppler frequency, the frequency shift, and the frequency spread components. The first two terms of Equation 2.13 are the same as the stationary target from Equation 2.7. The third term in Equation 2.13 is the Doppler shifted frequency that is impressed onto the frequency shift of the second term due to the target's motion [27]. This term will shift the range from the target's true range and can be calculated by the equation:

$$R_s = \frac{vT_r f_0}{\Delta f} \qquad (2.14)$$

where $\mathbf{R_s}$ is the range shift. This can also be expressed in terms of processed range bins as:

$$L_{rbs} = \frac{2vT_r f_0 N}{c} = \frac{2vNT_r}{\lambda_0} \qquad (2.15)$$

where $\mathbf{L_{rbs}}$ is the range bin shift and λ is the wavelength.

The term f_{spread} is a result of the interaction of the stepped frequency and the motion of the target. Because there is a pulse to pulse change in frequency, the Doppler shift will not be constant even if the target's velocity is constant. The Doppler shift for the nth pulse can be represented as $\frac{2vn\Delta f}{c}$. Therefore, the return from a target using N pulses of a stepped frequency will contain N frequency components in the complex data domain [27]. When the DFT is taken to produce range information, the spread in frequency of $\frac{2vN^2 T_r \Delta f}{c}$ will result in a range spread of vNT_r. In terms of range bins, this is equal to:

$$P_{rbs} = \frac{vNT_r}{\Delta R} = \frac{2vN^2T_r\Delta f}{c} \tag{2.16}$$

where $\mathbf{P_{rbs}}$ is the range bin spread. The spread in range makes it difficult to determine range accuracy and magnitude. Instead of a point scatter being located in one bin, it will now be spread across $\frac{vNT_r}{\Delta R}$ bins. The spreading factor will cause a point scatterer to occupy a region of L to $L + \frac{vNT_r}{\Delta R}$ bins [27]. A correction factor must be applied to remedy this spread.

In order to counteract the spreading factor from the fourth term in Equation 2.13, one must multiply the received signal from N pulses with the correction factor below before taking the DFT [27]:

$$C_1(n) = e^{-j4\pi vn^2T_r\Delta f/c} \;=\; e^{-j2\pi f_{spread}} \tag{2.17}$$

The correcting factor $\mathbf{C_1}$ will rotate the samples in the opposite direction and cancel the spread of the signal. The correcting factor will place all the components of a point scatterer in one location [27].

The range shift can also be included in the correcting factor by amending Equation 2.17 to account for the third term in Equation 2.13 to become:

$$C_2(n) = e^{-j4\pi(vf_0nT_r+vn^2T_r\Delta f)/c} \tag{2.18}$$

The use of correcting factor $\mathbf{C_2}$ will remove target motion while retaining the high resolution characteristics of a stepped frequency waveform [27].

In order to use the correction factor properly, one must have a good estimation of the target's velocity. If the target's velocity is not known, many estimates may be used between the target's min and max expected velocity. This compensation technique will place the target peak into clutter and also spread the clutter out beyond its range domain of $\frac{cT}{2}$ [27]. In order to maintain high resolution and range accuracy,

the following steps must be performed to cancel out clutter effects on the velocity corrected data:

1. Take the DFT of the N sampled weighted received signal according to a range bin (of width $\frac{cT}{2}$) from the stepped frequency waveform.

2. Cancel the clutter (stationary components) by zeroing out points associated with stationary scatterers in the range domain.

3. Convert this data back into the frequency domain by taking the IDFT of the clutter free data.

4. Apply the velocity compensation formula from Equation 2.18. Estimate the target's velocity or use several velocities.

5. Convert the data back into the range domain by taking the DFT of the corrected data. This will show the true target position and range profile [27].

Precise scattering locations from Doppler shifted data are difficult to determine. If the scattering center cannot be located and treated, the overall target RCS is negatively affected and its survivability is jeopardized. The above technique assumes we know the target's velocity and that it is constant over the signal's duration. However, moving parts on a target will cause a relative velocity change from pulse to pulse. For this reason, TFRs are used to analyze the return signal in both frequency and time simultaneously.

2.4 Time Frequency Representations

As mentioned earlier, Fourier analysis is used to identify the frequency components of a time dependent signal. However, this technique cannot describe when those frequency components occurred in time. The lack of time resolution in Fourier analysis calls for the use of Time Frequency Representations when the analysis of a time varying signal is needed. A signal that varies in time can be defined as non wide sense stationary or just non-stationary for short. TFRs are used to analyze,

modify and synthesize non-stationary signals. The three-dimensional plot produced by a TFR allows one to determine which spectral components of a signal vary with time [25].

There are two major groups of TFRs: linear and quadratic. The linear group of TFRs consist of the Short Time Fourier Transform and the Wavelet Transform. For the purpose of this thesis, only the STFT is analyzed. "Linear TFRs satisfy the superposition principle which states that if $\mathbf{x(t)}$ is a linear combination of signal components, then the TFR of $x(t)$ is the same linear combination of the TFRs of each of the signal components" [25].

Quadratic TFRs are branched into the energetic or correlative interpretations. The energetic interpretation is best represented by the Wigner distribution ($\mathbf{WD}$). The Wigner distribution seeks to combine information from the instantaneous power $\mathbf{p_x(t)} = |x(t)|^2$ and the spectral energy density $\mathbf{P_x(f)} = |X(f)|^2$, where $\mathbf{X(f)}$ is the frequency domain transformed signal of $x(t)$. The ambiguity function ($\mathbf{AF}$) represents the best correlative interpretation of the quadratic TFR. The correlative TFR seeks to combine information from the temporal correlation $\mathbf{r_x}(\tau) = \int_t x(t + \tau)x^*(t)dt$ and the spectral correlation $\mathbf{R_x}(\nu) = \int_f X(f + \nu)X^*(f)df$, where τ represents a time delay and ν represents a Doppler shift [25].

The Short Time Fourier Transform, the Wigner distribution, and the ambiguity function are all related through the Cohen class of Time Frequency distributions. In 1966, Leon Cohen developed a general method for generating an infinite number of bilinear Time Frequency distributions based on a generalized equation and a change-able kernel function. A bilinear distribution seeks to accurately represent the energy of a signal in time and frequency [20]. Cohen's class of TFRs is a general expression indicating that a specific TFR can be created using Cohen's generalized bilinear distribution function. Other types of TFRs seek to achieve Time-Frequency accuracy through statistical, parametric, spatial and temporal models [20]. In this section, the Short Time Fourier Transform, the Wigner distribution, and the ambiguity func-

tion are described, analyzed and tied together through a summary that relates them to the generalized Cohen bilinear Time Frequency distribution function [20]. The Cochleagram is also offered as an alternative spatial/temporal TFR model [20].

2.4.1 The Short Time Fourier Transform. A common linear TFR used for RCS processing is the Short Time Fourier Transform. The Short Time Fourier Transform of the signal $x(t)$ can be represented by the equation [11, 18, 23]:

$$STFT_x(t, \omega) = \int_{-\infty}^{\infty} x(\tau)\omega(\tau - t)e^{-j\omega\tau}d\tau \qquad (2.19)$$

where $\omega(\mathbf{t})$ is a window function.

The STFT breaks the non-stationary signal into windows of time and then transforms these segments into the frequency domain through the Fourier transform [8]. It is assumed that the rate of variation in time is relatively slow in order to compute the change in frequency over the defined time period [2]. The windowing function $\omega(t)$ can be centered at a particular time. However, it should extract a finite portion of the sequence $x(\tau)$ such that the spectral content of the section is approximately stationary over the windowing [15]. Time resolution can be acquired by sliding the windowing along the time axis.

The STFT is commonly plotted on two axes, with the vertical axis representing frequency content ω and the horizontal axis representing time index t. The magnitude is represented as a color pattern on the plot. The representation of the STFT in this manner is commonly called a spectrogram.

For practical reasons, the STFT must be calculated in discrete windows $\omega(n)$. The discrete STFT for a window defined by the region $0 \leq n \leq N - 1$ is defined by the equation [8]:

$$STFT_x(k, l) = \sum_{n=0}^{N-1} x(k - n)\omega(n)e^{j(2\pi/N)ln} \qquad (2.20)$$

13

where l and $k = 0, 1, 2,..., $ N-1 and $\omega(n)$ is a window function.

The type and width of the windowing used in the STFT is very important in revealing the frequency content over the time evolution of the signal. For instance, a rectangular time window will produce side lobes that distort the transform. For this reason, the windowing function should have small side lobe amplitude levels in order to resolve independent frequency content located in the same vicinity [15]. Such windows include the Hamming and Hamm windows.

Window lengths should be chosen in order to cover stationary parts of the signal. For rapidly changing frequency content, a small window length N is required. However, a decrease in window length also means a decrease in frequency resolution due to the Time-Frequency (TF) resolution properties of the Discrete Fourier Transform. As we know, when conducting a Fourier transform there is an inverse relationship between resolution in the frequency domain and in the time domain. If one wants to acquire high resolution in the frequency domain, they must use long segments of time, which conversely degrades time localization. Similarly, if one wants high localization in time, frequency resolution will be lost. Therefore, for a rapidly changing signal, it becomes almost impossible to resolve signal components which are close in frequency within a short window duration [30]. Because of this, the STFT is an inadequate TFR if the time variations of the frequency content change quickly relative to time [2,8,30].

The time and frequency resolution errors in the STFT make it a poor tool for conducting TFR plots of electromagnetic (EM) target signatures. The STFT of non-stationary RCS data causes smearing of features due to the frequent range changes over the sampling period. Because of this, the STFT has relatively inferior resolution to other TFR techniques. Quadratic TFR techniques such as the ambiguity function, Wigner distribution (WD) and the Pseudo Wigner distribution (PWD) can be used to analyze time varying signals with higher Time-Frequency localization capabilities. These techniques can be applied to EM type signals to analyze non-stationary RCS data [8,30].

2.4.2 The Ambiguity Function. The ambiguity function (AF) is the matched filter response of a radar signal with time delay τ and Doppler shift ν [14]. It is a bilinear distribution (a distribution of two independent variables) developed as a means of studying the ambiguity of a radar signal in time and Doppler shift in order to determine a target's equivalent range and velocity [10]. The ambiguity function of the complex signal $x(t)$ is defined by the equation:

$$AF(\tau, \nu) = \int_{-\infty}^{+\infty} x(t + \tau/2)x^*(t - \tau/2)e^{-j\nu t}dt \tag{2.21}$$

where the asterisk denotes the complex conjugate. The ambiguity function serves to describe a target through range and velocity. A positive τ implies a target is farther from the radar than the predetermined value ($\tau = 0$). Likewise, a positive value ν means the target has positive closing velocity [10, 14]. It is important to understand that τ and ν represent differences in range and velocity of the resolved targets rather than actual ranges and velocities of the targets [10].

The formulation of the AF can easily be understood through an analysis of Section 2.3.2. The output of the matched filter under a zero Doppler condition is called the autocorrelation function and can be expressed by the equation [27]:

$$R(\tau) = \int_{-\infty}^{+\infty} s(t + \tau/2) \cdot r^*(t - \tau/2)dt \tag{2.22}$$

where $s(t + \tau/2)$ is the transmitted signal and $r^*(t - \tau/2)$ is the return signal.

For a moving target, the return signal is equal to the Doppler shifted transmitted signal represented by the equation [27]:

$$r(t - \tau/2) = s(t - \tau/2)e^{-j\nu t} \tag{2.23}$$

A substitution of Equation 2.23 into Equation 2.22 yields Equation 2.21, where $x(t + \tau/2)$ replaces $s(t + \tau/2)$ [10, 14].

15

The ambiguity function has four properties that are crucial to its understanding [14].

- **Property 1.** The AF is Maximum at (0,0).

$$|AF(\tau, \nu)| \leq |AF(0,0)| = 1 \qquad (2.24)$$

The AF can not be higher anywhere than the origin. The energy in the AF is normalized to one.

- **Property 2.** The AF has constant volume.

$$\int_{-\infty}^{+\infty} \int_{-\infty}^{+\infty} |AF(\tau, \nu)|^2 d\tau d\nu = 1 \qquad (2.25)$$

The total volume of the AF under normalized conditions is equal to one.

- **Property 3.** The AF has symmetry about the origin.

$$|AF(-\tau, -\nu)| = |AF(\tau, \nu)| \qquad (2.26)$$

It is sufficient to calculate only two quadrants of the AF. Additional information can be deduced from the symmetry property.

- **Property 4.** Linear FM shearing effect.

  The complex envelope $x(t)$ has an ambiguity function of $AF(\tau, \nu)$ through:

$$x(t) \Leftrightarrow |AF(\tau, \nu)| \qquad (2.27)$$

The addition of a Linear Frequency Modulated (LFM) pulse in the transmitted radar signal will result in a shearing of the AF as described in the equation:

$$x(t)e^{(j\pi k t^2)} \Leftrightarrow |AF(\tau, \nu - k\tau)| \qquad (2.28)$$

where $k = \pm\frac{B_{eff}}{T}$ [14].

Although it has been shown that a LFM pulse will shear the AF, the LFM will also improve delay resolution. It is also to be noted that a positive slope ridge passing from the third to the first quadrant of the AF will inherently give positive error in estimating target range (target appears to be farther than it really is) and lower closing velocity (target appears to be slower than it really is through negative Doppler) [14].

Analysis of the AF is done through delay and velocity cuts. For instance, a cut along the delay axis can be done by setting $\nu = 0$, yielding the equation:

$$|AF(\tau, 0)| = \left| \int_{-\infty}^{+\infty} x(t + \tau/2)x^*(t - \tau/2)dt \right| = |R(\tau)| \tag{2.29}$$

where $R(\tau)$ is the autocorrelation function. This will produce the zero Doppler cut of the AF giving us the range window. The autocorrelation function of $x(t)$ is equal to the inverse Fourier transform of the power spectral density. Knowing this, the use of LFM pulses will expand the power spectrum and narrow the range window [14].

Another interesting cut of the AF is the Doppler cut. This is accomplished by setting $\tau = 0$, which produces the equation:

$$|AF(0, \nu)| = \left| \int_{-\infty}^{+\infty} |x(t)|^2 e^{-j\nu t}dt \right| \tag{2.30}$$

The zero delay cut is the Fourier transform of the magnitude squared of the complex envelope $x(t)$, meaning it is only a function of the amplitude [14].

For RCS image processing, the ambiguity function must be modified to fit the type of radar signal used. As stated earlier, a common type of radar signal used for imaging is the coherent pulsed stepped frequency waveform. This type of signal offers good range resolution due to the overall bandwidth and good Doppler resolution from the extended duration of the coherent signal. The AF in this form is represented by the equation [14]:

17

$$|AF(\tau,\nu)| = \left|\left(1 - \frac{|\tau|}{T}\right) sinc\left[T\nu\left(1 - \frac{|\tau|}{T}\right)\right]\right| \times \left|\frac{sin\{N\pi[\nu + \Delta f(\tau/T_r)]T_r\}}{Nsin\{\pi[\nu + \Delta f(\tau/T_r)]T_r\}}\right| \quad |\tau| \leq T$$

$$(2.31)$$

where T is the time duration of the pulse, T_r is the time duration between pulses, N is the number of pulses, and Δf is the frequency step. It is important to note that if $T\Delta f < 1$, the autocorrelation function over the delay $|\tau| < T$ exhibits additional lobes [14].

According to Levanon, the first null of the autocorrelation function will occur at $\tau_{null} = \frac{1}{N\Delta f}$ and grating lobes will appear at a delay of $\tau = \frac{n}{\Delta f}$. The first null on the Doppler axis will occur at $\nu_{null} = \frac{1}{NT_r}$ and the first Doppler ridge will cross the Doppler axis at $\nu_{peak} = \frac{1}{T_r}$. To avoid grating lobes on the zero-Doppler axis, one must keep $T\Delta f < 1$. If no weighting is used, it is best to keep $\Delta f \leq 1 - \frac{1}{N}$ [14].

In order to implement the AF effectively on a non-stationary RCS signal, a technique must be implemented to resolve velocity and range on moving and stationary targets. A technique to resolve Doppler from a pulsed stepped frequency can be done through stretch processing [14]. Stretch processing will produce a two-dimensional delay-Doppler response. This process can easily be implemented on AFIT's own RCS range system. The output of the frequency sweep for a single azimuth angle θ will be designated as the vector U containing M complex elements, one per pulse. Under zero-Doppler conditions, the complex output U would be sent to a single IFFT to produce range information. However, because the target has velocity, U will be transformed into a bank of M Doppler filters, each version of U possessing a different Doppler shift. This can easily be accomplished by using Matlab® to perform the computation $DFTMTX * diag(U)$. The Matlab® function $DFTMTX$ is the Discrete Fourier transform matrix in a Galois field. The function is described by the Matlab® reference document as:

"$dm = DFTMTX(alph)$ *returns a Galois array that represents the discrete Fourier transform operation on a Galois vector, with respect to the Galois scalar*

18

alph. The element alph is a primitive nth root of unity in the Galois field $GF(2m) = GF(n + 1)$; that is, n must be the smallest positive value of k for which $alph^k$ equals 1. The discrete Fourier transform has size n and dm is an n-by-n array. The array dm represents the transform in the sense that dm times any length-n Galois column vector yields the transform of that vector."

Similarly, the `Matlab`® function *diag* is described by the reference document as:

"X = diag(v,k) when v is a vector of n components, returns a square matrix X of order $n + abs(k)$, with the elements of v on the kth diagonal. $k = 0$ represents the main diagonal, $k > 0$ above the main diagonal, and $k < 0$ below the main diagonal."

The computation $DFTMTX * diag(U)$ is accomplished by performing the following steps:

1. Compute $DFTMTX(M)$. This will produces the $M \times M$ complex matrix of values around the unit circle whose inner product has a column vector length M and gives the discrete Fourier transform of the vector.

2. Multiply the $DFTMTX(M)$ matrix by a $M \times M$ diagonal matrix whose diagonal elements are the M elements of U. The resulting $M \times M$ matrix has rows containing the complex array of a different Doppler progressing version of U.

3. Each row can now be processed by adding weights and taking the IFFT. The absolute value of the matrix is taken to reveal the response of the Doppler filters used in the stretch processing [14].

The resulting AF will have the sloped ridge associated with a LFM pulsed AF. The ridge in the AF makes it difficult to resolve delay from Doppler. In order to separate delay from Doppler properly, a Costas code should be used that is of length M. A Costas code differs from a LFM pulse in that it uses a randomlike frequency evolution [14]. The coding difference is scene in Figure 2.1. In both signals, there is one dot in each row and column. This means that at any time slice, there is only one

transmitted frequency. However, the random order of the frequency pulses from the Costas code ensures that the number of coinciding delay-Doppler shifts of N points can only be one, as opposed to the LFM pulse which could have multiple coinciding points due to its sloping pattern [14]. If a Costas code is used, the processor should reorder the inputs to the IFFT according to the carrier frequency. Weighting is not required under random like signals such as the Costas code [14].
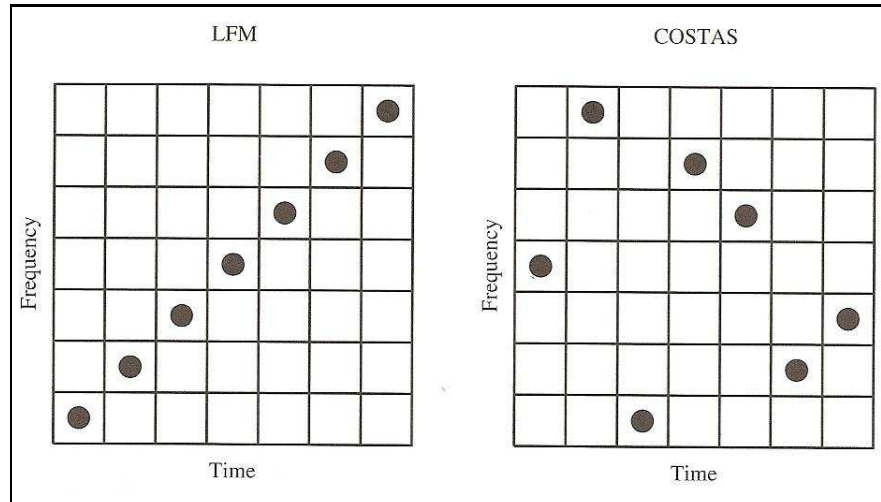
Figure 2.1:   LFM vs. Costas Code [14]

2.4.3   The Wigner Distribution.   The Fourier transform pair of the ambiguity function is the Wigner distribution [30]. The WD is a quadratic TFR that is of the energetic interpretation [25]. The Wigner Distribution has been employed as an alternative to TF analysis to overcome the shortcomings of the STFT [30]. It provides high resolution in both time and frequency by satisfying time and frequency marginals in terms of instantaneous power in time and energy spectrum in frequency [30]. For signal concentration, the WD is superior to other TFRs [11].

In order to define the Wigner distribution, let $R_x(t, \tau)$ be the instantaneous autocorrelation of a complex signal $x(t)$, defined by [30]:

$$R_x(t, \tau) = x(t + \tau/2)x^*(t - \tau/2) \tag{2.32}$$

As defined, the instantaneous autocorrelation is the product of the complex signal shifted from the left and to the right by means of the time delay variable, τ [30]. Given this, the Wigner distribution of $x(t)$ is defined as the Fourier transform of the instantaneous autocorrelation, $R_x(t, \tau)$, with respect to the time delay τ by [4, 5, 7, 11, 17, 21, 23, 30]:

$$WD_x(t, \omega) = \int_{-\infty}^{\infty} x(t + \tau/2) x^*(t - \tau/2) e^{-j\omega\tau} d\tau \tag{2.33}$$

where x^* is a complex valued signal. In order to use the Wigner distribution on sampled data, a discrete form of Equation 2.33 must be applied in the form [8, 28]:

$$WD_x(k, l) = 2 \sum_{n=0}^{N-1} x(k + n) x^*(k - n) e^{i(4\pi/N)ln} \tag{2.34}$$

where k represents time, l represents the transformed spatial domain, n represents a discrete sample, and N represents the total number of samples. According to [7, 8, 10, 17], the auto-Wigner distribution of any real or complex value is real, where $W_f(t, \omega) = W_f^*(t, \omega)$. The realness of the Wigner distribution is a consequence of the Hermiticity property of the product inside the integral [7]. Although the WD is real, it is not always positive [7]. The Wigner distribution is superior to the ambiguity function in that it preserves time and frequency domain shifts and does not have the resolution versus localization trade-off problems of the STFT [8].

The Wigner distribution does have difficulties however. If $x(t)$ is frequency limited or time limited then so will the Wigner distribution. The Wigner distribution is also a bilinear function of the waveform $x(t)$. This means that when the signal is the sum of various independent components, i.e. $x(t) + y(t)$, the Wigner distribution is:

$$WD_{x+y}(t, \omega) = WD_x(t, \omega) + 2Re[WD_{x,y}(t, \omega)] + WD_y(t, \omega) \tag{2.35}$$

and will have the unwanted "cross-term" contribution $2Re[WD_{x,y}]$ in addition to the two auto-components $WD_x(t,\omega) + WD_y(t,\omega)$ [11]. The cross-term contribution $WD_{x,y}(t,\omega)$ is defined as:

$$WD_{x,y}(t,\omega) = \int_{-\infty}^{\infty} x(t+\frac{\tau}{2})y^*(t-\frac{\tau}{2})e^{-j\omega\tau}d\tau \qquad (2.36)$$

Cross-term contributions will lie between two auto-components and are oscillatory. The frequency of the cross-term effect will increase with respect to the separation of the time-frequency location of the individual components [11, 26]. Cross-term contributions produce a peak value twice as high as the auto-components [11]. "For independent multicomponent signals, the cross-terms introduce contributions that are unwanted and that must be somehow minimized" [8]. With a complicated signal, the cross-component terms make it difficult to interpret a Wigner distribution [11, 26]. Cross-term interference carries redundant information that obscures the primary features of a signal [30]. A plot of a Wigner distribution of a two-component signal with cross-term effects is seen in Figure 2.2.
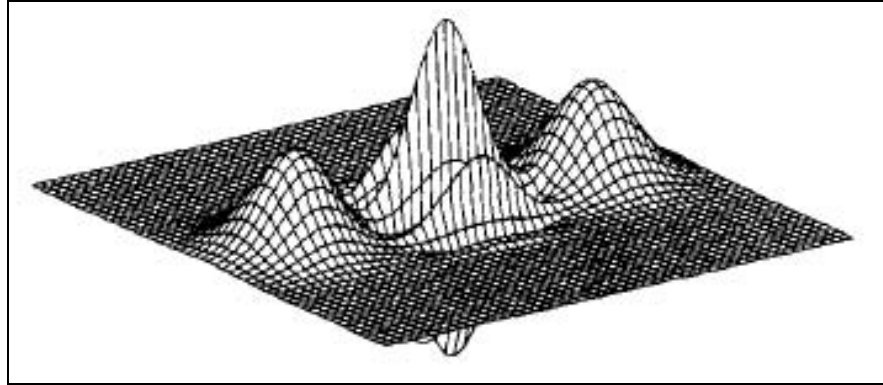
Figure 2.2:   Cross-term contributions from a two-component signal generated from a Wigner distribution.

Figure 2.2 is taken from [11] so the reader has an understanding of the unwanted contributions the cross-terms create. In Figure 2.2, the auto-components are the outside lobes, while the cross-term effect lies between the auto-components and has twice the amplitude as expected. In the above example, it is easy to recognize the

cross-term contribution. However, for more complicated signals, it is often extremely difficult to resolve individual components from the cross-term contamination.

Several variants of the WD have been developed to combat the effects of the cross-term contribution while still preserving the independence of the time and frequency resolution [2, 30]. It is possible to apply low pass filtering to suppress the high frequency components of the cross-term. Smoothing of the WD is also a practical solution through the Pseudo Wigner distribution.

2.4.4 The Pseudo Wigner Distribution. In order to suppress the cross-term contributions, a Pseudo Wigner Distribution (PWD) is used. To digitally evaluate the PWD, the signal must be discretized to the form [8, 9]:

$$PWD_x(k,l) = 2 \sum_{n=0}^{N-1} x(k+n)x^*(k-n) \cdot \omega_x(n)\omega_x^*(-n)e^{i(4\pi/N)ln} \qquad (2.37)$$

where the window function $\omega_x = exp(-\alpha t^2)$ is of Gaussian form, and α is a positive real number that controls the width of the time window.

As one can see, Equation 2.37 is closely related to the STFT from Equation 2.20. The major difference between the two equations lies with the function to which the Fourier transform is taken. According to Equation 2.20, the STFT transforms only the return signal within the time slice $x(k-n)$. The WD and PWD instead use the transform of the signal's autocorrelation, where the autocorrelation changes as a function of time. Visually this is represented in Figure 2.3.

In short, the PWD of a non-stationary signal offers more advantages than the WD. The PWD can be computed from windowed data and introduces little smearing in the time domain as opposed to the high degree of smearing as seen in the STFT. Also, because the WD or PWD are not always positive gives advantages in instantaneous characterization of a non-stationary signal. The cross-term interference also offers realistic insight to the physical results. One can use windowing that suppresses

23

k=0		k=1		k=2		k=3	
0	-0*	1	1*	2	2*	3	3*
1	-1*	2	0*	3	1*	4	2*
2	-2*	3	-1*	4	0*	5	1*
3	-3*	4	-2*	5	-1*	6	0*
4	-4*	5	-3*	6	-2*	0	-1*
5	-5*	6	-4*	0	-3*	1	-2*
6	-6*	0	-5*	1	-4*	2	-3*
f(k+n)	f*(k-n)	f(k+n)	f*(k-n)	f(k+n)	f*(k-n)	f(k+n)	f*(k-n)

Figure 2.3:   A visual representation of the sliding autocorrelation function used in the WD and PWD before the Fourier transform is taken.

the cross-term influence. One can also find a time window that reveals useful cross-term contributions while suppressing useless ones. For RCS target analysis, the PWD proves to be the best at manifesting target characteristics that were hidden from other TFRs. [8].

2.4.5   Cohen Class Relation.   It is important to understand that the Short Time Fourier Transform and Wigner distribution are considered members of the Cohen class of Time Frequency Representations. Proposed by Leon Cohen in 1966, the generalized Cohen distribution function utilizes bilinear transformations, where a time and frequency shift in the signal is represented as an equivalent time and frequency shift in the distribution, as seen by the equation [20, 30]:

$$C_x(\tau, \omega; \Phi) = \frac{1}{2\pi} \int_{\infty}^{\infty} \int_{\infty}^{\infty} \int_{\infty}^{\infty} \Phi(\tau, \varepsilon) e^{i(\varepsilon t - \omega\tau - \varepsilon\mu)} x(\mu + \frac{\tau}{2}) x^*(\mu - \frac{\tau}{2}) d\mu d\tau d\varepsilon \quad (2.38)$$

where $\Phi(\tau, \varepsilon)$ is the kernel function and determines the TFR [8–10, 20, 30]. For example, to produce the STFT, the kernel function is set to:

$$\Phi_s(\tau, \varepsilon) = \int_{\infty}^{\infty} \omega(\mu + \frac{\tau}{2}) \omega(\mu - \frac{\tau}{2}) e^{i\varepsilon\mu} d\mu \quad (2.39)$$

yielding Equation 2.19. Likewise, for the Wigner distribution, $\Phi(\tau, \varepsilon) = 1$, yielding Equation 2.33 [8,30]. Any Cohen class distribution can be formed by multiplying the TFR's kernel $\Phi(\tau, \varepsilon)$ with the ambiguity function $AF_x(\tau, \varepsilon)$ and then performing the double Fourier transform [8,10,20,30]. In this sense, the kernel is a weighting function on the ambiguity function in the (τ, ε) domain [8].

An interesting relationship between the ambiguity function and Wigner distribution arises upon close inspection of Equation 2.38. One can see that the Wigner distribution and the ambiguity function are a Fourier transform pair:

$$AF_{x,y}(\tau, \nu) = \int_t \int_f WD_{x,y}(t, f)e^{-j2\pi(\nu t - \tau f)}dtdf \qquad (2.40)$$

2.4.6 The Cochleagram. Time-Frequency techniques can also be studied through the Cochleagram. The Cochleagram is a measure of the ear's cochlear activity as a function of location along the cochlea.

The cochlea is the structure in the ear by which sound is transformed into an electrical signal to the nerves. The pressure wave from sound causes a displacement of the cochlear fluids. This wave interacts with the stiffness of the basilar membrane to produce a progressive travelling wave on the membrane. When the basilar membrane moves up and down, a relative movement will occur between the tectorial membrane and the organ of corti, this results in a bending of the hairs. The wave travels up the cochlea from the base all the way to the apex [19]. The basilar membrane can be viewed as the processing unit for the cochlea [3]. Figure 2.4 illustrates the position of the cochlea in the human ear. Figure 2.5 illustrates the interactions between the tectorial membrane and the basilar membrane.

High frequency waves peak at the base of the cochlea where the basil membrane is the smallest. Because high frequency waves peak at the base, high frequency sound is transduced near the base of the cochlea. Likewise, low frequency sounds peak near the apex of the cochlea where they are transduced [19]. The pattern of movement in

25
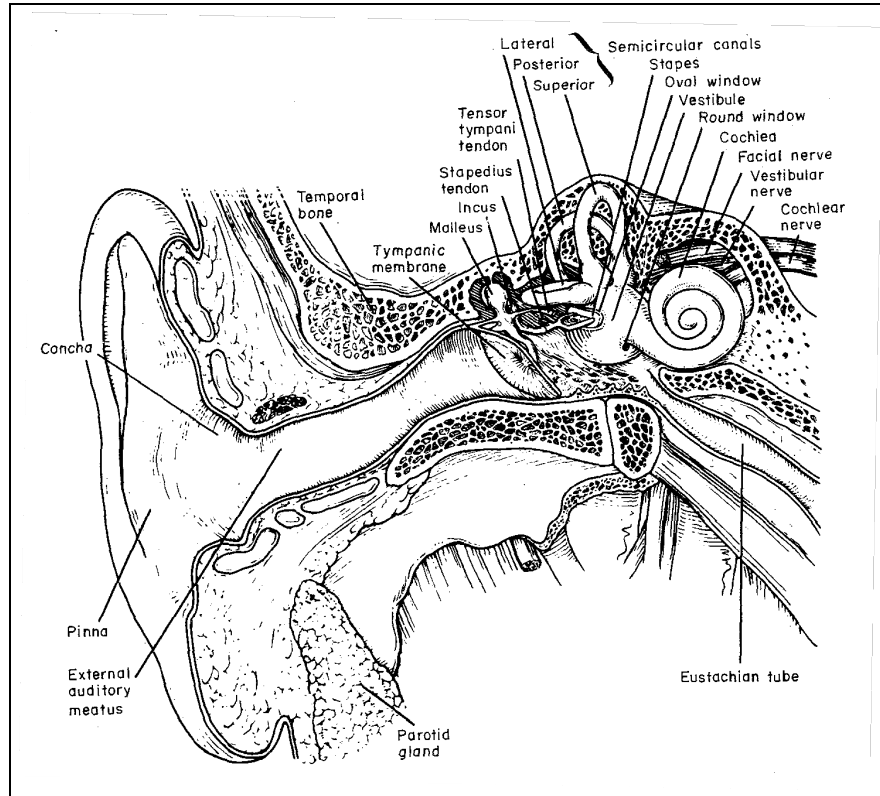
Figure 2.4: Anatomy of Human Ear [19].
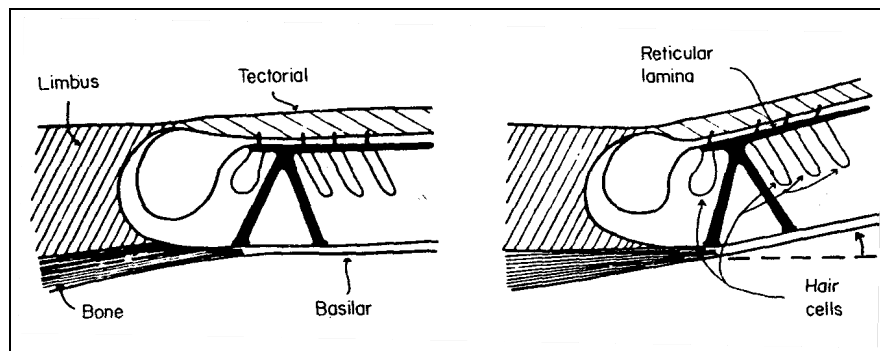
Figure 2.5: As the basilar membrane is deflected, the hair cells bend and cause electrical conduction [19].

the basilar membrane depends on the frequency of the sound. The system shows a high degree of frequency selectivity [19].

Electrical conduction occurs through the deflection of the stereocilia by the travelling wave which opens and closes ion channels in the stereocilia. The wave-like motion of the pressure wave modulates the current being driven into the hair

26

cell by the combined effects of the positive endocochlear potential and the negative intracellular potential [19]. Potential changes can be measured with electrodes [19].

Because the position along the cochlea is highly responsive to a single sound frequency, cochlear models represent the sound signal as a function of time and frequency [24]. The resulting Cochleagram is a two dimensional representation of sound. A commonly used cochlear model is the Lyon's model, designed by Richard F. Lyon. In his model, sound is filtered by a cascade of band pass filters. This models the response of the basilar membrane at any point along its length, where the center frequency decreases along the length. Therefore, different distances along the basilar membrane are tuned to a specific frequency similar to a spectrum analyzer [13]. The output of each filter is half-wave rectified to simulate the hair cell detector and then coupled into an automatic gain control to simulate the adaptation process. Each filter output is called a channel. There are typically 50-100 channels that are used to make the model of the cochlear process. The output of this model is a sample by sample estimate of the probability of firing of the auditory process [24, 29]. The half-wave rectifiers detect the output of the second order filter and serve to convert the motion of the basilar membrane along the cochlea into a signal that retains the frequency content and fine time information [6, 16]. Figure 2.6 illustrates this process.
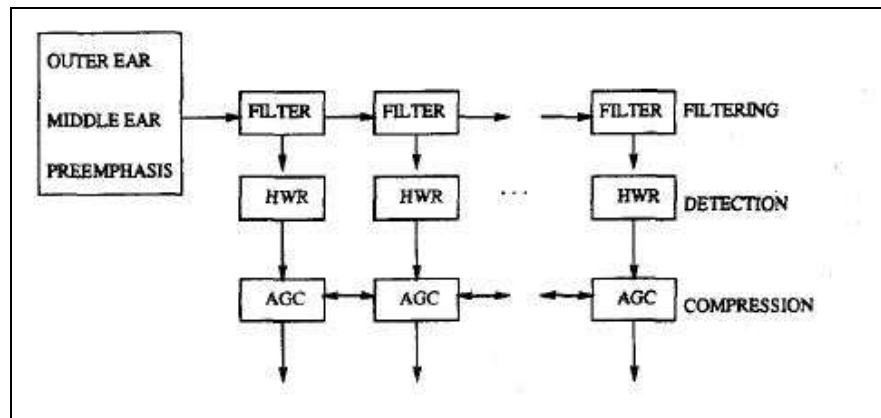
Figure 2.6:   Lyon's Cochlear Model [16]

The Time-Frequency manifestation created through the Cochleagram can be applied to RCS type signals. The RCS response of a target can be modeled as a

27

function of theoretical range through the phasor of the backscatter signal. The correlation of the backscatter's phase and that of a phasor created through theoretical range values along the target can provide the target's frequency response and location response simultaneously. This information can be used to locate RCS flare spots with high accuracy.

III. Implementation of Time Frequency Representations on Non-Stationary RCS

3.1 Introduction

The analysis of Time Frequency Representations on non-stationary targets requires a controlled data set. This section describes the data acquisition process used to obtain the non-stationary RCS data. Target schematics and descriptions are provided which detail their purpose and TFR expectations. Descriptions of the standard STFT, Gaunaurd's STFT, the Wigner distribution and the Scene Match function are provided. The implementation of these TFR's is also given to include their associated Matlab$^{®}$ code.

3.2 Necessary RCS Data For TFR Analysis

Non-stationary RCS data from a controlled target set was used to analyze the effectiveness of various Time Frequency Representations. The target set incorporated regions of stationary and non-stationary RCS. Both modes of scattering were required to analyze the effectiveness of TFRs in locating regions of RCS scatter under non-stationary conditions. The stationary components provided a reference location for regions of scattering, while the non-stationary components induced the unwanted range and Doppler phase effects into the backscatter signal.

3.2.1 AFIT Range Data Acquisition Process. Non-stationary RCS data was collected from AFIT's anechoic chamber range to compare the performance of various Time Frequency Representations. The range has a tapered design with dimensions of 14x45x26 ft. Schematics of the AFIT anechoic chamber are provided in Figures 3.1 and 3.2. A photo of the range facing the target mount pedestal is provided in Figure 3.3.

Measurements and data acquisition were accomplished using the Agilent Technologies E8362B Parametric Network Analyzer (PNA). This system is implemented as a coherent pulsed stepped frequency radar. The radar system provides both ver-
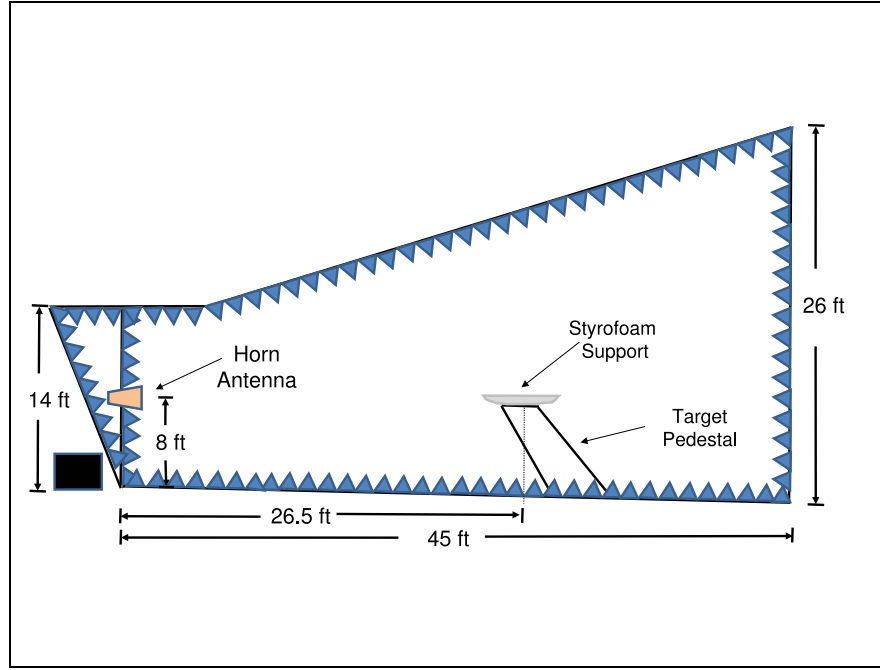
Figure 3.1:   AFIT anechoic chamber: side view.
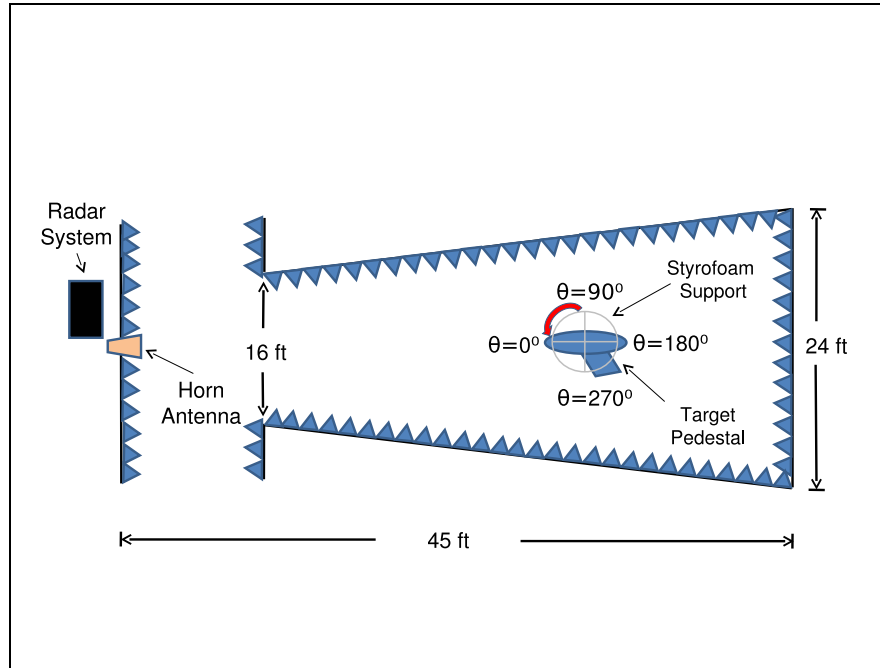
Figure 3.2:   AFIT anechoic chamber: top view.

tical and horizontal polarizations with an effective frequency band of $6 - 18$ GHz. The PRI of the system was set to $T = 250$ ns due to the range's size and gating properties. The IF bandwidth for the system was set to 300 Hz. This provided 480

30
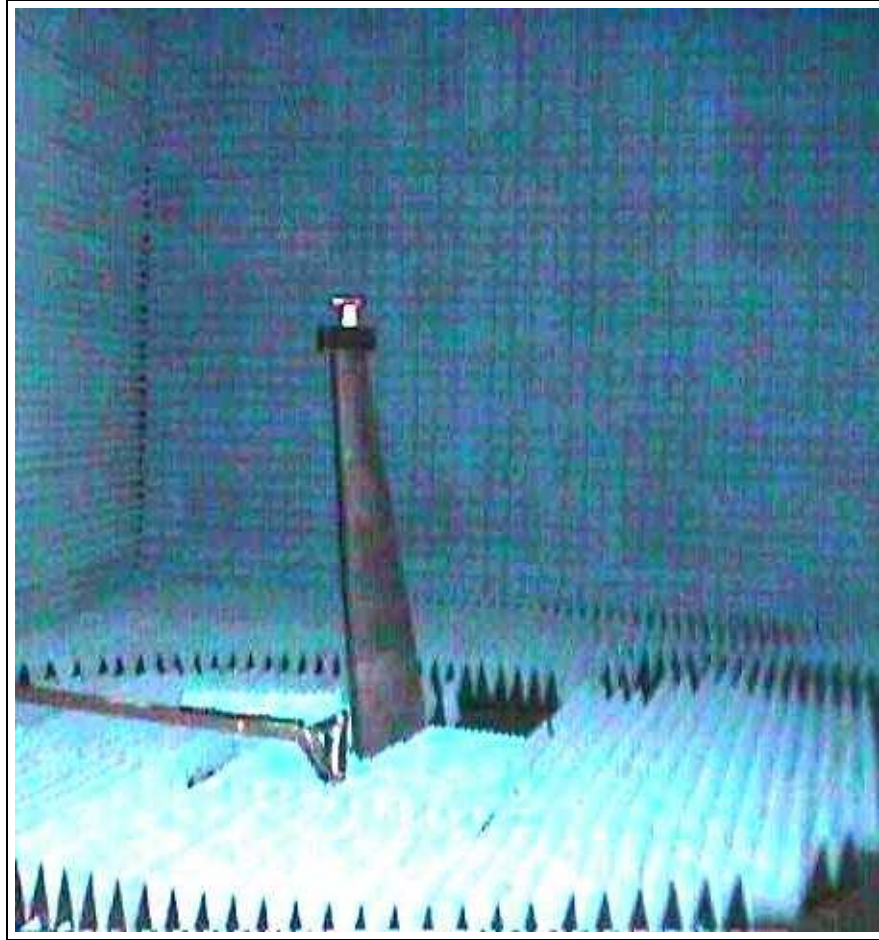
Figure 3.3:   AFIT anechoic chamber photo facing the target mount pedestal.

samples/pulses at each frequency during the frequency sweep. These samples were integrated and recorded as a trace point on the PNA. After the samples were taken for a specific frequency, the PNA stepped to the next trace point at another center frequency until the entire frequency sweep was completed. The large number of pulses provided sufficient SNR for the frequency response at each emitted frequency [1]. For this thesis, the Agilent PNA generated the RF, modulated the RF, and measured the RF returns. The AFIT RCS 1.00.vi LabView software controlled the radar. The LabView software was able to control the entire data collection once the user input the frequency range, the frequency step size, the rotational span, the rotational step size and the antenna's polarization.

The quiet zone of the target mount pedestal was approximately 1 ft^2 over the frequency range of interest and defined by the region that had less than 1 dB of attenuation at its farthest extent. The target mount pedestal, shown in Figure 3.4, was located 26.5 ft from the antenna horn. It has a single axis of rotation that is co-planar to the ground and capable of full $\theta = 0 \; to \; 360°$ azimuth sweep angles as depicted in Figure 3.2.

For each target, azimuth measurements were taken from $\theta = 0 - 360°$ with an angular step of $\Delta\theta = 0.25°$. This provided 1440 angular measurements which provided fine RCS measurements around the entire target. A frequency sweep from $6 - 18 \; GHz$ was used, maximizing the limits of the horn antennas. The frequency step, Δf, was set to 10 MHz -providing a bandwidth of 12 GHz and a range resolution of 0.49 in. The RCS data from each target was recorded as a matrix containing the magnitude and phase for each pulse and azimuth angle θ. Therefore, for each target, there were 1440 azimuth angular measurements taken to include 1200 backscatter returns for each azimuth angle θ. It is important to remember that each of the 1200 backscatter returns had a magnitude and phase that were functions of the frequency of the emitted pulse and the physical properties of the target.

In order to calibrate the range data, background and calibration measurements were performed. The AFIT chamber background measurements were achieved by measuring the target mount and pedestal with the full azimuth measurements from $\theta = 0 - 360°$ with an angular step of $\Delta\theta = 0.25°$. These measurements were coherently subtracted from the target measurement data to achieve the true scattering features from only the target. This process mitigated the effects from the environment on the target measurements. Calibration targets, shown in Figure 3.5 and Figure 3.6, with known exact RCS solutions were also measured. These measurements enabled calculating the overall RCS measurements of the targets. This was done to determine system losses and account for them.

Figure 3.4: AFIT anechoic chamber target mount pedestal. The photo was taken from the backside of the pedestal, where the Styrofoam mount that supported all of the targets can easily be seen. The power cable that drove the motor unit ran through the Styrofoam support and was looped inside of the elliptical foam absorber to suppress its interference effects on the backscatter. The cable can be seen running down the backside of the pylon.

The acquisition of the correct RCS backscatter from the target was achieved by appropriately isolating only the scattering from the target. The first step in the RCS

Figure 3.5:   Front View 3.25" Calibration Cylinder.

Figure 3.6:   Front View 4.50" Calibration Cylinder.

acquisition process was to calibrate the data to an absolute RCS quantity. An RCS quantity is typically represented as decibels per square meter, or $dBsm$. Calibration of the target's RCS was accomplished by taking the scattered field measurements of the target, $\vec{E}_{tar}^{S}$, the target mount, $\vec{E}_{tbk}^{S}$, the calibration target, $\vec{E}_{cal}^{S}$, and the target background, $\vec{E}_{cbk}^{S}$. The theoretical value of the calibration target, σ_{cal}, was applied to

the measurement results so they could be translated into an absolute value in $dBsm$. Mathematically the operation is:

$$\sigma_{tar} = \left| \frac{\vec{E}^S_{tar} - \vec{E}^S_{tbk}}{\vec{E}^S_{cal} - \vec{E}^S_{cbk}} \right|^2 \sigma_{cal} \qquad (3.1)$$

3.2.2 Target Design.   Targets were designed to be simple so TFR RCS analysis could be easily accomplished. Fourteen targets were developed. Each target contained certain features that could easily be identified during post processing. A description, purpose, and schematic for each target is given below. For each target group that was similar in nature, a photograph is provided to give the reader a better understanding of the structural geometry.

1. **Target 1**

   Description: A single 1 *in* steel sphere was placed at the center of the Styrofoam support.

   Purpose: To have a single stationary scatterer that does not change RCS with respect to azimuth angle θ or time.

2. **Target 2**

   Description: In addition to Target 1's configuration, a 1 *in* steel sphere was placed 6 *in* away from the center of the Styrofoam support on the $\theta = 0°$ line.

   Purpose: To resolve two scattering centers in the post processed image. The sphere located at the center does not change its range with respect to the azimuth angle θ. However, the off center sphere does change its range with respect to θ. Both targets were stationary over the sampling period, meaning there were not any rotating components active during the frequency sweep. This target demonstrates a simple stationary RCS environment.
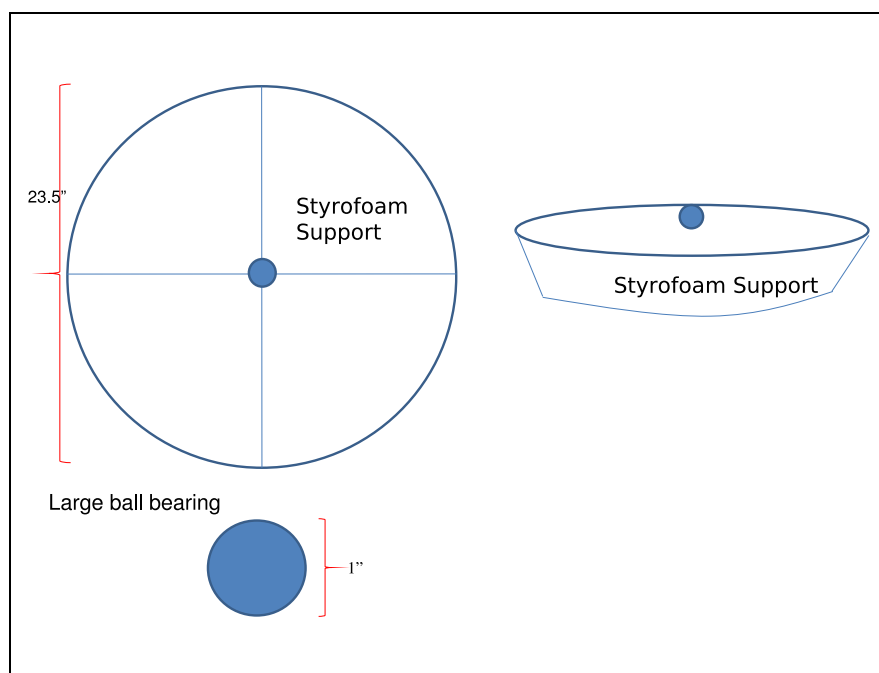
Figure 3.7:   Target 1 Schematic.
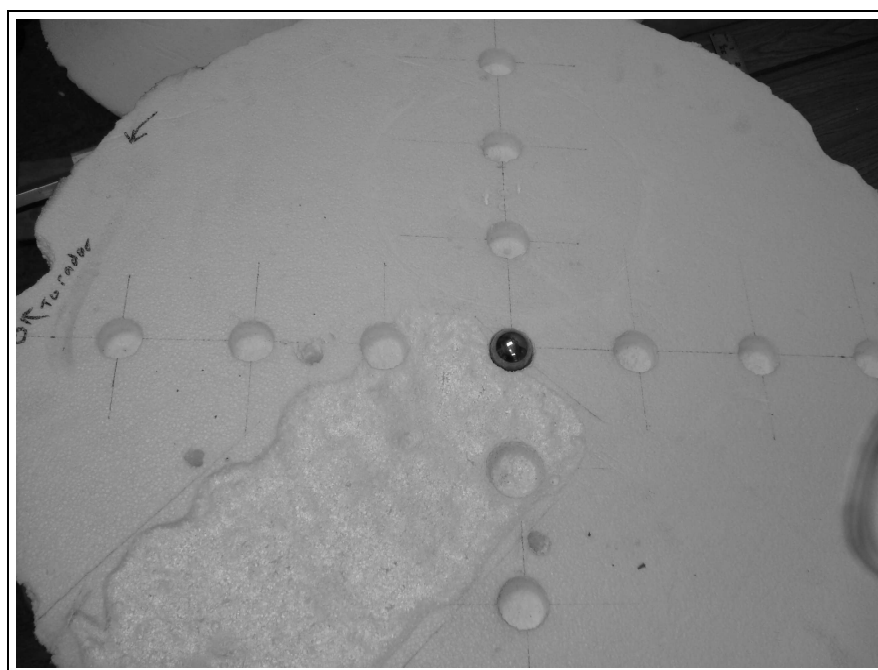
Figure 3.8:   Target 1 Range Photo.
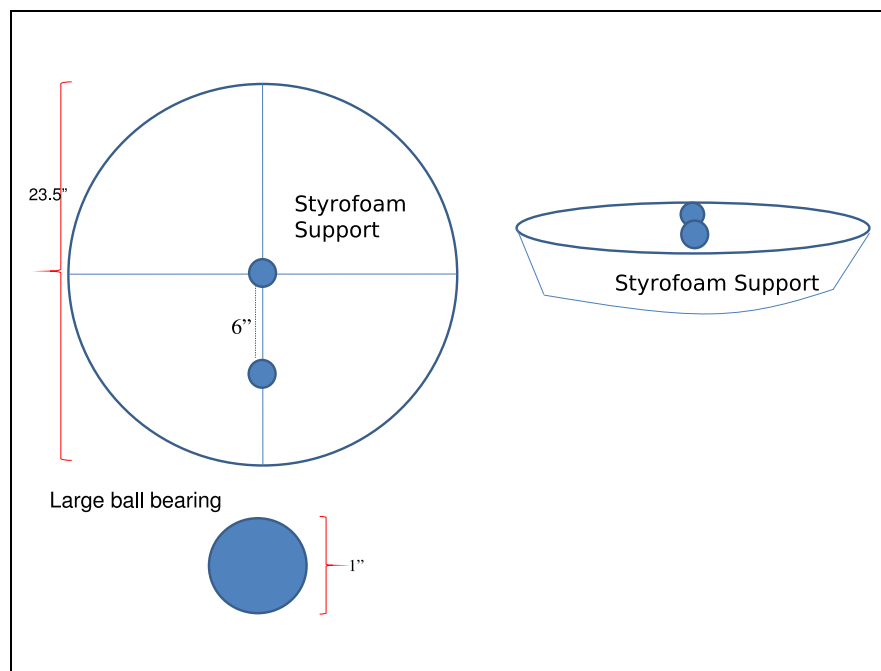
Figure 3.9:   Target 2 Schematic.

3. **Target 3**

    Description: A metallic cone was placed $4.5\ in$ off the center of the Styrofoam support with a height of $2.5\ in$.

    Purpose: The cone in this target houses the motor and gearing unit. The structure was designed to rotate a pair of ball bearings to provide non-stationary RCS data for subsequent tests. The target provides only the cone's RCS, it does not have any non-stationary contributors. The RCS should only change with respect to azimuth angle θ.
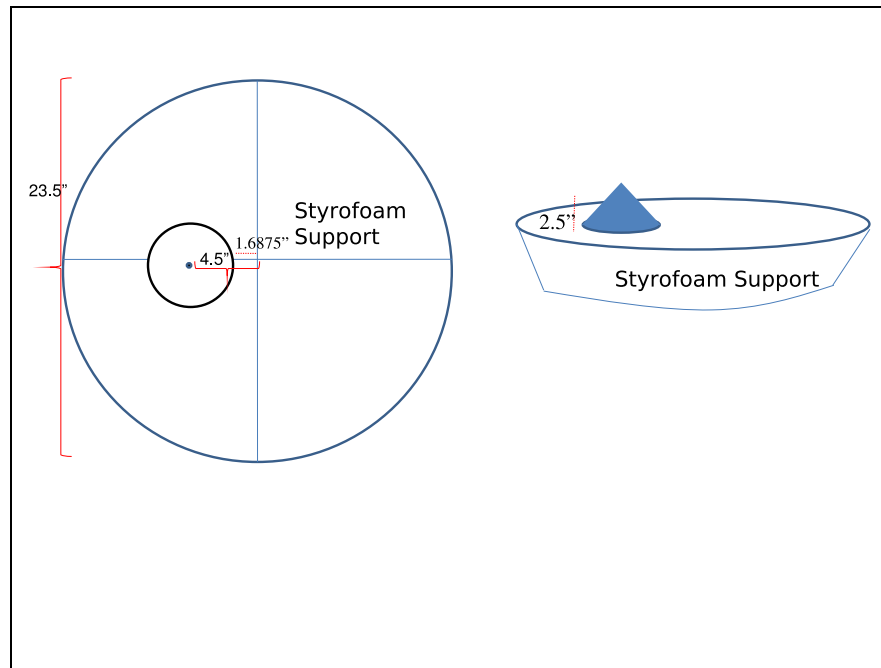
Figure 3.10: Target 3 Schematic.

4. **Target 4**

    Description: Target 3 was modified to have two rotating ball bearings mounted onto the top of the metallic cone. The ball bearings measured $0.39\ in$ and had their centers separated by $2\ in$. The ball bearings were supported by a circular Styrofoam structure that had a diameter of $6.25\ in$. The structure, as seen in Figure 3.12, was mounted to a gearbox internal to the cone.
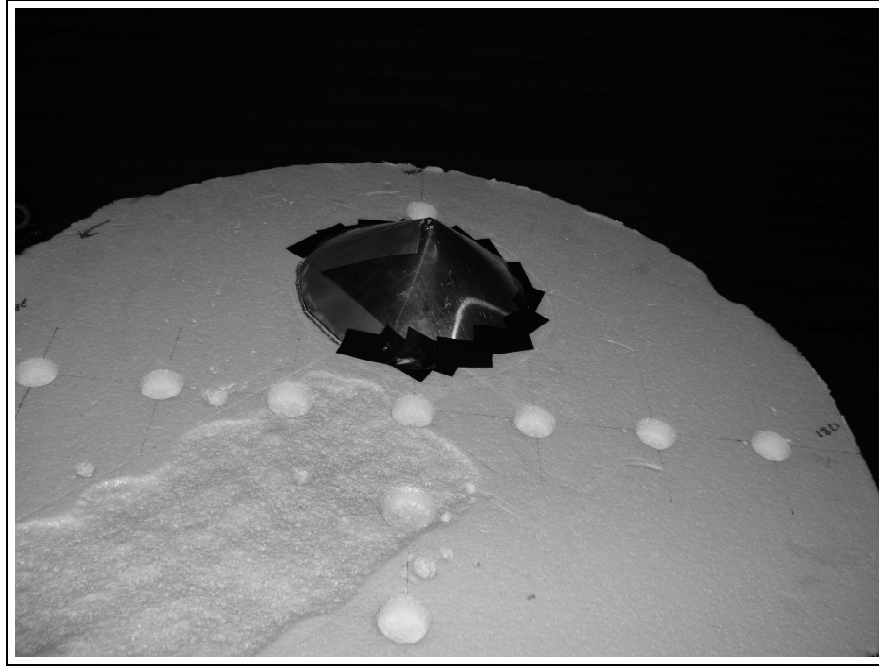
Figure 3.11: Target 3 range photo. The metallic cone was held down with electrical tape.
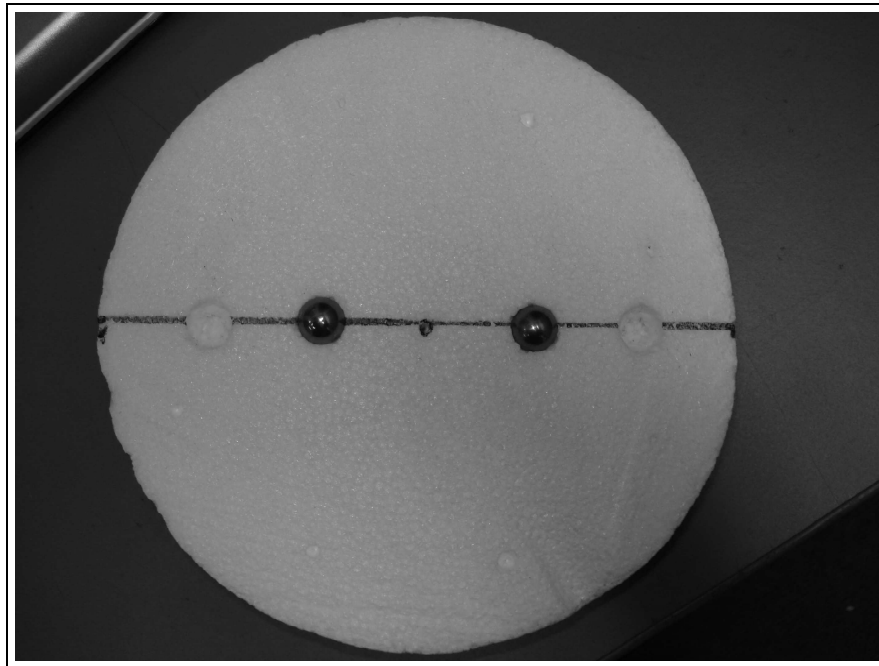
Figure 3.12: Non-Stationary Styrofoam Support Structure.

For this target, the gear box was set to rotate at a fixed speed of 10.25 *rpm*. Given that it took 4 seconds to complete a frequency sweep, the rotational speed

equated to the ball bearing unit rotating a total of 246° per sweep. Power was delivered to the motor unit by running a cable through the Styrofoam support structure and down the back side of the target mount pedestal. The wiring was connected to a power supply that delivered steady voltage throughout the test and was shielded from the radar by the foam absorber.

Purpose: To determine the effects the non-stationary components had on the backscatter RCS without interactions from other structures. This target was used as a baseline measurement when analyzing more complicated non-stationary targets.
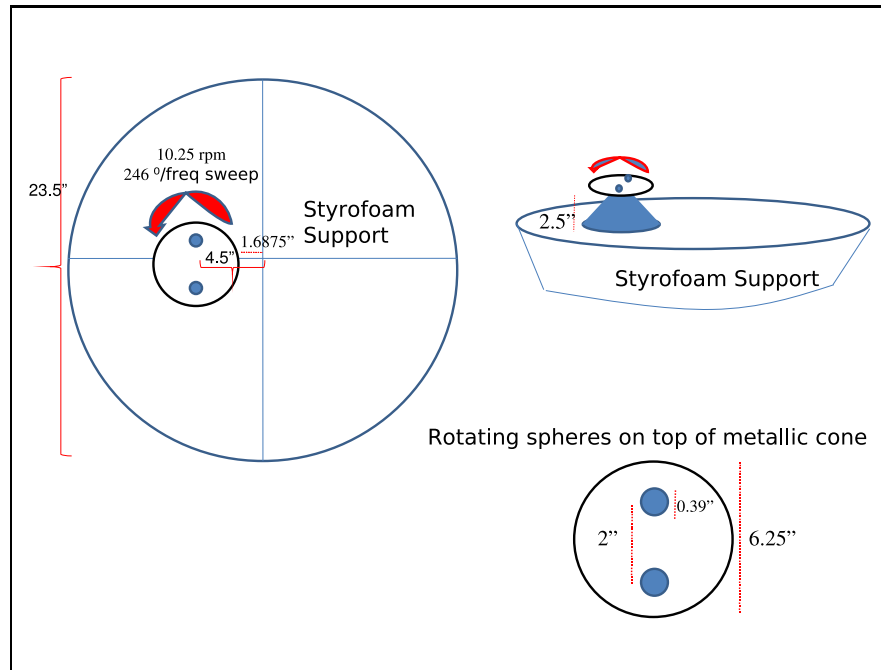
Figure 3.13:   Target 4 Schematic.

5. **Target 5**

   Description: A 1 *in* steel sphere was added to the Target 3 configuration. The sphere was placed 6 *in* from the center of the Styrofoam support on the $\theta = 0°$ line.

   Purpose: To have a RCS data set that included only the effects from the metallic cone and the 1 *in* sphere. The RCS data was stationary over the frequency sweep

and changed only as a function of θ. The data set was used to identify the two scatterers and their interacting effects. The RCS data from this target was used to compare the effects a non-stationary target, using a similar configuration, would impose on the backscatter.
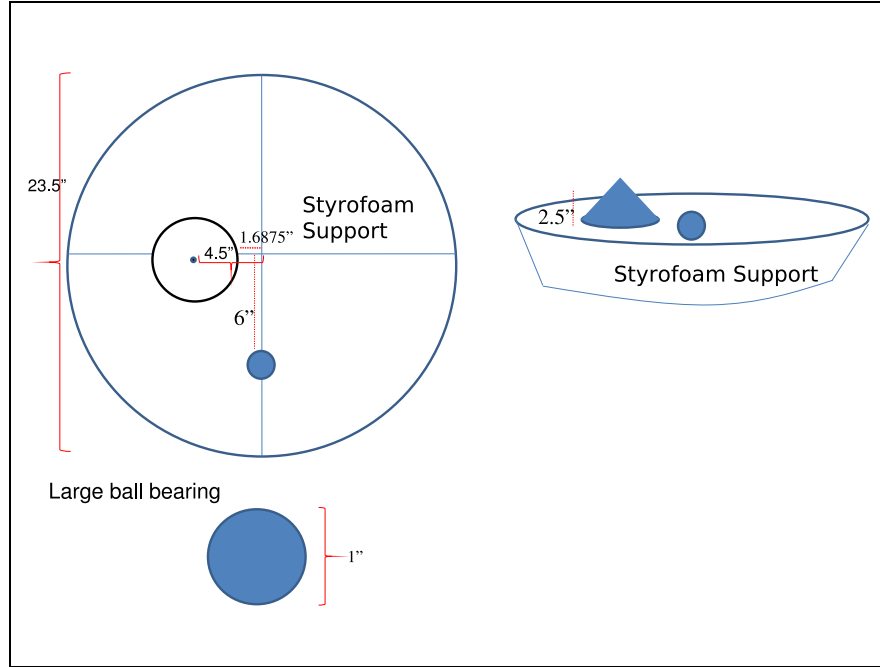
Figure 3.14:   Target 5 Schematic.

6. **Target 6**

Description: Target 5 was modified to include the rotating ball bearing structure on top of the metallic cone. The gear box was set to rotate at a fixed speed of 10.25 rpm. Given that it took 4 seconds to complete a frequency sweep, the ball bearing unit rotated a total of 246° per sweep.

Purpose: The target was designed to add non-stationary components to the design of Target 5. The impressed non-stationary phase components from the rotating ball bearings created the non-stationary RCS that was desired for TFR analysis. In this test, the RCS of the target was a function of azimuth angle θ and the non-stationary conditions from the rotating ball bearings.
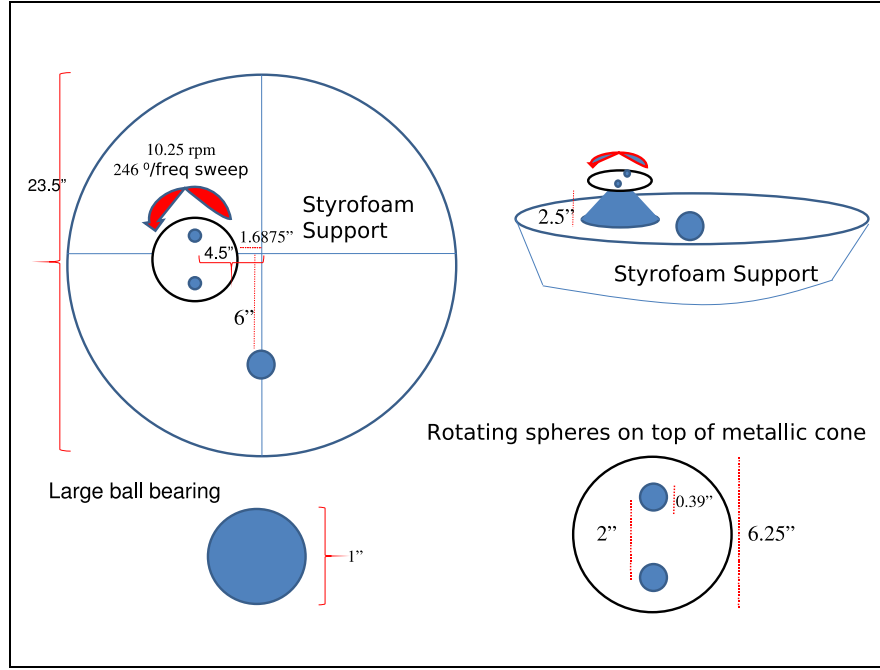
Figure 3.15:   Target 6 Schematic.

7. **Target 7**

Description: A copper trihedral was added to Target 3's configuration. The trihedral was placed 6 *in* from the center of the Styrofoam support on the $\theta = 0°$ line.

Purpose: Similar to Target 5, the RCS data set included only the effects from the metallic cone and the trihedral. A trihedral has a non-symmetric RCS pattern compared to the sphere and the cone. The RCS strength of the trihedral also changes as a function of aspect angle. Therefore, the RCS data for this target was stationary over the frequency sweep and only changed as a function of θ. The data set was used to identify the two scatterers and their interacting effects. The RCS data from this target was used to compare the effects a non-stationary target, using a similar configuration, had on the backscatter.

42
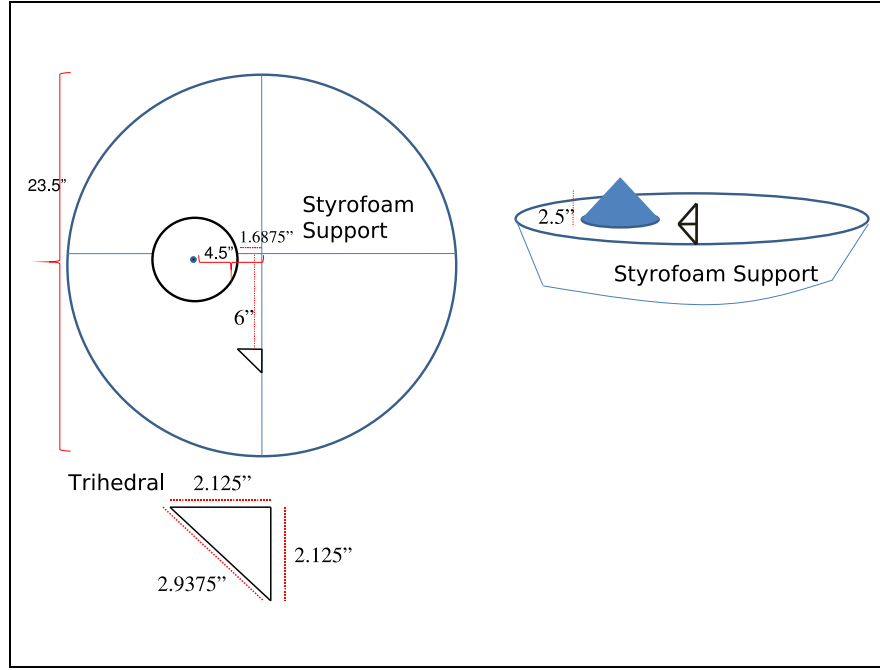
Figure 3.16:   Target 7 Schematic.

8. **Target 8**

Description: Target 7 was modified to include the rotating ball bearing structure. The ball bearing structure was stationary and positioned on the median of the Styrofoam mount as depicted in Figure 3.17.

Purpose: This target was designed to understand the scattering from the cone, ball bearings and trihedral configuration without the effects from the impressed Doppler frequency components. The RCS results from this target were compared with non-stationary versions of the same target configuration in order to understand how Doppler components affect complex geometry targets.

9. **Target 9**

Description: This target used the same configuration as Target 8 except the ball bearing rotational structure rotated at 2.07 rpm, equating to 49.25° per frequency sweep.

Purpose: The target was designed to understand the effects a slow rotational speed had on the overall non-stationary RCS. The rotation speed was set to the
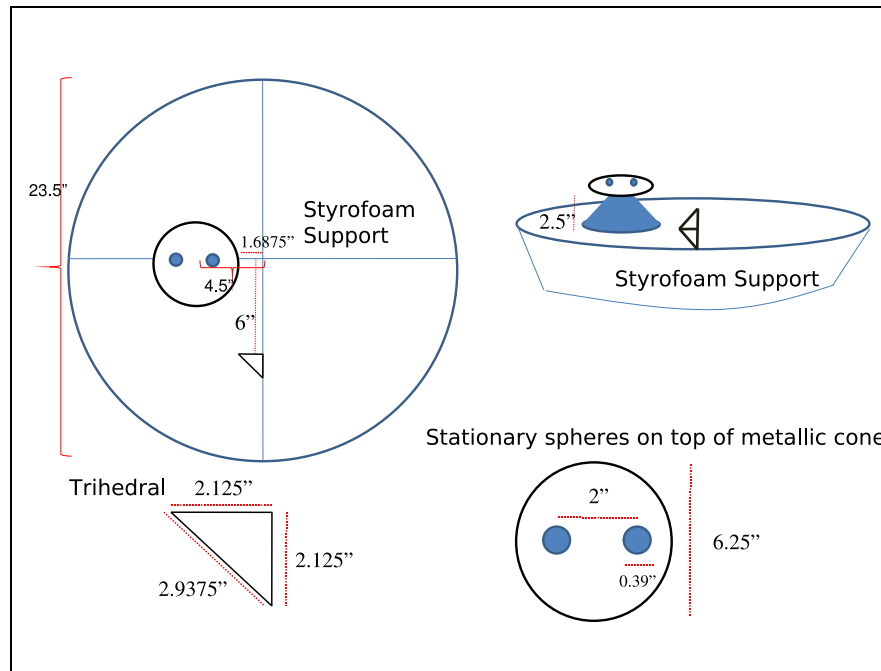
Figure 3.17:   Target 8 Schematic.
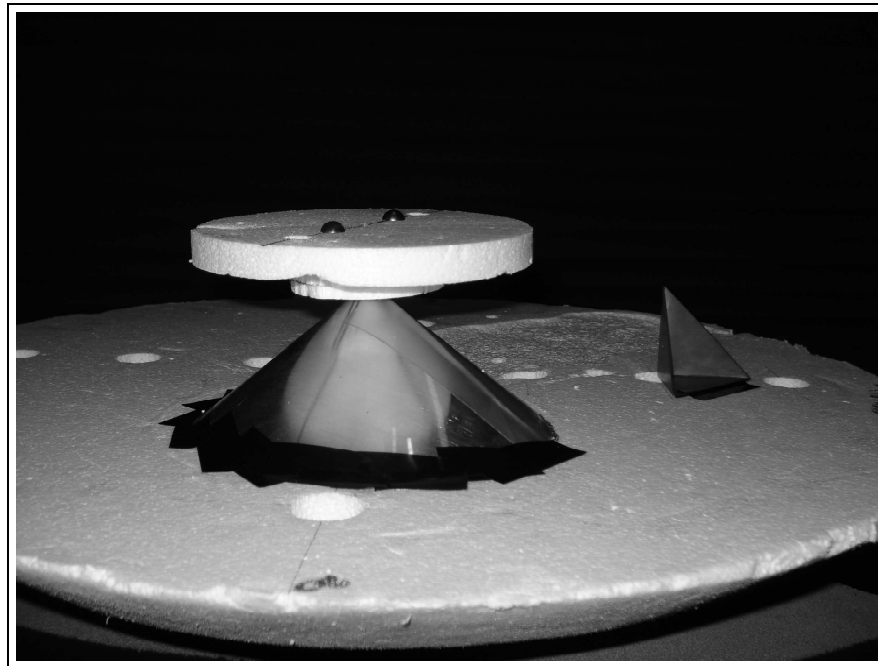
Figure 3.18:   Target's 8-11 Range Configuration.

minimum constant rotational speed allowed by the motor and gearing unit. The results from this target were compared to Target's 10 and 11 to fully understand

how the physical speed of the non-stationary components adversely affected RCS localization.
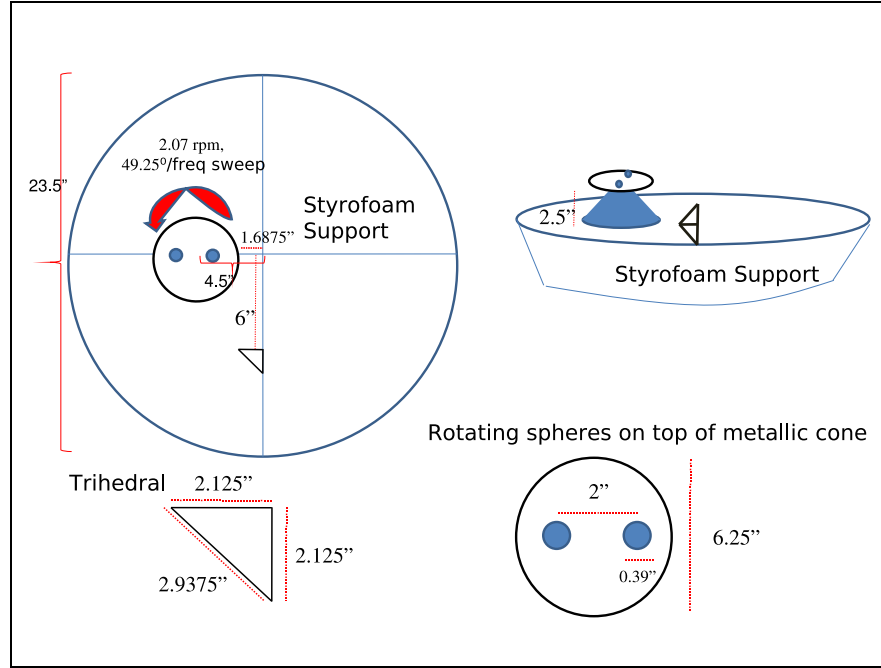
Figure 3.19:   Target 9 Schematic.

10. **Target 10**

Description: This target had the same configuration as Target 9. However, the rotational ball bearing structure was set to 10.25 rpm, which equated to 246° per frequency sweep.

Purpose: By increasing the rotational speed of the ball bearings, one hoped to impress a higher frequency shift, f_s, and Doppler frequency, f_d, onto the backscatter. Multiple rotational speeds of the same target configuration provided sufficient data to compare the accuracy of TFRs under varying non-stationary conditions.

11. **Target 11**

Description: This target used the same structural configuration as Target's 9 and 10 except the ball bearings rotated at 38 rpm, which equated to 912° per frequency sweep.
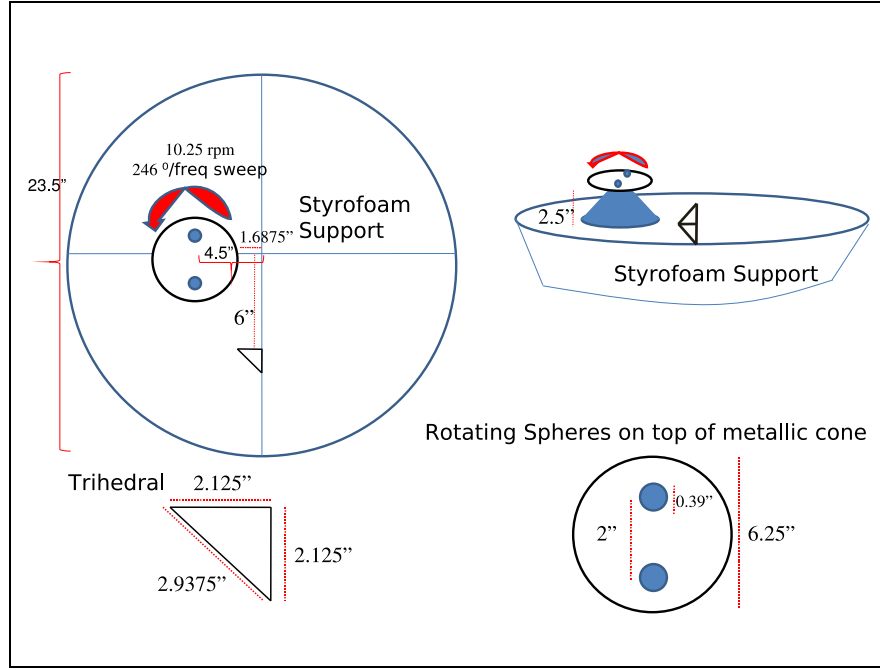
Figure 3.20:   Target 10 Schematic.

Purpose: This target provided an additional data set to analyze the effects from non-stationary components. This target had the fastest rotational speed of all the targets tested. Therefore, the impressed Doppler components should be the most extreme of all the data sets. It is important to understand the conditions needed to use TFRs effectively. The rotational speed differences among Target's 9, 10 and 11 allows one to predict the suitable conditions needed to apply TFRs appropriately. For example, if the target was a rotocraft, one would like to have the blades rotate an entire revolution during the frequency sweep in order to capture every possible RCS scatterer when viewed from a fixed azimuth angle θ. If TFRs can not localize the RCS contributors under these conditions, the blade rotation may need to be reduced relative to the time it takes for a frequency sweep to occur. Therefore, instead of having the frequency sweep correlate to a blade rotation of 360°, one may need to reduce the rotational span to 180° per frequency sweep and take two measurements to achieve the full rotational effects. It is important to remember that during a RCS range test, a short test duration is desired in order to keep conditions stationary over the testing

46

period. The longer a test takes, the more likely instruments and conditions will vary from steady state and adversely affect data. For these reasons, it is important to determine the limitations and strengths of each TFR under varying non-stationary conditions so one can use them appropriately.
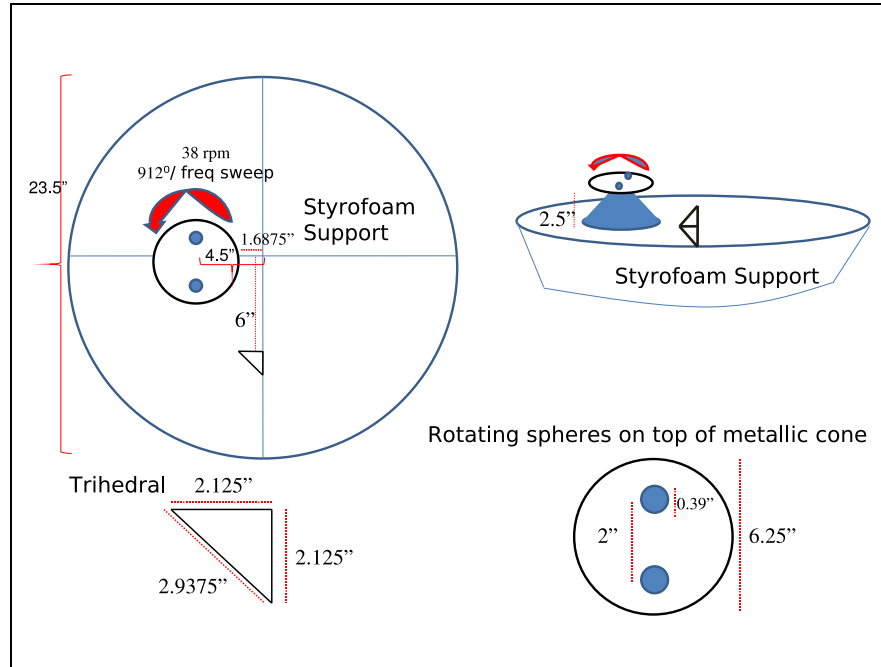
Figure 3.21:   Target 11 Schematic.

12. **Target 12**

Description: This target had the same configuration as Target 8 except the ball bearings were separated by 4 in instead of 2 in. The ball bearings were also stationary over the sampling period making the target's RCS stationary.

Purpose: By comparing Target's 8 and 12, one can better understand the contributions made to the overall target RCS from the ball bearings.

13. **Target 13**

Description: This target had the same configuration as Target 12 except the ball bearing rotational speed was set to 2.4 rpm, equating to 57.7° per frequency sweep.
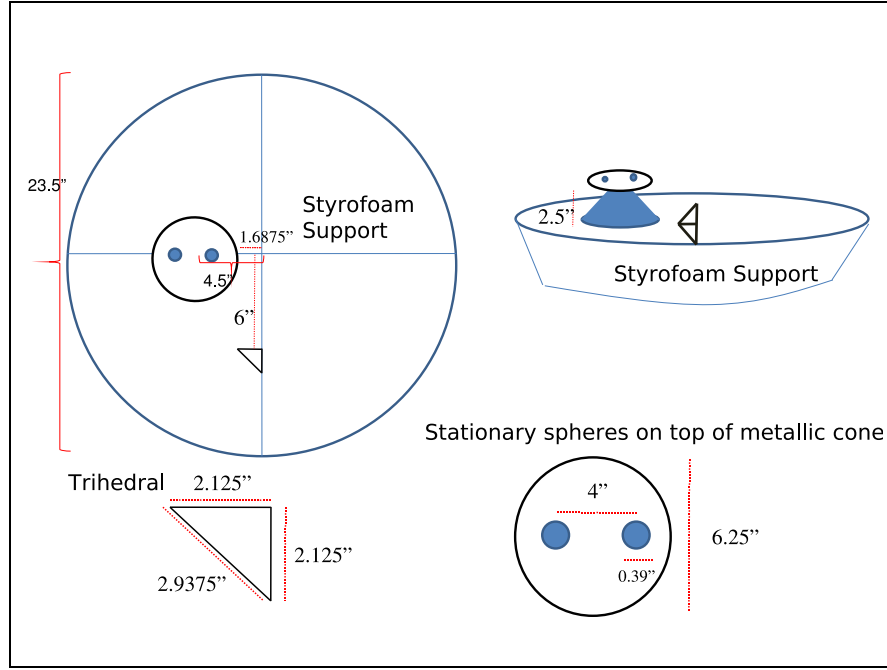
Figure 3.22:   Target 12 Schematic.

Purpose: Obtain another non-stationary data set using the complex trihedral target configuration. This data set provided additional knowledge on the effects non-stationary components play in RCS imaging.

14. **Target 14**

Description: This target was similar to Target 12. However, one ball bearing was replaced by a two-sided copper corner reflector. The corner reflector measured 1x0.75 *in* and was set at a right angle centered on the median of the Styrofoam rotational platform. The rotational speed of the ball bearing and reflector was set to 2.14 *rpm* equating to 51.8°. The rotational speed was set close to that of Target 12. However, the exact speeds could not be matched due to the limitations of the power supply.

Purpose: This target was more complicated than any other target. The goal was to understand the effects a non-stationary scatter had on the overall target RCS if the non-stationary component's RCS was angle dependent. The ball bearings used in previous targets did not change their individual RCS with
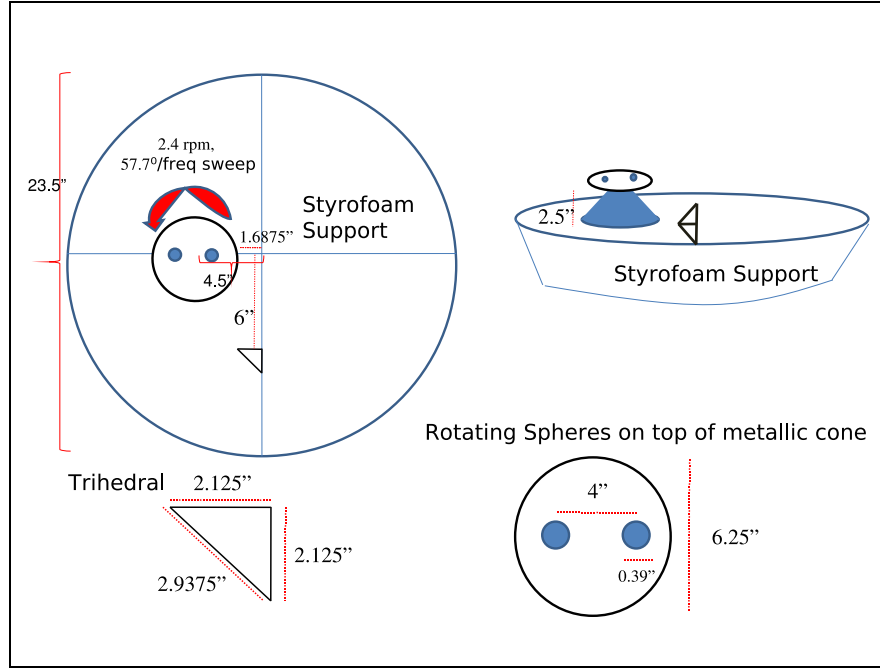
Figure 3.23:   Target 13 Schematic.

respect to viewing angle. This means that when the ball bearings rotated, the RCS contribution from them did not change as the motor changed their position relative to the radar. The right angle reflector that replaced one of the ball bearings in this target did change its RCS with respect to viewing angle. This means that as the motor rotated the structure around, the right angle reflector changed its RCS and the overall RCS of the structure. This scattering arrangement tried to simulate the complicated non-stationary environment a rotocraft creates when taking RCS measurements.

3.3   Process Required to Analyze Data

All target sets were analyzed using the TFRs described in Section 2.1. A comprehensive comparison between the TFRs was done to establish the best TFR to use when analyzing non-stationary RCS signals. The implementation of each technique is explained and justified.

49
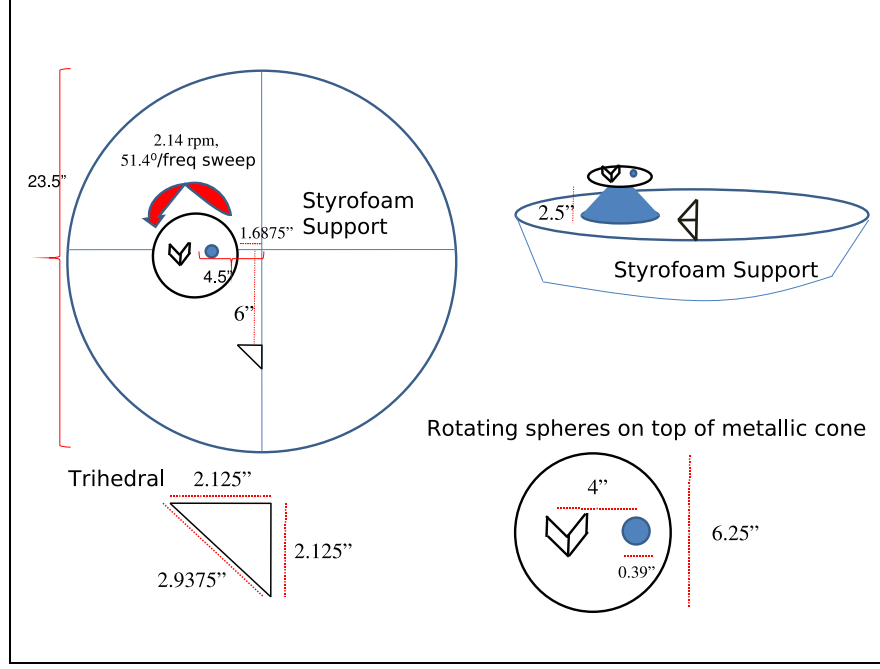
Figure 3.24:   Target 14 Schematic.

3.3.1   Azimuth vs. Range Plots.   Azimuth vs Range plots for all targets were created using a modified version of the AFIT Process `Matlab`® code developed by Dr. Collins as seen in Section VII.3. These plots provide the reader with an understanding for why TFRs are needed to locate scattering centers in a non-stationary RCS environment. In general, the code takes the Fast Fourier Transform of the backscatter return data at a certain azimuth angle and transforms it into the spatial domain. The transformed data reveals the RCS of the target at a specific range at the measured angle. The resulting plot illustrates the target's RCS with respect to range and azimuth. A Hamming window was applied to the data to reduce sidelobes.

3.3.2   The Short Time Fourier Transform.   Currently, the Short Time Fourier Transform is the standard TFR used when analyzing a time varying RCS. The characteristics of the STFT are explained in Section II. Two methods to compute the STFT of the collected target RCS data were implemented.

50

3.3.2.1 Standard STFT.   Using the standard definition of the Short Time Fourier Transform, the complex backscatter return from the pulse train at a fixed azimuth angle θ was divided into equal segments. The number of segments chosen was equal to the time resolution desired. Time scaling on the STFT was done by normalizing the time axis to the time it took for a frequency sweep to occur. The frequency sweep took approximately 4 seconds due to the large bandwidth and the amplifier switching that occurred at 8 GHz. The radar frequency sweep occurred in two discrete sections, $6 - 8\ GHz$, and $8 - 18\ GHz$. Each frequency band was controlled by a separate amplifier. During the full $6 - 18\ GHz$ sweep, the amplifiers switched causing a short delay.

To clarify the development of the standard STFT, a description of the segmentation process for a time resolution of 0.8 s is offered. For this scenario, the backscatter return data, which was 1200 samples long, was divided into 5 equal segments each having 240 samples. The first segment used data samples n=1-240, the second used n=241-481, the third used the next 240 samples and so forth, until all 1200 returns were accounted for. Range information was retrieved by taking the DFT of each segment and applying proper scaling. The transformed range segments were cascaded into a single matrix so one could view range RCS and time at a specific azimuth angle. A simple illustration of this STFT technique is depicted in Figure 3.1 using 4 time values and 8 backscatter returns.

Table 3.1:   STFT: Standard

Time Segments	t_1	t_2	t_3	t_4
$r(f_n)$	$r(f_1)$	0	0	0
	$r(f_2)$	0	0	0
	0	$r(f_3)$	0	0
	0	$r(f_4)$	0	0
	0	0	$r(f_5)$	0
	0	0	$r(f_6)$	0
	0	0	0	$r(f_7)$
	0	0	0	$r(f_8)$
	$\underbrace{\qquad}_{DFT_{Range_1}}$	$\underbrace{\qquad}_{DFT_{Range_2}}$	$\underbrace{\qquad}_{DFT_{Range_3}}$	$\underbrace{\qquad}_{DFT_{Range_4}}$

51

The STFT algorithm was implemented using `Matlab`®. For each target, the STFT was taken at azimuth angles $\theta = [0, 60, 90, 120, 180, 240, 300]°$. At each of these angles, the return data was divided into $[2, 5, 10, 20, 30]$ segments in order to give varying degrees of time resolution for the same angular data. These segments correlated with a time axis resolution of $2 \, s$, $0.8 \, s$, $0.4 \, s$, $0.2 \, s$, and $0.13 \, s$. The multiple time resolution values were needed to show the inverse relationship between time and range accuracy when computing the STFT. The `Matlab`® code for this function can be seen in Section VII.4. The `Matlab`® function displays the target area $+/- 15 \, in$ as seen in Section VII.4.

3.3.2.2 STFT: Gaunaurd and Strifors. A different implementation of the STFT, based on a TFR paper by Gaunaurd and Strifors, was developed in `Matlab`® using Equation 2.20. In this approach, the STFT was implemented using a growing window of samples instead of a fixed window. The value N in Equation 2.20 was interpreted to be the total number of frequency response samples instead of just the fixed window length. This implementation varied from the standard implementation of the STFT in that the number of backscatter returns sent to the DFT function was based on the time segments chosen. Instead of using an equal amount of return pulses in each data segment, as in the standard implementation of the STFT, each time segment used the previous data in addition to the new time segment of data. When these time segments were transformed into the spatial domain, each subsequent time segment used more bandwidth than the previous. Figure 3.2 depicts how the time segments were comprised.

3.3.3 Scene Match Function. An ambiguity function and Cochleagram inspired Scene Match function was implemented for each target set. The ambiguity function, as described by Equation 2.21, was modified to account for only the effects range had on the phase of the signal as seen in Equation 3.2.

Table 3.2:   STFT: Strifors and Gaunaurd.

Time Segments	t_1	t_2	t_3	t_4
$r(f_n)$	$r(f_1)$	$r(f_1)$	$r(f_1)$	$r(f_1)$
	$r(f_2)$	$r(f_2)$	$r(f_2)$	$r(f_2)$
	0	$r(f_3)$	$r(f_3)$	$r(f_3)$
	0	$r(f_4)$	$r(f_4)$	$r(f_3)$
	0	0	$r(f_5)$	$r(f_4)$
	0	0	$r(f_6)$	$r(f_5)$
	0	0	0	$r(f_7)$
	0	0	0	$r(f_8)$
	$\underbrace{\qquad}_{DFT_{Range_1}}$	$\underbrace{\qquad}_{DFT_{Range_2}}$	$\underbrace{\qquad}_{DFT_{Range_3}}$	$\underbrace{\qquad}_{DFT_{Range_4}}$

$$|SM(f_n, R)| = \left| \int_{-\infty}^{+\infty} r(f_n) S^*(f_n, R) dR \right| \qquad (3.2)$$

where $r(f_n)$ was the complex backscatter return and $S(f_n, R)$ was the range phasor signal described by:

$$S(f_n, R) = Ae^{-j\phi_n}, \quad where \quad \phi_n = 2\pi(f_0 + n\Delta f)\frac{2R}{c} \ and \ A \ = \ 1. \qquad (3.3)$$

In Equation 3.3, R represents the distance from the target to the center of the target pedestal. The radar system was gated and calibrated to have the exact center of the target pedestal set to $R = 0$. From Equation 2.6, one can determine ϕ_n from the target distance R.

The Scene Match function was implemented in Matlab® by taking the two dimensional cross correlation of the return signal at a specific azimuth angle θ with the $S(f_n, R)$ matrix from Equation 3.3. The $S(f_n, R)$ matrix incorporated range values from $+/-15\ in$. The farthest dimensions of any target were $+/-\ 8\ in$. A range window of 30 in was used in order to encompass the entire target and any effects, such as Doppler shift, that would cause ϕ_n to exceed its expected range value. Using Equation 2.9, the range step size ΔR was set to the range resolution of 0.49 in. Therefore, the range vector used in Matlab® had 60 samples. Figure 3.25 illustrates

the two dimensional cross correlation used to determine the Scene Match function. The illustration is truncated for visual reasons, but the reader should understand that signals $r(f_n, \theta)$ and $S(f_n, R)$ were 1200 pulses (f_n) long. Metric units were used in Matlab® for calculations and then converted to SI units for plotting purposes.
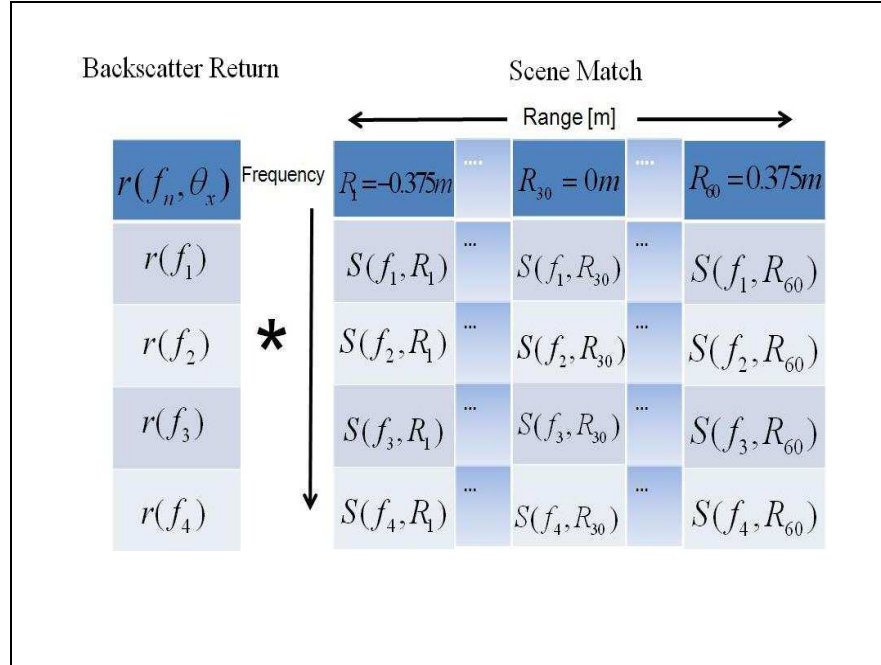
Figure 3.25:   Scene Match Function: The left column represents the return signal as a function of frequency. The cross correlation of this signal and each column in the $S(f_n, R)$ matrix was computed to determine the correlation from each return pulse to a specific range.

The end result of the Scene Match function using the Matlab® code from Section VII.6 produced plots showing the correlation between the backscatter return and range from pulse to pulse at a specific azimuth angle θ.

3.3.3.1   Scene Match To Include Non-Stationary Components.   Section 3.3.3 provides the reader with an understanding of the dependence the backscatter return has on range. However, the simplified calculation of ϕ_n from Equation 2.6 did not take into account the effects from the target's non-stationary components. Targets with non-stationary components were modeled to include a Doppler frequency

component and a range shift from pulse to pulse. Equation 2.12 offers a more accurate description of the signal's phase ϕ by including the target's velocity. In addition to the Doppler components introduced by Equation 2.12, the range shift induced by the rotation of the ball bearings from pulse to pulse was included to yield a more accurate model of ϕ as described by Equation 3.4.

$$\phi_n = 2\pi(f_0 + n\Delta f)\frac{2(R_0 + R_n + vnT_r)}{c} \tag{3.4}$$

where $R_n = r_b \sin(\theta_{b_n})$ as illustrated in Figure 3.26. This variant of ϕ was implemented in Matlab® as described in Section VII.7.
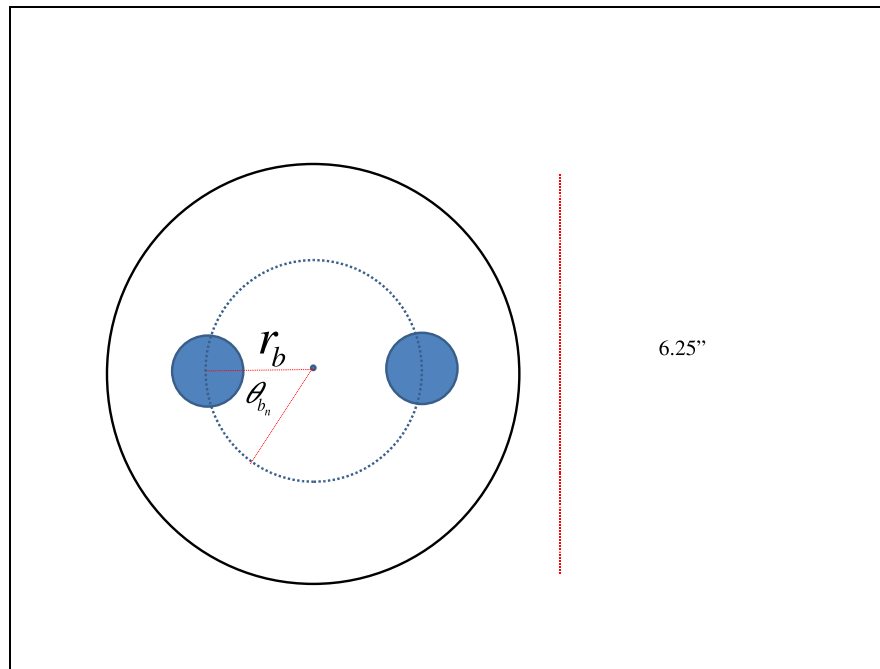
Figure 3.26: Non-stationary range shift components used for the calculation of R_n.

Although the incorporation of Doppler velocity and range shift were important in accurately modeling the signal's phase ϕ, it is important to understand that ϕ is a function of many variables to include not only range and target velocity, but multi-bounce interactions and phase interference from the scatterers. For a simple target, it is possible to model ϕ as a function of range, range shift and velocity. However, as the

target gets more complicated, it becomes increasingly difficult to model ϕ accurately. The limitations of this are apparent when using the Scene Match function results to predict scattering locations.

3.3.4 The Wigner Distribution and Psuedo Wigner Distribution.   As described in Sections 2.4.3 and 2.4.4, the Wigner and Psuedo Wigner distribution functions are powerful Time-Frequency techniques. They provide the ability to view the time and spatial domain simultaneously with a higher degree of fidelity than the Short Time Fourier Transform.

Processing of the target RCS data using the discrete Psuedo Wigner distribution function from Equation 2.37 was implemented in `Matlab`® , as seen in Section VII.8. The PWD was implemented over the WD in order to suppress the unwanted cross-terms. Windowing was applied using the Gaussian form $e^{-\alpha t^2}$ with α set to 1. Range and time axis scaling were applied to match the AFIT range dimensions and the frequency sweep respectively. For each target, both polarizations and angular measurements at $[0,60,90,120,180,240,300]°$ were plotted.

IV. Time Frequency Representation Analysis

4.1 Target RCS Data

RCS data was obtained on all fourteen targets using AFIT's anechoic chamber. For the scope of this thesis, AFIT's anechoic chamber provided sufficient data for the analysis of the TFRs tested. The stationary and non-stationary data obtained were critical in making comparisons between the TFRs.

As stated in Section III, RCS data from each target was recorded as a matrix containing the complex magnitude and phase for each pulse, azimuth angle, and polarization. To be clear, azimuth measurements for each target were taken from $\theta = 0 - 360°$ with an angular step of $\Delta\theta = 0.25°$. This provided 1440 angular measurements and a cross range resolution of $0.035\ in$. At each angle, a pulsed step frequency sweep from $6 - 18\ GHz$ occurred. The frequency step, Δf, was set to $10\ MHz$, providing a bandwidth of $12\ GHz$ and a range resolution of $0.49\ in$. In short, each target had 1440 azimuth measurements with 1200 backscatter returns at each azimuth angle θ. Both horizontal and vertical EM polarization responses were recorded for all targets.

The data was recorded by the Agilent PNA and converted to a useable $\texttt{Matlab}^{\circledR}$ *.mat* file from a read Lintek program provided by AFIT. The data was processed using the TFRs described in Section III. The $\texttt{Matlab}^{\circledR}$ code for each of the TFRs can be reviewed in Section VII.

In order to value the TFRs as they pertain to non-stationary signals, one must understand the limitations of the Fourier transform as it applies to a stepped frequency radar. As discussed in Section 2.1, the Fourier transform is commonly used to convert the frequency domain response of a target into a useable Radar Cross Section as a function of range. This process works well for stationary targets, but loses its power under non-stationary conditions. This limitation must be understood in order for one to make sense out of a non-stationary signal.

4.1.1 The Discrete Fourier Transform. The strengths of the Fourier transform, as it applies to RCS localization from a pulsed stepped frequency radar, lie in the assumption that the target was stationary over the sampling period. The discrete Fourier transform, as depicted in Equation 4.1, reveals the importance phase has on the function.

$$DFTx(k) = \sum_{n=0}^{N-1} x(n)e^{-j(2\pi kn/N)} \tag{4.1}$$

where $x(n)$ represents the frequency response of a return pulse, time is represented as k, having values $= 0, 1, 2, ..., N - 1$, and phase, ϕ_n, is represented by $2\pi kn/N$ [2]. A complete comprehension of this formula is paramount to understanding the importance phase has on scattering locations. This relationship is visualized using hypothetical stationary and non-stationary response data as seen in Figures 4.1 and 4.2.

Figure 4.1 represents the DFT of a stationary target. The column on the left represents the complex backscatter return data from the frequency sweep. In this example, the complex response is represented as a magnitude A_x, and a unit circle phasor. This data is multiplied by a matrix based on the function $e^{-j2\pi ft}$. The unit circle phasor from $e^{-j2\pi ft}$ is a function of both frequency and time, where the rows in the matrix change as a function of frequency, and the columns change as a function of time. Therefore, the phasor in each cell represents a specific frequency and time value through $e^{-j\phi(f,t)}$. This complex number is represented pictorially by the unit circle phasor.

It is important to understand that time is synonymous to range information. Range information is calculated from the distance an electromagnetic wave travels over a certain time period. Although it is not apparent when looking at the complex magnitude and phase associated with each pulse of the frequency response, time information is inherent and can be extracted by multiplying the complex response by

58
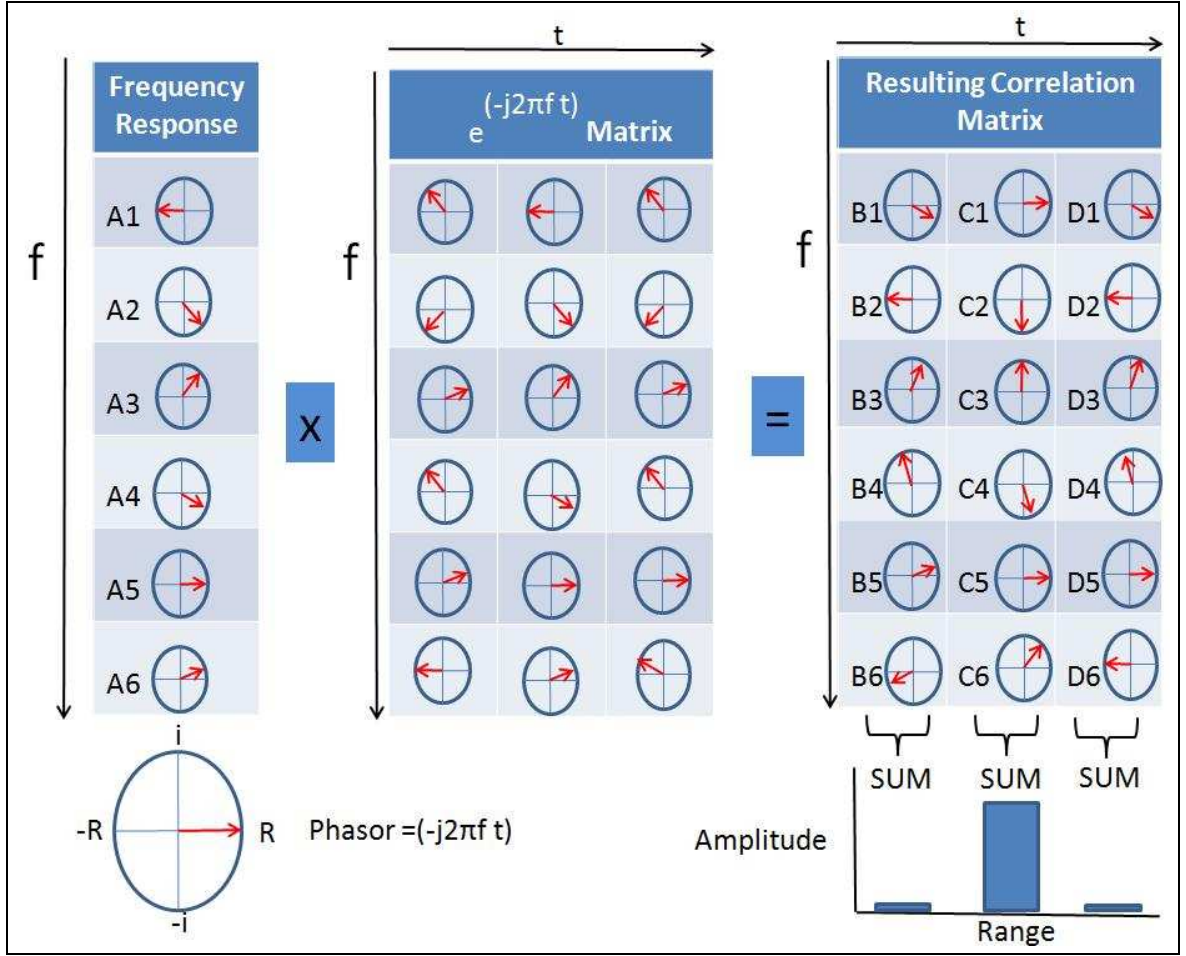
Figure 4.1: DFT on stationary target response. The left column represents the frequency sweep backscatter response from the target. It is a complex value containing magnitude, represented as A_x and phase -depicted as a unit circle phasor. This column is multiplied by the DFT matrix based on the emitted frequency and time. The result is the correlation from pulse to pulse in time, which corresponds to a range. The columns are integrated and the absolute value is taken to reveal the response in range.

an equivalent complex value based on $e^{-j2\pi ft}$. The multiplication yields correlated frequency responses in time, which can be converted to range information.

The result of the multiplication between the frequency response and the $e^{j2\pi ft}$ matrix yield a correlation matrix containing complex values. The importance of the correlation matrix lies with the resulting phasor from the multiplication of the two

complex numbers. One must remember that when two complex numbers are multiplied, their phases add. A frequency sweep response that is correlated to a specific time value will produce a vector of phases that is composed of conjugate pairs. The phase conjugate pair is a result from the correlated sampling of the frequency sweep and the associated time/range vector. As the phase of the frequency response rotates as a function of frequency, conjugate phases produced from subsequent frequency responses will cancel each other out in the integration of the correlated matrix if the time vector used in the multiplication shares the same phase of the frequency sweep response. This means that at a specific time column, one frequency response will take the form $e^{-j\phi}$ while a subsequent frequency will take the form $e^{j\phi}$. When the time column is integrated, phases that are conjugates will yield only a real values. This can be shown using Euler's identity in the following equation:

$$
\begin{aligned}
Ae^{-j\phi} + Ae^{j\phi} &= A(cos(\phi) - jsin(\phi)) + A(cos(\phi) + jsin(\phi)) \\
&= A * 2cos(\phi)
\end{aligned}
$$

The importance of this concept can be seen using the hypothetical response from Figure 4.1. In the resulting product matrix, one notices that column's 1 and 3 do not have conjugated phases. It is also noticed that the phases seem random and uncorrelated from pulse to pulse. However, column 2 yields phases that have a conjugate. The conjugate phases in this column are the result from the correlation between the frequency response and its associated time vector in the correlation matrix. Again, when the time columns are integrated, columns with phases that are not correlated will approach 0, while phases that have correlation yield a summation of the real components.

The absolute value of the resulting summations yield the range response. This is represented by the range vs amplitude plot in Figure 4.1. From this plot we see

the target's location is associated with the time value represented in column 2. The phasors from columns 1 and 3 do not have correlation and subsequently yield a near 0 summation. The near 0 summation equates to zero scattering features at column 1 or 3's range equivalent. It is to be understood that even if the resulting phase is purely imaginary or a negative real number, the conjugate addition will yield a purely real number. Therefore, it does not matter where the phasor is pointing in the column, just as long as it has a conjugate. Conversely, if the resulting phases do not have a conjugate and they appear to be random, their summation will yield 0. This concept is jaded using only the six response from Figure 4.1. However, if one imagines that the frequency response was the result of 6000 pulses, the randomness of the phasor integration associated with uncorrelated pulses would approach 0, while correlated pulses in time would surely yield range information.

The power of the DFT to locate a target accurately in range when using a pulsed step frequency radar fails when the target moves during the frequency sweep. From the DFT discussion, it is understood that phase correlation at specific time values yields accurate range information. If the target moves during the frequency sweep, the time information inherently built into the return backscatter will change from pulse to pulse. When the DFT is taken, multiple time values will share correlated phasors. Due to the movement of the target over the frequency sweep, the correlated phases only last over a limited frequency band in the correlation matrix. The correlation ends when the target scattering features moves out of the associated time value. When the integration occurs, the target's non-stationary scattering feature is represented in multiple time columns. The resulting range vs amplitude plot will yield a target that spreads its response energy in multiple locations thus reducing the range localization ability on scattering centers. This is illustrated by the rise in column's 1 and 3 and the reduction in column 2 in Figure 4.2.
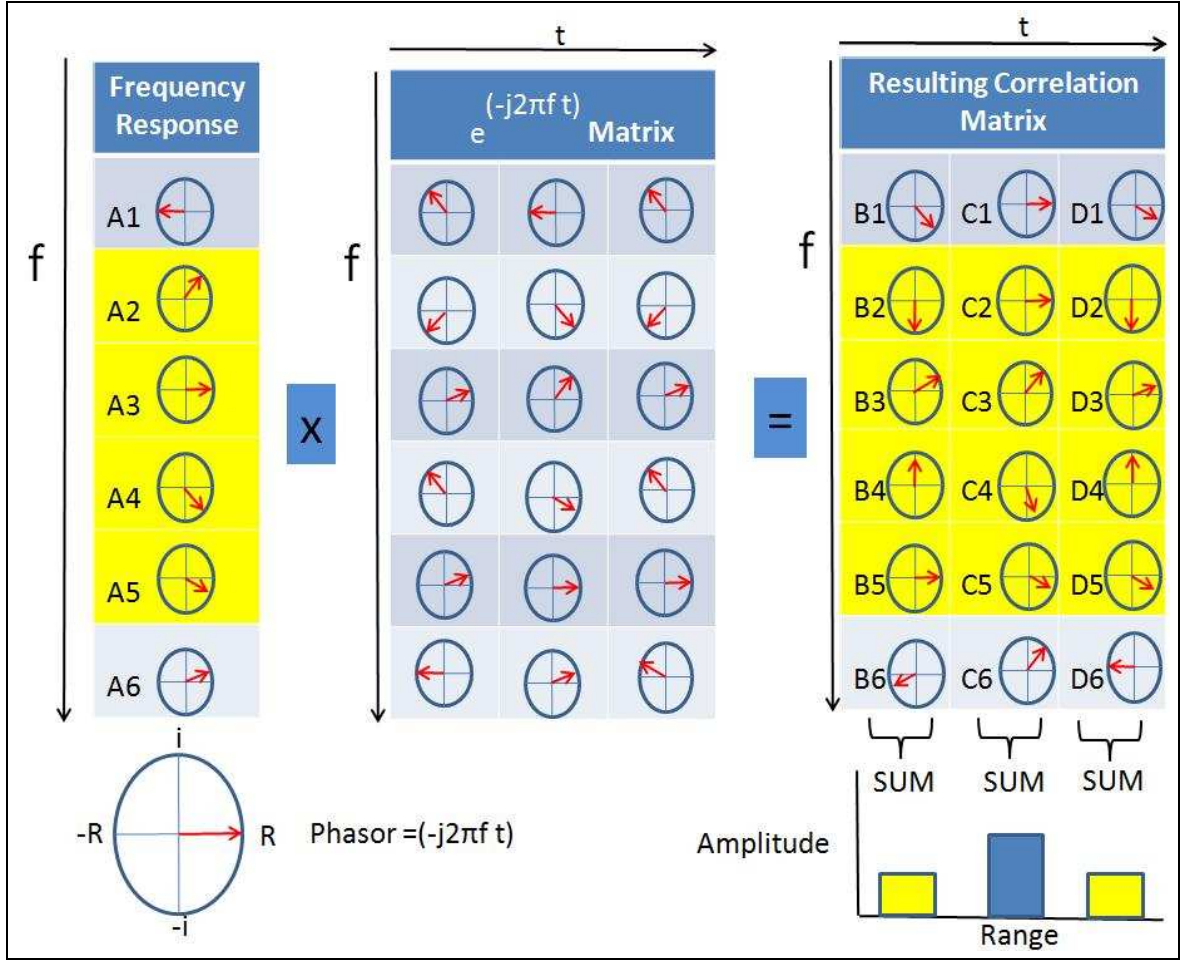
Figure 4.2: DFT of a non-stationary target response. The yellow cells indicate a change in the target's range as compared to Figure 4.1. The non-stationary range places the same scattering feature in multiple range locations indicated by the range vs amplitude plot.

4.2 TFR Analysis

In order to analyze and compare the effectiveness of the Time Frequency Representations represented in this thesis, one must fully understand the scattering characteristics of the target in test. Comprehension of the target enables the tester to determine the strengths and weaknesses of a particular TFR. This approach was valid for the scope of this thesis. However, in realistic low observable diagnostic testing, a total comprehension of the scattering effects from the vehicle in test may not be known. Therefore, LO diagnosticians should have confidence in the TFR chosen to

locate scattering centers in a non-stationary environment. Confidence in TFR application can be achieved through simple tests, as seen in this thesis.

As described in Section III, the targets were designed to be simple in the sense that the scattering locations were easily defined and had limited interference effects. Targets were designed so one could isolate a particular scattering feature or phenomena. In general, targets were designed to increase in complexity in order to determine the limits of the TFRs.

This section analyzes the performance of each TFR on certain targets. It is impractical to cover every combination of target, polarization, and angle; therefore, the RCS data set used for comparison was objectively chosen based on RCS response characteristics. Simple scattering responses were chosen over more complicated returns. For example, if the response from a particular EM polarization localized scattering centers better than the other, it was used to test the TFRs. The same discretionary method was applied to angular data - the most localized scattering centers were used for analysis. This simple strategy was used in order to easily compare the TFRs both quantitatively and qualitatively. Lastly, to be clear, each TFR was compared using the exact same target data set (i.e. angle and polarization).

The Time Frequency Representations were analyzed and compared using range vs time plots generated by their corresponding $\texttt{Matlab}^{®}$ program. The TFR plots were organized in a figure set for easy side by side comparison. The comparative format is represented in Figure 4.3 and is the same for every data set used. The target, azimuth angle θ, and polarization are strictly stated for each comparative plot.

Analysis of each TFR begins with an interpretation of the Range vs Azimuth plot. This allows one to better understand the backscatter phenomena associated with each target. Scattering phenomena that alters the RCS beyond the direct specular returns are discussed to include: creeping wave effects, traveling wave effects, multibounce and non-stationary effects. Once the expectations of the target's backscat-

63

Target Tested	Range Vs Azimuth
Wigner Distribution	Scene Match

(a)

STFT (2 time intervals)	STFT Gaunaurd (2 time intervals)
STFT (5 time intervals)	STFT Gaunaurd (5 time intervals)

(b)

STFT (10 time intervals)	STFT Gaunaurd (10 time intervals)
STFT (20 time intervals)	STFT Gaunaurd (20 time intervals)

(c)

Figure 4.3:   (a) This figure represents the first of three comparisons used to analyze the TFRs. It contains a schematic of the target tested with its corresponding Range Vs Azimuth plot and the TFRs of the Wigner distribution and the Scene Match function.
(b) The second figure comparison includes the standard STFT and Gaunaurd's STFT plots as a function of 2 and 5 time intervals.
(c) The last comparative figure includes the standard STFT and Gaunaurd's STFT plots as a function of 10 and 20 time intervals.

ter return are understood, the Scene Match function, Wigner distribution, standard STFT and Gaunaurd STFT are analyzed. These techniques are compared and discussed to determine where each technique can be applied and where they fail.

4.2.0.1 Target 1 Analysis. Target 1 was an important target design for this thesis because it offered a single stationary isotropic scatterer with a known RCS. The purpose of this design was to insure the TFRs returned a similar physical representation from their plots, i.e. a single stationary isotropic scatter. The TFR comparison contained both polarizations to assure the reader that the RCS data from each horn antenna was valid. The resulting comparisons for both polarizations should be nearly identical due to the polarization response independence from a single metallic sphere. All measurements were conducted at $\theta = 90°$. The resulting comparison can be seen in Figure's 4.4, 4.9, 4.11, 4.5, 4.10 and 4.12.

Figure 4.4 and 4.5 are the vertical (TT) and horizontal (PP) respective polarizations associated with the description from Figure 4.3 subfigure a. They contain the schematic of Target 1, Range vs Azimuth, Wigner distribution and Scene Match function plots. The data set used to create the plots was obtained from Target 1 using the frequency response at $\theta = 90°$. For subsequent target descriptions, it will be assumed that the reader understands the origins of each plot given the description from Figure 4.3.

The Azimuth vs Range plots from Figure's 4.4 and 4.5 represent the RCS of the target in dB. These plots clearly yield a single stationary metallic sphere with a diameter of 1 *in* located at the center of the target mount pedestal. According to both Azimuth vs Range polarization plots, the first strong backscatter occurred at approximately -0.5 *in* with a return of -38 dB from all azimuth angles. This reflection location was exactly equal to that of the placement of the metallic sphere. As one can see from the plots, the strong return was visible through $+2$ *in* even though the physical boundaries of the sphere end at $+0.5$ *in*. This return is a result from the creeping wave effect on the sphere.
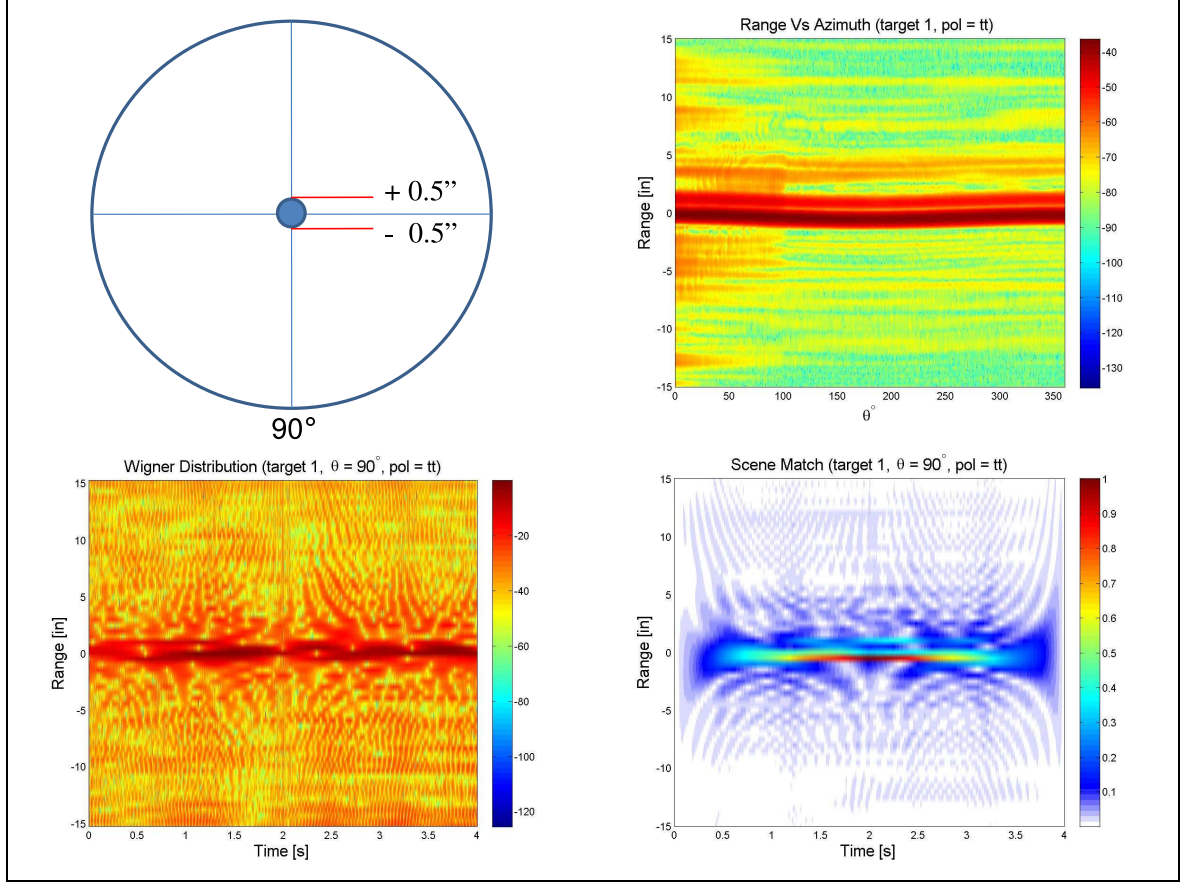
Figure 4.4: Target 1: Pol=TT, $\theta = 90°$. Includes Target 1 schematic, Range Vs Azimuth, Wigner distribution (TFR) and Scene Match.

The creeping wave effect induced a delay on the backscatter which correspondingly changed the phase ϕ of the return signal. According to Knott, a creeping wave is a type of a traveling wave that is emitted along surfaces shadowed from the incident wave [12]. For a sphere, a creeping wave sheds its energy continuously as it goes around the sphere and will reemerge as a second response from the initial EM incident wave as depicted by Knott in Figure 4.6 [12].

If the circumference of the sphere is between 1 and 10 wavelengths, the RCS will exhibit an oscillatory behavior due to the interference from the front face optics like return and the creeping wave that propagates around the backside. This phenomena occurs in the resonant region and is illustrated by Knott in Figure 4.7. The equation
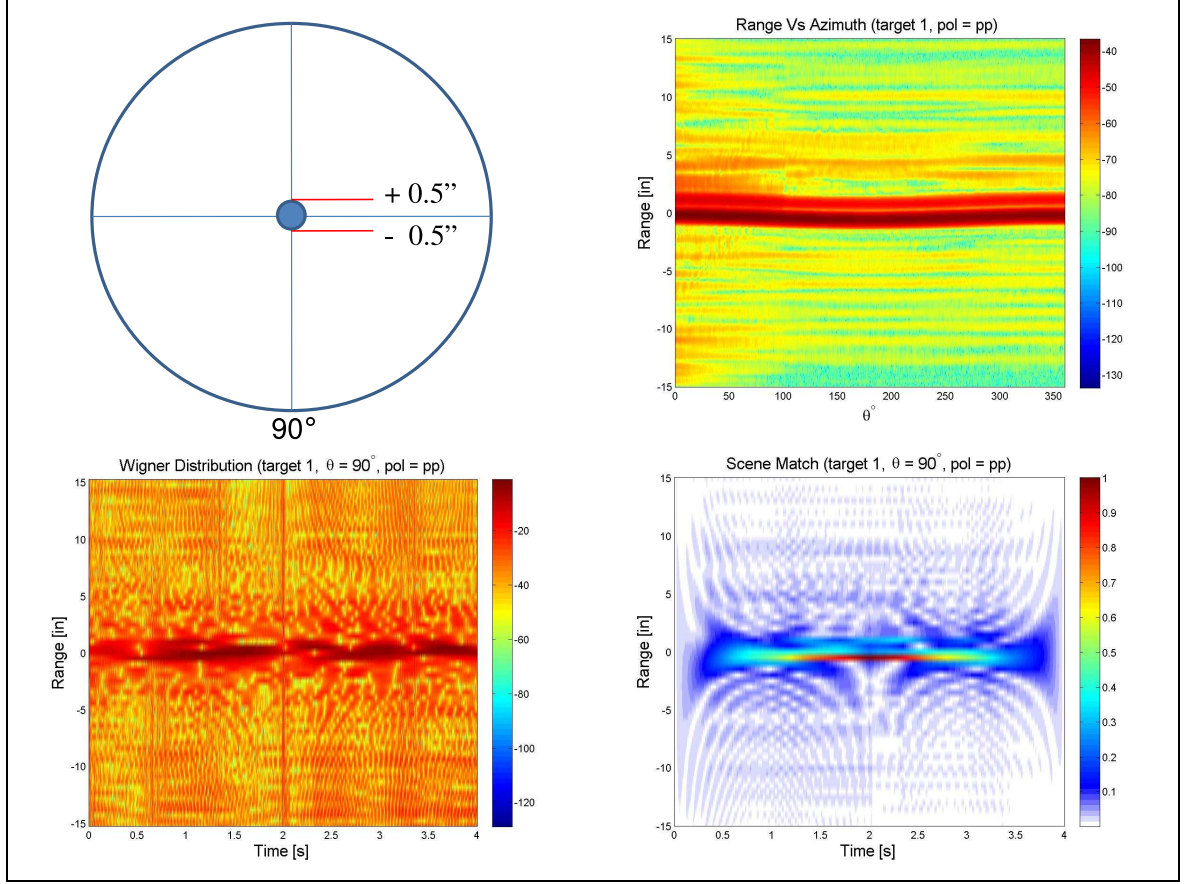
Figure 4.5:   Target 1: Pol=PP, $\theta = 90°$, TFR's a.

$ka = \frac{2\pi a}{\lambda}$ represents the ratio of circumference to wavelength to which the resonant region is determined [12].

Given the dimensions of the sphere in Target 1, all wavelengths used in the frequency sweep fell in the resonant region ($ka = 1.59 \Leftrightarrow 4.78$). Given this, the sphere had two contributors, the initial specular diffraction from the near edge, and the secondary creeping wave that followed the surface around the backside of the sphere [12]. For both polarizations, the creeping wave induced a range delay equal to $2r + \pi r = (2 + \pi)r$, where r is the radius of the sphere. In the case of Target 1, the the creeping wave delay was 2.57 in. Therefore, the creeping wave effects should have occurred in range through $\sim 2.07\ in$, and had a RCS lower than that of the initial specular return, which it did. This phenomena was expected and was accounted for in each TFR technique. The accuracy of the Range vs Azimuth plot for the Target 1
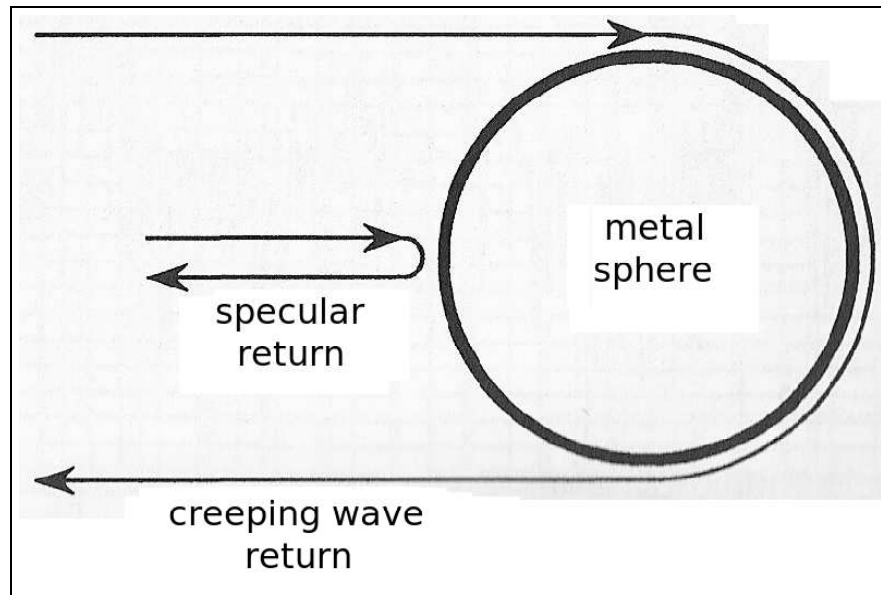
Figure 4.6:   Creeping wave interactions with sphere depicted by Knott [12].
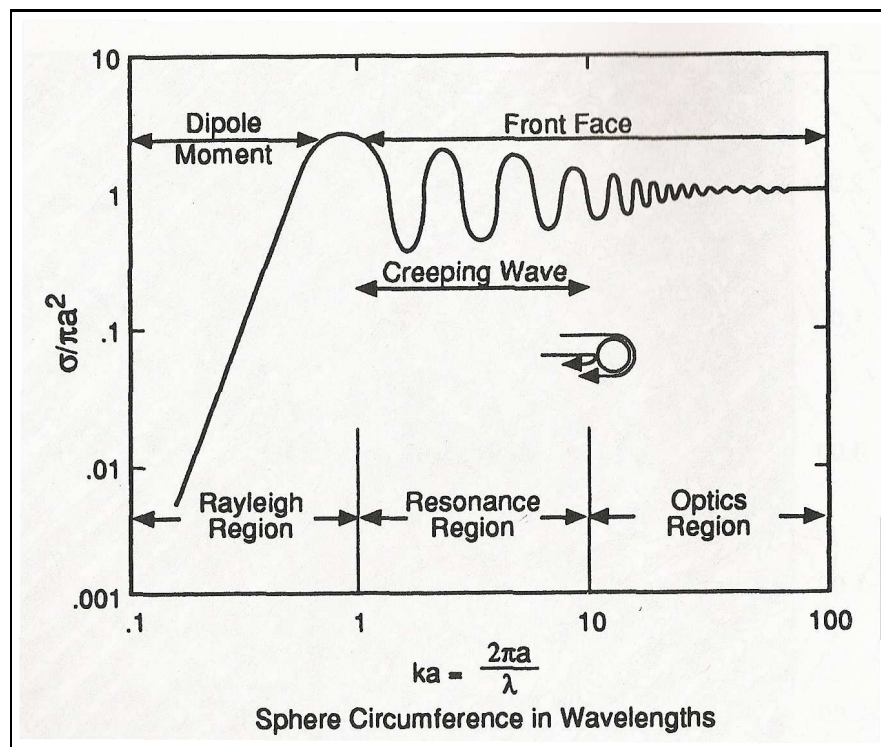
Figure 4.7:   Resonant region depicted by Knott [12].

response reassures the reader that the radar system worked properly. The DFT of the

frequency response produced the expected results. This assures us that the phasor information for each pulse corresponded most strongly to the location of the sphere.

The Wigner distribution plot was represented as a RCS in dB to stay true to its interpretation as an energetic response over time. From Figure's 4.4 and 4.5, the WD plot accurately places the strongest return at roughly $0\ in$. However, the strong response in both polarizations does not stay constant throughout the duration of the frequency sweep. Figure 4.8 reveals a slight variation in amplitude from $time = 0-4\ s$ at a range value of $0\ in$ for both polarizations.
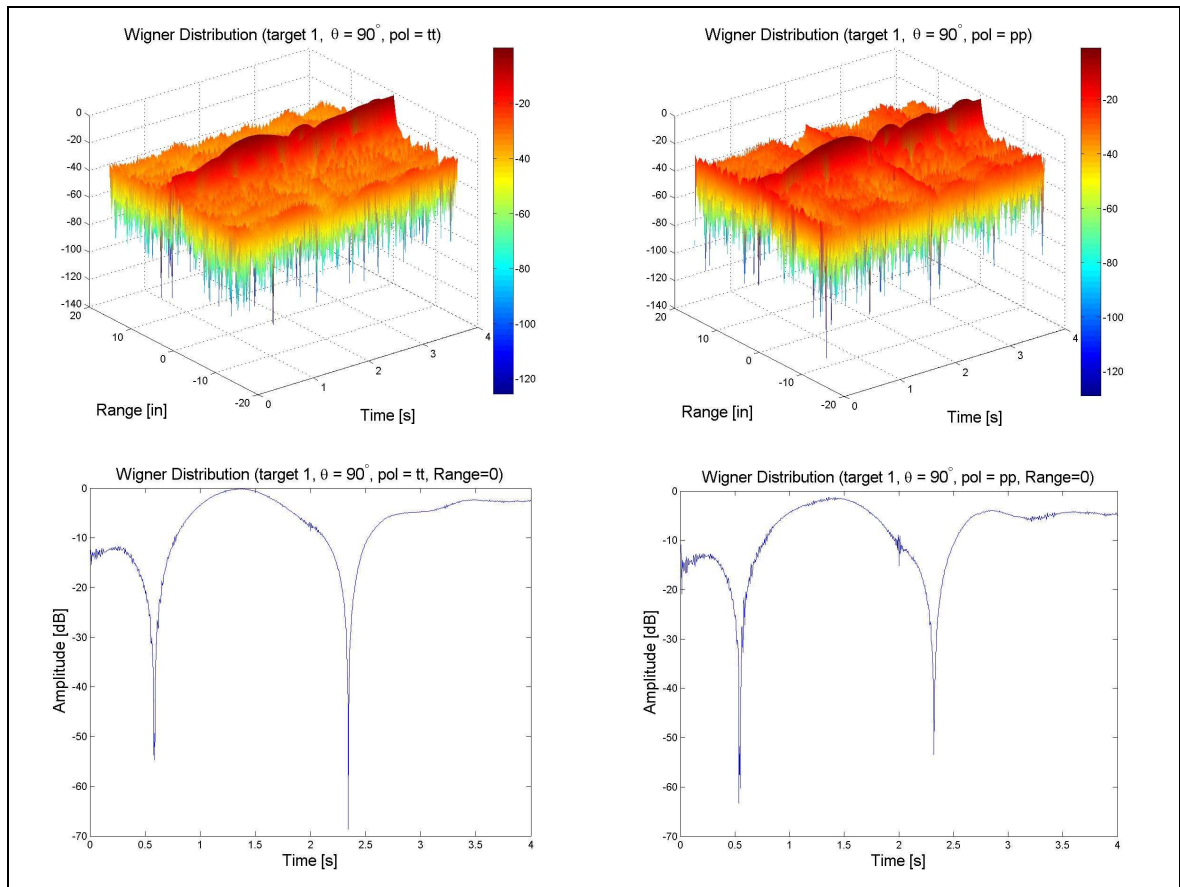
Figure 4.8:   Wigner distribution amplitude variation Target 1

The variations are not much, but because the target was stationary over the sampling period, the responses should have stayed constant. The creeping wave effects witnessed in the Azimuth vs Range plot lend one to suspect that they were contributing to the variation of RCS in range over time. From the discussion on the

69

interference effects from the creeping wave in the resonant region, one can deduce that the change in frequency will cause the return wave to construct positively and negatively as a function of the circumference to wavelength ratio. Therefore, the backscatter response of the sphere may have changed as a function of frequency.

Although the Wigner distribution depicted a strong backscatter return at 0 in, the power levels throughout the plot were high relative to the Azimuth vs Range plot. The high power levels are attributed to the way the Wigner distribution was created. In short, the return RCS data was multiplied by a conjugated time shifted response and then sent through a Fourier transform process similar to the DFT process described in Section 4.1.1. Range data acquired from the WD was also based on the correlation of the frequency sweep response and a time and frequency matrix. Like the Fourier transform, this process produced correlated pulses at specific ranges. However, because the WD used the product $f(n+k)f^*(n-k)$ instead of $f(n)$, the resulting phasor from this product correlated with multiple time instances in the Time-Frequency matrix and produced scattering locations that were non-physical. The bottom line is the WD did locate scattering centers of correlated pulses, but it also erroneously produced returns for uncorrelated pulses. The cross-term limitations described become more unmanageable when the backscatter response is the result of many scatterers. For the most part, this was not an issue for the analysis of Target 1. Target 1's signal, as understood from the Azimuth vs Range plot, was a composition of the initial specular return and the creeping wave. The proximity of these two terms does not change the phasor of the response data drastically. Therefore, when the WD was taken, the cross-term pollution was not too obstructive. The results from the WD on Target 1's data matched closely to what was expected from the theory described in Section 2.4.3.

The Scene Match function, as described in Section VII.6, plotted the normalized correlation between the scene and the target's frequency response. For Target 1, both polarizations at $\theta = 90°$ were processed and are depicted in Figure's 4.4 and 4.4. As one can determine from the figures, the Scene Match function accurately placed the

scattering center of the sphere in range for both polarizations. However, the beginning and end of the time period ($t = 0 - 0.5$ and $t = 3.5 - 4$ s) were lost. The loss of range information at these times was not accurate because the target was stationary over the entire sampling period. Range information was lost at these limits due to the frequency response from the sphere. To understand this, one must understand how the Scene Match function was created.

The formulation of the Scene Match as described in Section 3.3.3, placed much emphasis on the phase characteristics of the matched scene. To form a clear range vs time plot, the phase from the frequency sweep response must be a function of isolated localized scatters. If the phase from the frequency response is the result of multiple scattering phenomena, the correlation between itself and the scene match matrix will reveal a spread in range. From the discussion on the creeping wave effects from the sphere, we understand that the return phase from Target 1 was a combination of the initial specular return and the delayed return from the creeping wave. Referring to Figure 4.7, as the frequency was swept, the characteristics of the creeping wave changed to cause constructive and destructive interference. This oscillatory interference pattern changed the phase of the backscatter return as a function of frequency. Because the time axis of the Scene Match function plots in Figure's 4.4 and 4.5 were really a function of frequency, one can determine that at the lower and upper frequency limits of the frequency sweep, destructive interference changed the phase characteristics of the backscatter return to a point were they were uncorrelated to the scene match. The energy in these regions was spread out over a range rather than tightly concentrated, as in the middle of the frequency sweep, which was represented during the $2 - 3$ s time range.

Although the Scene Match function is not considered a TFR to the academic world, it did provide the essential requirements of representing time and range information simultaneously. At highly correlated frequencies, the Scene Match function placed the target's scattering locations accurately.

71

The Short Time Fourier Transform of the Target 1 data set was accomplished using the standard definition and the definition Gaunaurd and Strifors provide according to Equation's 2.19 and 2.20 respectively. Target 1 was analyzed using various time intervals as discussed in Section 3.3.2. Processing of both polarizations and time intervals of $T_i = 2, 5, 10$ *and* 20 were plotted for the target data set as illustrated in Figure's 4.9, 4.10, 4.11 and 4.12. The range of time intervals gives the tester the full spectrum of time and range resolution characteristics. As a reminder, a high resolution in time corresponds to a low resolution in range. Conversely, a low time resolution corresponds to a high resolution in range. Therefore, multiple time intervals of the same data set allows one to understand the target better throughout the duration of the sampling period.
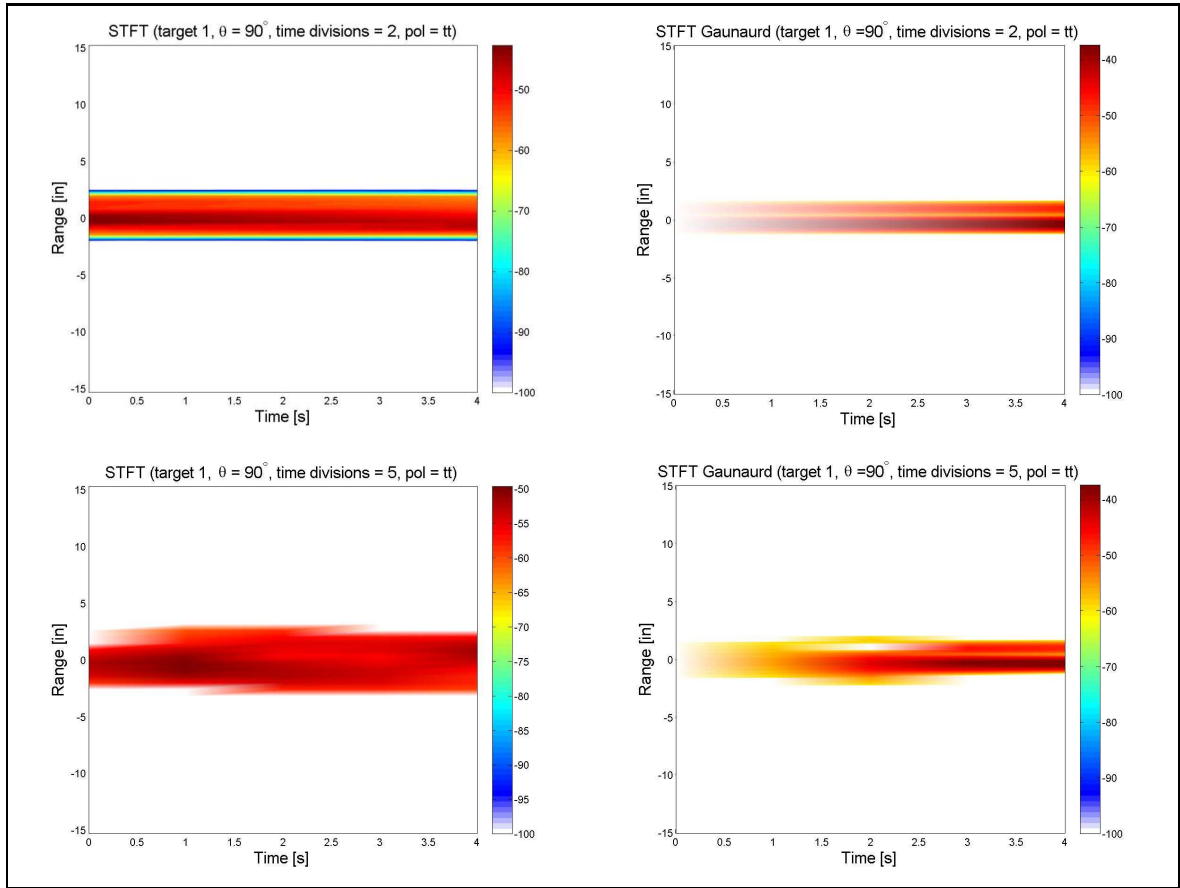
Figure 4.9:   Target 1: Pol=TT, $\theta = 90°$, TFR's b.
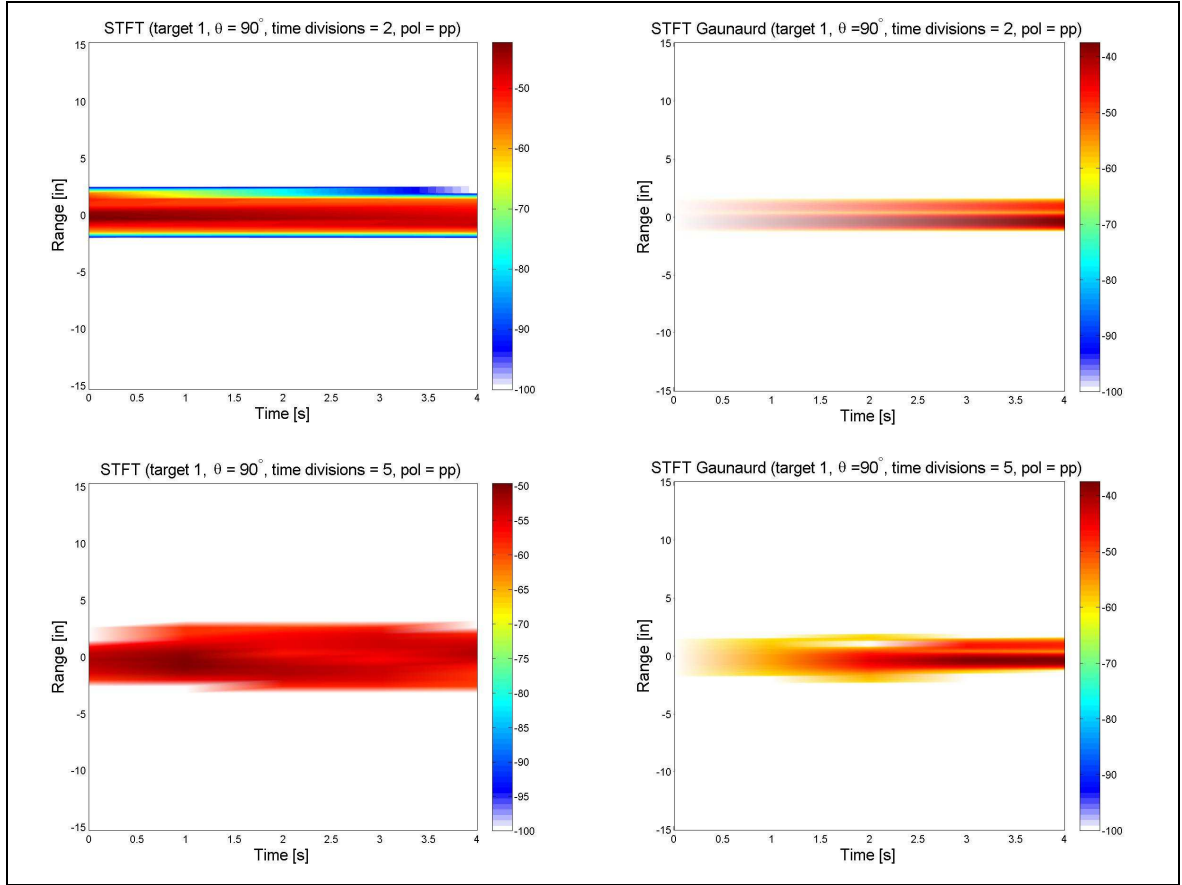
Figure 4.10: Target 1: Pol=PP, $\theta = 90°$, TFR's b.

The plots produced by the standard STFT and Gaunaurd's STFT for both polarizations, as depicted Figure's 4.9, 4.10, 4.11 and 4.12, reveal similar scattering information. Both TFRs were represented as functions of time and range and used the dB scale for representation of RCS scattering power. A cutoff of -60 dB was applied to each plot in order to isolate everything above the noise floor, which for the AFIT anechoic chamber was -60 dB. A Hamming window was also applied to the data to suppress unwanted sidelobes.

Both versions of the STFT did a good job of placing the scattering center of the sphere around 0 in. However, the accuracy in range waned as time divisions increased. This resolution loss was expected due to the inverse relationship between time and frequency resolution from the Fourier transform. A comparison of the standard STFT and Gaunaurd's STFT at time divisions of 2, 5, and 10 revealed that the standard

73
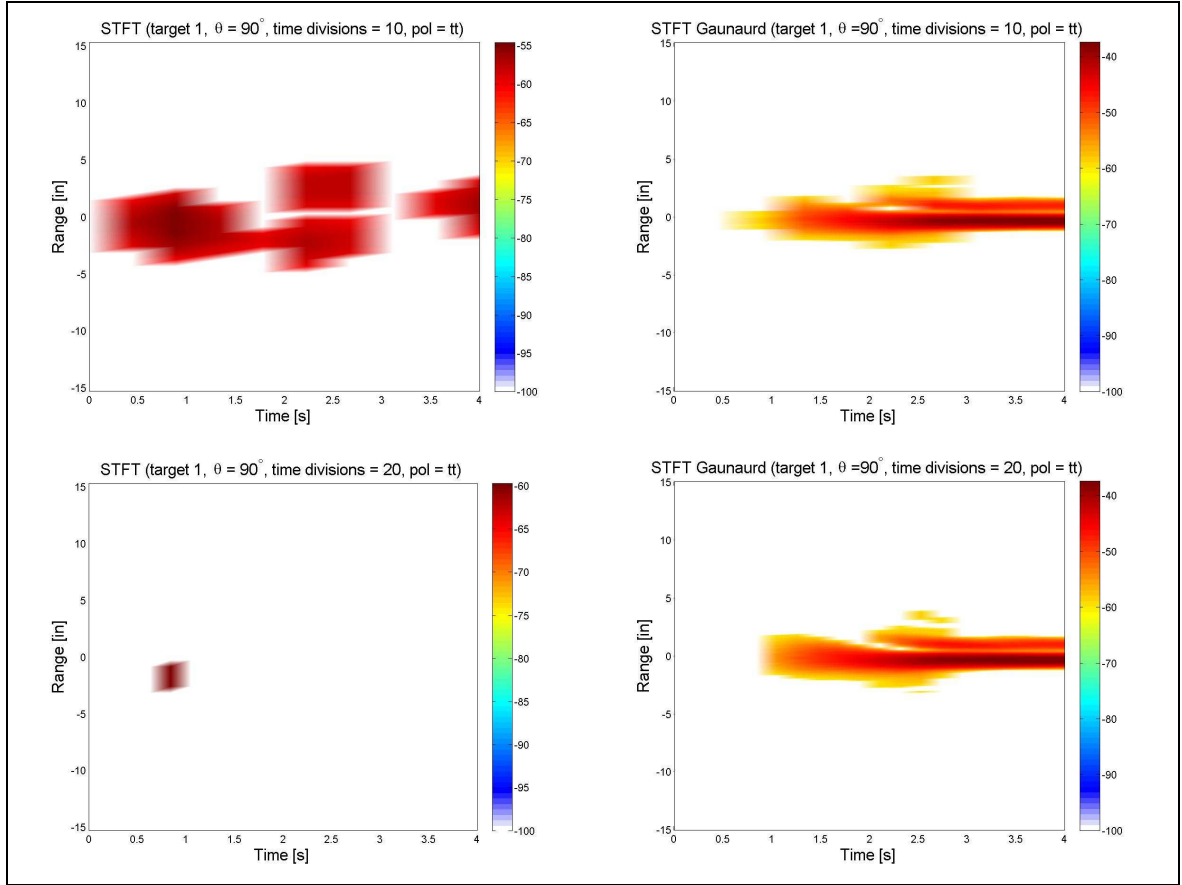
Figure 4.11:   Target 1: Pol=TT, $\theta = 90°$, TFR's c.

STFT placed scattering centers throughout the time duration while Gaunaurd's did not. Gaunaurd's STFT failed to deliver range information at the earliest samples of the sweep. Gaunaurd's STFT did however place the scattering center of the sphere more accurately than the standard STFT. The strengths and weaknesses of these two TFRs are easily understood from the math they were derived from. Simply stated, the standard STFT should have had lower resolution than Gaunaurd's STFT due to the number of samples used in the Fourier transform. The standard STFT used a uniform number of samples per time interval to create the range information, while Gaunaurd's STFT used an increasing amount of sampling data per time interval. From our knowledge on the Fourier transform, we can see that Gaunaurd's version should have more phase correlation than the standard version purely based on the number of samples used. The strengths of Gaunaurd's STFT over the standard version

74
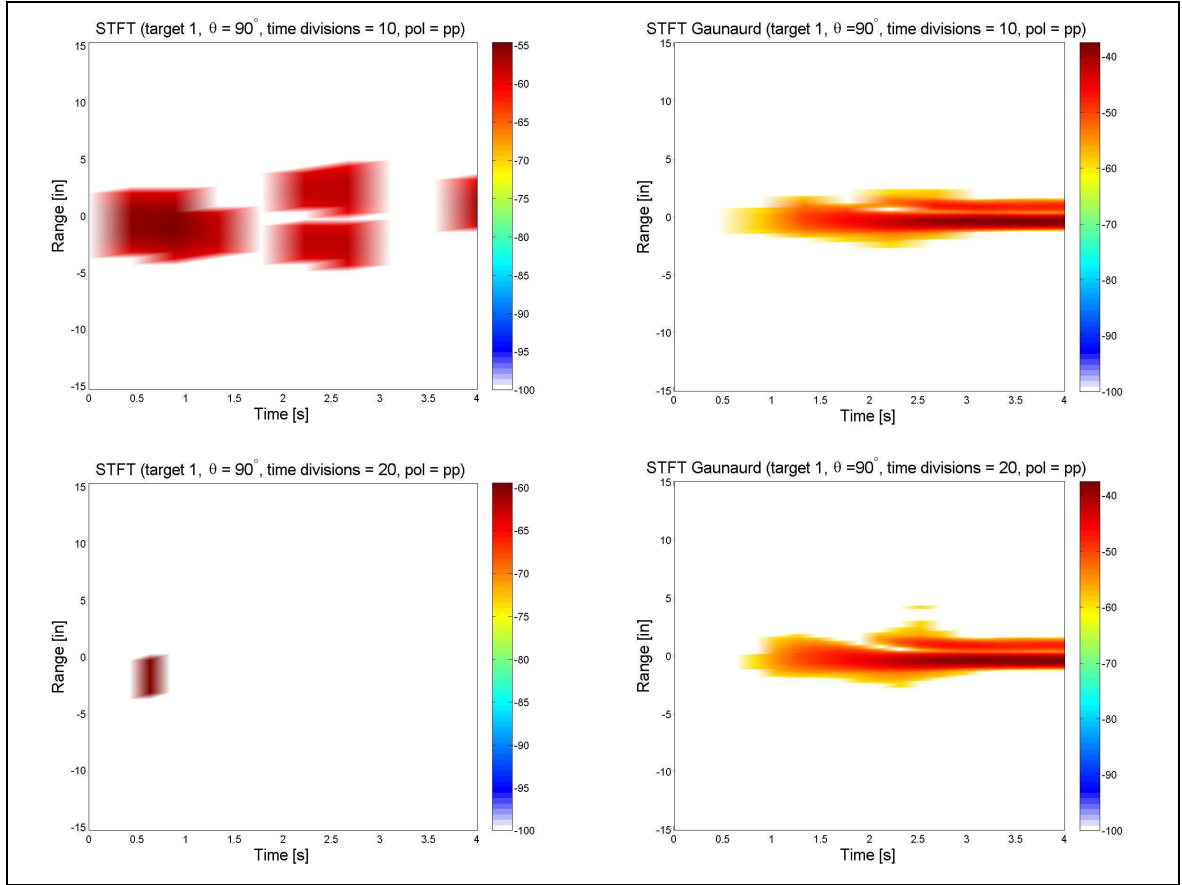
Figure 4.12:   Target 1: Pol=PP, $\theta = 90°$, TFR's c.

also limit its ability to locate scattering features in time. This became more evident during the analysis of subsequent targets. Given this, a full understanding of the TFR's strengths and weaknesses can lead to a good understanding of the target's scattering features over time.

4.2.1 Target 2.   The TFR analysis on Target 2 was done using the frequency response data at the azimuth angle $\theta = 0°$ and the PP polarization. To be clear, the TT polarization data gave nearly identical results and can be viewed in the Section 8.1. TFR analysis of Target 2 was important for the understanding of how each TFR treated stationary isolated scatterers. As in Target 1, an understanding of the scattering phenomena occurring in Target 2 must be understood before TFR analysis

can be accomplished. For this, we look at the Azimuth vs Range plot illustrated in Figure 4.13.
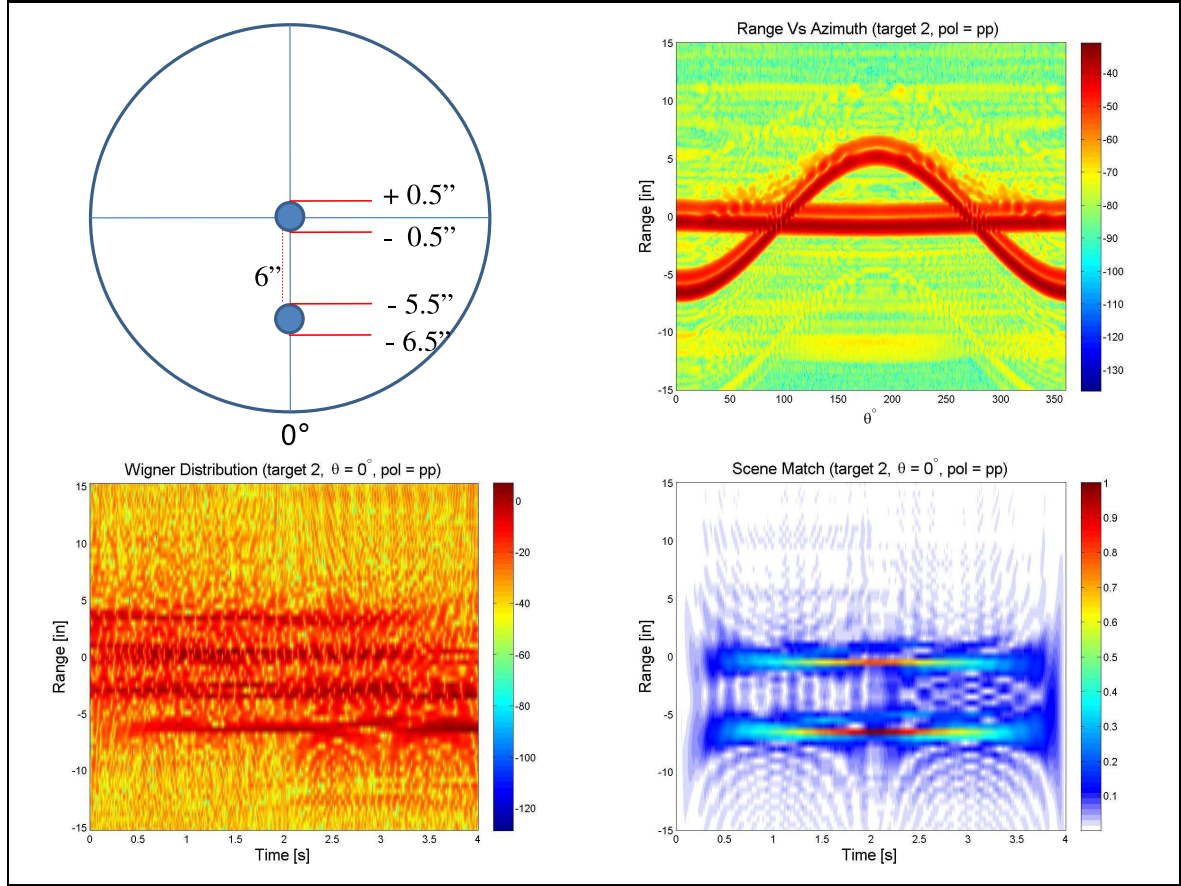
Figure 4.13:   Target 2: Pol=PP, $\theta = 0°$, TFR's a.

From the Azimuth vs Range plot in Figure 4.13 we clearly see two isolated isotropic scatterers. The backscatter return from these two spheres clearly matches their physical location as a function of azimuth angle. At $\theta = 0°$, it is clear that the two scatterers share similar scattering features and are separated by a distance of 6 in. From Target 1 analysis, it is understood that the backscatter return for a metallic sphere is the combination of the initial specular return and the delayed creeping wave return. These two scattering features are clearly seen from both scattering locations in the Range vs Azimuth plot. Therefore, while analyzing the TFRs, we must account for both the specular and creeping wave effect on each sphere.

According to the Wigner distribution plot in Figure 4.13, the TFR was able to accurately place Target 2's physical scattering centers at range locations of 0 and -6 in. However, this TFR also placed scattering centers at -3 and 4 in. The non-physical placement of these scattering centers is of concern. From the theory behind the WD in Section 2.4.3, it is understood that when the analyzed signal is a combination multiple independent signals, the WD will produce unwanted cross-terms between the auto-components, as depicted in Figure 2.2. In Target 2's case, each sphere represented a separate auto-component. The WD of the combined signal of these two auto-components produced the unwanted cross-term component that occurred between them. This unwanted cross-term effect was accounted for, but the scattering location that appeared at 4 in cannot be attributed to the same cross-term effect. A quick assessment of this scattering feature might incline one to say it is an artifact of multibounce. This is not the case since the Range vs Azimuth plot did not produce a similar artifact at 4 in. The most probably explanation for this artifact lies with the correlative matrix the WD used to create the distribution. As discussed from Target 1 analysis, the WD will create a value from uncorrelated pulses. Because the signal processed was from multiple components, it is possible that they did correlate to the $e^{j4\pi ln/N}$ matrix in the WD in addition to the autocomponent seen at -3 in. The bottom line is that the WD failed to accurately produce useable scattering features for analysis. Even if one could predict and discard the cross-term artifact at -3 in, the artifact at 4 in was unforeseeable and could be mistaken for a physical scatterer.

The Scene Match function depicted in Figure 4.13 worked similarly to that of Target 1. It successfully placed the scattering centers in range for most of the sampling period but failed at the ends. The lack of range data at the ends of the frequency sweep is attributed to the same limitations the singular sphere had in Target 1. The low and high frequency regions of the frequency sweep did not overwhelmingly interact with the metallic spheres to correlate their return phases to the matched scene. Although this modified TFR had limitations at the extremes of the frequency sweep, it offered a high degree of range resolution in the middle frequency band range.

The standard and Gaunaurd STFT produced similar results on the Target 2 data set according to Figure's 4.14 and 4.15.
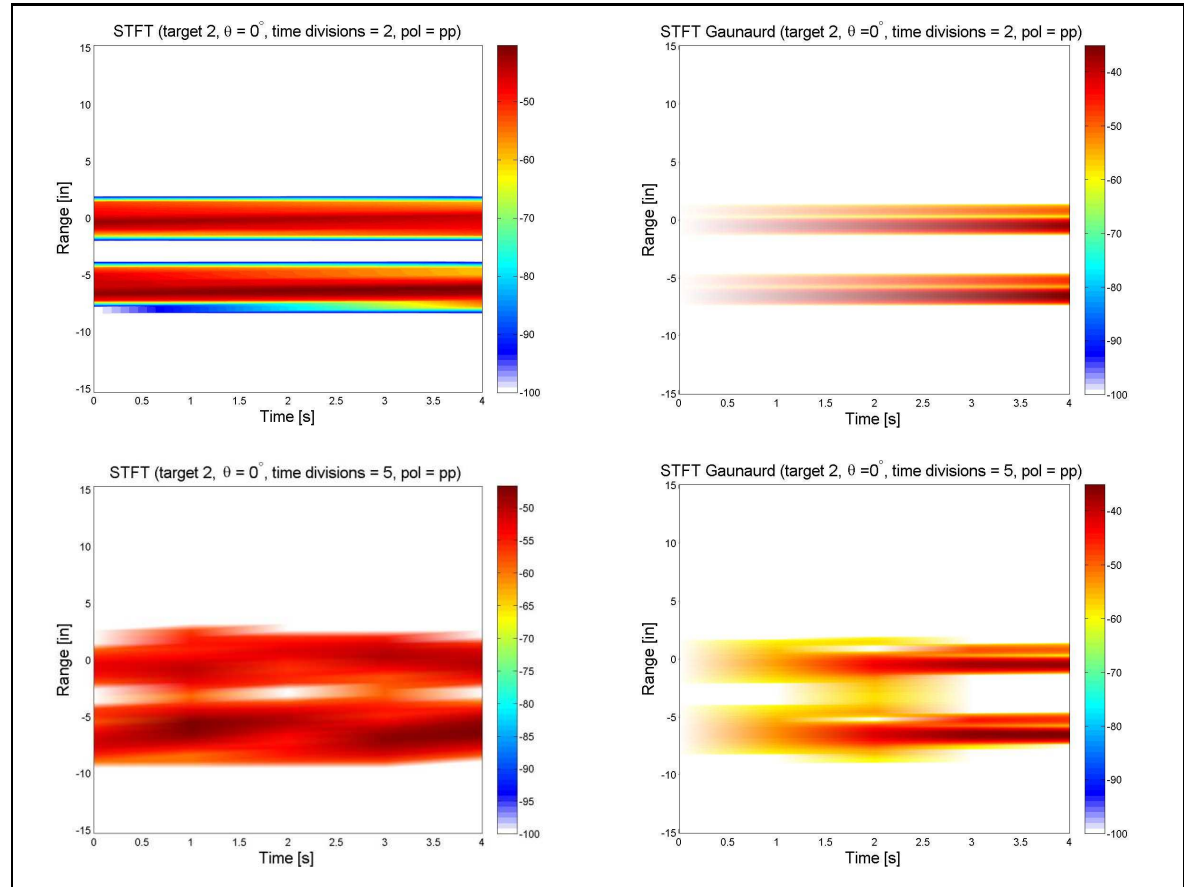
Figure 4.14:   Target 2: Pol=PP, $\theta = 0°$, TFR's b.

From Figure's 4.14 and 4.15 one can see how both TFRs loose range resolution as time intervals increase. Again, the standard STFT did not produce the localization of the scattering centers as well as Gaunaurd's STFT but it did produce the features throughout the entire time duration. It is to be noticed that as the time intervals increased, Gaunaurd's STFT offered higher range resolution. This strength was due to the higher frequency bandwidth used by Gaunaurd's STFT throughout the function. Although this appears to be advantageous, one is not to be misled. The high bandwidth exploited by Gaunaurd's function used information that occurred in previous time slices to increase the resolution. Therefore, the information used did not all come from the same time segment as did the standard STFT.
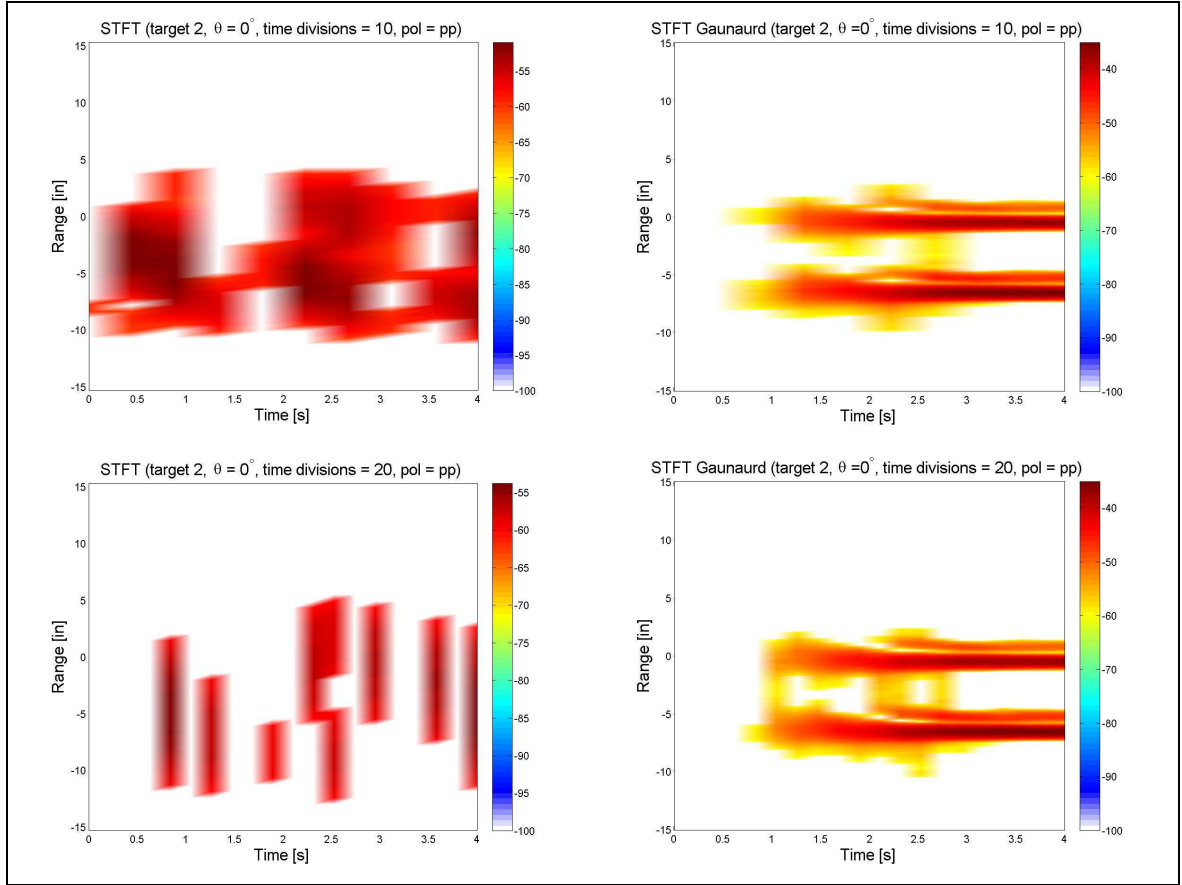
Figure 4.15:   Target 2: Pol=PP, $\theta = 0°$,TFR's c.

4.2.2 Target 3 and 4.   TFR analysis on Target's 3 and 4 were done simulta-neously. The reason for this was to isolate the non-stationary components represented in Target 4. Both targets were structurally similar. Target 4 was identical to Target 3 with the addition of the rotating metallic spheres described in Figure 3.12. The purpose of this comparison was to determine how accurately the TFRs identified the rotating ball bearings as a function of time. Analysis of these targets was done using the TT polarization. Figures containing the PP polarization are found in Section 8.2.

The foundation of the scattering phenomena between Target's 3 and 4 was accomplished by comparing the Azimuth vs Range plots in Figure's 4.16 and 4.17.

The Azimuth vs Range plot in Figure 4.16 clearly shows three strong responses throughout the angular measurement. Specifically, at $\theta = 90°$, strong responses
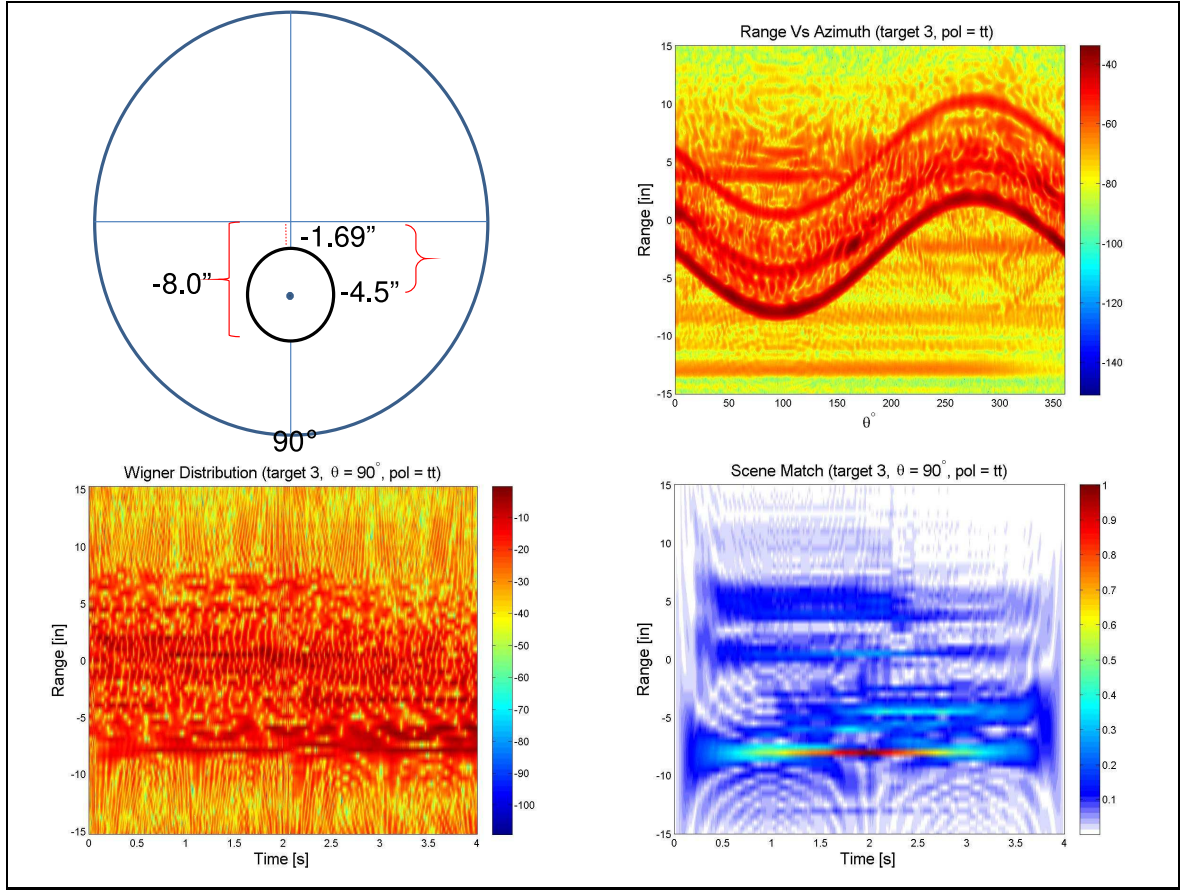
Figure 4.16:   Target 3: Pol=TT, $\theta = 90°$, TFR's a.

occurred at range values of $-8, -4.5, \ and \ -1 \ in$. These range values correlated to the front edge of the cone, the top of the cone, and the creeping wave effect from the cones shape. The other scattering features throughout these ranges were caused by interference effects. The scattering features described from Figure 4.16 were compared against the Azimuth vs Range plot in Figure 4.17 to determine the effects the non-stationary components had on the frequency response. Figure 4.17 clearly shows the impact the non-stationary components had on the backscatter RCS. From this figure, one can see how the scattering features are smeared over a large range. This smearing was the result of the phase changes induced by the rotating ball bearings. The components that contributed to the smearing can be analyzed through Equation 2.13. The RCS smearing induced by the ball bearings makes it impossible to determine the instantaneous RCS at a specific angle using the Azimuth

80
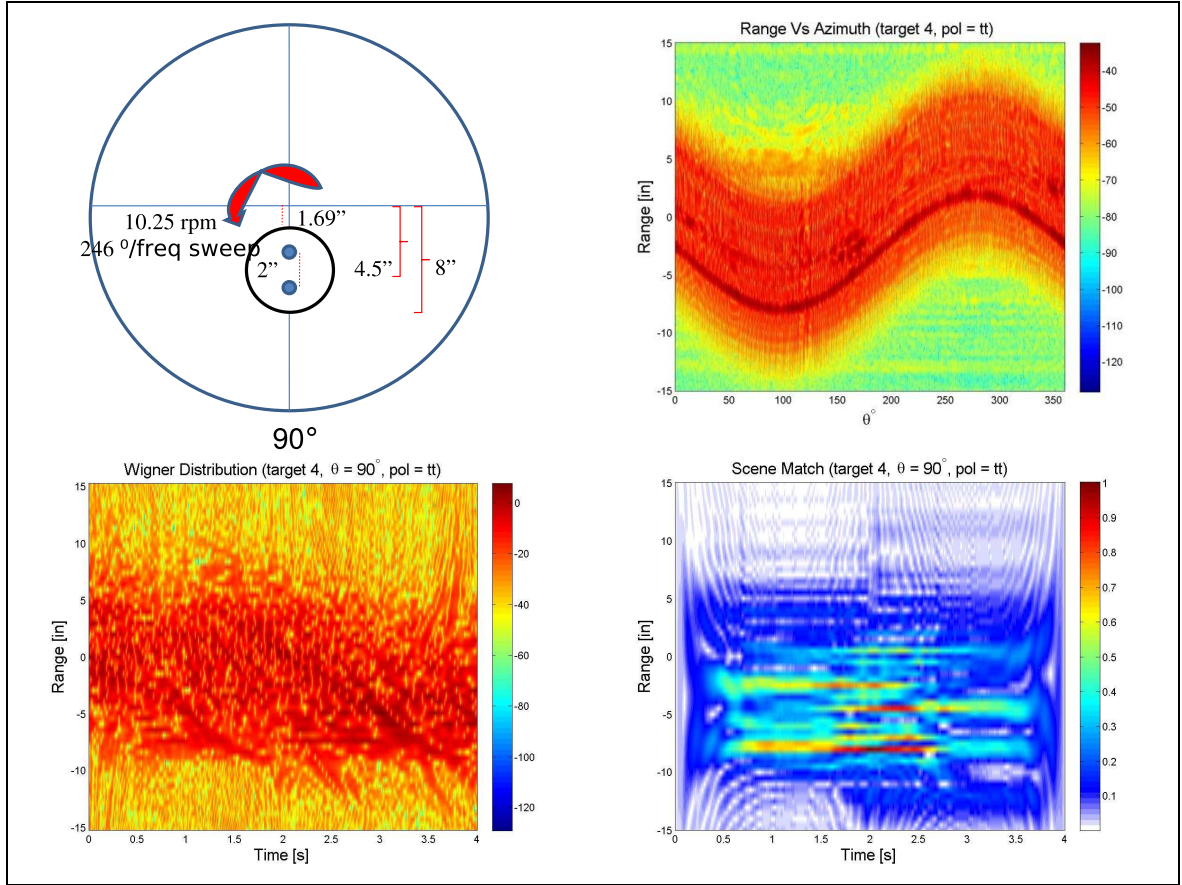
Figure 4.17:   Target 4: Pol=TT, $\theta = 90°$, TFR's a.

vs Range plot. This happens because the Azimuth vs Range plot averages out time when producing the range domain from the Fourier transform. Therefore, in order to determine the instantaneous RCS, one must use TFRs.

The instantaneous RCS from Target 4, as seen in Figure 4.17, was difficult to interpret using the Wigner distribution. An analysis of the non-stationary RCS was done by comparing Target 4's WD to that of Target 3's, located in Figure 4.16. The WD for Target 3 was consistent with the Range vs Azimuth plot in locating scattering centers at -8, -4.5, and -1 in. However, these returns were hard to distinguish from other RCS clutter that littered the Time-Frequency plot. The WD generated strong returns in the -8 in to 8 in range for all time. These cross-term effects made scattering localization near impossible. In order to make use of the WD under these

81

conditions, a comparison was made to find contrasts between the WD of Target 3 and 4.

At first look, the WD produced for Target 4 contained the same convoluted RCS pattern that persisted in Target 3. However, upon close inspection, one can see two "S" shaped patterns in Figure 4.17 at time values 0.5 to 1.5 s and from 1 to 4 s occurring at ranges of -3.5 to 7 in and 5 to -6 in respectively. These subtle differences were exploited to determine possible scattering centers of the ball bearings.

In order to be clear on the expected range locations of the specular return from the ball bearings as a function of time, a plot was made using the rotational rate of $246°$ per frequency sweep as depicted in Figure 4.18. It is important for the reader to remember that the purpose of this comparison was to locate the scattering centers from the ball bearings over time. The ability to do this could validate the WD as a viable tool for non-stationary RCS analysis.
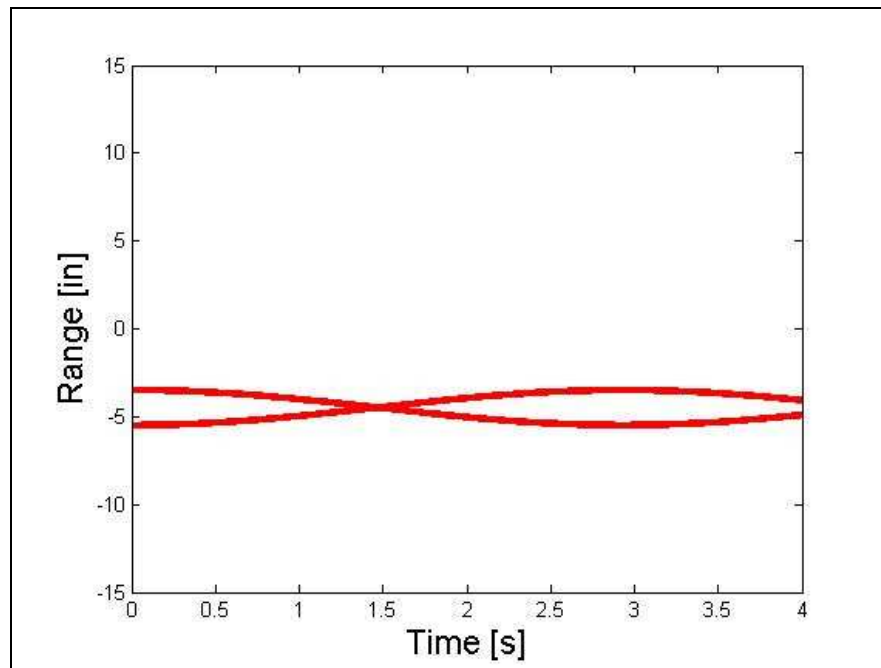

Figure 4.18:   Hypothetical Target 4 ball bearing rotation.

The specular scattering locations of the ball bearings in Figure 4.18 are hypothetical. The actual rotation of the ball bearings followed the same pattern, but the exact position to time coordinates varied. The purpose of this plot was to find a similar pattern in the WD. Figure 4.19 enlarges the WD plot from Figure 4.17 to better locate the scattering features from the target.
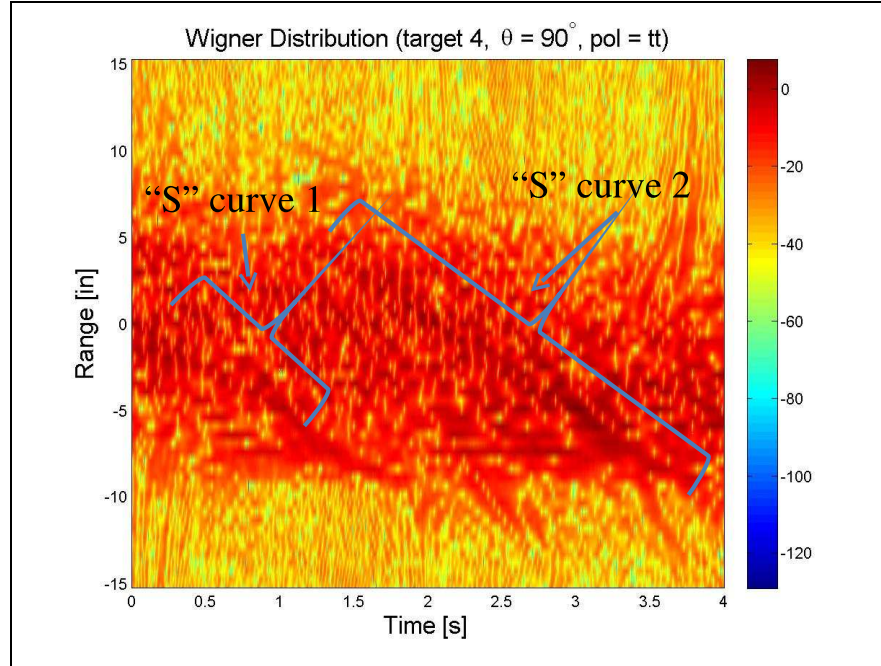
Figure 4.19:   Wigner distribution for Target 4. The brackets highlight possible scattering features from the rotation of the ball bearings.

According to Figure 4.19, it was possible that the first "S" shaped curve from time values $0.5\ to\ 1.5\ s$ represented one of the ball bearings rotating towards the radar. Although the curve was in the same range vicinity as the ball bearings $(-3.5\ to\ 5.5\ in)$, the range limits over the same time period did not match up with a physical possibility. According to Figure 4.18, it should have taken the ball bearings about $3\ s$ to make half a revolution. This inconsistency limits the confidence one can have about the Wigner distribution. The second "S" shaped curve in Figure 4.19 also does not fit possible specular range values for the ball bearings. The feasible time values of this curve appear at $1\ to\ 4\ s$, but the range extent goes from $5\ to\ -6\ in$. The large

83

range extent could be caused from creeping waves and multibounce phenomena, but the specular return should still be clearly present. Because the range spread was so great, one must not place confidence in the Wigner distribution. The cross-term contributions play havoc in the ability to make sense out of a multicomponent signal.

The analysis of Target 4's non-stationary RCS was analyzed in a similar fashion using the Scene Match function. The non-stationary effects caused by the rotating ball bearings were compared to Target 3's stationary RCS. Given this, the Scene Match plot for Target 3, which is depicted in Figure 4.16, clearly agrees with the Range vs Azimuth plot in placing the main scattering effects in range. The Scene Match plot gives us the added advantage of knowing when those scattering contributors occurred. For instance, the scattering component located at -4.5 in occurred in the later half of the frequency sweep according to the Scene Match plot. This information was not evident when looking at the Range vs Azimuth plot.

As was the hope for the WD, the desire behind the Scene Match plot was to locate the ball bearings as a function of time in order to validate it as a viable TFR. The hypothetical specular scattering position, from Figure 4.18, was used as an aid to locate the ball bearings. The stationary effects from Target 3 were also considered to find the differences between the two plots. An important observation between the Scene Match plots of Target's 3 and 4 show that both plots produced the same stationary scattering positions. However, Target 4's plot had additional scattering features not located in Target 3's. These differences were caused solely by the ball bearings. An overlay comparison of the two plots revealed three distinct differences. These additions are illustrated in Figure's 4.20 and 4.21. Figure's 4.20 and 4.21 were created by a Scene Match subtraction program developed in Matlab® . The program, found in Section VII.10, coherently subtracted Target 3's Scene Match response from Target 4. Theoretically this should reveal only the non-stationary differences and subtract out the stationary components. Figure 4.20 represents the unfiltered Scene Match subtraction while Figure 4.21 represents a filtered version in order to isolate the non-stationary characteristics.
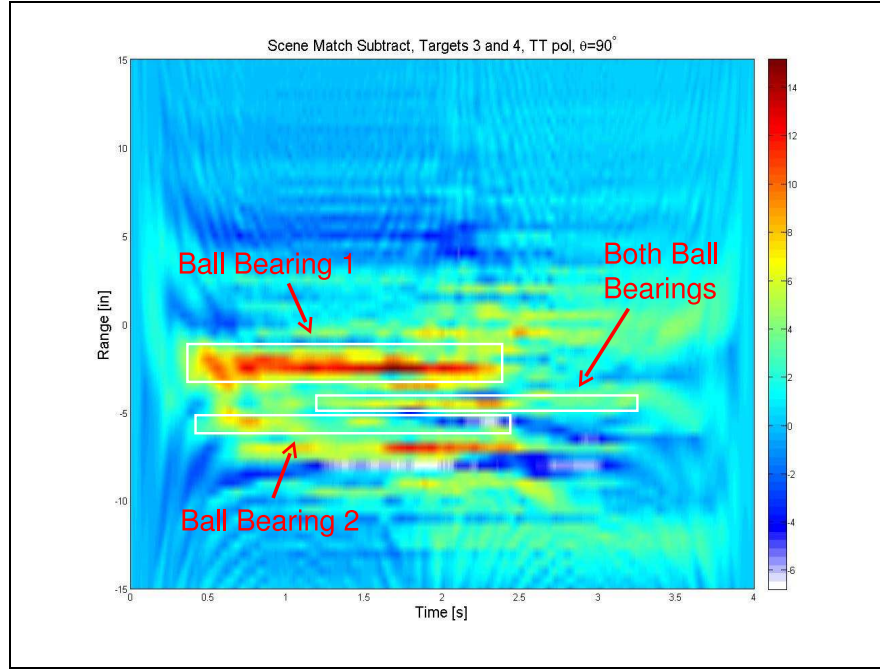
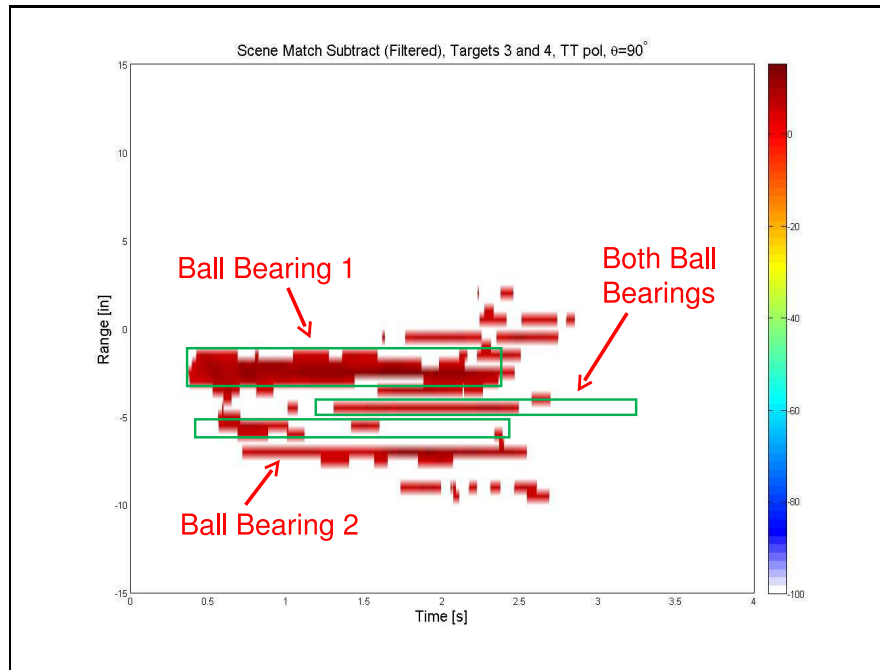Figure 4.20:   Scene Match Subtraction Target's 3 and 4.

Figure 4.21:   Filtered Scene Match Subtraction Target's 3 and 4.

The three scattering features highlighted in Figure's 4.20 and 4.21 are within the range of feasible locations for the ball bearings. The scattering features also resemble

the hypothetical path taken by the ball bearings in Figure 4.18. As one may notice, the three additional segments do not curve as fluidly as the hypothetical path. One must know however, that the hypothetical path assumes that the PRI of the radar was constant throughout the frequency sweep. Although the PRI was set to $250\ ns$, the actual frequency sweep had a distinct pause and continuation. The pause occurred at $8\ GHz$ due to the way the radar system was designed. There were two amplifiers for the system, one handled $6 - 8\ GHz$ and the other from $8 - 18\ GHz$. The amplifier switching that occurred caused the system to have a defined break in sampling. Given that the PRI was set to $250\ ns$ and there were 480 pulses per frequency, the time the target was actually irradiated was $0.144\ s$. Obviously this time period was far less than $4\ s$. Therefore, the remaining $3.85\ s$ inherent to the frequency sweep was the result of the switching time between amplifiers. The result from this switching gave the TFR two distinct positions rather than a continuous change from pulse to pulse. Using this theory, the time values associated with the frequency band $6 - 8\ GHz$ were $0 - 0.66\ s$, and for $8 - 18\ GHz$ the time values were $0.66 - 4\ s$. Remember however, it did not take the radar these times to sweep the signal. The total time was averaged between the two frequency band sweeps and the duration of the switching. From this theory, one can expect two distinct locations for the ball bearings appearing at the times $0 - 0.66\ s$ and $0.66 - 4\ s$. According to Figure's 4.20 and 4.21, the discrete range change happened over the time period $1.5 - 2.5\ s$. This change happened at the expected ranges for the ball bearings but did not happen discretely as expected. From the plot, the ball bearings held two possible values at the same time, which did not make sense. The unclear RCS pattern from the Scene Match function could be a result from multi-bounce or other EM phenomena. Although the Scene Match function did not produce a perfect range vs time plot of the ball bearings, it did give much better insight into the target's flare spots than the Wigner distribution.

Substantial RCS information from the non-stationary components in Target 4 were difficult to extract from either the standard STFT or Gaunaurd's STFT. As in the other TFRs, Target 3's plots were used as a baseline measurement. The standard

STFT and Gaunaurd's STFT for both targets can be viewed in Figure's 4.22, 4.23, 4.24, 4.25.
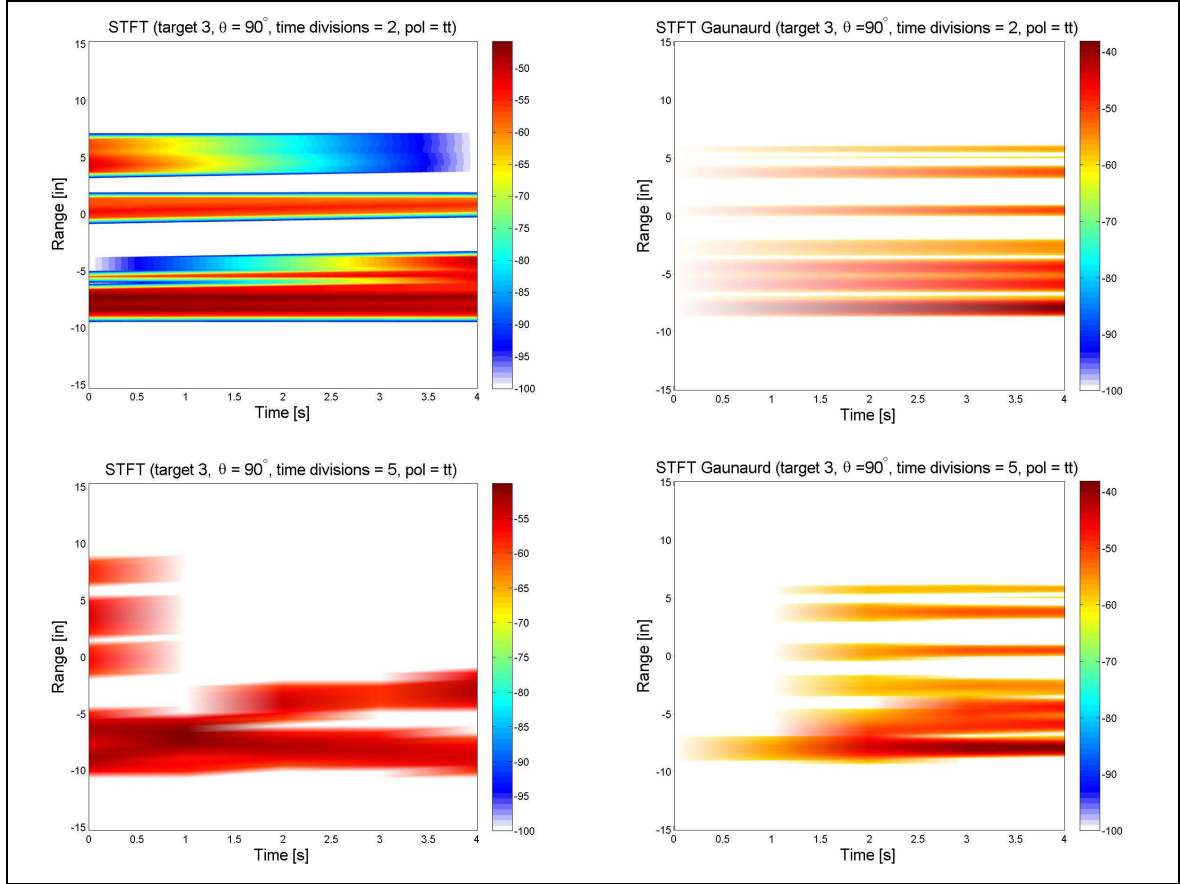

Figure 4.22:   Target 3: Pol=TT, $\theta = 0°$,TFR's b.

The first comparison was between the two versions of the STFT using 2 time divisions and 5 time divisions. The standard STFT at 2 time divisions produced a vague resemblance to the hypothetical rotation of the ball bearings in Figure 4.18. As one can view in Figure 4.23, there are two distinct responses at -5.5 and -3.5 in. These responses faded in time and reemerged as a single response at -4.5 in. The characteristics of this track can also be seen in the 5 division plot. Early in time there are two distinct values at ranges of -5.5 and -3.5 in. At 2 s the responses end at these ranges and the -4.5 in response emerges.

A similar pattern was produced by Gaunaurd's STFT. In these plots, two distinct RCS scatterers appear at -3.5 and -4.5 in. These two scatterers seem to be on
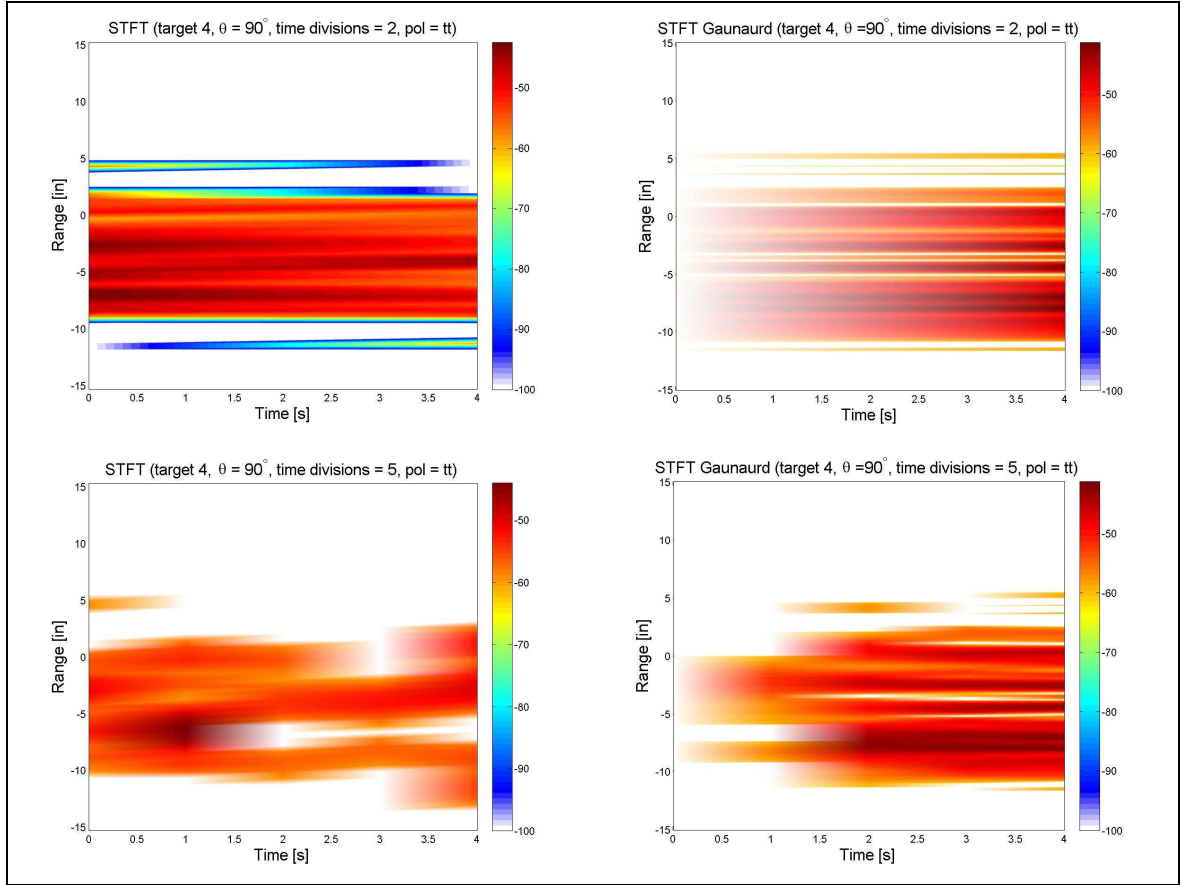
Figure 4.23:　　Target 4: Pol=TT, $\theta = 0°$, TFR's c.

a course for convergence. It is unclear if these two lines represent the ball bearings, but they do fall within the accepted range possibilities.

Gaunaurd's STFT was much more revealing that the STFT at 10 and 20 time divisions. The standard STFT had vast regions of no data. The reason for this was that most of the data was filtered out because the power levels were too low. The data that remained was of little use. It is possible that at 10 time divisions the two ball bearings are resolvable from $t = 0 - 1.5$ s, but this is unlikely given the poor resolution. Gaunaurd's STFT at both 10 *and* 20 time divisions appears to reveal possible scattering locations for the ball bearings over a majority of the frequency sweep. As evident by Figure 4.25, both plots share the similar crossing behavior predicted by the hypothetical ball bearings in Figure 4.18. This similarity is encouraging.
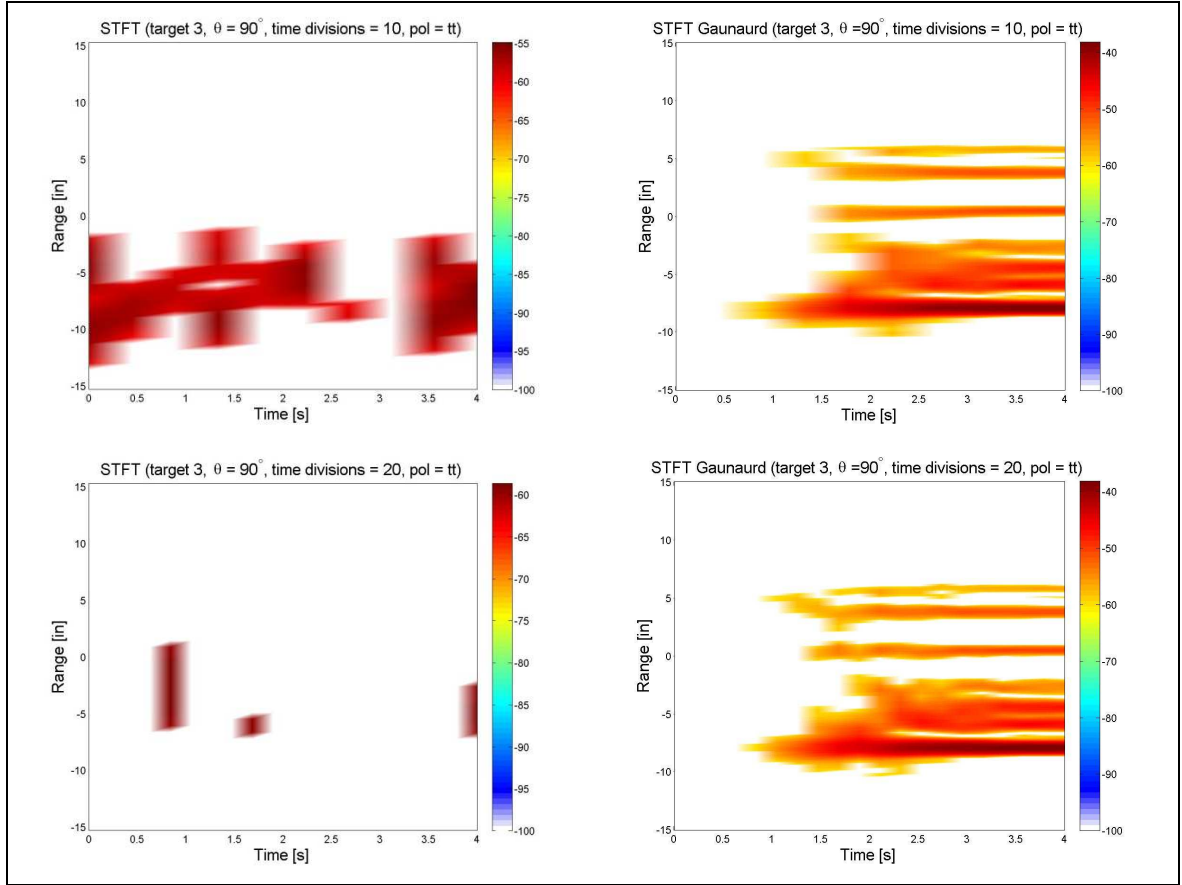
Figure 4.24:   Target 3: Pol=TT, $\theta = 0°$, TFR's c.

For thoroughness, it is important to comment on the plots produced by the standard STFT and Gaunaurd's STFT using the PP polarization. These plots, located in Figure's H.8 and H.9, exhibit similar scattering phenomena as the TT polarization. The 5 and 10 time division plots using the standard STFT were particularly interesting because they contain a similar trace pattern for both ball bearings that correlate closely to the hypothetical case in Figure 4.18. Although the resolution was poor in both plots, the reader can still see the weave pattern consistent with the rotation of the ball bearings. Gaunaurd's STFT under the PP conditions also exhibits the weave pattern seen in the STFT for plots using 5, 10 and 20 time divisions. One can clearly see the crossing behavior of the spheres occurring in all plots around $1\ s$. The separation between the two spheres widened as time increased and the resolution of the two spheres increased as expected. At $time\ =\ 4\ s$, Gaunaurd's plots offerred high
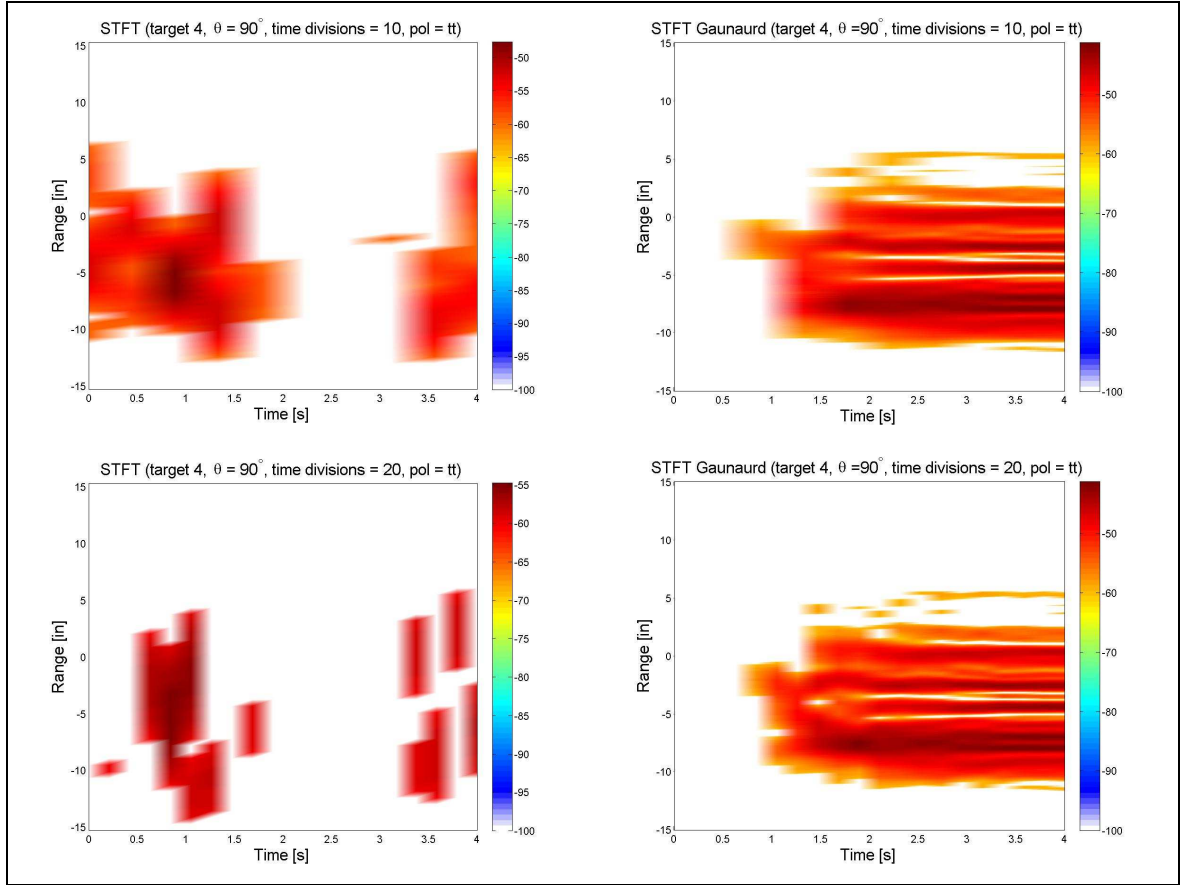
89

Figure 4.25:   Target 4: Pol=TT, $\theta = 0°$, TFR's c.

resolution for both ball bearings. In order to interpret these plots properly, one must understand the scattering features that happened earlier in time and remove them from the later time features. This means that the center scattering features located at $-5\ in$ must be understood to be the scattering features that occurred when the two ball bearings were crossing earlier in time. Understanding this technique is important in diagnosing scattering features using Gaunaurd's STFT.

4.2.3   Targets 8, 9, 10, and 11.   The following section analyzes a target set that was structurally identical but varied in the rotational speed of the non-stationary ball bearings. The purpose of this was to determine if the TFRs had limits on their ability to resolve scattering features under increasingly non-stationary conditions. Target's 8, 9, 10 and 11 were used to explore the non-stationary limits. This target

set was physically identical to Target 4 with the addition of the trihedral placed 6 *in* from the center of the Styrofoam target mount. The analysis of the TFRs were done using the TT polarization at $\theta = 0°$. In this section, each TFR was analyzed using the resulting plots on all four targets simultaneously. This provided the ability to resolve the non-stationary scattering features as a function of rotational speed.

4.2.3.1 Azimuth vs Range. For consistency and clarity, the non-stationary effects from each target are discussed. The non-stationary effects were clearly depicted in the Azimuth vs Range plots for each target. As stated, the difference between each target was the rotational speed of the ball bearings. The speed of rotation for Target's 8-11 were: 0, 46°, 246°, *and* 912° per frequency sweep respectively. This gave a large range of rotational speeds between targets. The increase in speed was evident in the non-stationary induced effects illustrated in Figure's 4.26, 4.27. 4.28 and 4.29.

As indicated by the schematics in Section III, the orbiting center for each target was located at 0 *in* and the rotational span of the ball bearings was from −1 *to* 1 *in*. From this, one would expect the scattering from the ball bearings to be contained within the 2 *in* diameter created by the circling ball bearings. This did not happen. As depicted in Figure's 4.26, 4.27, 4.28 and 4.29, the scattering spread varied greatly between targets. For instance, the scattering spread induced by the slowly rotating ball bearings in Target 9 had little impact on the scattering features around the non-stationary center. However, as the speed of the rotation increased, the scattering spread in range also increased. As an example, according to Figure 4.28, the spread induced by the rotational speed of 246° per frequency sweep in Target 10 covered the entire dimensions of the target. Even worse, the spread induced by the 912° per frequency sweep rotation from Target 11 covered the entire range window from −15 *to* 15 *in*. The spread in range induced by the non-stationary components was an artifact from the inability of the Fourier transform to produce correct range information from uncorrelated phases as described in Section 4.1.1. Although the non-
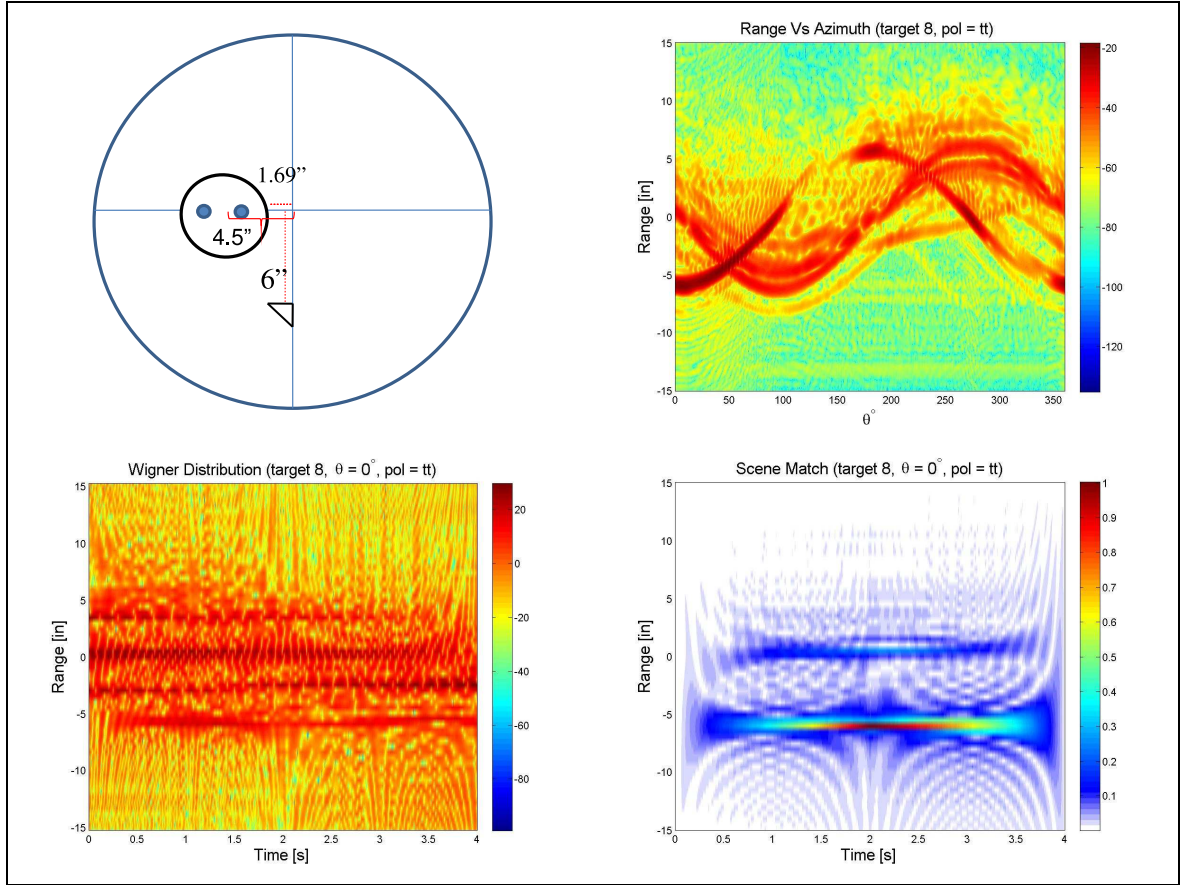
Figure 4.26:   Target 8: Pol =TT, $\theta = 0°$, TFR's a.

stationary components corrupted the placement of themselves in range, the stationary components were not affected. This observation was evident through the range local-ization of the trihedral in each target. The main point to be taken from the Range vs Azimuth plots is that RCS localization of non-stationary components becomes increasingly difficult to accomplish as the non-stationary components increase their speed relative to the frequency sweep.

4.2.3.2   Wigner Distribution.   In order to analyze the TFRs properly, an understanding of the scattering produced by the rotating ball bearings must be understood. Figure's 4.30, 4.31, and 4.32 offer the reader a hypothetical path for each target based on the rotational speed of the ball bearings. The traces in these plots were created from the specular returns from the ball bearings.
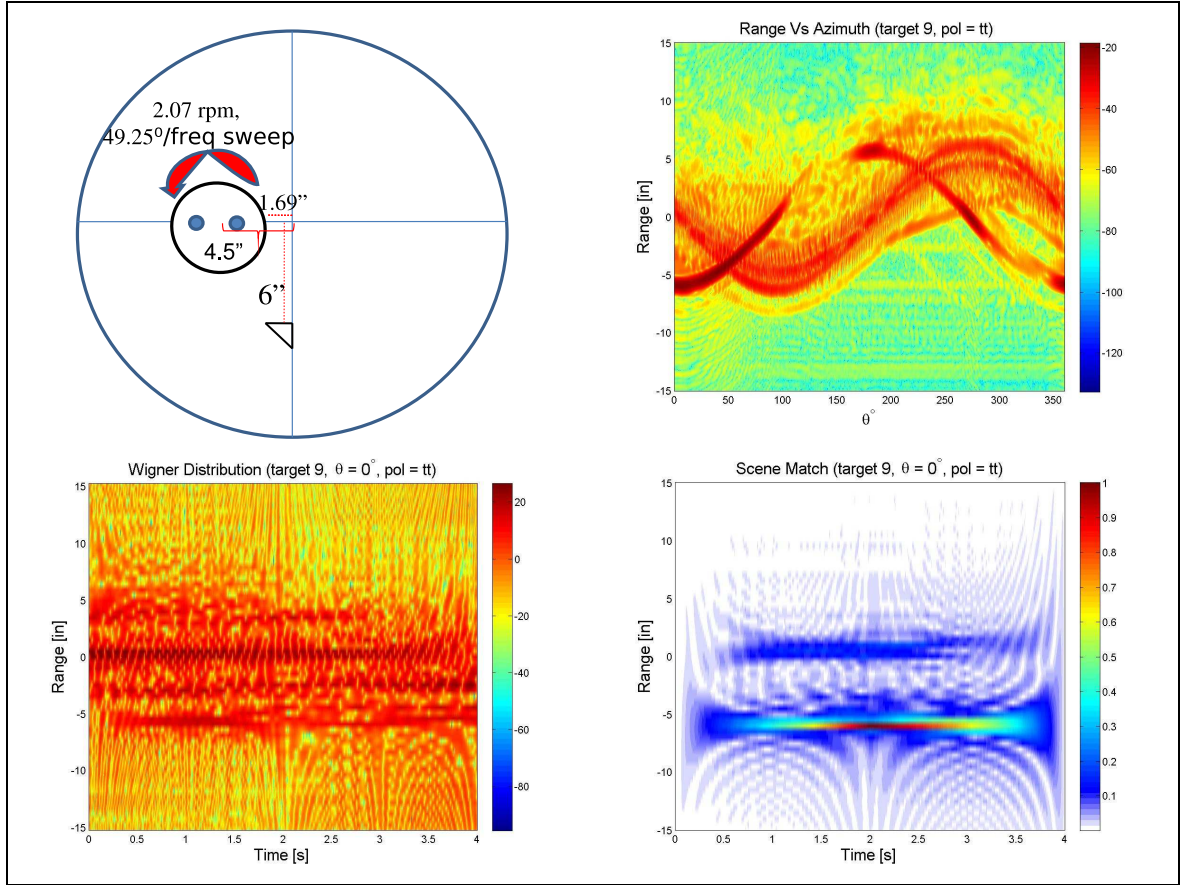
Figure 4.27:   Target 9: Pol =TT, $\theta = 0°$, TFR's a.

The Wigner distribution did not clearly reveal the location of the ball bearings for any of the targets as illustrated by Figure's 4.26, 4.27, 4.28 and 4.29. The plots produced for each target depicted similar scattering features as seen from the WD on Target 2 in Figure 4.13. The similarities between these distributions were from the two strong scatterers located at 0 and 6 in and the cross-terms created by them. There were two notable changes that occurred in the Wigner distributions as the rotational speed increased. The first observation was that the scattering features that occurred at range values of 0 and 6 in waned as the rotational speed increased. This was caused by the increasingly uncorrelated phases induced by the higher rotational speeds. Due to the way the Wigner distribution was created, the function used uncorrelated pulses at the later time samples to create range information. This mathematical operation resulted in a low resolution as time progressed and as the speed of the rotating ball
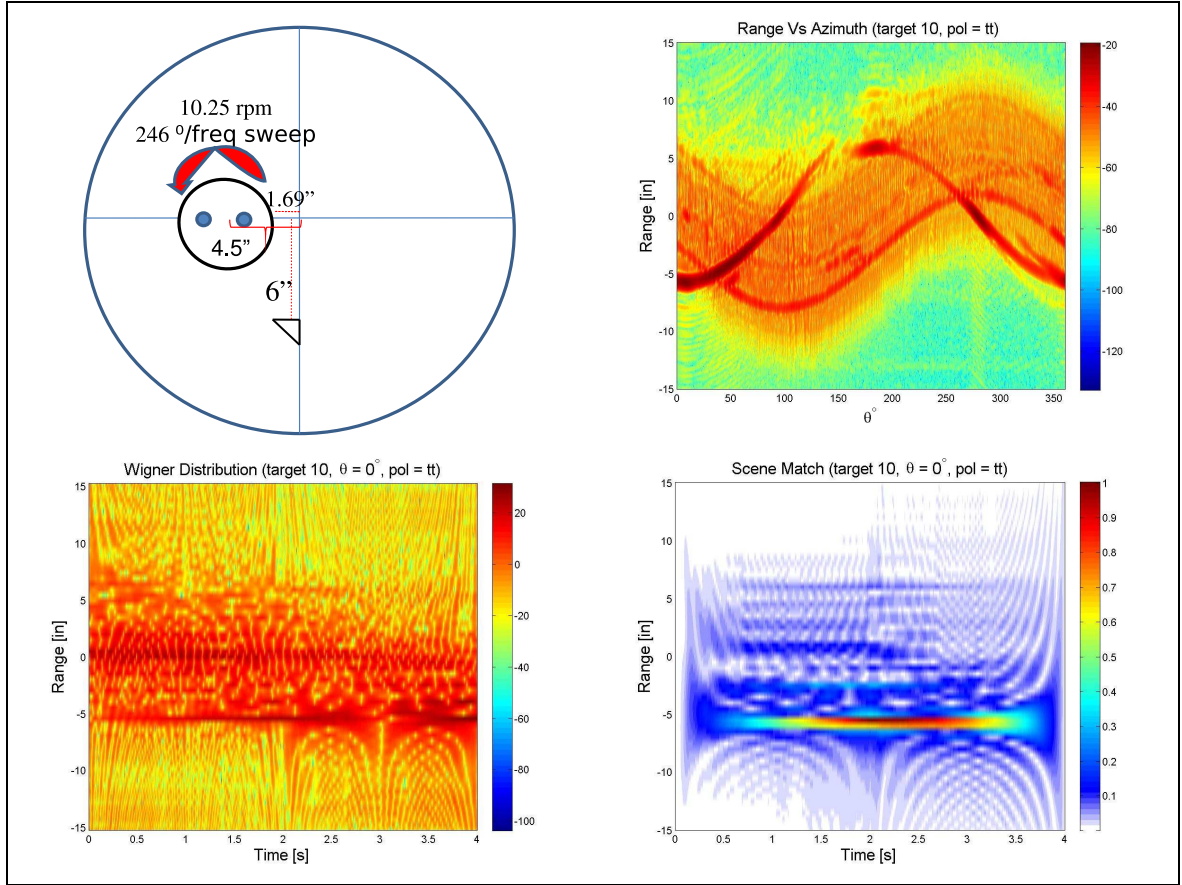
Figure 4.28:   Target 10: Pol =TT, $\theta = 0°$, TFR's a.

bearings increased. The second observation was that the Wigner distribution did not produce the expected wavelike patterns depicted in Figure's 4.30, 4.31, and 4.32. The reason for this was unknown, but the bottom line is that the Wigner distribution failed to resolve the non-stationary scatterers.

4.2.3.3 Scene Match.   The Scene Match function was able to accurately place the stationary components of the target set. However, the abilities of the Scene Match function to locate the non-stationary components were limited at best. The plot produced for Target 8, represented in Figure 4.26, clearly shows the strong scattering centers at $-6 \ in$ and at $0.25 \ in$ produced by the trihedral and cone respectively. The response at $0.25 \ in$ was the result of the cone's placement $4.5 \ in$ off the center of the pedestal on the axis that was normal to the radar. The ball
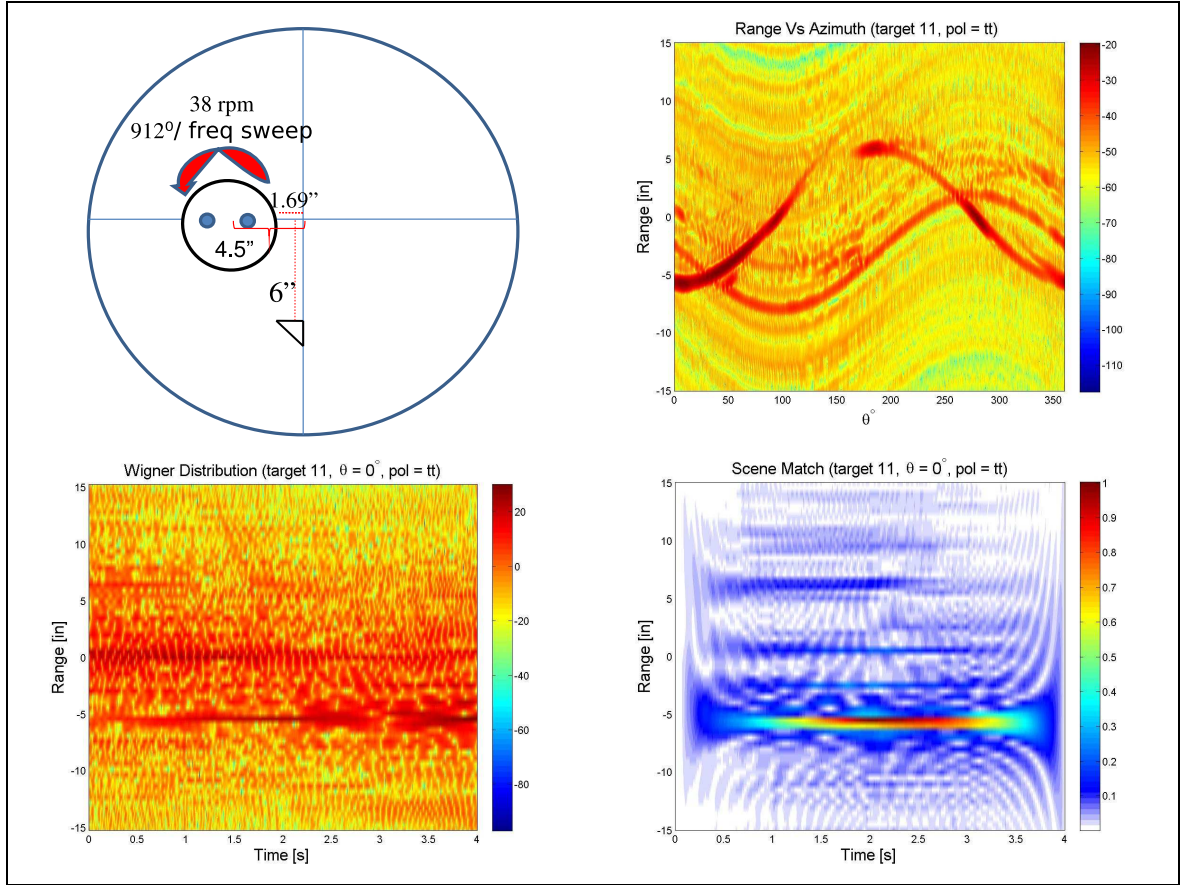
Figure 4.29: Target 11: Pol =TT, $\theta = 0°$, TFR's a.

bearings were co-planar, which gave them an identical position in the Scene Match function. This was validated by the scattering feature located at $0°$ in the Azimuth vs Range plot. For Target's 9, 10, and 11, the Scene Match function clearly placed the scattering from the trihedral correctly in range. Although the function worked well for stationary scatterers, it did not provide a clear understanding of the location of the ball bearings as a function of time.

The rotational position of the ball bearings for Target 9 were difficult to interpret from the Scene Match function. Given that the rotation speed was slow, one would expect little change in the ball bearings position over the frequency scan. The plot produced for this target revealed a possible non-stationary scatter located at a range of 0 to 1 in throughout the plot. The scatterer seemed to shift its position from 0 to -1 in through the time period 1 to 3 s. The resolution in this range was poor, which
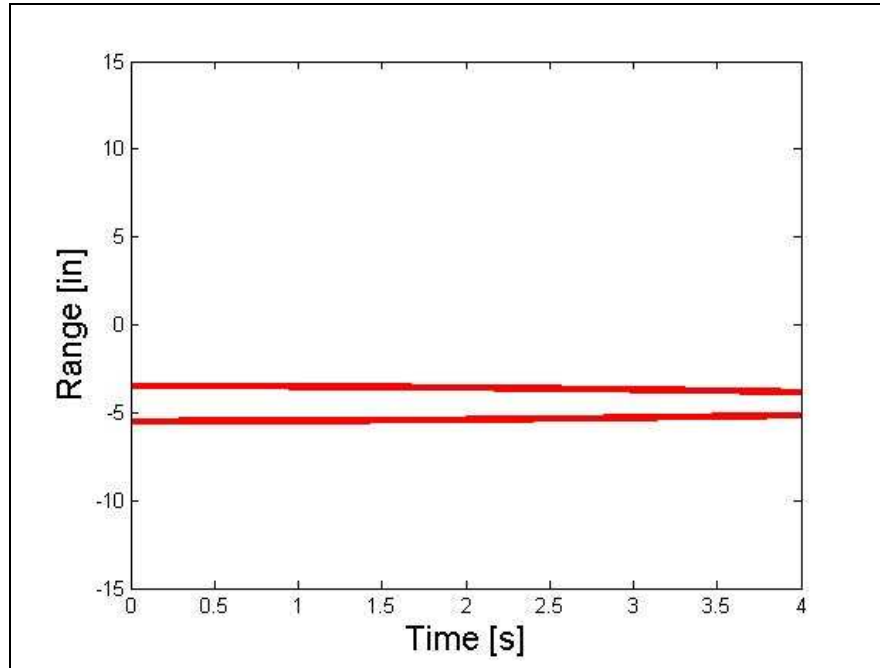
95

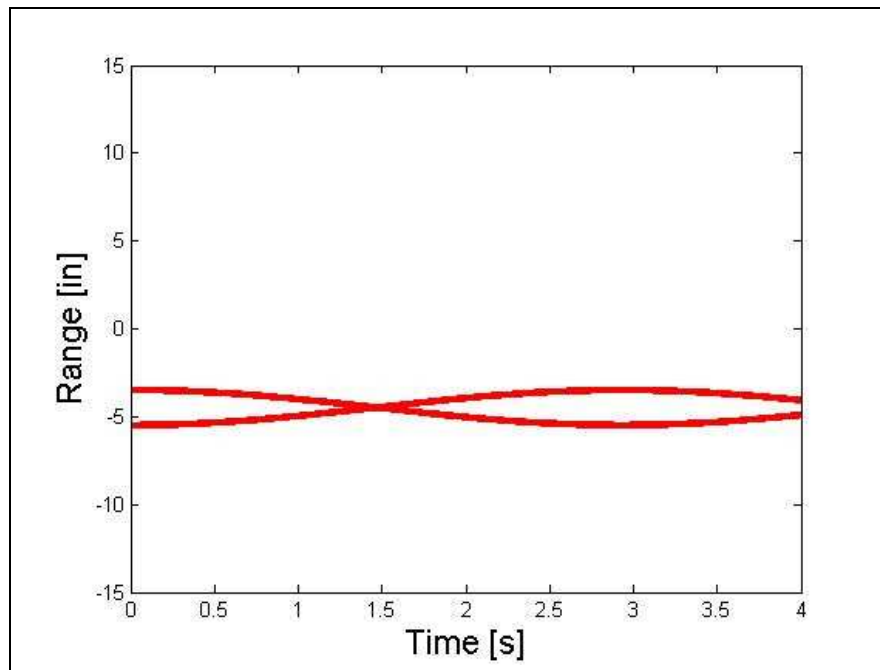Figure 4.30:   Hypothetical Target 9 ball bearing rotation.

Figure 4.31:   Hypothetical Target 10 ball bearing rotation.

made diagnosing the abilities of the Scene Match function difficult. The rotating ball

bearings were affected by the same creeping wave phenomena witnessed from Target
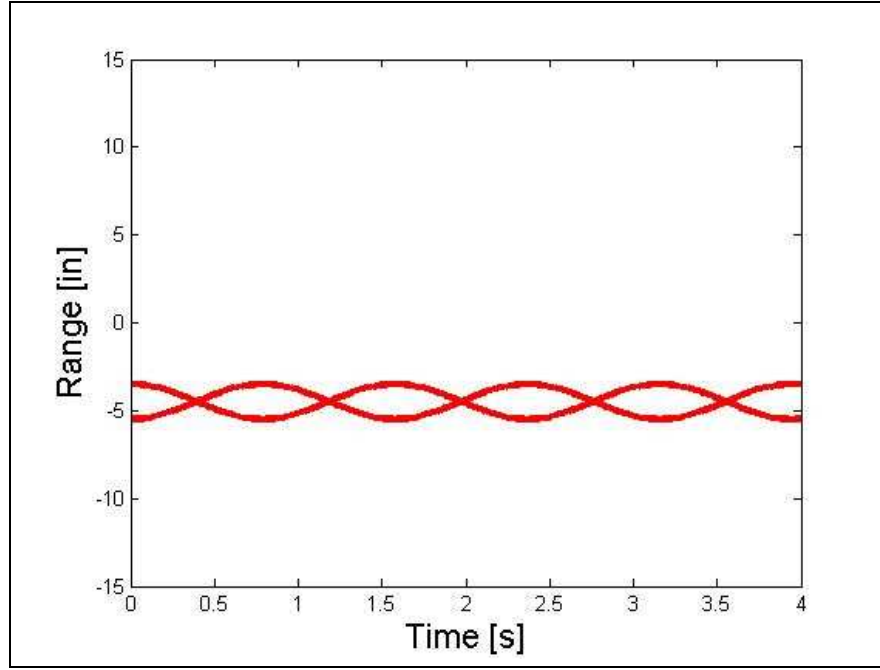
96

Figure 4.32:   Hypothetical Target 11 ball bearing rotation.

1. Given this, the target's position would appear to be smeared over a larger range than it actual encompassed.

The plot produced for Target 10 was slightly more revealing. In this plot, there appeared to be two scattering centers located at ranges of -1 and 1 in at time values of 0.5 to 2 and then converged to 0 in from 2 to 2.5 s. This convergence agrees with the hypothetical ball bearing positioned illustrated in Figure 4.31. Interestingly, the Scene Match for Target 10 produced non-physical scattering centers at -2.5 and 2.5 inches. These scattering features could be caused by multibounce effects. However, this seems unlikely considering they were not evident in Target 8's plot represented in Figure 4.26.

Finally, the Scene Match function did not offer any positional information on the ball bearings for Target 11. As seen in Figure 4.29, the plot produced a single steady response at 0.25 in. It was anticipated that the scattering would yield the convoluted weave pattern represented in Figure 4.32. However, the resulting Scene Match offered little information besides that of the stationary scatterers.

97

The Scene Match function did not offer significant insight into the scattering locations of the non-stationary scatterers. This was especially apparent during the high speed rotations from Target 11. It was possible that the Scene Match was revealing the position of the ball bearings in Target's 9 and 10, but the resolution was so poor it was hard to declare their locations with confidence. With this being said, the Scene Match function serves best at locating stationary scatterers.

4.2.3.4   The Short Time Fourier Transform.   The Standard STFT and Gaunaurd's STFT were used to analyze Target's 8, 9, 10, and 11. To be consistent, the TT polarization at $\theta = 0°$ was analyzed for each target with the addition of the PP polarization for Target 9. The PP polarization was added because it contained additional insight not seen in the TT case. The abilities of the two versions of the Short Time Fourier Transform varied greatly. It was apparent from the following plots that Gaunaurd's STFT was clearly superior in detecting stationary and non-stationary targets. The STFT results for Target 8 are located in Figure's 4.33 and 4.34; Target 9 in Figure's 4.35, 4.36, 4.37 and 4.38; Target 10 in Figure's 4.39 and 4.40; and Target 11 in Figure's 4.41 and 4.42.

The variation between the two versions of the STFT were clear even without a non-stationary component. The results from Target 8 clearly reveal that Gaunaurd's STFT offered a much higher degree of resolution than the standard form. An analysis of the standard STFT for Target 8 shows that it was able to resolve the two scatters located at −6 *and* 0 *in* reasonably well using 2 time divisions. However, at 5, 10 and 20 time divisions the TFR failed to locate even the stationary scatters with reasonable accuracy. Gaunaurd's STFT offered a higher degree of flare spot localization in every comparative time division plot. Although the resolution spread out as the time divisions increased, the resolution was still high enough to determine where the scattering body was located. The only limitation of Gaunaurd's STFT was it did not produce range information from early samples. This drawback was seen in previous comparisons.
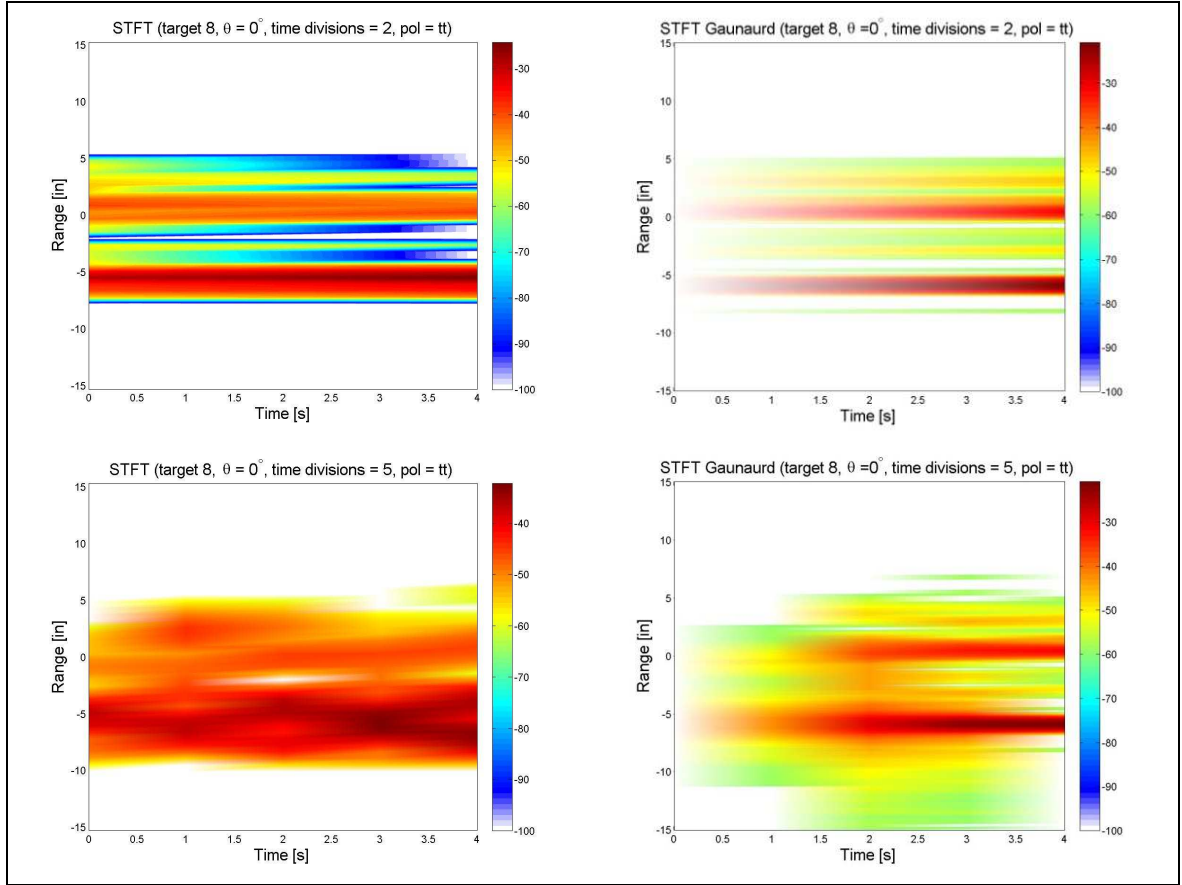
Figure 4.33:   Target 8: Pol =TT, $\theta = 0°$, TFR's b.

The standard and Gaunaurd versions of the STFT for Target 9 located in Figure's 4.35, and 4.36 produced similar results to that of Target 8. Both versions produced strong scattering centers around 0 and -6 in. However, the standard STFT produced two distinct scatters around 0 *and* 2 *in* using 2 time divisions. Given the slow rotational speed of the target, these two scatterers could possibly be the ball bearings. As more time divisions were used in the STFT, the resolution waned drastically and neither stationary or non-stationary scatters were resolvable. Gaunaurd's STFT did not show the two distinct scatterers in any of the plots produced for Target 9. However, Gaunaurd's plots, in both the 10 and 20 time division cases, produced a wavelike pattern similar to the expected specular trace from Figure 4.30. Given that the rotational speed was too slow to resolve multiple path crossings, it was unclear if
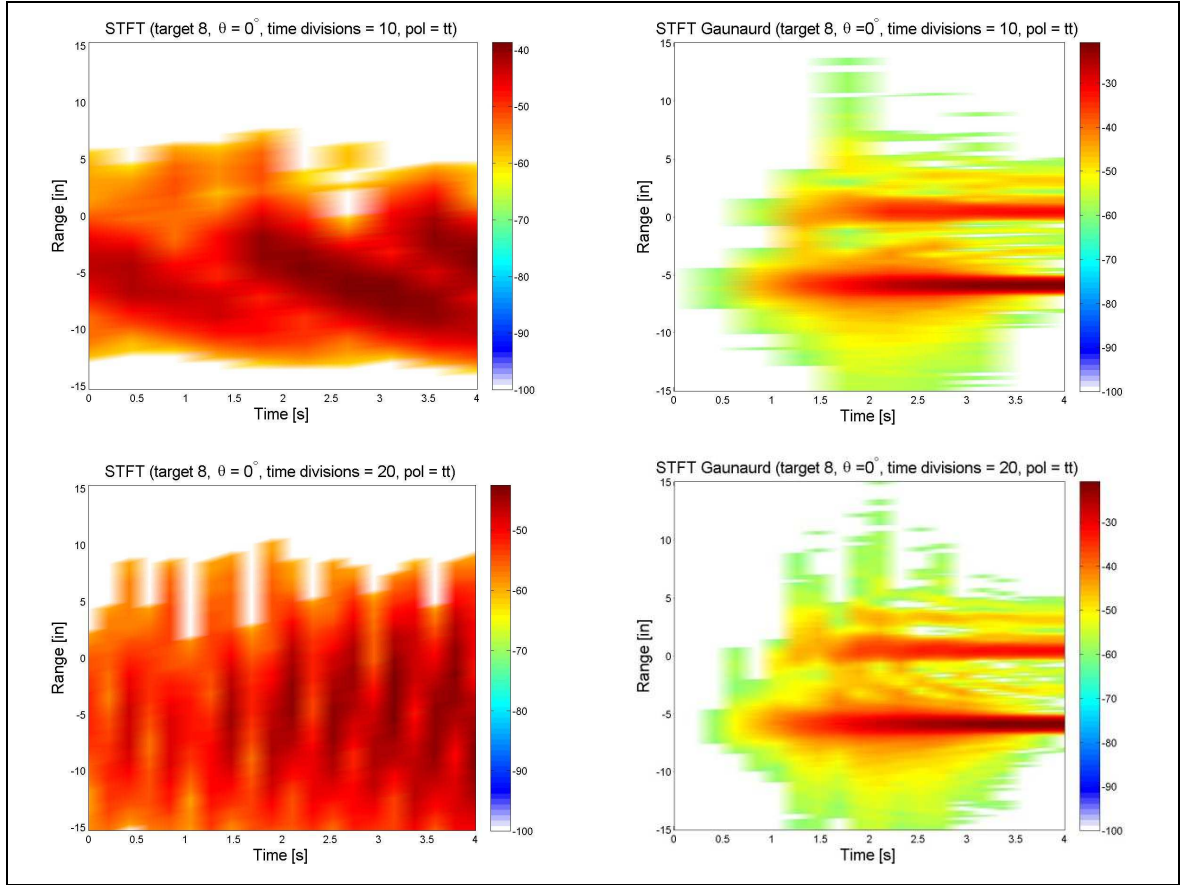
Figure 4.34:   Target 8: Pol =TT, $\theta = 0°$, TFR's c.

the wave pattern produced was from the rotation of the ball bearings or just general processing anomalies.

The STFT results for Target 9 PP polarization were included to give additional insight into the strength of Gaunaurd's STFT over the standard STFT. According to Figure's 4.37 and 4.38, Gaunaurd's STFT plots produced two distinct scatterers in the vicinity of the two ball bearings. These two scatters are placed around -1 *and* 1 *in* and are clearly visible in each of the time division plots used. The 10 time division plot was perhaps the most interesting. In this plot, one can clearly see the slight wave pattern produced by the rotation of the ball bearings. The high degree of resolution in these plots gives us great confidence in Gaunaurd's STFT.
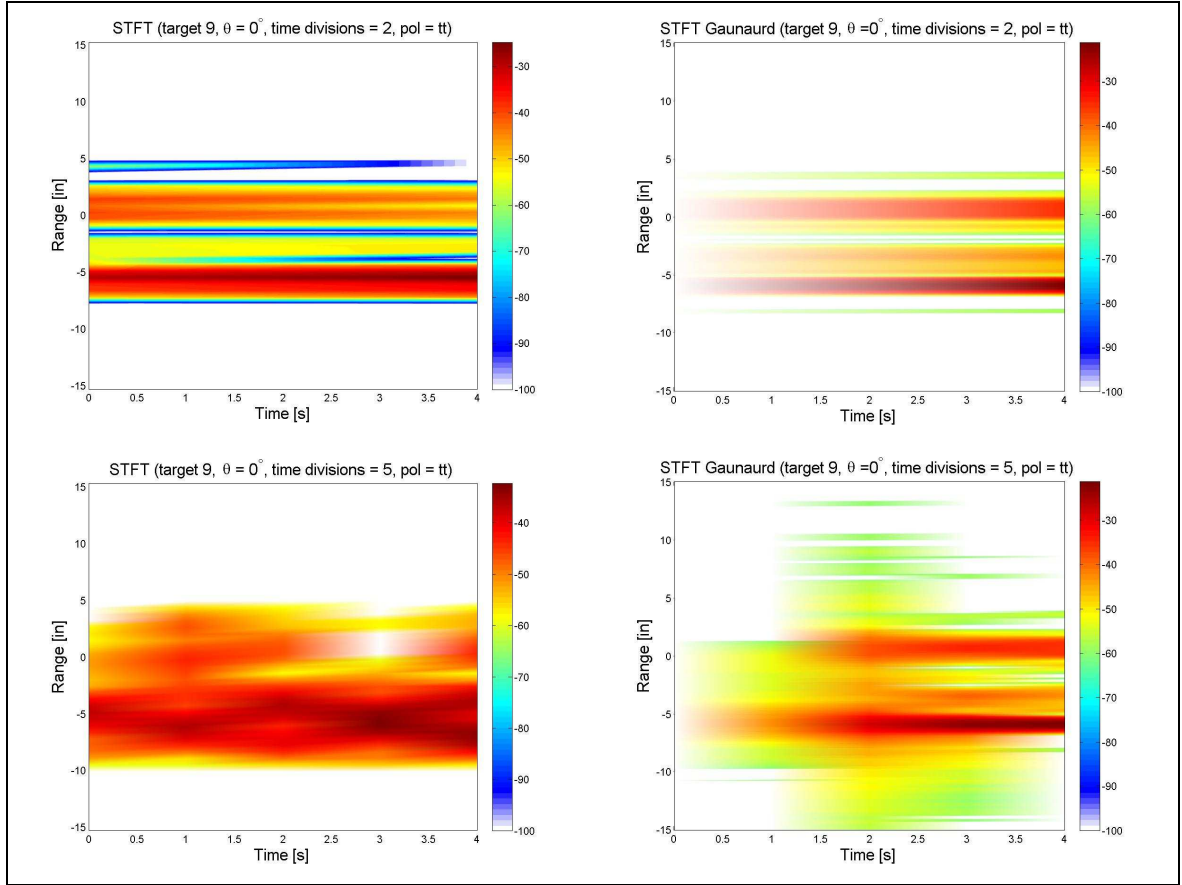
Figure 4.35:   Target 9: Pol =TT, $\theta = 0°$, TFR's b.

The standard STFT offered little knowledge of the non-stationary scatters for Target 10. Even the stationary scatterers were unresolvable beyond 2 time divisions. The increase in the ball bearings rotational speed greatly affected the accuracy of the standard STFT. The plots produced by Gaunaurd's STFT offered high resolution for both stationary and non-stationary scatterers. As the time divisions increased, one was clearly able to resolve the weave-like pattern the ball bearings created. The 10 division plot, located in Figure 4.40, was the most revealing of Gaunaurd's plots. In this plot, one can clearly distinguish the crossing pattern exhibited by the ball bearings. This pattern closely matched the hypothetical specular trace from Figure 4.31, giving us great confidence in the ability of Gaunaurd's STFT to resolve non-stationary components.
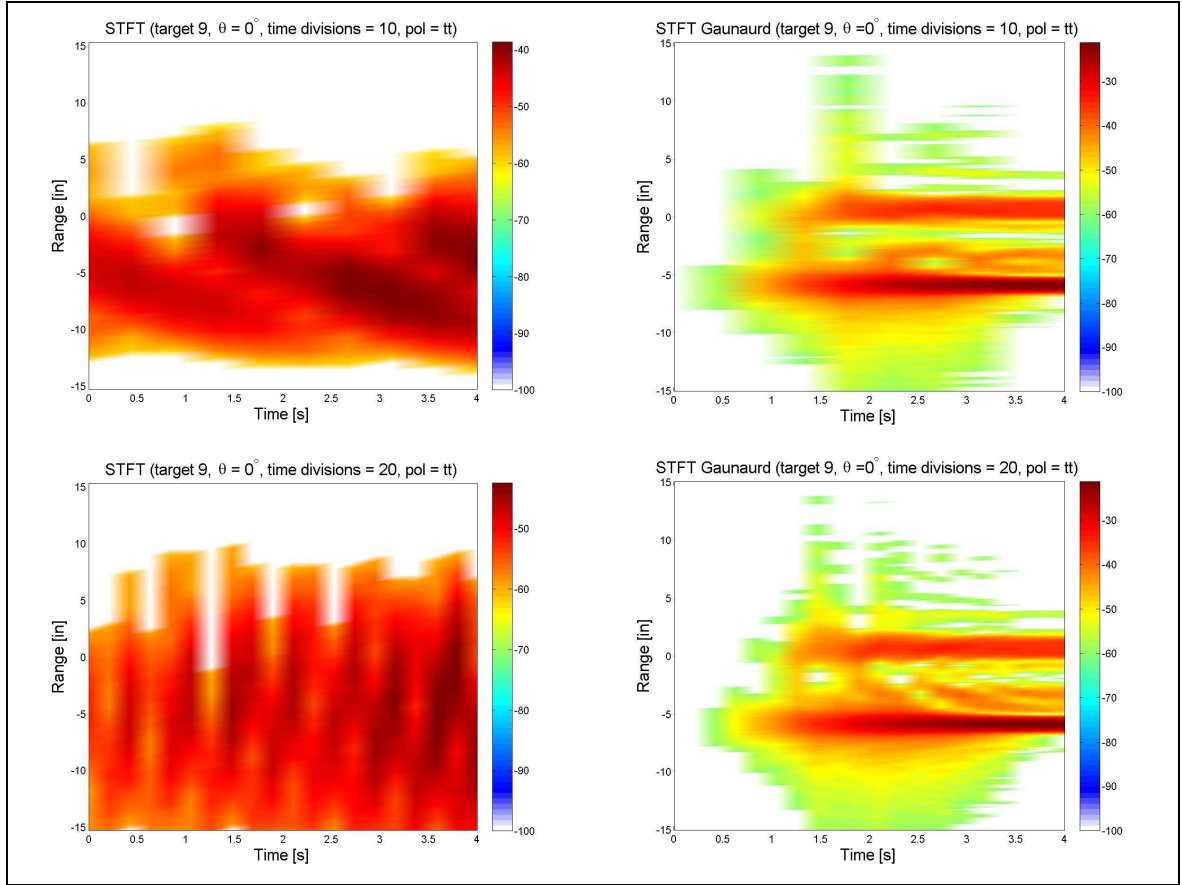
101

Figure 4.36:   Target 9: Pol =TT, $\theta = 0°$, TFR's c.

Both the standard STFT and Gaunaurd's STFT struggled to represent the conditions of Target 11 accurately. The standard STFT was only able to accurately represent the stationary scatterers in the 2 time division plot. It was unable to locate the non-stationary scatters under any time divisions used. The speed of the rotating ball bearings greatly limited the abilities of the standard STFT.

Gaunaurd's STFT offered much more insight into Target 11 than the standard STFT did. Gaunaurd's STFT was able to locate the stationary scatterers for each time division relatively accurately. For the non-stationary scatterers, it produced a wave-like pattern for time divisions 10 and 20 that vaguely resembled the expected pattern illustrated in Figure 4.32. The quick rotational rate of the ball bearings limited Gaunaurd's STFT in placing the ball bearings accurately in range for each time sample. Although the resolution was limited, Gaunaurd's STFT offered significant
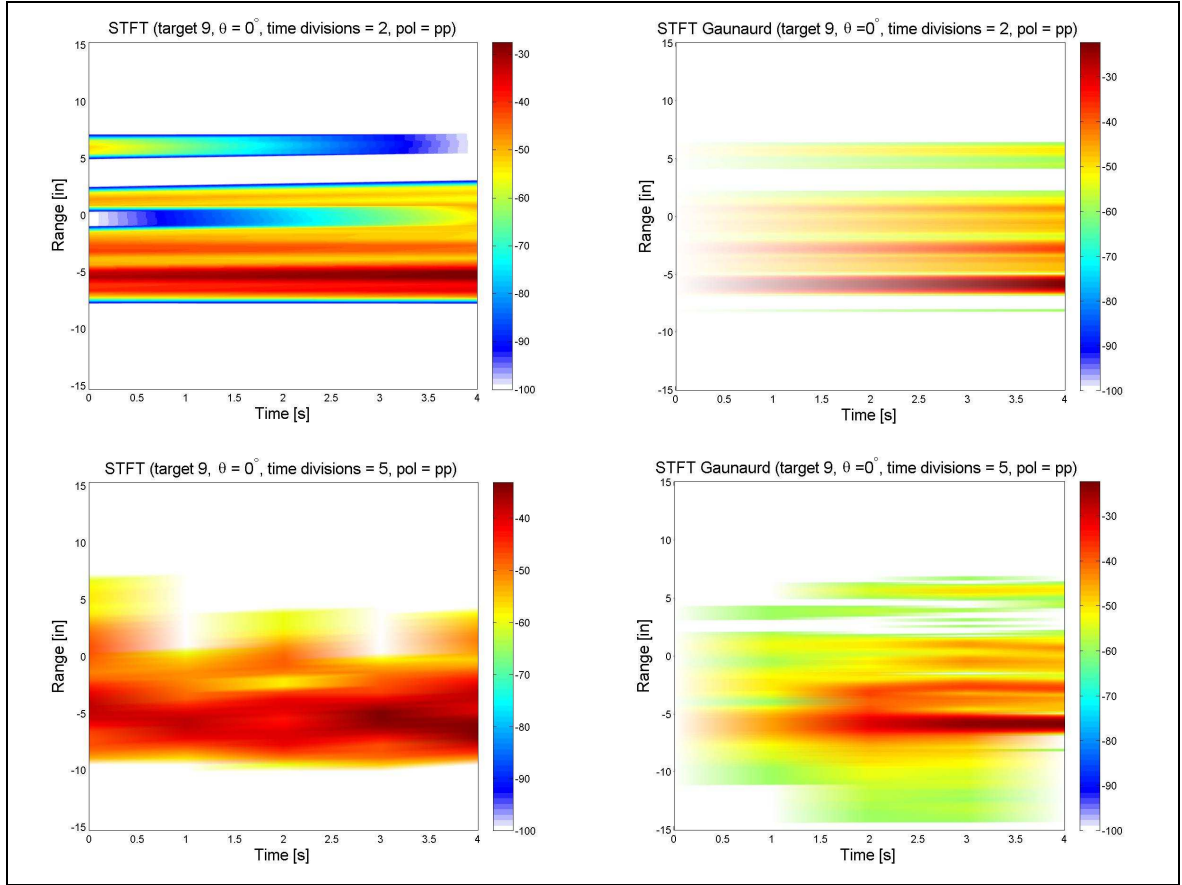
Figure 4.37:   Target 9: Pol =PP, $\theta = 0°$, TFR's b.

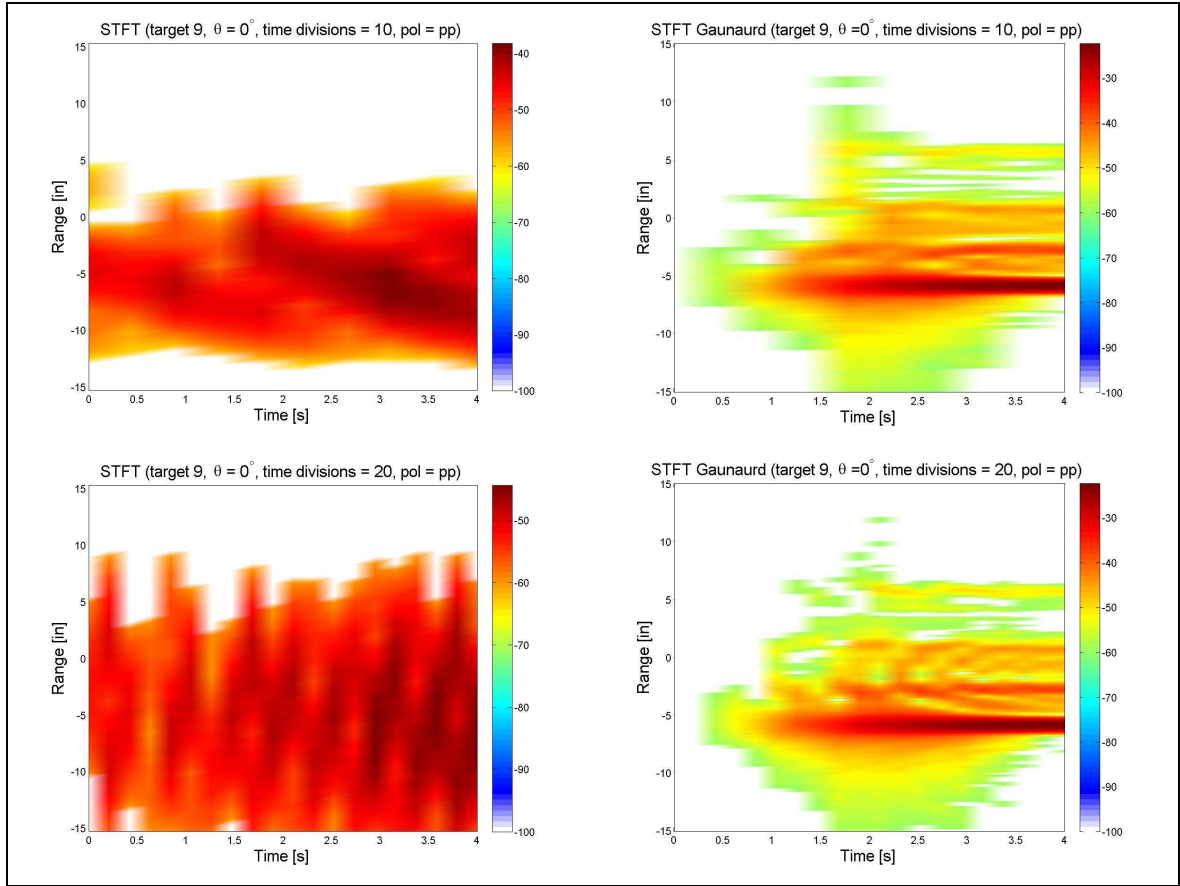advantages over the standard form. It located both the non-stationary and stationary scatters much more accurately.
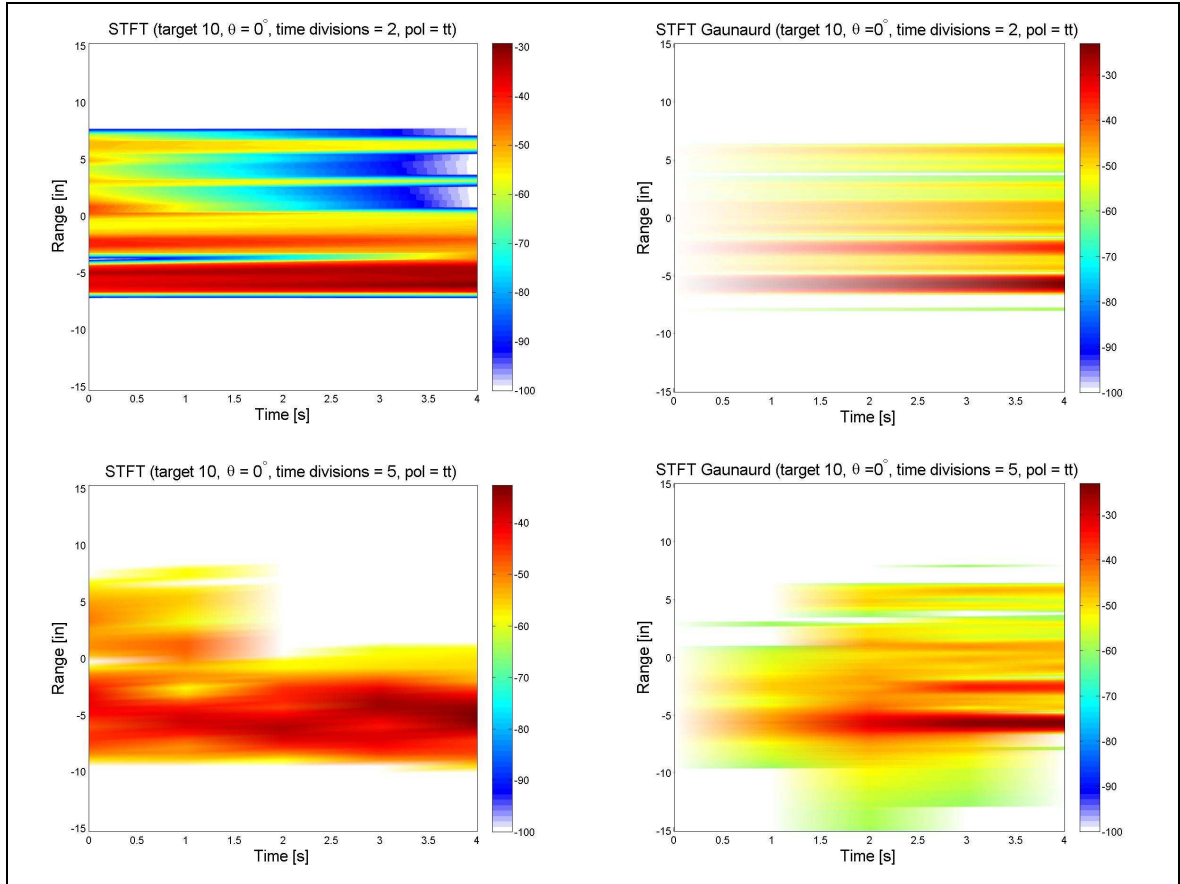
Figure 4.38:   Target 9: Pol =PP, $\theta = 0°$, TFR's c.

Figure 4.39:   Target 10: Pol =TT, $\theta = 0°$, TFR's b.
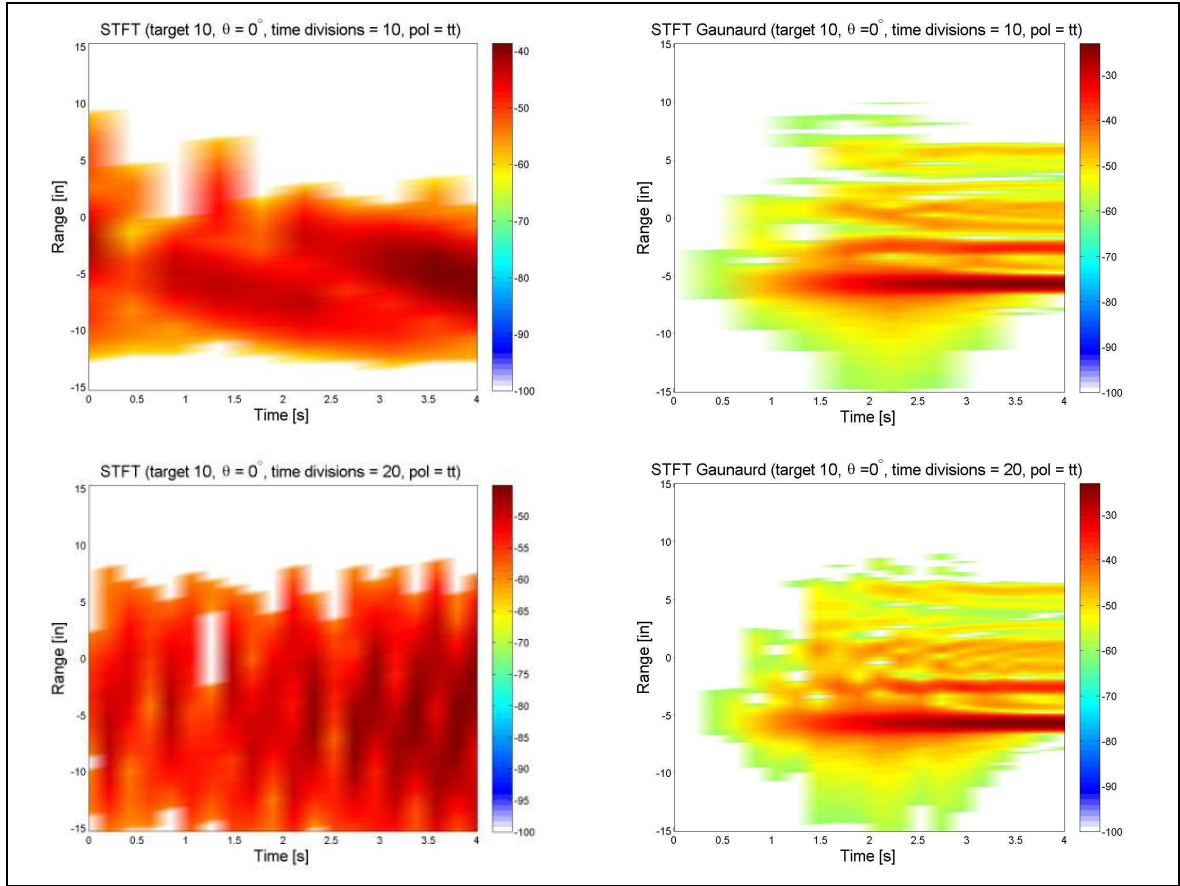
Figure 4.40:   Target 10: Pol =TT, $\theta = 0°$, TFR's c.
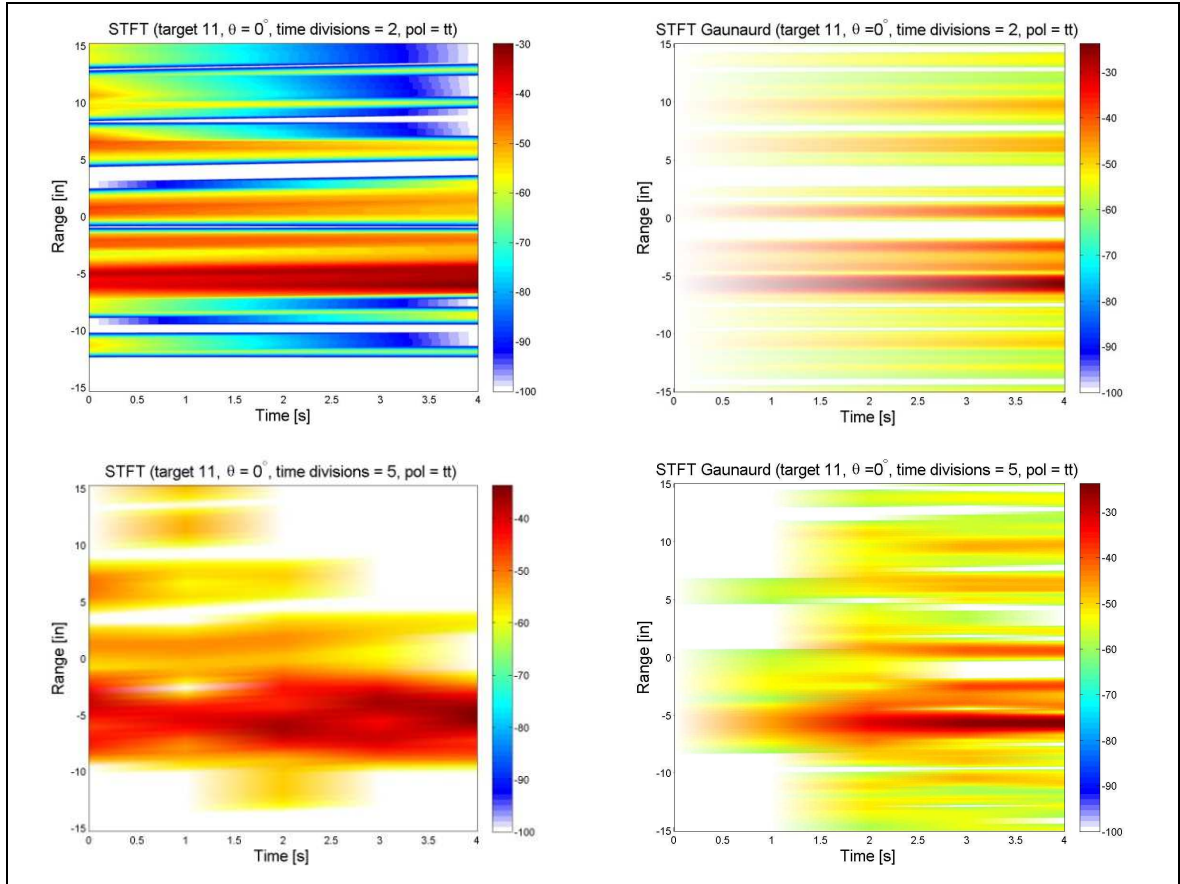
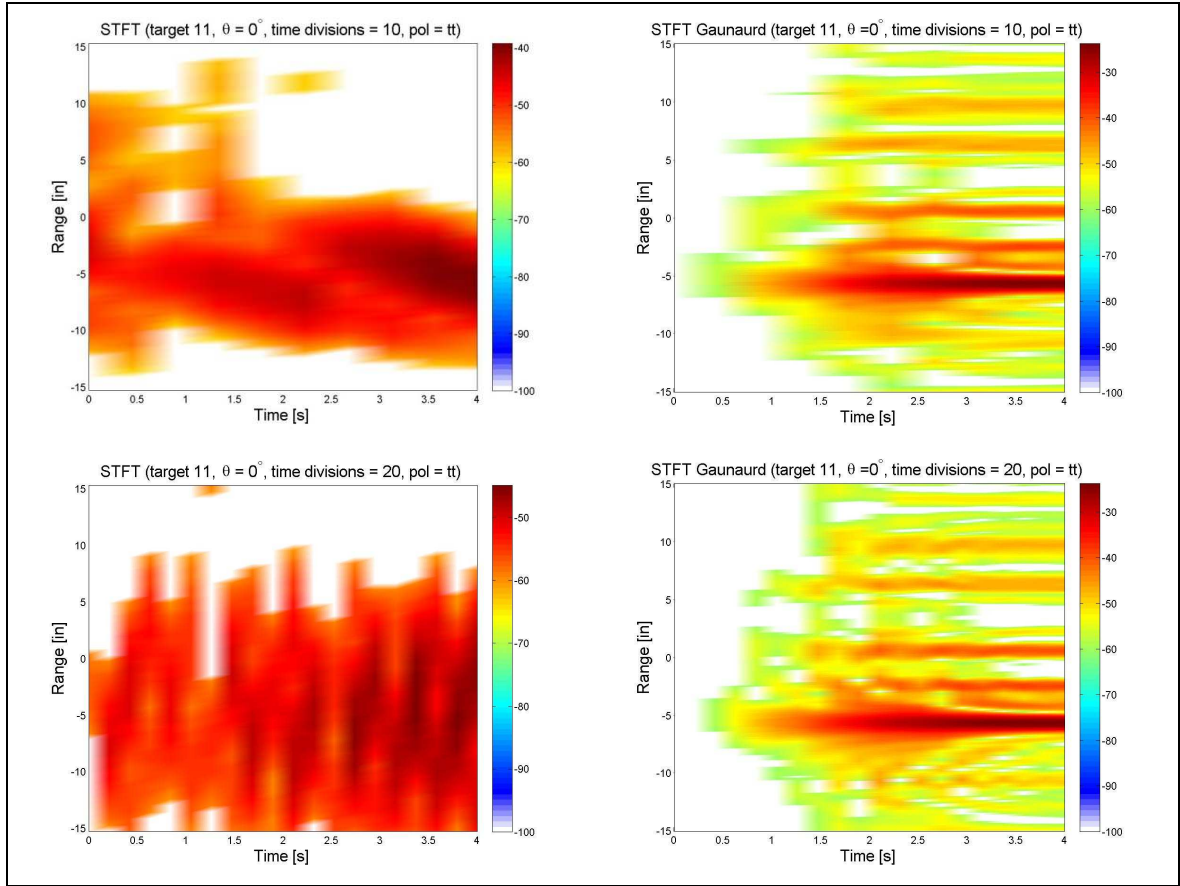Figure 4.41:   Target 11: Pol =TT, $\theta = 0°$, TFR's b.

Figure 4.42:   Target 11: Pol =TT, $\theta = 0°$, TFR's c.

V. Conclusions

5.1 Non-Stationary Scattering Localization Through Time Frequency Representations

The results from Section IV offer the LO community additional insight into the usage of Time Frequency Representations for the purpose of analyzing non-stationary signals. Although the results did not resoundingly favor a particular TFR over the others, it was clear that certain TFRs were better suited for non-stationary and stationary RCS flare spot localization. Of the four TFRs analyzed, Gaunaurd's STFT and the Scene Match function offered the greatest insight into the scattering locations of the non-stationary targets. The standard STFT and Wigner distribution provided little insight into the scattering locations of either stationary or non-stationary targets. A multiple TFR approach is recommended to accurately place non-stationary and stationary scatters.

Based on the testing results, the Gaunaurd STFT, the Scene Match function and the Range vs. Azimuth function should be used in concert to determine the scattering locations of non-stationary targets. Similar to the approach used for target analysis in Section IV, an understanding of the backscatter phenomena created by the weapon system in test must be accomplished. Only after a thorough understanding of the target's scattering features are understood, can one apply TFR analysis. This means the tester should understand how the phases of the return pulses were formed. For instance, the delay phase response from Target 1's single sphere was understood to be from the creeping wave effect. The delay in time induced a phase shift onto the backscatter which placed the backscatter return off center from the sphere's physical location. Target 1's misplacement in range, through the effects of the creeping wave, were simple to understand. However, if the target becomes increasingly complicated, one might misinterpret this delay to be from an additional scattering feature. Therefore, it is important for the tester to have a thorough understanding of the contributors that created the backscatter's phase. Only after this has been accomplished can one apply the TFRs to isolate the non-stationary component's effects on the overall RCS.

The standard STFT was able to locate the stationary scatters moderately well using only low time division processing. High time division processing resulted in unsatisfactory resolution, which made non-stationary flare localization impossible. The Wigner distribution worked well for only the simplest of scatterers. Multi-component scatters created unwanted cross-terms that polluted the time-range plot so terribly that resolving even stationary components was challenging. The task of pinpointing the non-stationary scatters as a function of time was impossible for even the simple geometry targets.

The limits of the TFRs should also be understood before they are implemented. From Section IV, it was understood that TFRs work best under minimal non-stationary conditions -meaning slow rotational speeds. In Section 4.2.3, neither the Scene Match nor Gaunaurd's STFT could place the non-stationary scatterers accurately for Target 11. The rotational speed was too great to create meaningful information on the location of the non-stationary components. However, both TFRs were able to place the non-stationary components reasonably well in Target's 9 and 10. The low rotational speeds in these targets allowed both functions to work moderately well in placing non-stationary components. It is recommended that the LO tester should strive to use the lowest non-stationary condition possible without compromising other requirements.

Lastly, one must fully understand how the TFR created the plot used for diagnosis. This means understanding the mathematical operations used to place the scatterers in range. This task is crucial for interpreting the TFR plots correctly. For instance, Gaunaurd's STFT was built on the concept of using increasingly larger segments of information when transforming the frequency domain into the time domain via the Fourier transform. This technique gives us unmatched resolution towards the end of the frequency sweep, but it also subtly includes information that occurred at the beginning of the frequency sweep that is non-physical to the time value it is representing. This ailment can be overcome by tracing the pattern of the non-stationary component through time and disregarding its past RCS shadow. Compensating analysis like this can only be done through a trained eye with a comprehensive under-

standing of the TFR used. Therefore, in order to maximize the information provided by the TFR, a thorough understanding of its creation is needed.

5.2 Limitations and Difficulties

Although recommendations were provided, the testing used to form those recommendations had limits. As discussed in Section IV, the radar system used was limited in bandwidth and was also plagued with an untimely amplifier switch during the frequency sweep. The amplifier switching created a brief discontinuity in the frequency sweep which caused a discrete change in the non-stationary return signal. Although this was accounted for, the discrete range change, inherent to the break in time from the amplifier switching, made diagnosis more difficult than it should have been. Another interesting ailment was caused by the cone used to house the motor. The cone contributed a much higher RCS than desired. The high RCS created by the cone made it difficult to isolate the ball bearings that rested within its extent. The shape of the cone also contributed unwanted multibounce and creeping wave effects that saturated large portions of the backscatter. From this, the isolation of the ball bearings, as a function of time, was made more difficult than it should have been.

It is important to note that the Wigner distribution might have been misrepresented given the type of signal processed. More specifically, the radar system used for this thesis returned data that was a function of frequency. Time information was created based on the time the radiated pulse left the horn antenna. The analysis of the Wigner distribution, based on this type of data, was probably incorrect or at least unfair. As stated by Equation 2.33, the Wigner distribution uses time data for its inputs and produces both time and frequency data for its outputs. In this thesis, the implementation of the WD used frequency data to produce frequency and time data. The usage of frequency based data as opposed to time based data is of concern. Interestingly, based on the literature, the plots produced by the WD for stationary scatterers were similar to the expected results. However, the WD failed to resolve non-stationary scatters for any of the targets. From the background research, the im-

111

plementation of chirp or impulse type radars have been used to successfully produce the Wigner distribution. It is possible that the usage of these types of radars could validate the WD as a viable TFR and the implementation I used was incorrect.

5.3 Future Research

Future research on the application of TFRs on non-stationary targets should focus on the usage of other types of radar systems to accurately identify scatters in time. It is my belief that radar systems that use pulse compression techniques, or that generate coded pulse sequences could possibly increase the accuracy for certain TFRs. For instance, the Cohen class of TFRs are best implemented when the signal is a function of time, not frequency. If an impulse radar or a chirp radar were used, the return signal would cover a large bandwidth and be a function of time. I believe the implementation of these types of systems could aid in the localization of flare spots from non-stationary signals. I also believe that the implementation of multiple systems and TFRs is the best way to analyze non-stationary signals.

5.4 Summary

The focus of this research has been on the implementation of Time Frequency Representations to detect RCS flare spots from non-stationary targets as a function of time and range. The analysis of four TFRs was accomplished on non-stationary data collected from AFIT's anechoic chamber. Through analysis, it is recommended that the tester uses multiple TFRs to best analyze the non-stationary effects induced by the target's movement. As it pertains to the scope of this thesis, the Azimuth vs. Range function, the Scene Match function and Gaunaurd's STFT served best to isolate the non-stationary scatters. Hopefully the results from this thesis inspire others to continue TFR research as it applies to analyzing non-stationary signals. The applications of this science not only serve the Department of Defense, but can also be used to help other sciences accurately identify non-stationary components in their signals.

VI.   Appendix A: AFIT Anechoic Chamber Setup

This Appendix contains the test setup and target photos. These photos give additional insight into the target's design and the AFIT anechoic chamber.
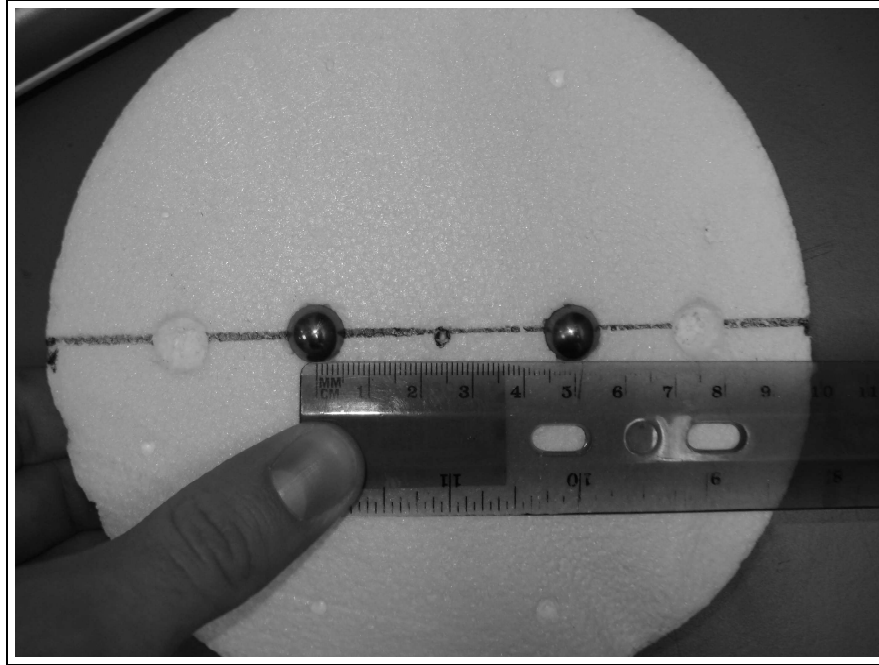

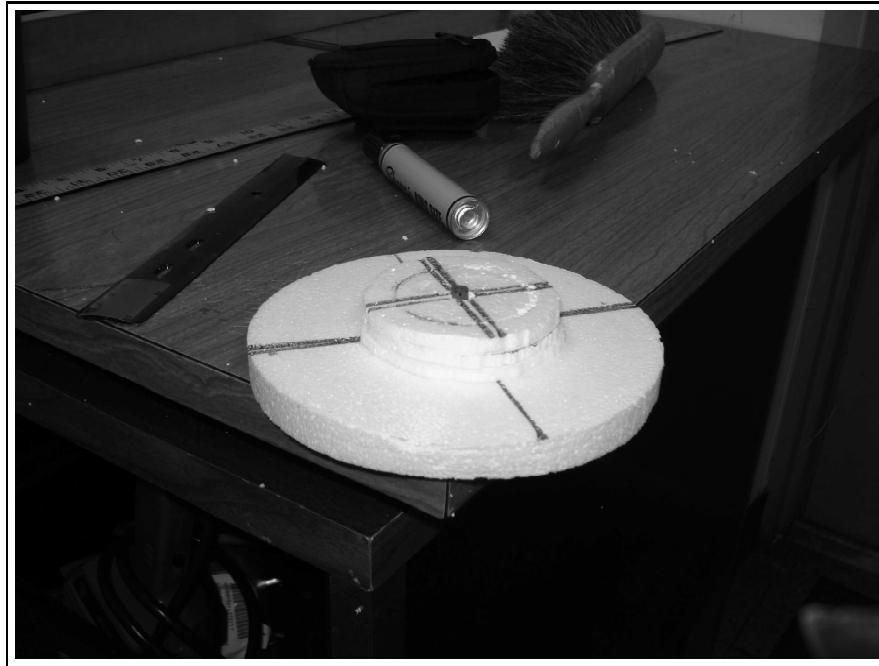Figure F.1:   Ball bearing separation.
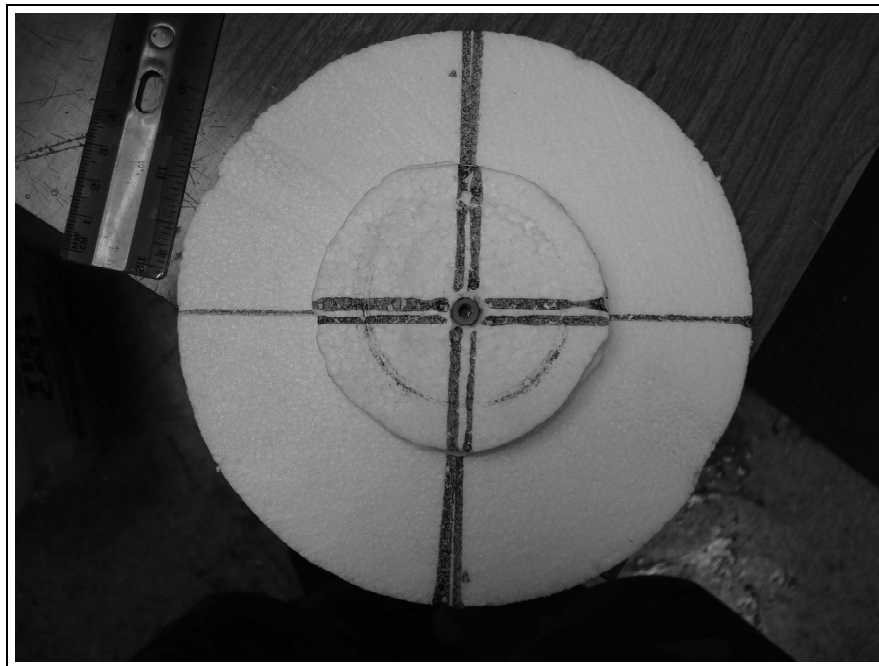
Figure F.2:   Rotating structure 1

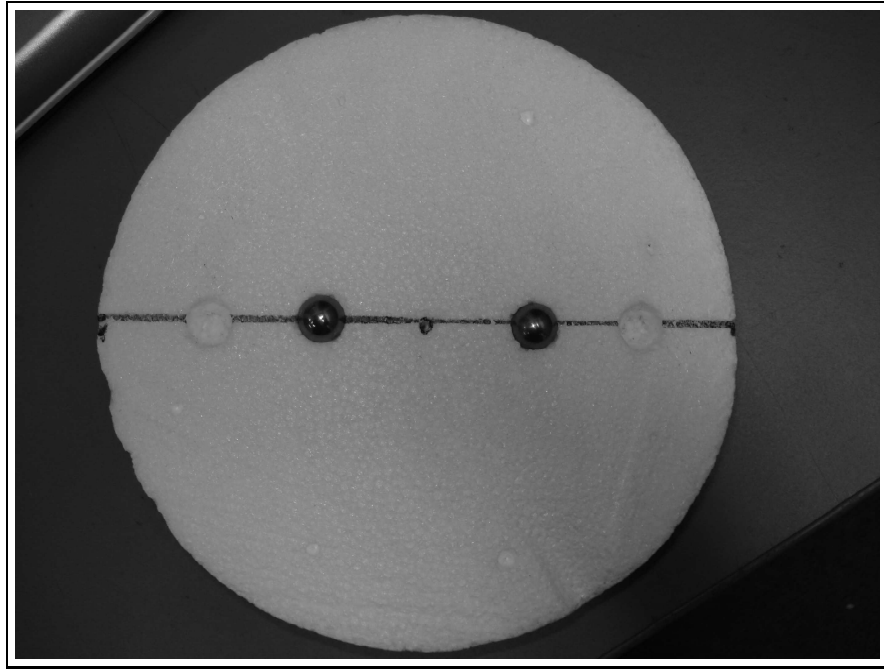Figure F.3:   Rotating structure 2

Figure F.4:   Rotating structure with ball bearings.

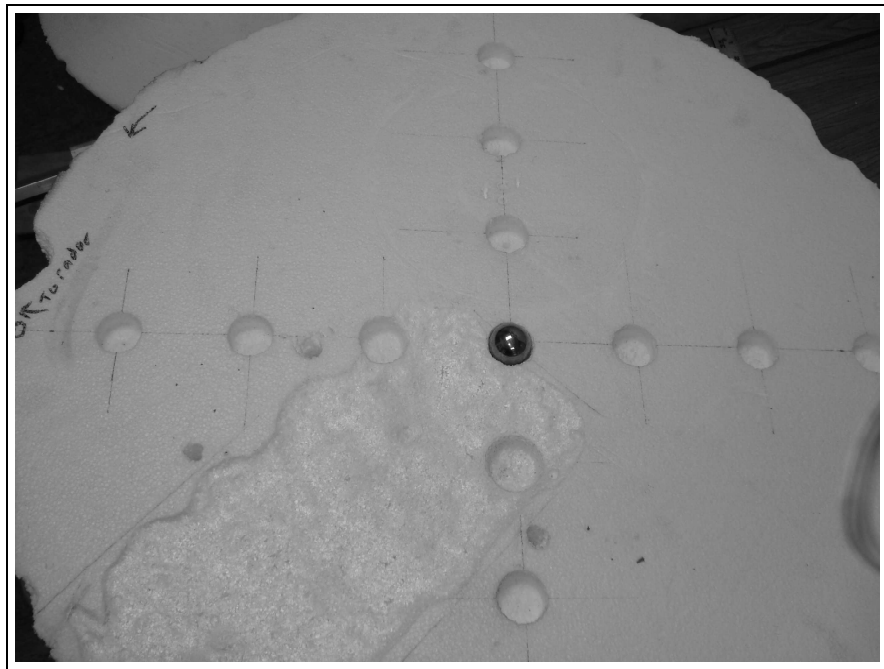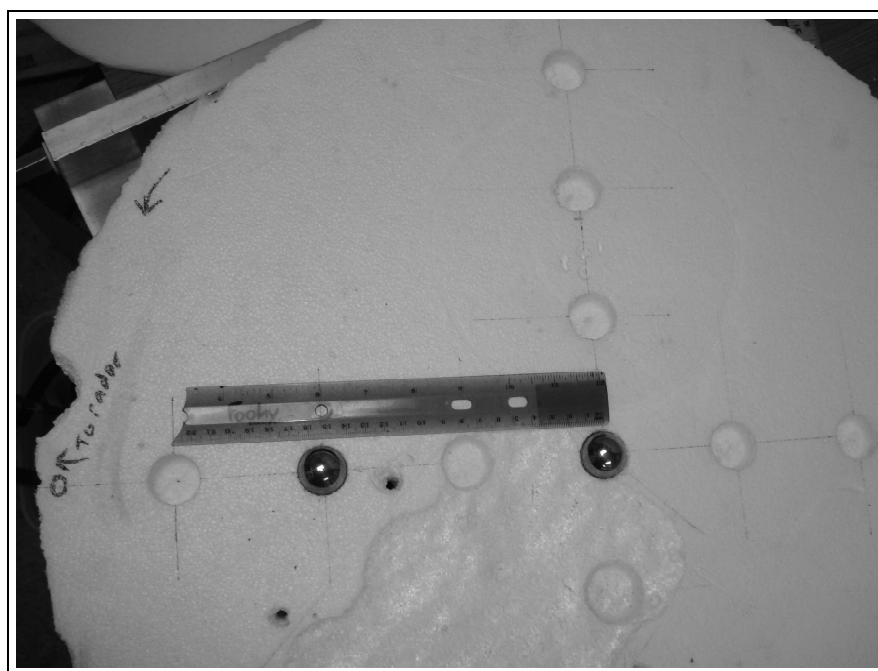Figure F.5:   Target 1 range photo.

Figure F.6:   Target 2 range photo 1.

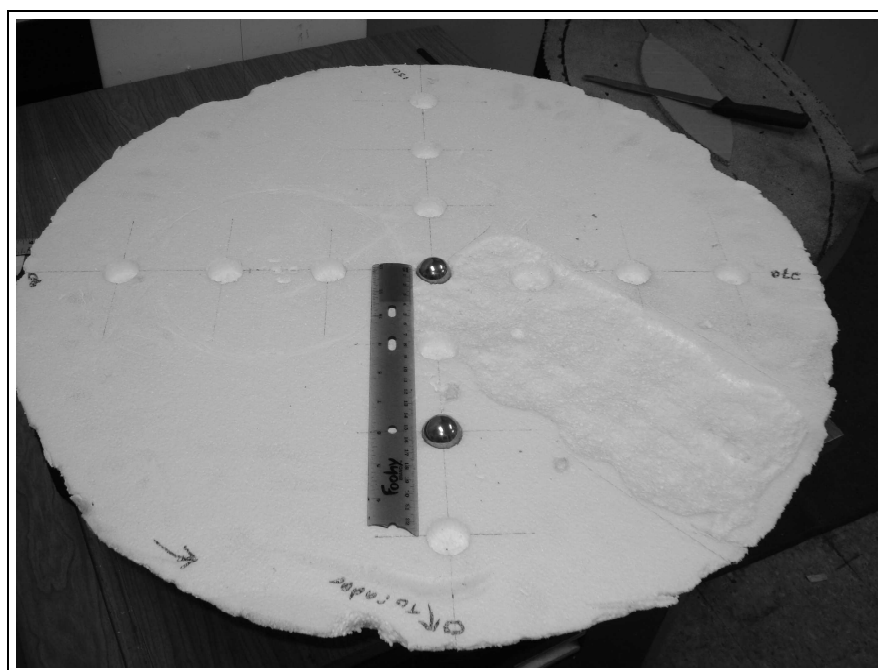Figure F.7:   Target 2 range photo 2.
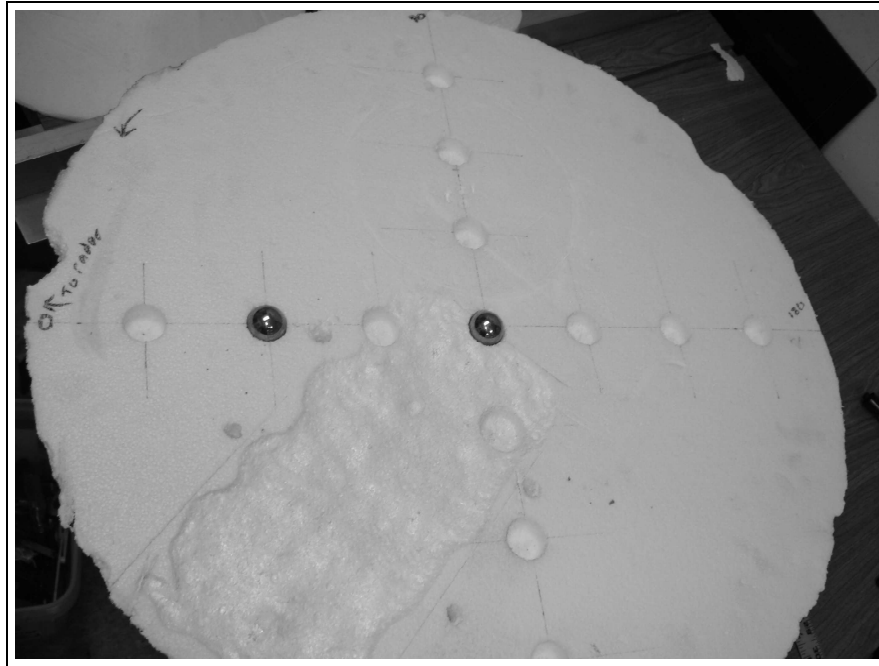
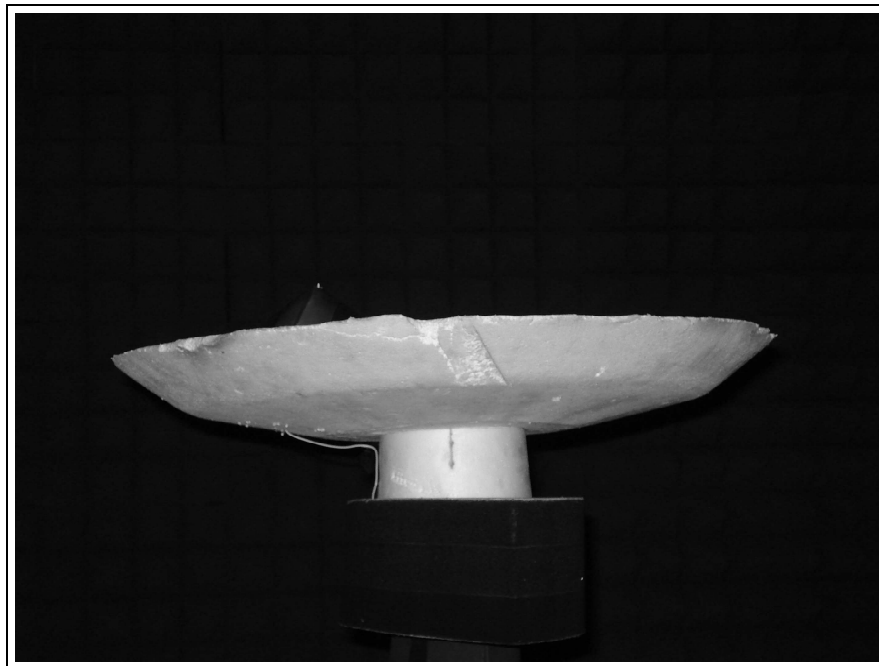Figure F.8:   Target 2 range photo 3.

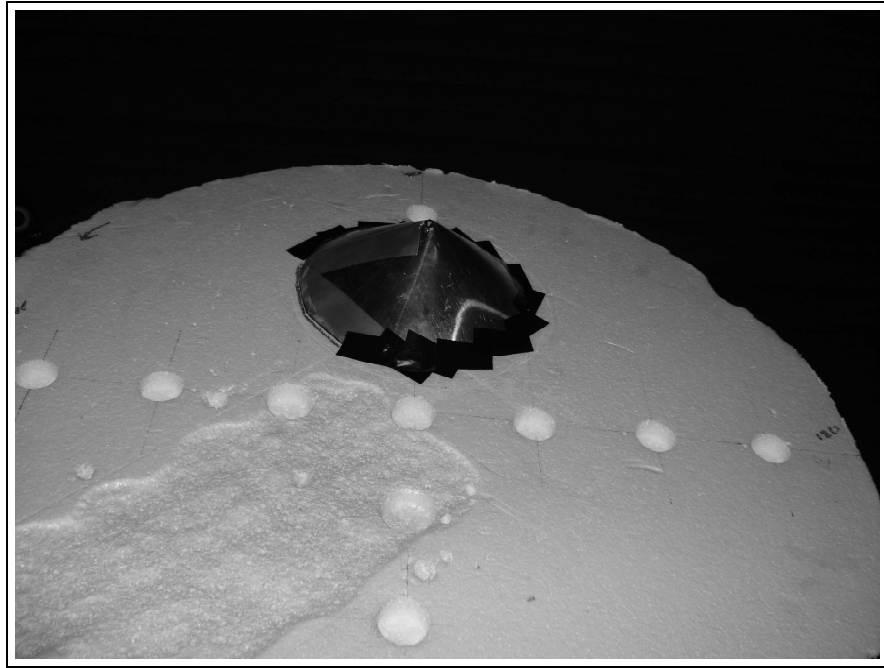Figure F.9:   Target 3 range photo 1.

Figure F.10:   Target 3 range photo 2.

Figure F.11:   Target pedestal.

Figure F.12:   Target pedestal wiring
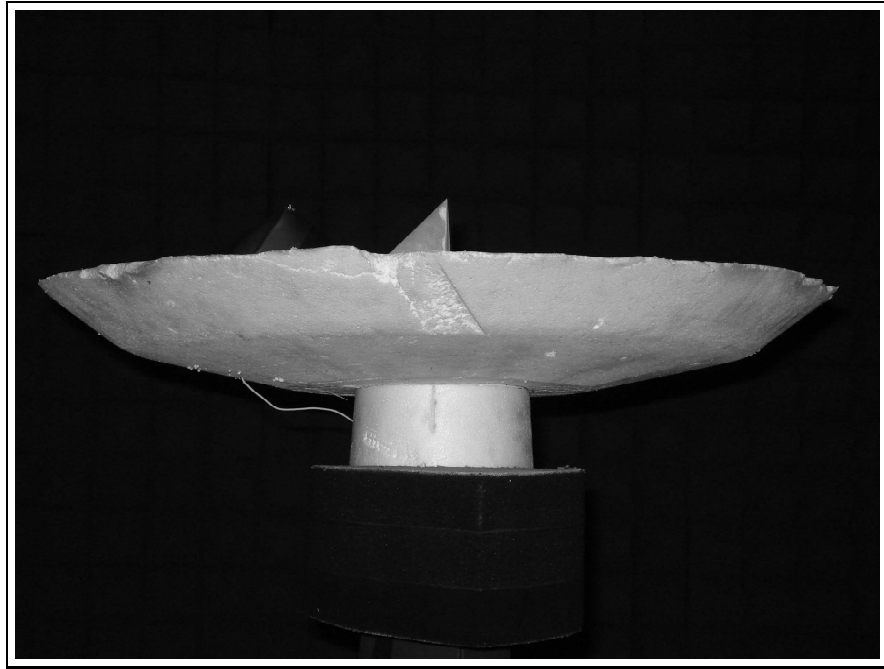
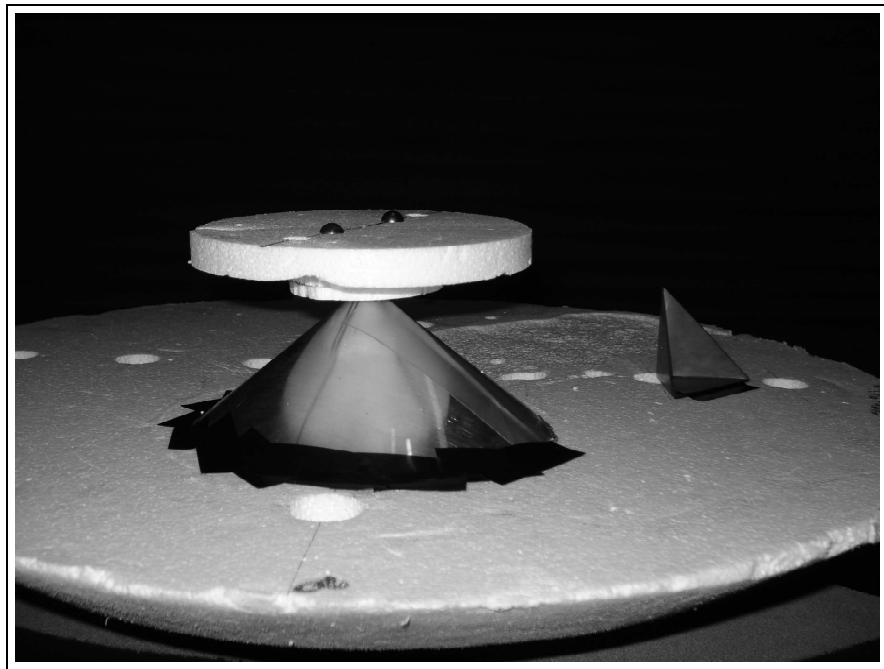Figure F.13:   Target with trihedral photo 1.
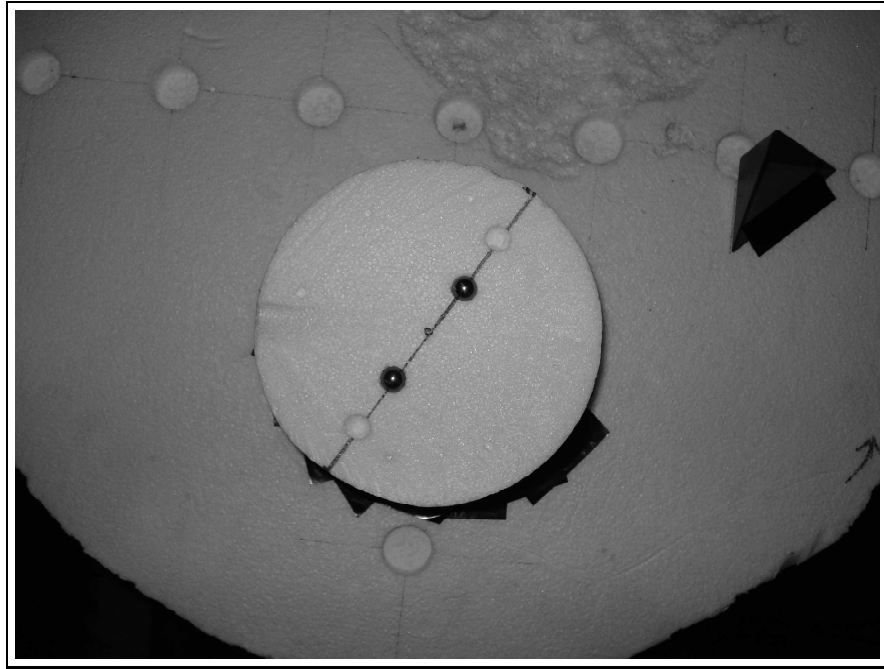

Figure F.14:   Target with trihedral photo 2.

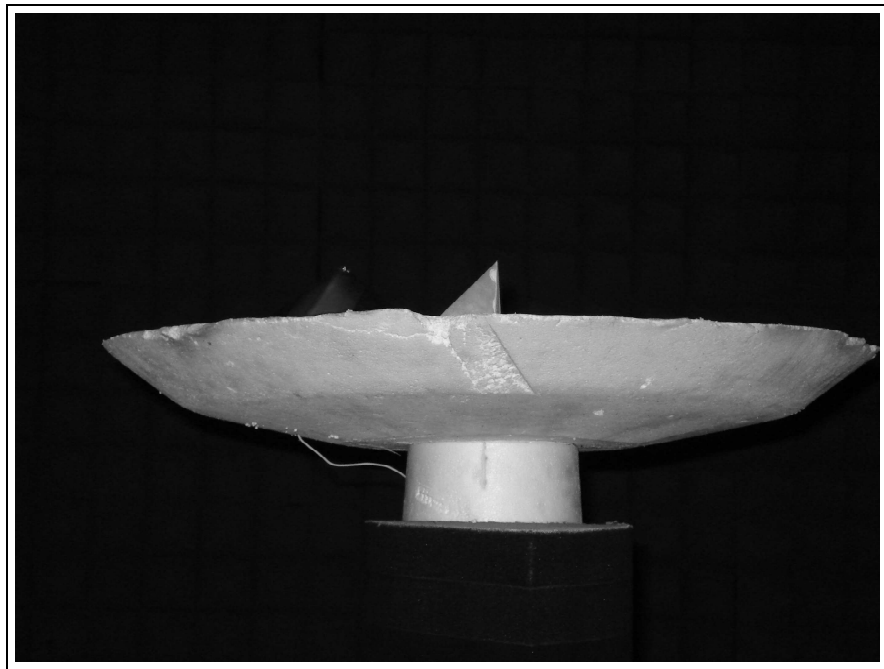Figure F.15:   Target with trihedral photo 3.

Figure F.16:   Target with trihedral photo 4.

122

VII. Appendix B: Matlab Code

This Appendix contains the `Matlab`® source code used to analyze the non-stationary RCS data. The `Matlab`® .m files include the AFIT Range Data Process, the Azimuth vs. Range function, the Calculate Range function and the Time Frequency Representations. The DFT function and the Scene Match subract function are also provided for additional insight.

7.1 AFIT Range Data Process

Listing VII.1:   Range Data Process(Appendix2/rangeDataProcess.m)

```matlab
% % Capt. John McShane

% Range Data Process
% Modification of Dr. Peter Collins Code
% % 20 Dec 2008

%% Reads Measured Data
% Adds location of AFIT routines to the MATLAB path, so they don't...
    have to
% be specificied everytime
cd('C:\Documents and Settings\jmcshane\My Documents\MATLAB\...
    Thesis_range_tests\jan_work')
path(path,...
    'C:\Documents and Settings\jmcshane\My Documents\MATLAB\...
        Thesis_range_tests\not_used_mfiles\old_thesis_work\...
        Final_project_data\AFIT_process');

path(path,...
    'C:\Documents and Settings\jmcshane\My Documents\MATLAB\...
        Thesis_range_tests\not_used_mfiles\old_thesis_work\...
        Final_project_data\AFIT_process\resource');

% Creates a path-like variable to the data files
path_to_measured_data = ...
    'C:\Documents and Settings\jmcshane\My Documents\MATLAB\...
        Thesis_range_tests\Thesis Range Data\8 Dec 08\';
%%
% Read each one with AFIT Function and provide feedback
cal_background = readLintek([path_to_measured_data '...
    cal_background_s.cbk']);
disp('Done with cal background')

cylinder_cal_375_measured = readLintek([path_to_measured_data '...
    cal_375.cal']);
disp('Done with 3.75 inch cal')

cylinder_cal_450_measured = readLintek([path_to_measured_data '...
    cal_450.cal']);
```

123

```matlab
    disp('Done with 4.50 inch cal')

31  target_1_background = readLintek([path_to_measured_data '...
        background.bkg']);
    disp('Done with cal target 1 background')

    target_1_measured = readLintek([path_to_measured_data 'target_2....
        tar']);
    disp('Done with Target 2 (two sphere)')
36
    save two_sphere.mat

    %%
    load two_sphere.mat % This is own personal mat file to make coding...
        easier.
41  %% may need to start from here.

    %% Adjusts for misalignment in the azimuth direction for the ...
        plates
    % This needs to be eyeballed, and you have to know what pattern to...
        expect
    % from the target under test
46  %
    % This could be critical because the exact target is assumed to be...
        lined
    % up, but not in this case b/c it is a cylinder
    %
    % Remember to re-run the block above because, the effect of the ...
        adjustments
51  % will be culmulative if you don't!!!!!

    %--------- Not really needed for this geometry ------%

    target_1_shift = 0;      % Negative is left
56
    target_1_background_shift = 0;

     target_1_measured.pp = circshift(target_1_measured.pp,[0 ...
        target_1_shift]);
     target_1_measured.tt = circshift(target_1_measured.tt,[0 ...
        target_1_shift]);
61
    %
     target_1_background.pp = circshift(target_1_background.pp,[0 ...
        target_1_background_shift]);
     target_1_background.tt = circshift(target_1_background.tt,[0 ...
        target_1_background_shift]);

66
    %% Reads Exact Data
    % Sets the path to the exact data to aviod typing it over and over...
        and
```

```matlab
    % over, etc...
    path_to_exact_data =...
71      'C:\Documents and Settings\jmcshane\My Documents\MATLAB\...
            Thesis_range_tests\not_used_mfiles\old_thesis_work\...
            Final_project_data\AFIT_process\Exact data\';
    % Gets the 3.75 inch cylinder exact data, note: both polarizations...
        come out
    % in the *.pp of the structure.  Thus, the third line to put it ...
        all in one
    % structure. In this format the .tt is vertical and the .pp is the...
        horizontal
    % polarization
76  cylinder_cal_375_exact = readExact([path_to_exact_data 'cyl375h....
        exact']);
    cylinder_cal_375_exactv = readExact([path_to_exact_data 'cyl375v....
        exact']);
    cylinder_cal_375_exact.tt = cylinder_cal_375_exactv.pp;

    % Same for 4.50 cylinder
81  cylinder_cal_450_exact = readExact([path_to_exact_data 'cyl450h....
        exact']);
    cylinder_cal_450_exactv = readExact([path_to_exact_data 'cyl450v....
        exact']);
    cylinder_cal_450_exact.tt = cylinder_cal_450_exactv.pp;
    disp('Done reading exact data')

86  %% Plots the calibration verification
    cylinder_cal_375_calibrated = calibrateRCS(...
        cylinder_cal_375_measured,cal_background,...
         cylinder_cal_450_measured,cal_background,...
            cylinder_cal_450_exact);
    plotCalVerify(cylinder_cal_375_calibrated,cylinder_cal_375_exact)
    disp('Done with calibration verification')
91
    %% Calibrates Target Data
    % Now, to calibrate the data
     cylinder_cal_450_calibrated_measured = ...
          calibrateRCS(cylinder_cal_450_measured,...
              cylinder_pylon_measured,...
96      cylinder_cal_375_measured,cylinder_pylon_measured,...
            cylinder_cal_375_exact);


    target_1_calibrated = ...
        calibrateRCS(target_1_measured,target_1_background,...
101     cylinder_cal_375_measured,cal_background,...
            cylinder_cal_375_exact);


    disp('Done calibrating measured data');

    %% Plots Uncalibrated Target Data, Global RCS
106  plotGlobalRCS(target_1_measured)
```

125

```
    %% Plots Calibrated Target Data, Global RCS
    plotGlobalRCS(target_1_calibrated)

    plotGlobalRCS('polar',target_1_calibrated)
111
    % disp('Done plotting global RCS')
    save two_sphere_final.mat
    %% Plots Calibrated Target Data, Global Range

116 %load 2_sphere_final.mat
    plotGlobalRange(target_1_calibrated)
```

7.2   Calculate Range

Listing VII.2:   Calculate Range(Appendix2/calculateRange.m)

```
  %Capt. John McShane
 2
  %Calculate Range
  %This code is a modified version of Dr. Peter Collins Calculate ...
      Range code
  function [out] = calculateRange(rcs,windowType,windowParameter)
  % <<< Part of the AFIT Processing Code Suite (Version 1.1, Jan ...
      2008) >>>
 7 %
  % [out] = calculateRange(rcs,windowType,windowParameter)
  %
  % FUNCTION:
  % Transforms frequency domain data to a range profile
12 %
  % INPUTS:
  % rcs = RCS data structure
  % windowType (optional) = name of desired window function
  % windowParameter (optional) = window parameter if required
17 % Note:  Available windows...
  %         barthannwin
  %         bartlett
  %         blackman
  %         blackmanharris
22 %         bohmanwin
  %         chebwin (windowParameter is max sidelobe level)
  %         flattopwin
  %         gausswin (windowParameter is 1/standard deviation)
  %         hamming
27 %         hann
  %         kaiser (windowParameter is beta parameter)
  %         nuttallwin
  %         parzenwin
  %         rectwin
32 %         triang
```

126

```matlab
%         tukeywin (windowParameter is ratio of flat to cosine ...
%            taper portion)
%
% OUTPUTS:
% out = Range data structure containing transformed data
% %
% Revision: Version 1.1, Jan 2008
%           Added material characterization modules
%           Cleaned up headers and related data type routines
% Version:  1.0  Original version, Dec 2007
% Copyright 2007, Peter J. Collins
% Air Force Institute of Technology



%% Add current directory to matlab's search path
currentDir = cd;
addpath(currentDir);
if exist(strcat(currentDir,'\resource'),'dir'); addpath(strcat(...
   currentDir,'\resource')); end

%% Check for errors
if  ~isstruct(rcs)
    disp('calculateRange ERROR:  Input must be a structure - ...
       aborting.')
    return
elseif length(rcs.frq)==1
    disp('calculateRange ERROR:  Input contains only one frequency...
        - aborting.')
    return
end

%% Initialize variables
out.rng = [];
out.ph = rcs.ph;
out.th = rcs.th;
out.tt = [];
out.pp = [];
out.tp = [];
out.pt = [];
out.header = rcs.header;
% Calculate some constants
if ~exist('windowType','var'); windowType = 'hamming'; end  % ...
   Hamming window
c = 2.997925e8;  % speed of light (m/s)
numFrq = length(rcs.frq);
bandwidth = 1e9*(rcs.frq(end)-rcs.frq(1)); % Frequency bandwidth (...
   Hz)
frqRes = bandwidth/(numFrq-1); % Frequency resolution (Hz)
unbRng = c/2/frqRes;  % Unambiguous range window (m)
rngWin = 0.5;  % Desired range window (m)
rngRes = c/2/bandwidth;  % Range resolution (m)
```

127

```matlab
    numRngBin = ceil(5*unbRng/rngRes);  % At least 5 samples/...
        resolution cell over desired range
    numRngBin = 2^(floor(log2(numRngBin))+1);  % Increase number to ...
        power of 2 for efficient FFT
    numCols = max(length(rcs.ph),length(rcs.th));

    %% Warnings
    if rngWin>unbRng
        disp('calculateRange WARNING:  Range window exceeds ...
            unambiguous range - aliasing may occur.')
    end

    %% Transform data
    for pol = {'tt' 'pp' 'tp' 'pt'}
        % Ignore polarization if no data
        if isempty(rcs.(char(pol))); continue; end
        % Window data
        if exist('windowParameter','var')
            iq = rcs.(char(pol)).*repmat(window(windowType,numFrq,...
                windowParameter),1,numCols);
        else
            iq = rcs.(char(pol)).*repmat(window(windowType,numFrq),1,...
                numCols);
        end
        % Pad data
        iq = [iq; zeros(numRngBin-numFrq,numCols)];  %#ok<AGROW>
        % Calculate the correctly normalized range
        out.(char(pol)) = (numRngBin/numFrq)*fftshift(abs(ifft(iq)),1)...
            ;
        % Calculate the appropriate range scaling
        out.rng = linspace(-unbRng/2,unbRng/2,numRngBin);
    end

    %% Create header
    out.header.FILENAME = strcat(rcs.header.FILENAME,' (',windowType,'...
        IR window)');
    out.header.BANDWIDTH = bandwidth/1e9;  % in GHz
    out.header.FRQRES = frqRes/1e9;  % in GHz
    out.header.UNBRANGE = unbRng/0.0254;  % in inches
    out.header.RANGERES = rngRes/0.0254;  % in inches
```

7.3   Azimuth Vs. Range Plot

Listing VII.3:   Azimuth vs Range Generator(Appendix2/azVRangeGenerator.m)

```matlab
%Capt. John McShane

%Azimuth vs. Range Generator
clear all
clc
```

```matlab
cd('C:\Documents and Settings\jmcshane\My Documents\MATLAB\...
   Thesis_range_tests\final_thesis_work')
for saved_file = {'target 1' 'target 2' 'target 3' 'target 4' '...
   target 5'...
9           'target 6' 'target 7' 'target 8' 'target 9' 'target 10'...
              ...
           'target 11' 'target 12' 'target 13' 'target 14'};

  saved_file_with_extension= ([char(saved_file),'.mat']);

14 load(saved_file_with_extension);

  for pol={'tt' 'pp'}


19 RCS_signal=target_1_calibrated; % RCS target tested from mat file

  %%

  range_values=3888:4305; %+/- 15 inches exactly
24

  range=calculateRange(RCS_signal);

  range_plot=range.(char(pol))(range_values,:);
29

  figure(1)
  pcolor(linspace(0,360,length(range.ph)),range.rng(range_values)...
     /0.0254,20*log10(abs(range_plot)))

34 colorbar;
  title(['Range Vs Azimuth (',char(saved_file),', pol = ',char(pol),...
     ')')],'fontsize',16)
  xlabel('\theta^\circ','fontsize',16)

  ylabel('Range [in]','fontsize',16)
39

  shading 'interp'


44 saveas(gcf,['C:\Documents and Settings\jmcshane\My Documents\...
     MATLAB\Thesis_range_tests\final_thesis_work\Figures\range vs az...
     \',char(saved_file),'\',char(saved_file),' ',char(pol),'.jpg'])

  end
  end
```

7.4 Standard STFT

```matlab
% Capt. John McShane

% Standard STFT
% This program produces the standard STFT for the target data.
% The user can change the target data using the variable ...
   saved_file
% The user can change the time steps and the angle using the ...
   respective
% variables
% The program will auto save the figures with the correct title ...
   for the
% STFT


clear all
clc
cd('C:\Documents and Settings\jmcshane\My Documents\MATLAB\...
   Thesis_range_tests\final_thesis_work')
for saved_file = {'target 1' 'target 2' 'target 3'...
         'target 4' 'target 5' 'target 6' 'target 7' 'target 8'...
         'target 9' 'target 10' 'target 11' 'target 12' 'target 13...
            ' 'target 14'};

saved_file_with_extension= ([char(saved_file),'.mat']);

load(saved_file_with_extension);

RCS_signal=target_1_calibrated; % RCS target tested from mat file
phi_length=length(RCS_signal.ph);

for pol={'tt' 'pp'}
    spectrogram_test=reshape(RCS_signal.(char(pol)),1201,1,...
       phi_length);

    sample_size=1200;


spectrogram_test=spectrogram_test(1:sample_size,1,1:phi_length);
for time_steps=[2 5 10 20 30]; %time steps


size=sample_size/time_steps; % Determine number of samples

a=squeeze(spectrogram_test);
data_matrix=reshape(a,size,time_steps,phi_length);
nfft=1024;

%% Apply windowing to data_matrix
```

```matlab
     windowing=hamming(size); %choose windowing that is desired {...
         rectwin, hamming)
     windowing_matrix=windowing*ones(1,time_steps); % make windowing ...
         matrix

48  %for phi=[0 60 90 120 180 240 300];
     for phi=[0 90];
     phi_2=(phi*4+1);

     windowing_f_matrix=windowing_matrix.*data_matrix(:,:,phi_2); % ...
         apply windowing to data
53

     zero_matrix=zeros(nfft-size,time_steps); % make zero matrix for ...
         padding

     zero_padded_matrix=[windowing_f_matrix;zero_matrix];
58  range_domain_matrix=20*log10(fftshift(ifft(zero_padded_matrix),1))...
         ;

     range_domain_matrix=-abs(range_domain_matrix);


63  %% filter out anything less than -60 dB
     db_cutoff=-60;

     for p=1:time_steps
     for s=1:length(range_domain_matrix(:,1))
68  if range_domain_matrix(s,p)<db_cutoff;
         range_domain_matrix(s,p)=-100;
     end
     end
     end
73  %%
     if size>nfft
         range=size;
     else range=nfft;

78
     %% Plot single angle of spectrogram (set time samples above and ...
         angle below)

     range_vector=linspace(-7.4948,7.4948,range)/0.0254;

83  range_values=486:539; % +/- 15 inches exactly

     figure(1)
     pcolor(linspace(0,4,time_steps),range_vector(range_values),...
         range_domain_matrix(range_values,:))
     xlabel('Time [s]','fontsize',16)
88  ylabel('Range [in]','fontsize',16)
```

131

```
      title(['STFT (',char(saved_file),', \theta = ',num2str(phi),'^\...
          circ, time divisions = ',num2str(time_steps),', pol = ',char(...
          pol),')')'],'fontsize',16)
      %apply colormap
      shading 'interp'
      load('C:\Documents and Settings\jmcshane\My Documents\MATLAB\...
          Thesis_range_tests\final_thesis_work\MyColormaps.mat')
93    colormap(mycmap);
      colorbar

      %%
      %saveas(gcf,['C:\Documents and Settings\jmcshane\My Documents\...
          MATLAB\Thesis_range_tests\final_thesis_work\Figures\...
          Standard_STFT\',char(saved_file),'\',char(saved_file),'_angle_...
          ',num2str(phi),'_time_divisions_',num2str(time_steps),'pol = ',...
          char(pol),'.fig'])
98    saveas(gcf,['C:\Documents and Settings\jmcshane\My Documents\...
          MATLAB\Thesis_range_tests\final_thesis_work\Figures\...
          Standard_STFT\',char(saved_file),'\',char(saved_file),'_angle_'...
          ,num2str(phi),'_time_divisions_',num2str(time_steps),'pol = ',...
          char(pol),'.jpg'])
      end
      end
       end
      end
103    end
```

7.5   Gaunaurd STFT

Listing VII.5:   STFT Gaunaurd(Appendix2/stftGaunaurd.m)

```
      %Capt. John McShane
 2
      %Guanaurd STFT
      %Discrete STFT change time according to Guillermo Gaunaurd
      % This program computes the STFT according to Equation 5 from The ...
          IEEE
      % paper by Gaunaurd titled Analysis by Means of Time-Frequency ...
          Wigner
 7    % Distributions. This calculates the STFT discretely. The program ...
          follows
      % the formula verbatim except when it multiplies the function f(k+...
          l) by the
      % exponential. Instead, I have taken the MATLAB fft of f(k+l) ...
          because it is
      % much faster than computing the summation. The code for the ...
          summation is
      % written below but takes an incredible ammount of time to compute...
          . The
12    % results are the same if using MATLAB fft however. Therefore, the...
          MATLAB
```

```matlab
% fft is used.

clc
clear all
cd('C:\Documents and Settings\jmcshane\My Documents\MATLAB\...
    Thesis_range_tests\final_thesis_work')

for saved_file = {'target 1' 'target 2' 'target 3'...
        'target 4' 'target 5' 'target 6' 'target 7' 'target 8'...
        'target 9' 'target 10' 'target 11' 'target 12' 'target 13...
        ' 'target 14'};


  saved_file_with_extension= ([char(saved_file),'.mat']);

load(saved_file_with_extension);


%RCS_signal=target_1_calibrated; % RCS target tested from mat file


for pol={'tt' 'pp'}

% load 1_sphere  % Load the target data
%
% pol='pp'; % Input polarization to test, options are 'pp'(...
    horizontal) or 'tt' (vertical)

for phi=[0 60 90 120 180 240 300]; %Set the angle of interest to ...
    take STFT on

%for phi=[0 90]; %Set the angle of interest to take STFT on
phi_2=(phi*4+1); %convert angle (phi) to angle in the data

for time_steps=[2 5 10 20 30]; % enter time divisions

data=target_1_calibrated.(char(pol))(:,phi_2);
data=data(:);

clear cal_background cylinder_cal_375_calibrated ...
    cylinder_cal_375_exact
clear cylinder_cal_375_exactv cylinder_cal_375_measured ...
    cylinder_cal_450_exact
clear cylinder_cal_450_exact cylinder_cal_450_exactv ...
    cylinder_cal_450_measured
clear target_1_background  target_1_measured


%%
rcs=target_1_calibrated;
c = 2.997925e8;  % speed of light (m/s)
numFrq = length(rcs.frq);
```

```matlab
   bandwidth = 1e9*(rcs.frq(end)-rcs.frq(1)); % Frequency bandwidth (...
       Hz)
   frqRes = bandwidth/(numFrq-1); % Frequency resolution (Hz)
   unbRng = c/2/frqRes;  % Unambiguous range window (m)
   rngWin = 0.5;  % Desired range window (m)
62 rngRes = c/2/bandwidth;  % Range resolution (m)
   numRngBin = ceil(5*unbRng/rngRes);  % At least 5 samples/...
       resolution cell over desired range
   numRngBin = 2^(floor(log2(numRngBin))+1);  % Increase number to ...
       power of 2 for efficient FFT
   numCols = max(length(rcs.ph),length(rcs.th));

67
   %% K Matrix computation
   % This cell computes how many samples of the RCS data will be sent...
        to the
   % FFT function based on time divisions. It produces a matrix of ...
       columns
   % that is time_divisions wide and a number of rows n samples of ...
       the data
72 % long. Each column has more samples considered. To run multiple ...
       iterations
   % of the same time divisions, uncomment the kmatrix save line and ...
       save it
   % once, comment it and then load it. The for loop takes awhile.

   % Start here, create different time matrix.
77 N=length(data);
   n=linspace(0,N-1,N); % make n vector
   n=n(:);


82 time_step_vector=linspace(1,time_steps,time_steps);
   k=linspace(1,N,time_steps);% make k vector has to be even numbers
   k=floor(k);
   kmatrix=[];

87 for index=time_step_vector
   kmatrix(:,index)=[ones(k(index),1);zeros(N-k(index),1)];
   end


92 %% Produce the data matrix
   % This cell will use the k matrix to pick the samples points used ...
       for each
   % time slice. It also multiplies this by the windowing chosen.

   data_matrix=data*ones(1,time_steps); % this is a matrix of the RCS...
        data by columns repeated N times
97 f_matrix=kmatrix.*data_matrix; %Using k matrix, pick out the ...
       samples used for time slice
```

```matlab
windowing=hamming(N); %choose windowing that is desired {rectwin, ...
    hamming)
windowing_matrix=windowing*ones(1,time_steps); % make windowing ...
    matrix

windowing_f_matrix=windowing_matrix.*f_matrix; % apply windowing ...
    to data

clear data_matrix f_matrix windowi'ng windowing_matrix  kmatrix

%% Use Matlab fft function to compute the fft and plot.
% This is much faster than using the summation of the exponential....
    Same
% results however.
%

windowing_f_matrix=[windowing_f_matrix; zeros(numRngBin-numFrq,...
    time_steps)];


range=length(windowing_f_matrix(:,1));

range_vector=linspace(-7.4948,7.4948,range)/0.0254;



plot_data=(numRngBin/numFrq)*fftshift(abs(ifft(windowing_f_matrix)...
    ),1);
plot_data=20*log10(abs(plot_data));


db_cutoff=-60;

for p=1:time_steps
for s=1:length(plot_data(:,1))
if plot_data(s,p)<db_cutoff;
    plot_data(s,p)=-100;
end
end
end


%% ZOOM in to +15,-15 inches
time_vector=linspace(0,4,time_steps);
range_values=3888:4305; % +/- 15 inches exact
figure(1)
pcolor(time_vector,range_vector(range_values),plot_data(...
    range_values,:));
title(['STFT Gaunaurd (',char(saved_file),', \theta =',num2str(phi...
    ),'^\circ, time divisions = ',num2str(time_steps),', pol = ',...
    char(pol),')'],'fontsize',16)
xlabel('Time [s]','fontsize',16)
```

```
142 ylabel('Range [in]','fontsize',16)
    %apply colormap
    shading 'interp'
    load('C:\Documents and Settings\jmcshane\My Documents\MATLAB\...
        Thesis_range_tests\final_thesis_work\MyColormaps.mat')
    colormap(mycmap);
147 colorbar
    saveas(gcf,['C:\Documents and Settings\jmcshane\My Documents\...
        MATLAB\Thesis_range_tests\final_thesis_work\Figures\...
        STFT_Gaunaurd\',char(saved_file),'\',char(saved_file),'_angle_'...
        ,num2str(phi),'_time_divisions_',num2str(time_steps),'pol = ',...
        char(pol),'.jpg'])
    end
    end
    end
152 end

    %%
```

7.6   Scene Match Function

Listing VII.6:   Scene Match Function(Appendix2/sceneMatch.m)

```
%Capt. John McShane

% Scene Match Function
 4 % This program calculates the correlation of the RCS data with ...
     range and
   % doppler.

   clc
   clear all
 9 cd('C:\Documents and Settings\jmcshane\My Documents\MATLAB\...
     Thesis_range_tests\final_thesis_work')

   for saved_file = {'target 1' 'target 2' 'target 3' 'target 4' '...
     target 5'...
             'target 6' 'target 7' 'target 8' 'target 9' 'target 10'...
             'target 11' 'target 12' 'target 13' 'target 14'};
14


   saved_file_with_extension= ([char(saved_file),'.mat']);

19 load(saved_file_with_extension);


   for pol={'tt' 'pp'} % Input polarization to test, options are 'pp...
     '(horizontal) or 'tt' (vertical)
```

136

```matlab
24   %for phi=[0 60 90 120 180 240 300]; %Set the angle of interest to ...
         take STFT on
     for phi=[0 90]; %Set the angle of interest to take STFT on
     phi_2=(phi*4+1); %convert angle (phi) to angle in the data

     data=target_1_calibrated.(char(pol))(:,phi_2);
29   data=data(:);

     Ro=0; %Range of target from center of pedastal
     % clear cal_background cylinder_cal_375_calibrated ...
         cylinder_cal_375_exact
     % clear cylinder_cal_375_exactv cylinder_cal_375_measured ...
         cylinder_cal_450_exact
34   % clear cylinder_cal_450_exact cylinder_cal_450_exactv ...
         cylinder_cal_450_measured
     % clear target_1_background
     % clear target_1_measured
     %%

39   rcs=target_1_calibrated;
     c = 2.997925e8;  % speed of light (m/s)
     numFrq = length(rcs.frq);
     bandwidth = 1e9*(rcs.frq(end)-rcs.frq(1)); % Frequency bandwidth (...
         Hz)
     frqRes = bandwidth/(numFrq-1); % Frequency resolution (Hz)
44   unbRng = c/2/frqRes;  % Unambiguous range window (m)
     rngWin = 0.762;  % Desired range window (m).=+/1 15 inches exactly
     rngRes = c/2/bandwidth;  % Range resolution (m)
     numRngBin = ceil(5*unbRng/rngRes);  % At least 5 samples/...
         resolution cell over desired range
     numRngBin = 2^(floor(log2(numRngBin))+1);  % Increase number to ...
         power of 2 for efficient FFT
49   numCols = max(length(rcs.ph),length(rcs.th));


     %% make Filter bank based on range and time.
     N=length(data); % Number of samples in the RCS data.
54
     %From equation 2.6 in Thesis. Assumes stationary target.
     freq_vector=linspace(6e9,18e9,N); %Create frequency vector
     freq_vector_rads=2*pi*(freq_vector);
     freq_vector_rads=freq_vector_rads(:);
59
     range_vector=linspace(-rngWin/2,rngWin/2,rngWin/rngRes); % create ...
         range vector from -rngWin/2 to +rngWin/2
     range_values=(2*range_vector./c); % last part of equation 2.6
     phi_freq_range=freq_vector_rads*range_values; % Create Matrix of ...
         all possible freq and range possibilities.
     freq_range_matrix=exp(i*phi_freq_range);
64
     freq_range_data_correlation=xcorr2(data,freq_range_matrix)';
```

137

```matlab
%% Plot the correlation of the freq_range matrix and the data for ...
    the
% specific angle.
%
 pulse_vector=linspace(1,N,2*N-1); % Pulse vector
range_vector=range_vector/0.0254; % convert to inches


scene_match=(abs(freq_range_data_correlation));
scene_match=scene_match/max(max(scene_match));


time_vector=linspace(0,4,2*N-1);
figure(1)
pcolor(time_vector,range_vector,scene_match)
xlabel('Time [s]','fontsize',16)
ylabel('Range [in]','fontsize',16)
title(['Scene Match (',char(saved_file),', \theta = ',num2str(phi)...
    ,'^\circ, pol = ',char(pol),')'],'fontsize',16)
shading 'interp'
load('C:\Documents and Settings\jmcshane\My Documents\MATLAB\...
    Thesis_range_tests\final_thesis_work\MyColormapsSceneMatch.mat'...
    )
colormap(mycmap);
colorbar
saveas(gcf,['C:\Documents and Settings\jmcshane\My Documents\...
    MATLAB\Thesis_range_tests\final_thesis_work\Figures\scene_match...
    \',char(saved_file),'\',char(saved_file),'_angle_',num2str(phi)...
    ,'pol = ',char(pol),'.jpg'])
%saveas(gcf,['C:\Documents and Settings\jmcshane\My Documents\...
    MATLAB\Thesis_range_tests\jan_work\Figures\scene_match\',char(...
    saved_file),'\',char(saved_file),'_angle_',num2str(phi),'pol = ...
    ',char(pol),'.fig'])
end
end
end
```

7.7 *Pulse Doppler Ambiguity Function*

Listing VII.7:   Pulse Doppler Ambiguity Function(Appendix2/pulseDopplerAF.m)

```matlab
%Capt. John McShane

%Pulse Doppler Scene Match function

% This program calculates the correlation of the RCS data with ...
    range and
% doppler.

clc
```

```matlab
   clear all
   cd('C:\Documents and Settings\jmcshane\My Documents\MATLAB\...
      Thesis_range_tests\jan_work')
   load 'target 2' % Load the target data

   saved_file = 'target 2' ;


    saved_file_with_extension= ([char(saved_file),'.mat']);

   load(saved_file_with_extension);

   pol='tt'; % Input polarization to test, options are 'pp'(...
      horizontal) or 'tt' (vertical)
   phi=0; %Set the angle of interest to take STFT on
   phi_2=(phi*4+1); %convert angle (phi) to angle in the data

   data=target_1_calibrated.(char(pol))(:,phi_2);
   data=data(:);

   Ro=0*0.0254; %Range of target from center of pedastal
   % clear cal_background cylinder_cal_375_calibrated ...
      cylinder_cal_375_exact
   % clear cylinder_cal_375_exactv cylinder_cal_375_measured ...
      cylinder_cal_450_exact
   % clear cylinder_cal_450_exact cylinder_cal_450_exactv ...
      cylinder_cal_450_measured
   % clear target_1_background
   % clear target_1_measured
   %%

   rcs=target_1_calibrated;
   c = 2.997925e8;  % speed of light (m/s)
   numFrq = length(rcs.frq);
   bandwidth = 1e9*(rcs.frq(end)-rcs.frq(1)); % Frequency bandwidth (...
      Hz)
   frqRes = bandwidth/(numFrq-1); % Frequency resolution (Hz)
   unbRng = c/2/frqRes;  % Unambiguous range window (m)
   rngWin = 0.75;  % Desired range window (m)
   rngRes = c/2/bandwidth;  % Range resolution (m)
   numRngBin = ceil(5*unbRng/rngRes);  % At least 5 samples/...
      resolution cell over desired range
   numRngBin = 2^(floor(log2(numRngBin))+1);  % Increase number to ...
      power of 2 for efficient FFT
   numCols = max(length(rcs.ph),length(rcs.th));


   %% make Filter bank based on range and time.
   N=length(data); % Number of samples in the RCS data.

   %From equation 2.6 in Thesis. Assumes stationary target.
   freq_vector=linspace(6e9,18e9,N); %Create frequency vector
```

```matlab
    freq_vector_rads=2*pi*(freq_vector);
    freq_vector_rads=freq_vector_rads(:);

    range_vector=linspace(-rngWin/2,rngWin/2,rngWin/rngRes); % create ...
        range vector from -.5m to .5 m
57  range_values=(2*range_vector./c); % last part of equation 2.6
    phi_freq_range=freq_vector_rads*range_values; % Create Matrix of ...
        all possible freq and range possibilities.
    freq_range_matrix=exp(i*phi_freq_range);


62  freq_range_data_correlation=xcorr2(data,freq_range_matrix)';

    %% Plot the correlation of the freq_range matrix and the data for ...
        the
    % specific angle.
    %
67   pulse_vector=linspace(1,N,2*N-1); % Pulse vector
    range_vector=range_vector/0.0254; % convert to inches

    % figure(1)
    % pcolor(pulse_vector,range_vector,abs(freq_range_data_correlation...
        ))
72  % xlabel('Pulses')
    % ylabel('Range [Inches]')
    % title({['Correlation Matrix for Freq and Range at \phi = ',...
        num2str(phi)];char(saved_file)})
    % shading ('interp')

77  time_vector=linspace(0,4,2*N-1);
    figure(1)
    pcolor(time_vector,range_vector,(abs(freq_range_data_correlation))...
        )
    xlabel('Time [s]')
    ylabel('Range [Inches]')
82   title({['Correlation Matrix for Freq and Range at \phi = ',...
        num2str(phi)];char(saved_file)})
    shading ('interp')
    colorbar

    %% Determine velocity of target for each pulse
87  %for Ro=linspace(-.2,.2,50)
     circumference=4*pi*0.0254; %meters for target 10
     velocity_max=circumference/25; % 1 rev in 25 seconds. in m/s

     theta=linspace(0,359,1201);
92   velocity_vector=velocity_max*cosd(theta);
    velocity_vector=velocity_vector(:);% Target velocities relative ...
        to radar system.
    %  frequency_sweep_time=4; % time it takes for one frequency sweep
    %  range_vector=frequency_sweep_time*velocity_vector; % create ...
        range vector from -.05m to .05 m
```

```matlab
 97  freq_vector=linspace(6e9,18e9,N); %Create frequency vector
     freq_vector_rads=2*pi*(freq_vector);
     freq_vector_rads=freq_vector_rads(:);

     length_ball_bearing_arm=1*0.0254; %Length of arm of ball bearing ...
         (2 inches)
102
     Rn=length_ball_bearing_arm*sind(theta); % make position value ...
         based on theta for ball bearings.
     Rn=Rn(:);

     Tr=250e-9; %PRF
107  velocity_values=(2*(velocity_vector*Tr+Ro+Rn)/c); % last part of ...
         equation 2.6
     phi_freq_velocity=freq_vector_rads(:)*velocity_values'; % Create ...
         Matrix of all possible freq and range possibilities.
     freq_range_matrix=exp(i*phi_freq_velocity);


112  freq_range_data_correlation=xcorr2(data,freq_range_matrix);

     %
     % frequency_sweep_time=4; % time it takes for one frequency sweep
     %  range_vector=frequency_sweep_time*velocity_vector; % create ...
         range vector from -.05m to .05 m
117  %
     % freq_vector=linspace(6e9,18e9,N); %Create frequency vector
     % freq_vector_rads=2*pi*(freq_vector);
     % freq_vector_rads=freq_vector_rads(:);
     %
122  %
     % velocity_values=(2*(range_vector+Ro)/c); % last part of equation...
          2.6
     % phi_freq_velocity=freq_vector_rads*velocity_values; % Create ...
         Matrix of all possible freq and range possibilities.
     % freq_range_matrix=exp(i*phi_freq_velocity);
     %
127  %
     % freq_range_data_correlation=xcorr2(data,freq_range_matrix);
     %%

     figure(2)
132
     pcolor(Rn/0.0254,pulse_vector,abs(freq_range_data_correlation))


     xlabel('Range Shift from Ro [in]')
137  ylabel('Pulse')
     title(['Correlation Matrix for Freq and Velocity at \phi = ',...
         num2str(phi),' and Range_0 = ',num2str(Ro),' [m]']);
     shading interp
```

```matlab
%colormap winter

figure(3)

pcolor(abs(freq_range_data_correlation))


xlabel('Range Shift from Ro [in]')
ylabel('Pulse')
title(['Correlation Matrix for Freq and Velocity at \phi = ',...
    num2str(phi),' and Range_0 = ',num2str(Ro),' [m]']);
shading interp
%colormap winter
%end
```

7.8 Wigner Distribution

Listing VII.8:   Wigner Distribution(Appendix2/wignerDistribution.m)

```matlab
%Capt John McShane
%Wigner Distribution
% 5 Feb 09
clear all
clc
tic


cd('C:\Documents and Settings\jmcshane\My Documents\MATLAB\...
    Thesis_range_tests\final_thesis_work')
% Read in .mat files containing target radar data
for saved_file = {'target 1' 'target 2' 'target 3' 'target 4' '...
    target 5'...
            'target 6' 'target 7' 'target 8' 'target 9' 'target 10'...
               ...
            'target 11' 'target 12' 'target 13' 'target 14'};



 saved_file_with_extension= ([char(saved_file),'.mat']);

  load(saved_file_with_extension);

for pol={'tt' 'pp'}
RCS_signal=target_1_calibrated.(char(pol)); % RCS target tested ...
    from mat file
%%

clear cal_background cylinder_cal_375_calibrated ...
    cylinder_cal_375_exact
clear cylinder_cal_375_exactv cylinder_cal_375_measured ...
    cylinder_cal_450_exact
```

```matlab
27  clear cylinder_cal_450_exact cylinder_cal_450_exactv ...
        cylinder_cal_450_measured
    clear target_1_background
    for phi=[0 60 90 120 180 240 300];

    % Because data taken at a 0.25 angle increments, find exact angle ...
        column
32  % using formula below.
    phi_2=(phi*4+1);

    % From Target RCS Matrix, pull single angle frequency sweep.
    wave=RCS_signal(:,phi_2); % Call this wave to comply with your DFT...
        function
37  wave=wave(:); % wave must be a column vector to work. Force to Col...
        vector

    N=length(wave); % Find length

    %% Start of DFT for WD
42  % l vector according to equation
    l_vector=linspace(0,N-1,N); %samples for each freq
    l_vector=l_vector';

    l_vector_dft=exp((i*4*pi/N)*l_vector);
47  l_vector_dft=l_vector_dft';

    l_matrix_dft=l_vector_dft'*ones(size(l_vector_dft));
    l_matrix_dft=l_matrix_dft';

52  %n vector
    n_vector=linspace(0,N-1,N); % each freq vector
    n_matrix=n_vector'*ones(size(n_vector));

    % DFT matrix, mulitply this by wave matrix
57  dft_matrix=l_matrix_dft.^n_matrix;
    dft_matrix=dft_matrix';
    %% make f(k+n) maxtrix
    for n=1:N;
        f(:,n)=circshift(wave,-n);
62  end

    f=circshift(f,1); % shift 1 row down you start at correct sample ...
        point

    %% make f(k-n) matrix.
67
    flip_wave=flipud(wave(2:N)); % gets rid of one 0 value, so it is ...
        not repeated.

    % Combine positive samples and "-time samples"
    big_wave=[flip_wave;wave];
72
```

143

```matlab
    %Create matrix for f(k-n)
    for n=1:2*N
        big_shift(:,n)=circshift(big_wave,n);
    end

    % from big shift matrix, pull out matrix that matches size of f(k+...
        n) matrix
    f_minus=big_shift(1:N,N:(2*N)-1);


%% *f(k-n) matrix  = conjugate.
    f_minus_conjugate=conj(f_minus);

    %% f product
    %  this is the product of the f(k+n) and f*(k-n);
    f_product=f.*f_minus_conjugate;


    for l=1:N;

l_matrix=dft_matrix(:,l)*ones(1,N);

    k_matrix=f_product.*l_matrix;

    %represents l is rows and k's are columns for all k's.
    k_sum(l,:)=2*sum(k_matrix); % multiply summation by 2 per WD ...
        equation

    end

    %% Convert to RCS value

    wigner_plot=(k_sum);

    wigner_plot=20*log10(abs(real((wigner_plot))));  % turn to RCS ...
        power


    %% Save matfiles to easily process later (Saves time)
    %save_file=(['C:\Documents and Settings\jmcshane\My Documents\...
        MATLAB\Thesis_range_tests\final_thesis_work\Figures\...
        wigner_distribution\',char(saved_file),'_angle_',num2str(phi),'...
        pol = ',char(pol),'.mat']);


%save(save_file, 'N', 'wigner_plot','phi','pol','saved_file')


    %% Create Range vector based on size of Anechoic chamber...Convert...
        to [in]
    range_vector=linspace(-7.4948,7.4948,N)/0.0254;
    range_values=570:632; %+/- 15 inches
```

144

```
    %% Truncate matrix to just +/- 15 inches
    wigner_plot=wigner_plot(range_values,:);
122
    %% Plot Wigner Distribution
    figure(1)
    pcolor(linspace(0,4,N),range_vector(range_values),wigner_plot);
    title(['Wigner Distribution (',char(saved_file),', \phi = ',...
        num2str(phi),', pol = ',char(pol),')',],'fontsize',16)
127 xlabel('Time [s]','fontsize',16)
    ylabel('Range [in]','fontsize',16)
    shading 'interp'
    colormap jet
    colorbar
132
    saveas(gcf,['C:\Documents and Settings\jmcshane\My Documents\...
        MATLAB\Thesis_range_tests\final_thesis_work\Figures\...
        wigner_distribution\',char(saved_file),'\',char(saved_file),'...
        _angle_',num2str(phi),'pol = ',char(pol),'.jpg'])
    %saveas(gcf,['C:\Documents and Settings\jmcshane\My Documents\...
        MATLAB\Thesis_range_tests\jan_work\Figures\wigner_distribution...
        \',char(saved_file),'\',char(saved_file),'_angle_',num2str(phi)...
        ,'pol = ',char(pol),'.fig'])

    toc
137
    end
    end
    end
```

7.9 DFT McShane

Listing VII.9:   DFT McShane(Appendix2/dftMcShane.m)

```
function [frequency_vector,fourier_transform] = DFT_mcshane(wave)

%%Capt. John McShane

5 %DFT Function
% This function takes the DFT of a wave form. It will output the ...
    DFT as a
% vector and the frequency vector. This can be plotted in the main...
     script
% if desired. It will also be commented out here in case someone ...
    wants to
% execute the plots within this function.
10
% tic % start clock

%profile on
```

```matlab
%wave=John_data.mag_phase;
wave=wave(:); % wave must be a column vector to work. Force to Col...
    vector

nyq_samples=length(wave);

time_step=1/nyq_samples; % time steps to meet nyquist

time_vector=0:time_step:1-time_step; %time vector computed for 1 ...
    sec


%% Start of DFT
% j vector, look at help for dft in Matlab to explain j
j_vector=linspace(0,nyq_samples-1,nyq_samples); %samples for each ...
    freq
j_vector=j_vector';

j_vector_dft=exp((-i*2*pi/nyq_samples)*j_vector);
j_vector_dft=j_vector_dft';

j_matrix_dft=j_vector_dft'*ones(size(j_vector_dft));
j_matrix_dft=j_matrix_dft';

%p vector, look at help for dft in Matlab to explain p
p_vector=linspace(0,nyq_samples-1,nyq_samples); % each freq vector
p_matrix=p_vector'*ones(size(p_vector));

% DFT matrix, mulitply this by wave matrix
dft_matrix=j_matrix_dft.^p_matrix;
dft_matrix=dft_matrix';

%wave matrix
wave_matrix=wave*ones(size(wave))';

% Create Fourier transform
fourier_transform=wave_matrix.*dft_matrix;
fourier_transform=sum(fourier_transform);


% create Frequency Vector for plotting
frequency_vector=linspace(0,nyq_samples,nyq_samples);


%Might have to comment this out..ask teacher
% determine cutoff frequency so aliasing doesnt occur.
cutoff_freq=length(wave)/2;

frequency_vector=frequency_vector(1:cutoff_freq); %truncate so no ...
    alias
```

```matlab
    fourier_transform=fourier_transform(1:cutoff_freq); %truncate so ...
        no alias


65 fourier_transform=fourier_transform(:); %Force Columns

    frequency_vector=frequency_vector(:); % Force Columns

    %profile viewer
70

    %toc % stop clock
```

7.10 *Scene Match Subtract*

```matlab
1 % Capt. John McShane

  % Scene Match Subtraction
  % This function subtracts two target scenes from each other in ...
      hope of
  % reavealing differences in the RCS scattering locations
6

  clc
  clear all
  cd('C:\Documents and Settings\jmcshane\My Documents\MATLAB\...
      Thesis_range_tests\final_thesis_work\scene_match\...
      scene_match_mat');
11
  target_a=3; %Input first target

  target_b=4; %Input second target

16 target_a= load(['target ',num2str(target_a),'_angle_90pol = tt']);

  target_b= load(['target ',num2str(target_b),'_angle_90pol = tt']);

  target_a_sm=target_a.scene_match; %get scene match  for target a
21
  target_b_sm=target_b.scene_match; %get scene match  for target a



26 N=length(target_a.range_vector); %Length of range vector

  subtractTaTb=target_b_sm-target_a_sm; %subtract a from b

  range_limits=10:52;
31
```

```matlab
figure(1)
%pcolor(target_a.time_vector,target_a.range_vector(range_limits),...
    subtractTaTb(range_limits,:));
pcolor(target_a.time_vector,target_a.range_vector,subtractTaTb);
xlabel('Time [s]','fontsize',16)
ylabel('Range [in]','fontsize',16)
title('Scene Match Subtract, Targets 3 and 4, TT pol, \theta=90^\...
    circ','fontsize',16)
shading 'interp'
colormap jet
colorbar

%put in cutoff filter so you can see details
db_cutoff=5;
for p=1:length(target_a.time_vector)
for s=1:length(target_a.range_vector)
if subtractTaTb(s,p)<db_cutoff;
    subtractTaTb(s,p)=-100;
end
end
end

% plot all targets
figure(2)
pcolor(target_a.time_vector,target_a.range_vector,target_a_sm)
xlabel('Time [s]','fontsize',16)
ylabel('Range [in]','fontsize',16)
shading 'interp'
colormap jet
colorbar


figure(3)
pcolor(target_b.time_vector,target_b.range_vector,target_b_sm)
xlabel('Time [s]','fontsize',16)
ylabel('Range [in]','fontsize',16)
shading 'interp'
colormap jet
colorbar


figure(4)
%pcolor(target_a.time_vector,target_a.range_vector(range_limits),...
    subtractTaTb(range_limits,:));
pcolor(target_a.time_vector,target_a.range_vector,subtractTaTb);
title('Scene Match Subtract (Filtered), Targets 3 and 4, TT pol, \...
    theta=90^\circ','fontsize',16)
xlabel('Time [s]','fontsize',16)
ylabel('Range [in]','fontsize',16)
shading 'interp'
colormap jet
colorbar
```

VIII. Appendix C: Additional TFR Results

This Appendix contains the TFR comparison results not described in Section IV.

8.1 Target 2 TT Results
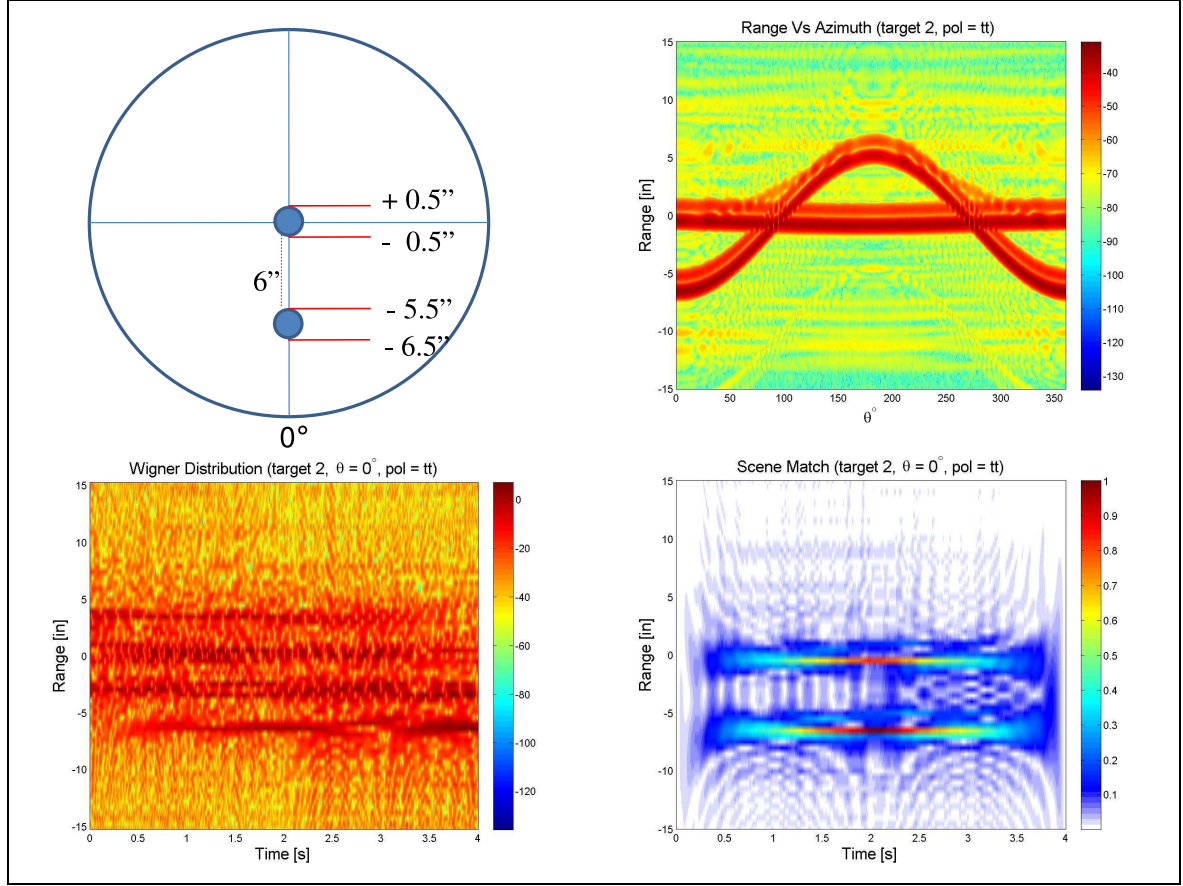
Figure H.1:   Target 2: Pol=TT, $\theta = 0°$, TFR's a.
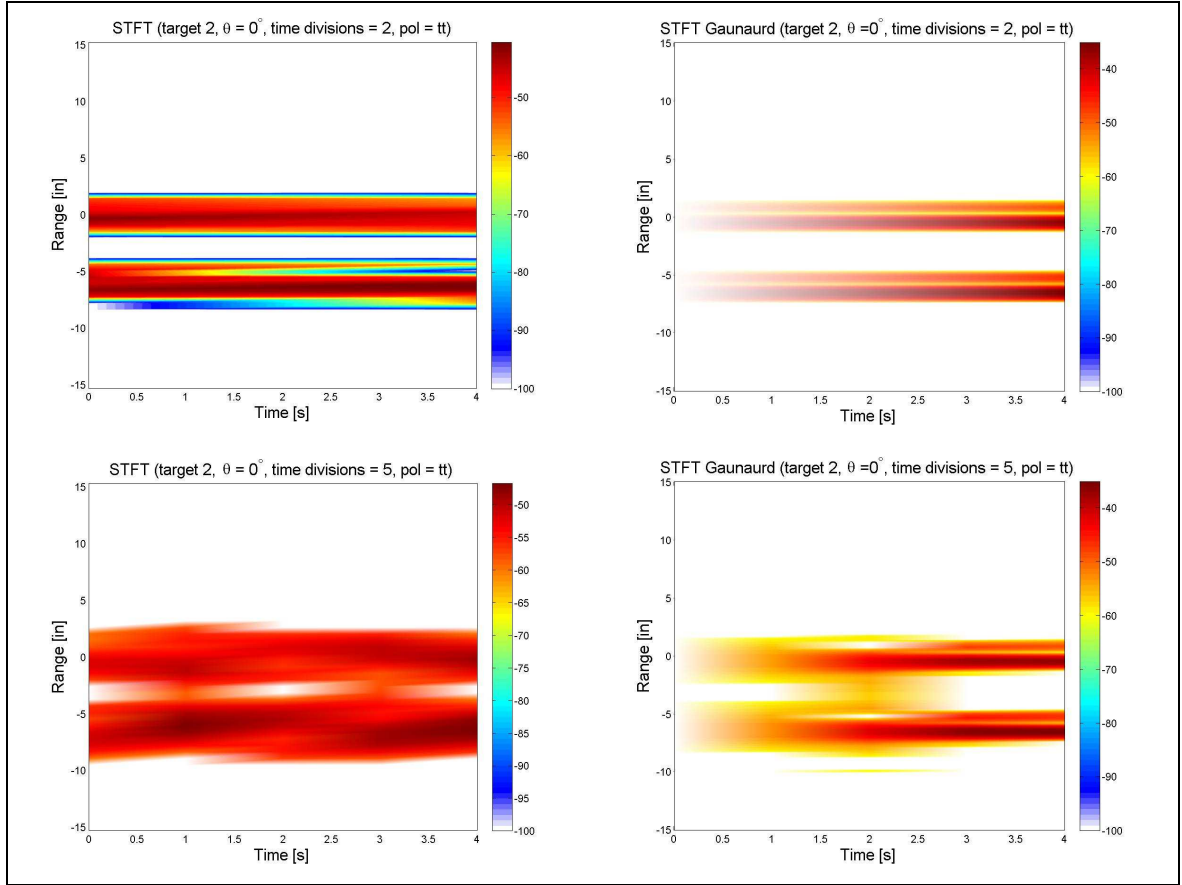
Figure H.2:   Target 2: Pol=TT, $\theta = 0°$, TFR's b.
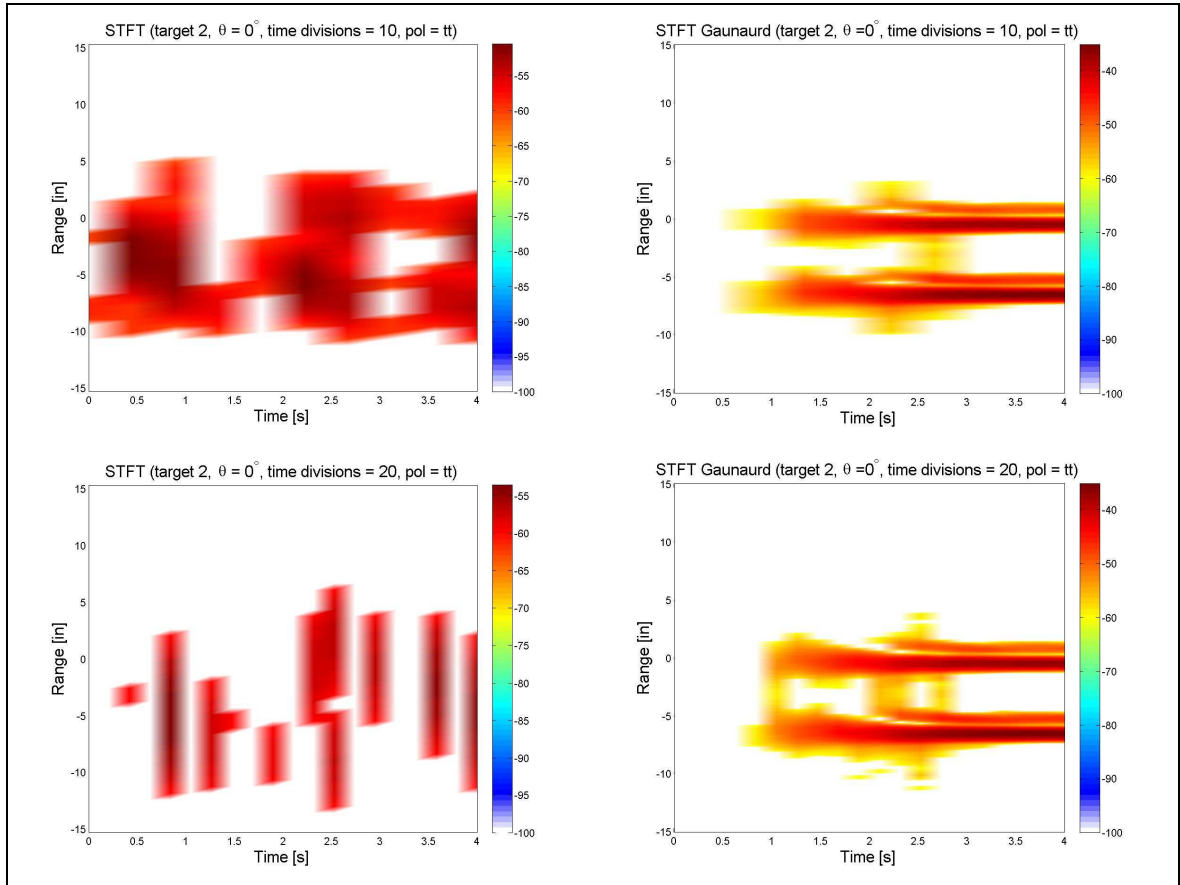
Figure H.3: Target 2: Pol=TT, $\theta = 0°$, TFR's c.

8.2   Target 3 and 4 PP Results
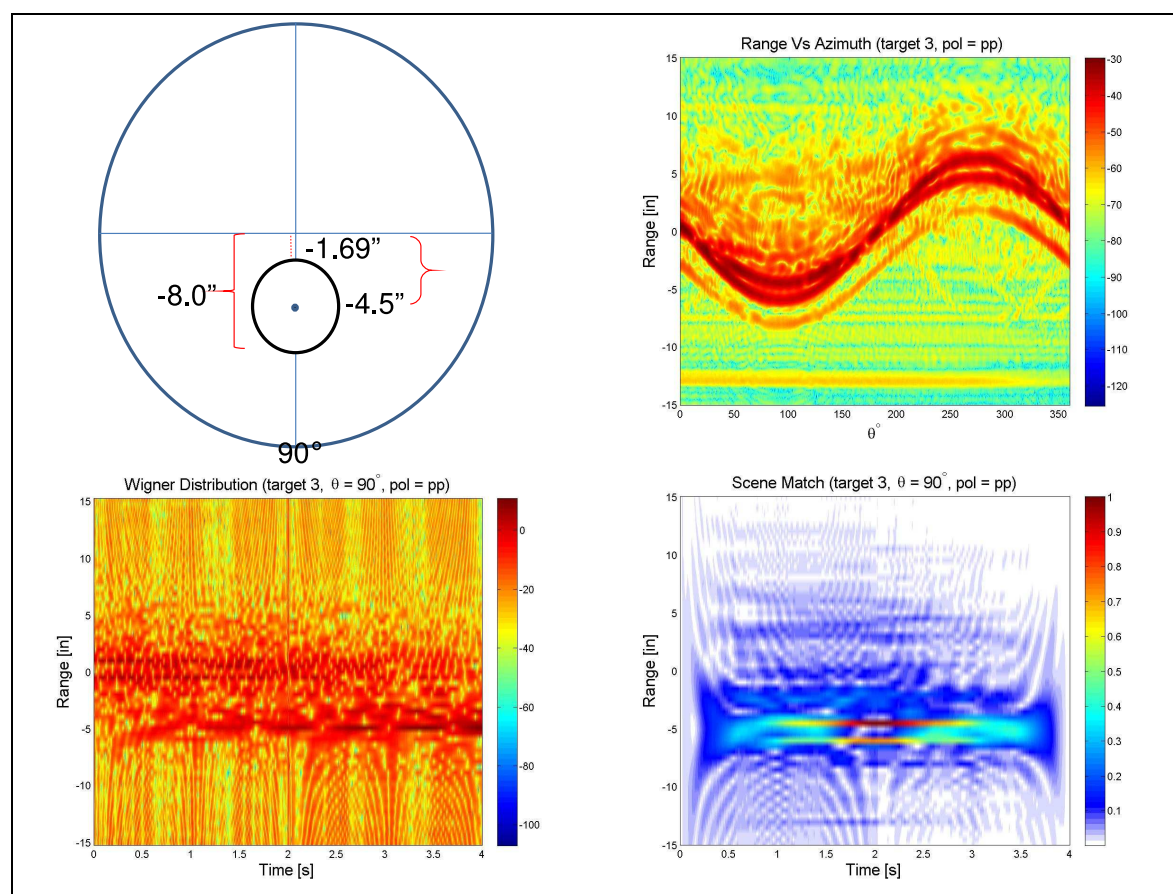


Figure H.4:   Target 3: Pol=PP, $\theta = 90°$, TFR's a.
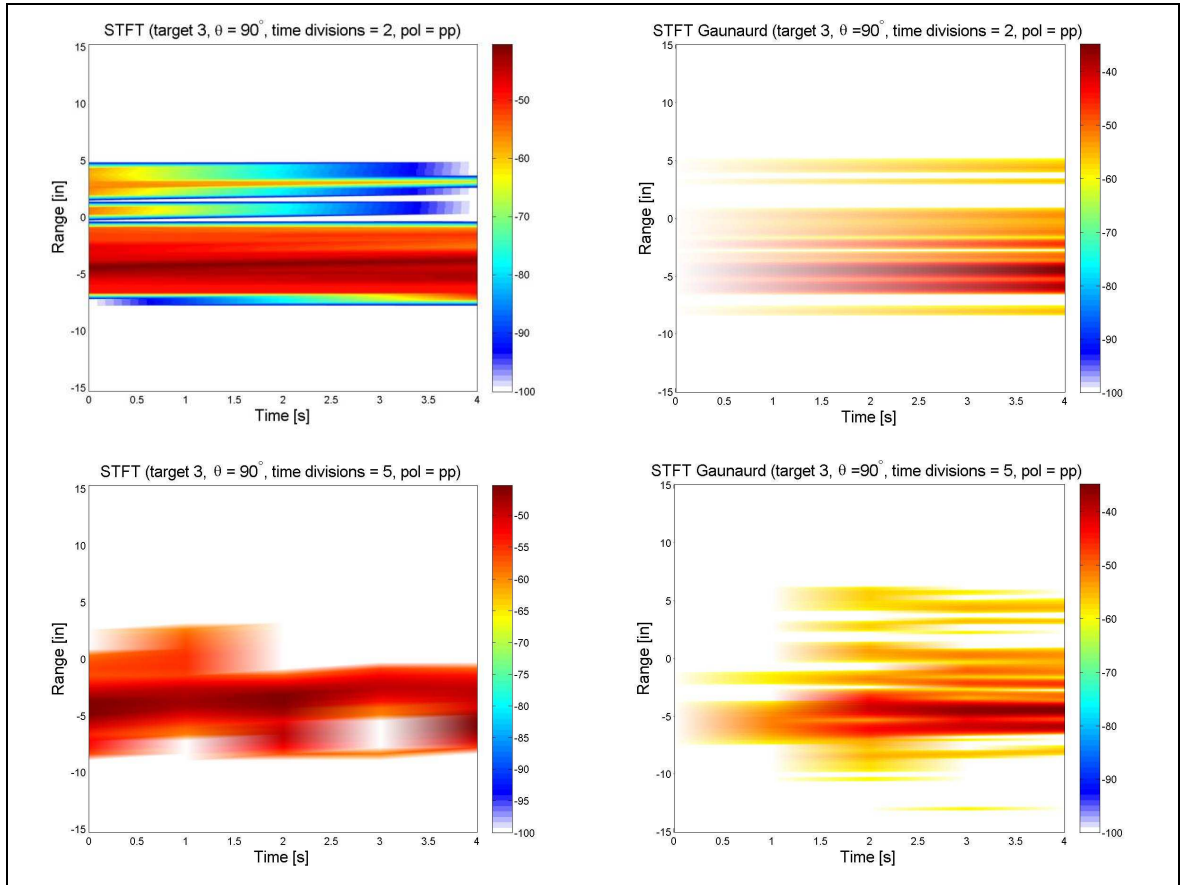
Figure H.5:   Target 3: Pol=PP, $\theta = 90°$, TFR's b.
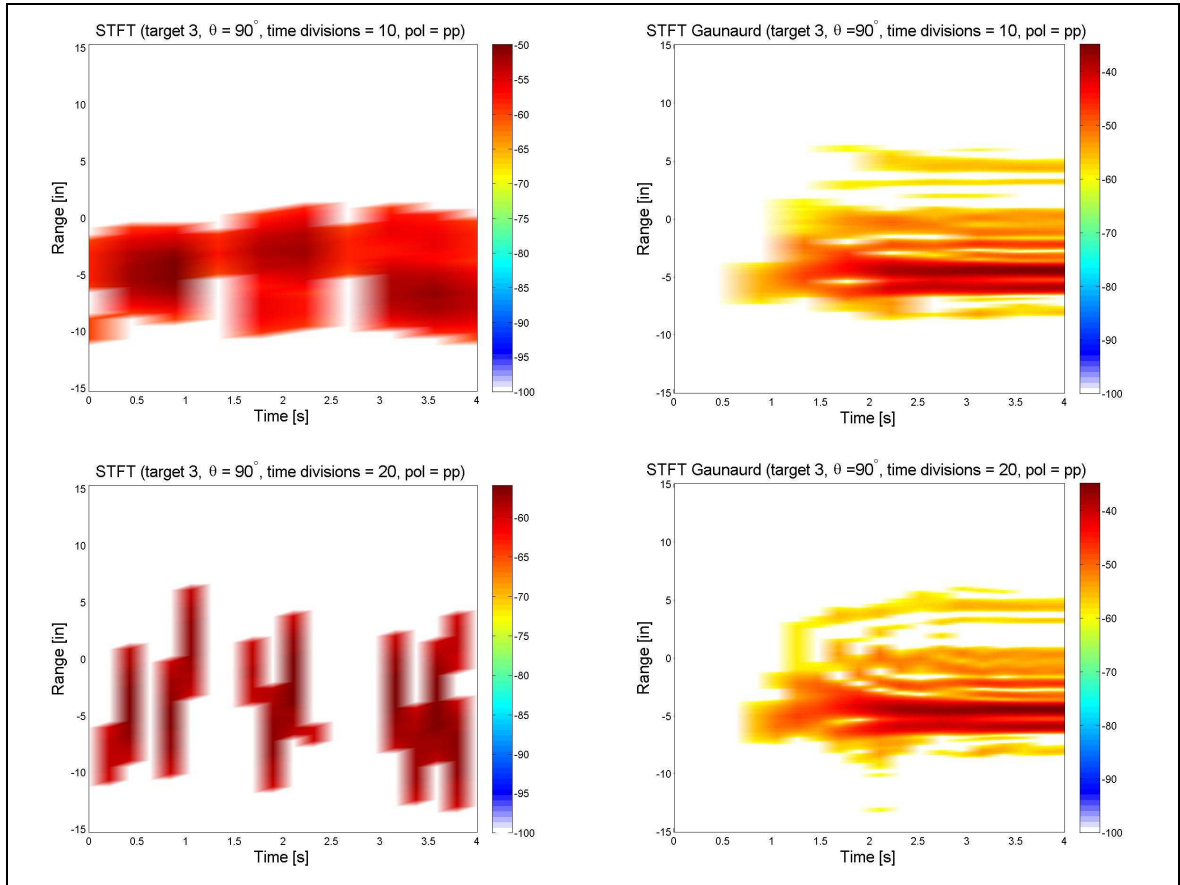
Figure H.6:   Target 3: Pol=PP, $\theta = 90°$, TFR's c.
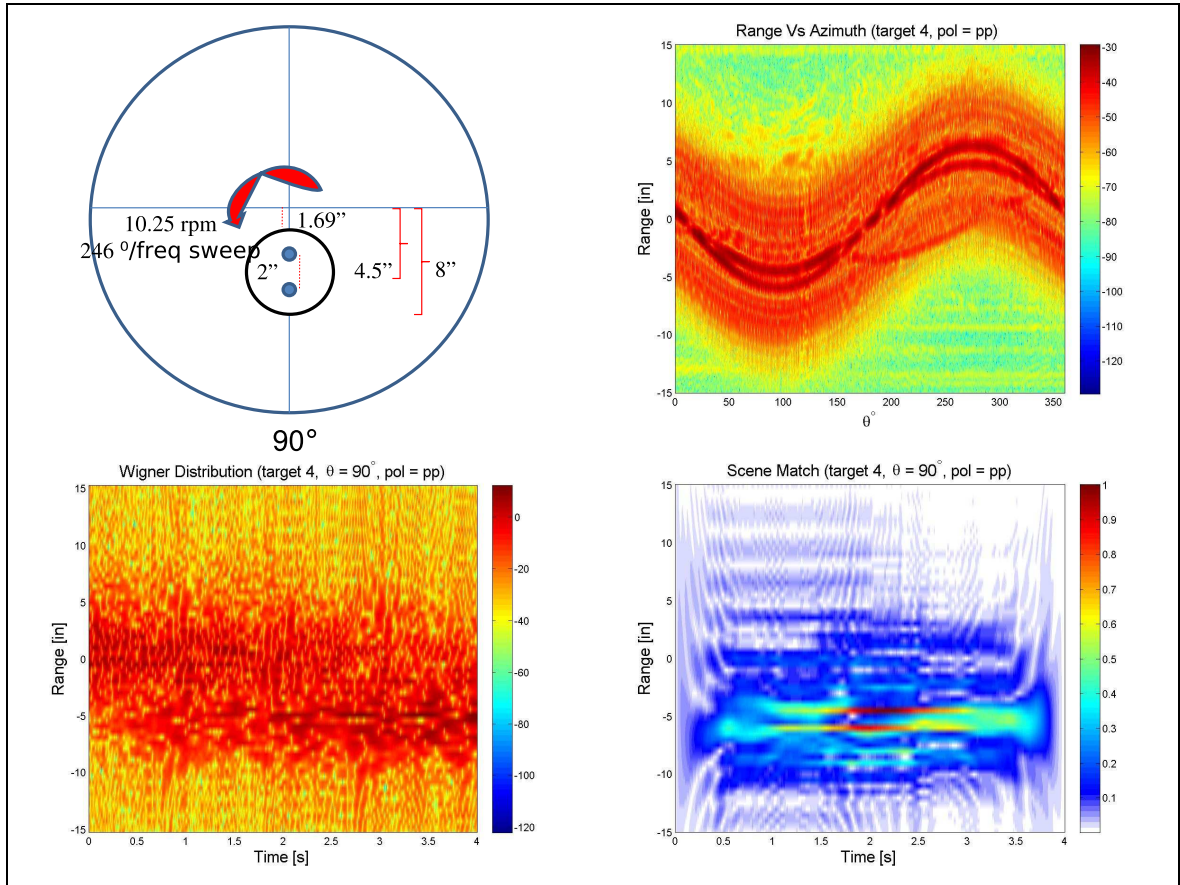
Figure H.7:   Target 4: Pol=PP, $\theta = 90°$, TFR's a.
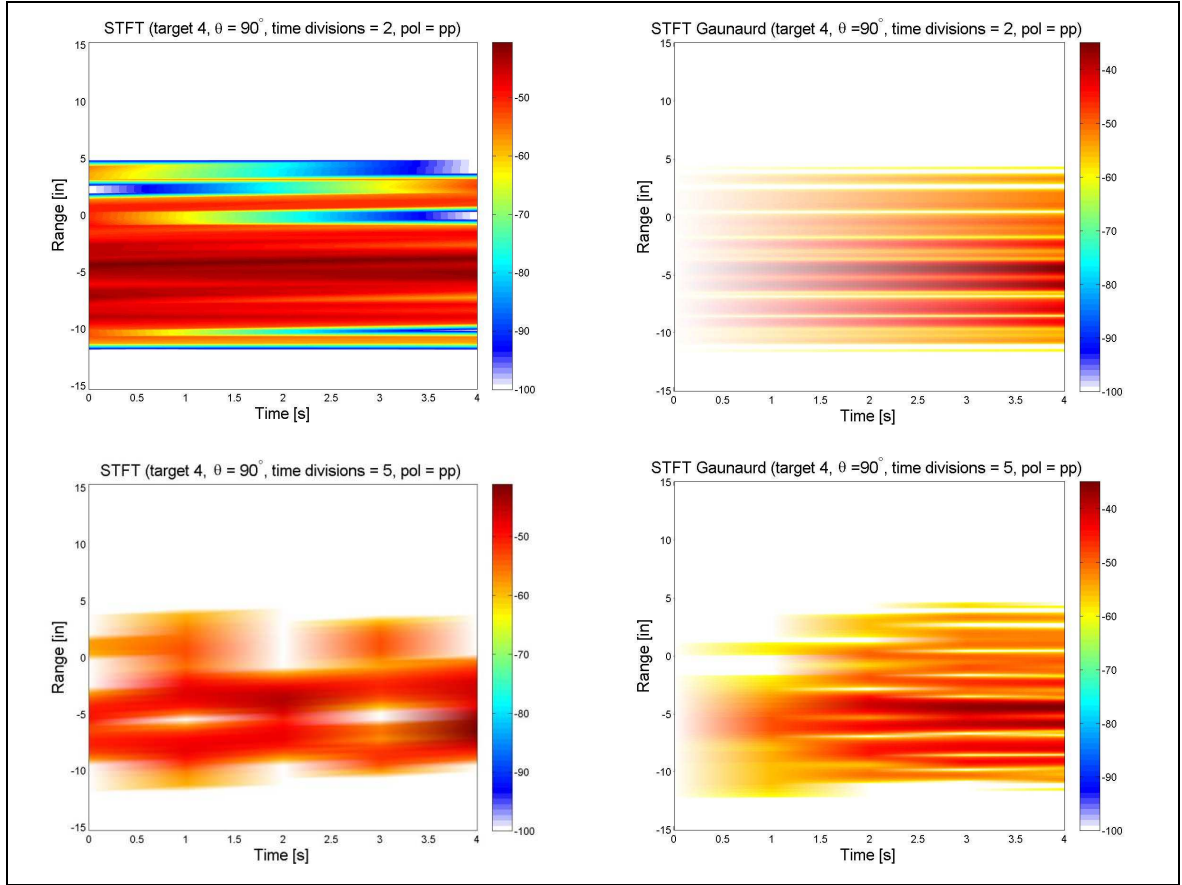
Figure H.8:   Target 4: Pol=PP, $\theta = 90°$, TFR's b.
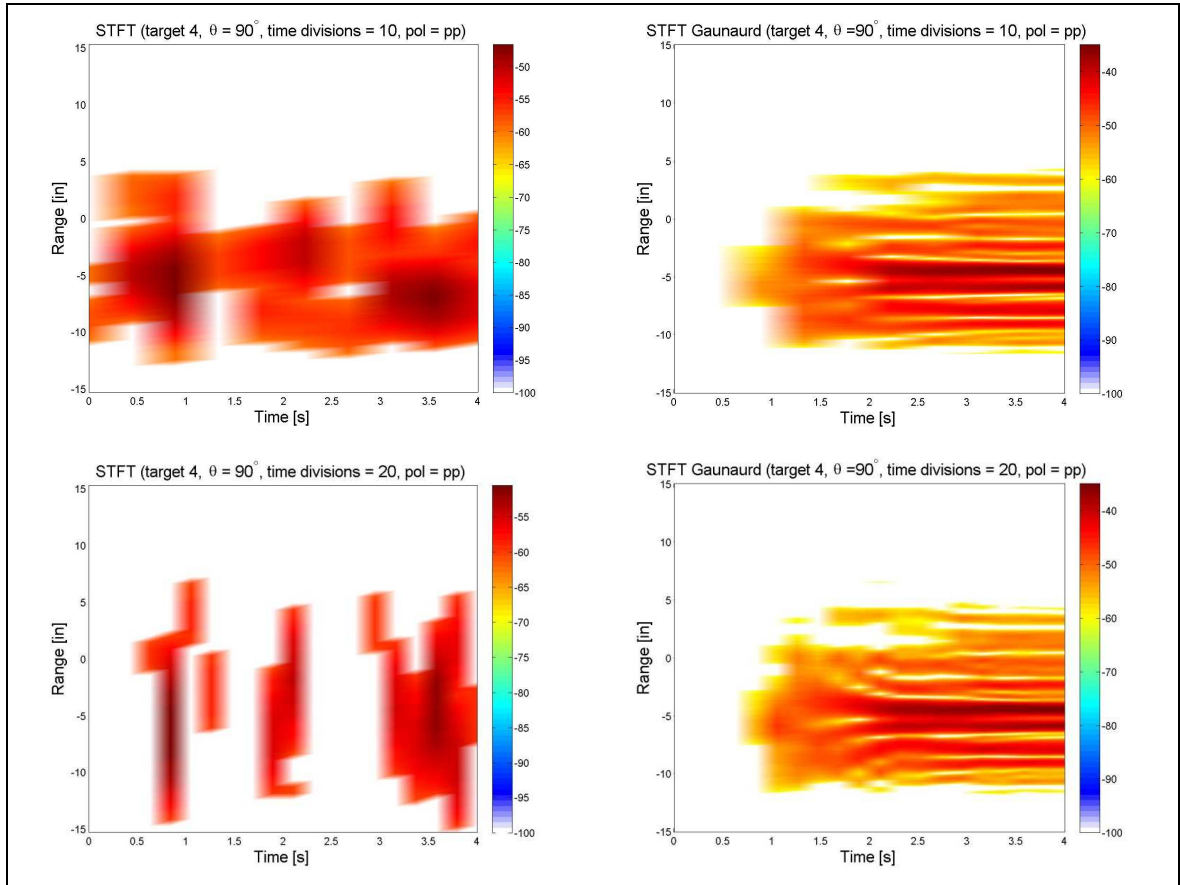
Figure H.9:   Target 4: Pol=PP, $\theta = 90°$, TFR's c.

8.3 Target 5 TT Results
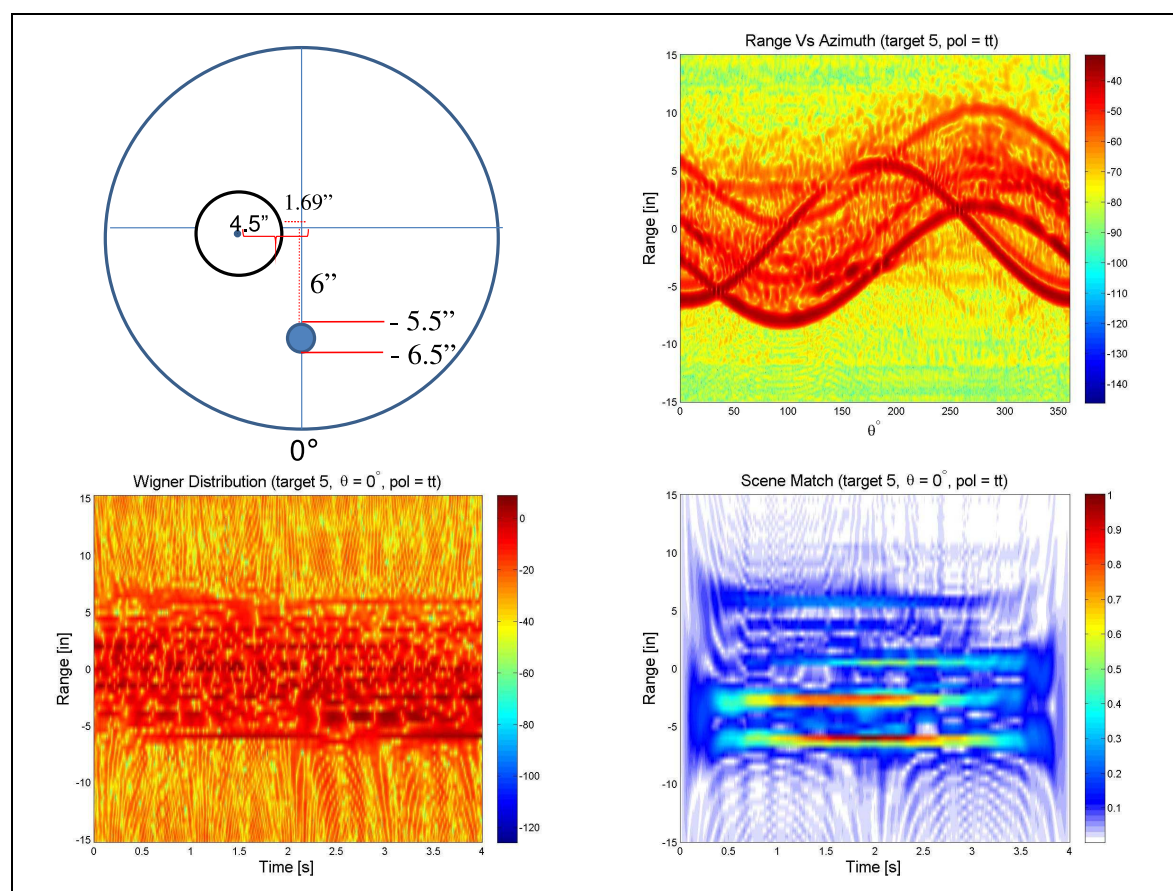
Figure H.10:   Target 5: Pol=TT, $\theta = 0°$, TFR's a.
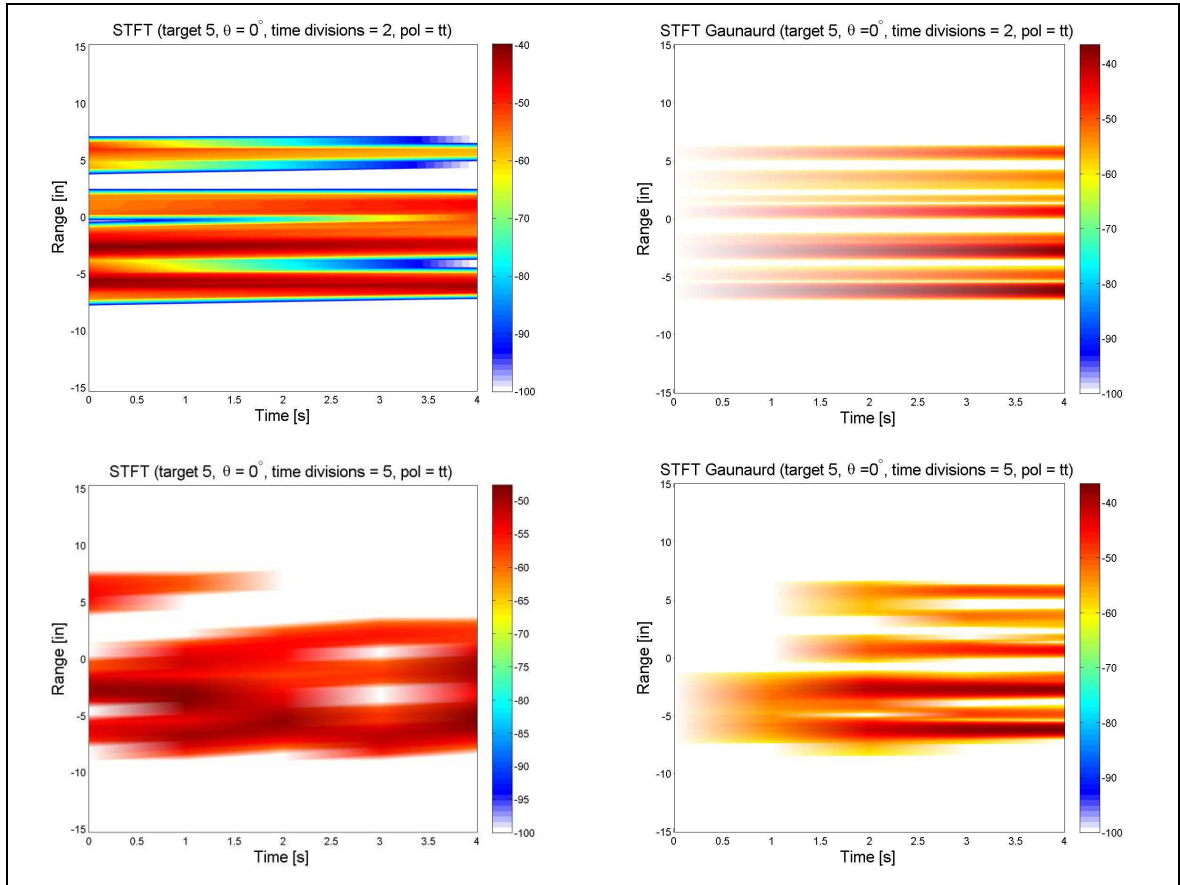
Figure H.11:   Target 5: Pol=TT, $\theta = 0°$, TFR's b.
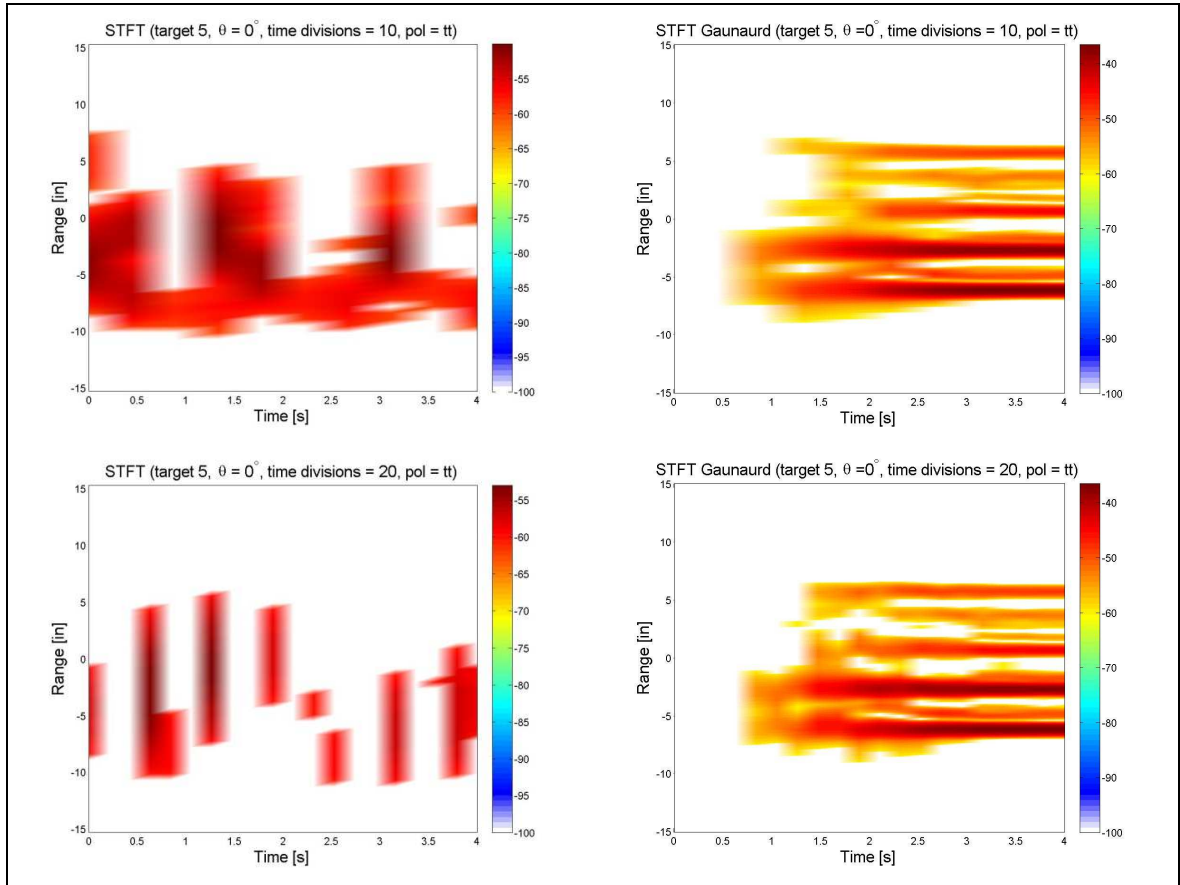
Figure H.12:   Target 5: Pol=TT, $\theta = 0°$, TFR's c.

8.4 Target 5 PP Results
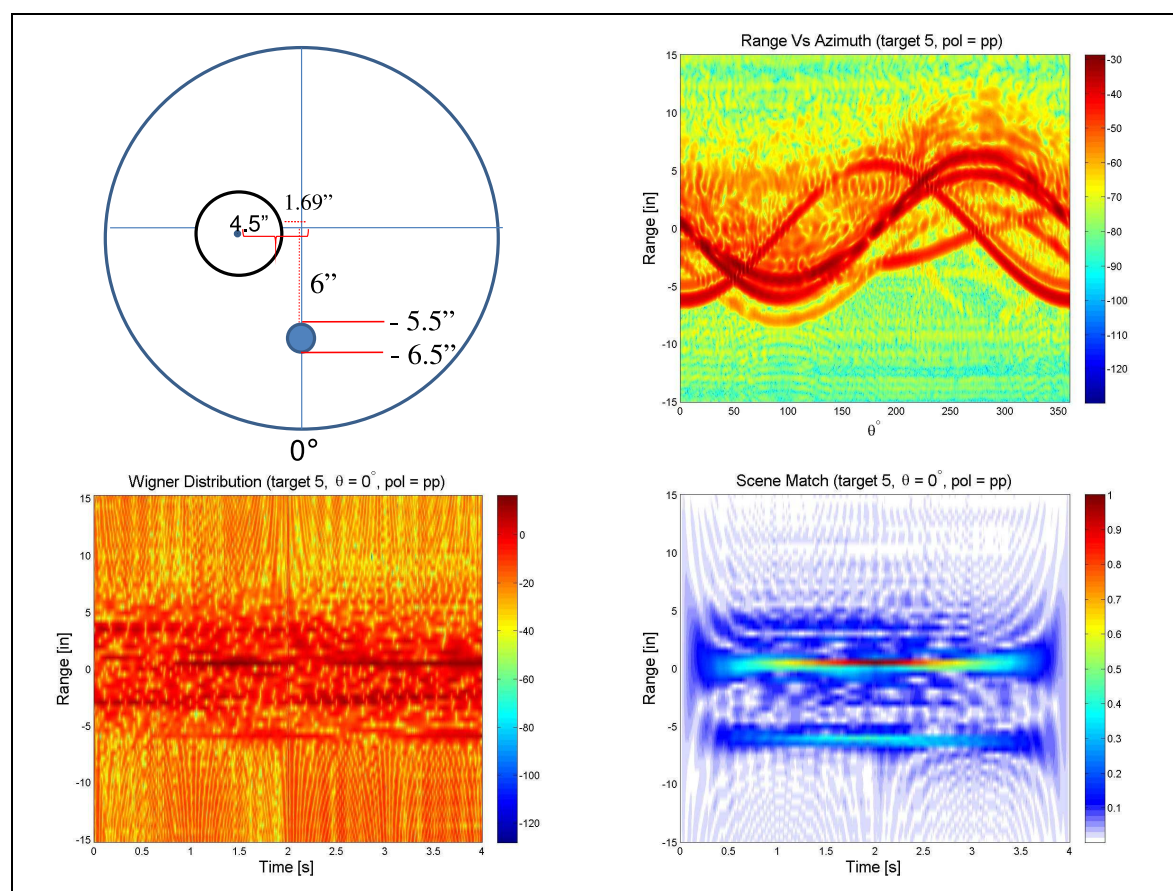
Figure H.13:   Target 5: Pol=PP, $\theta = 0°$, TFR's a.
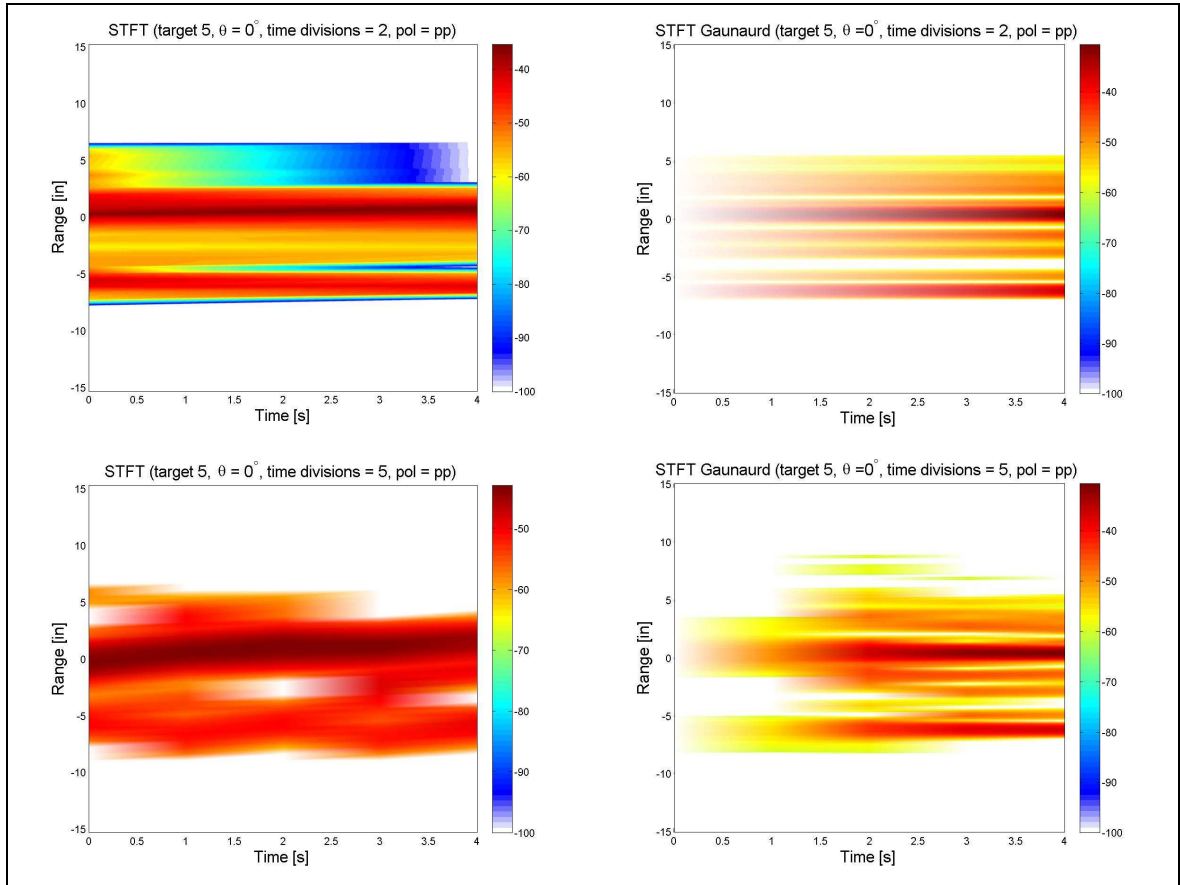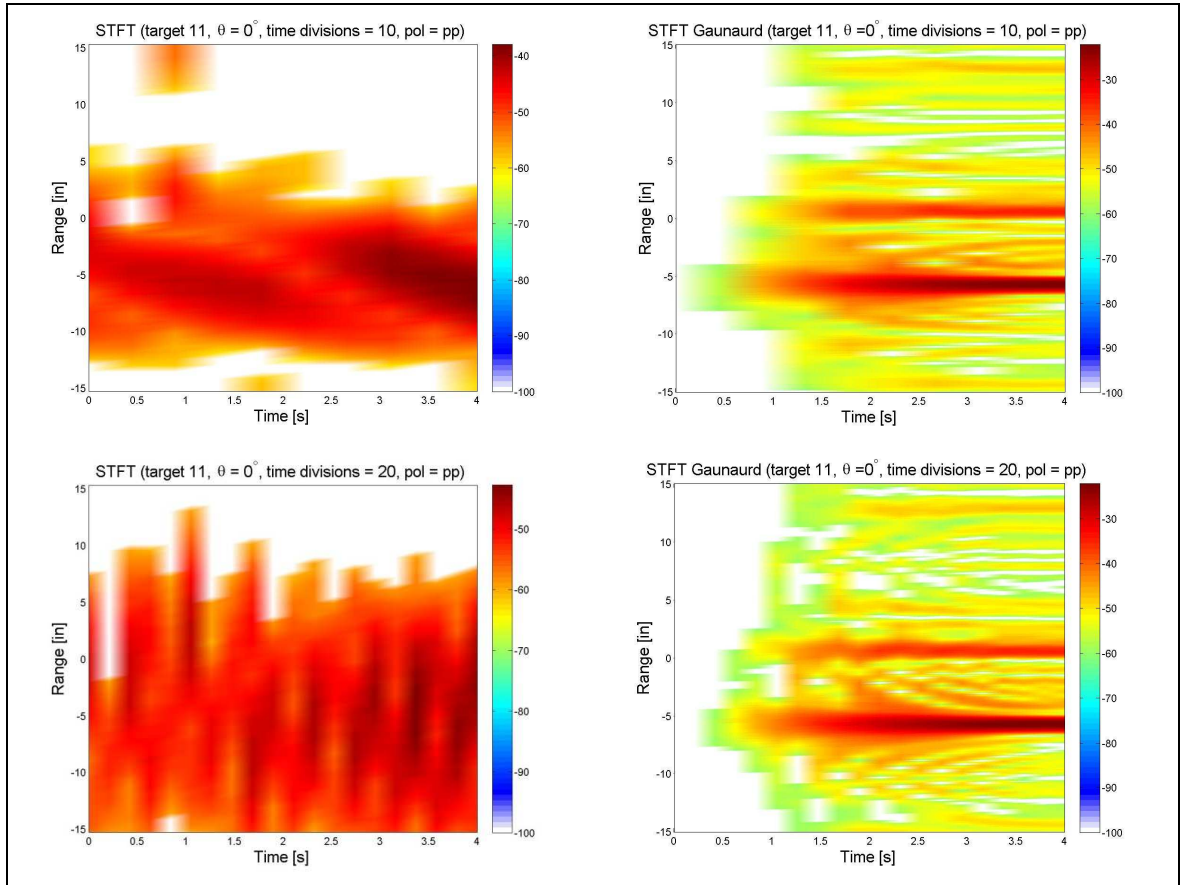
Figure H.14:   Target 5: Pol=PP, $\theta = 0°$, TFR's b.
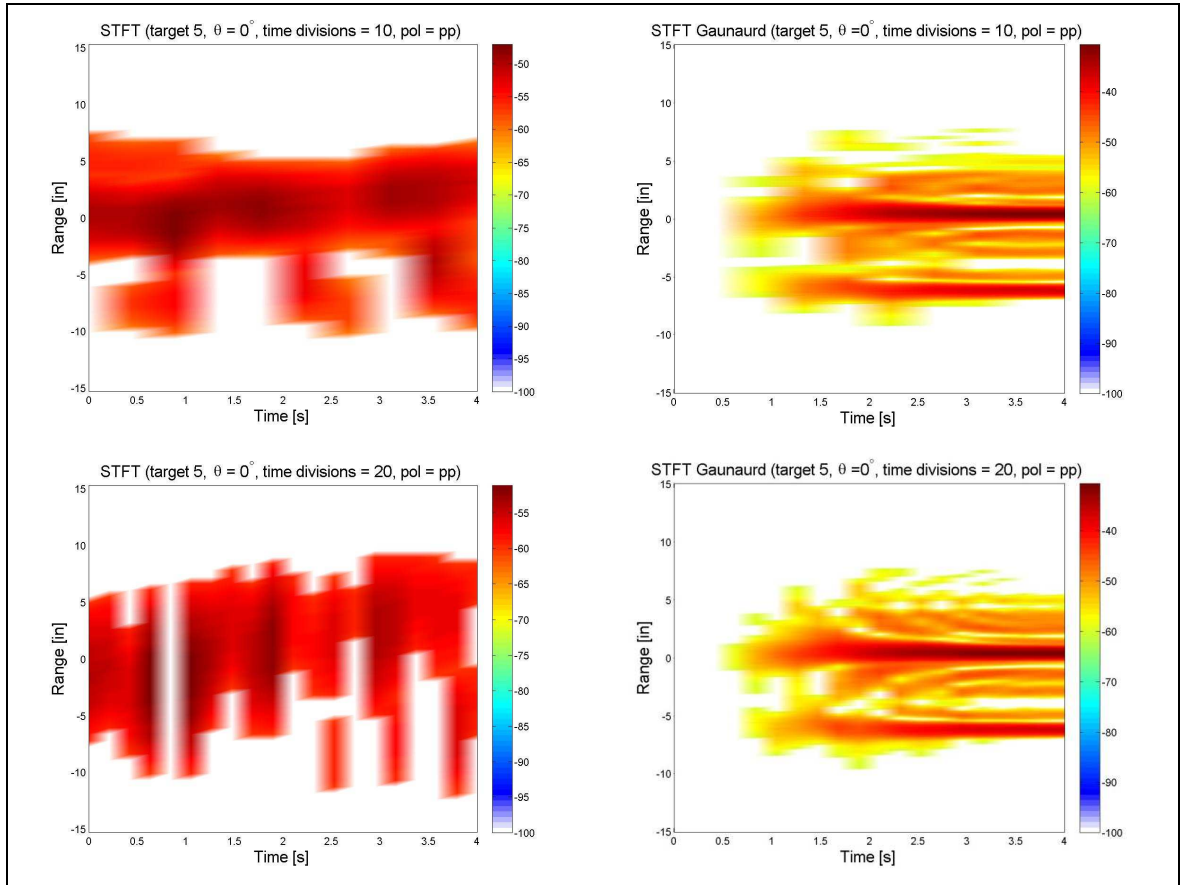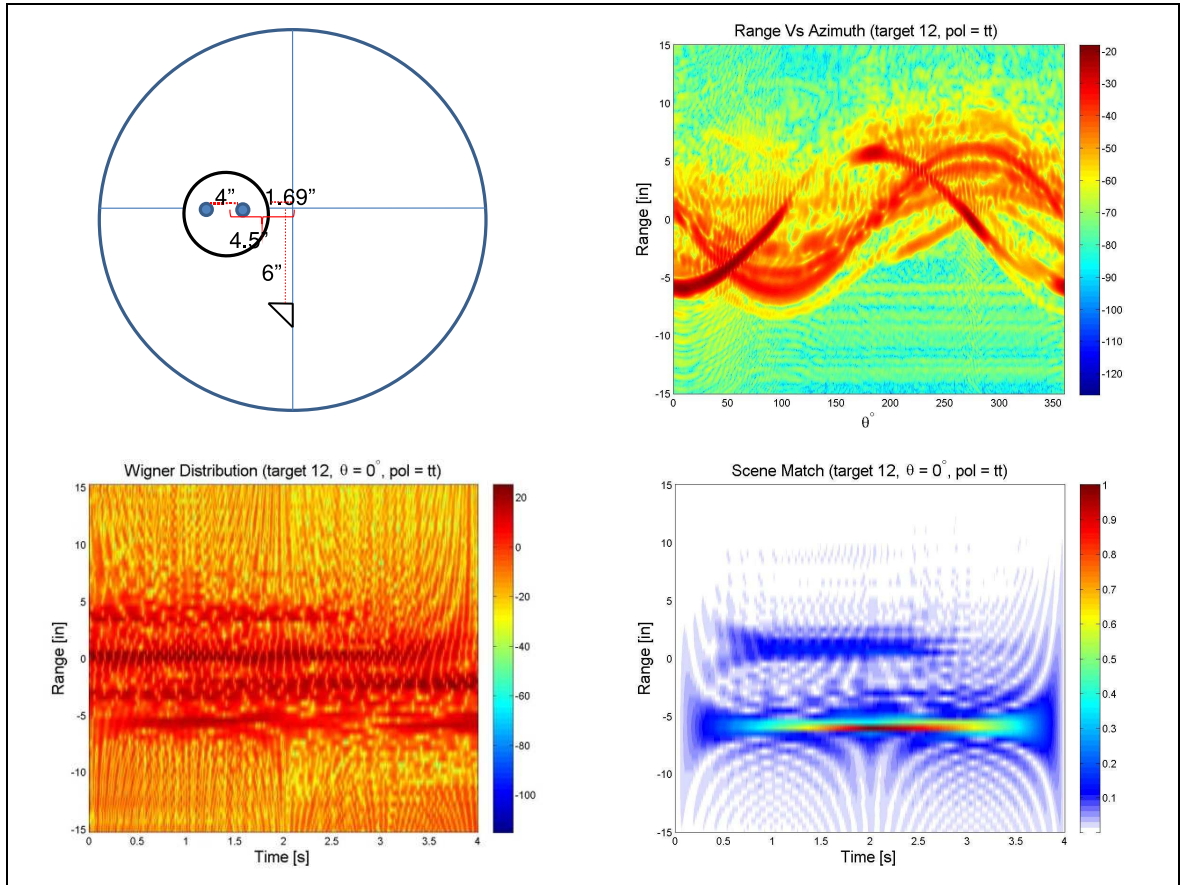
Figure H.15: Target 5: Pol=PP, $\theta = 0°$, TFR's c.

8.5   Target 6 TT Results
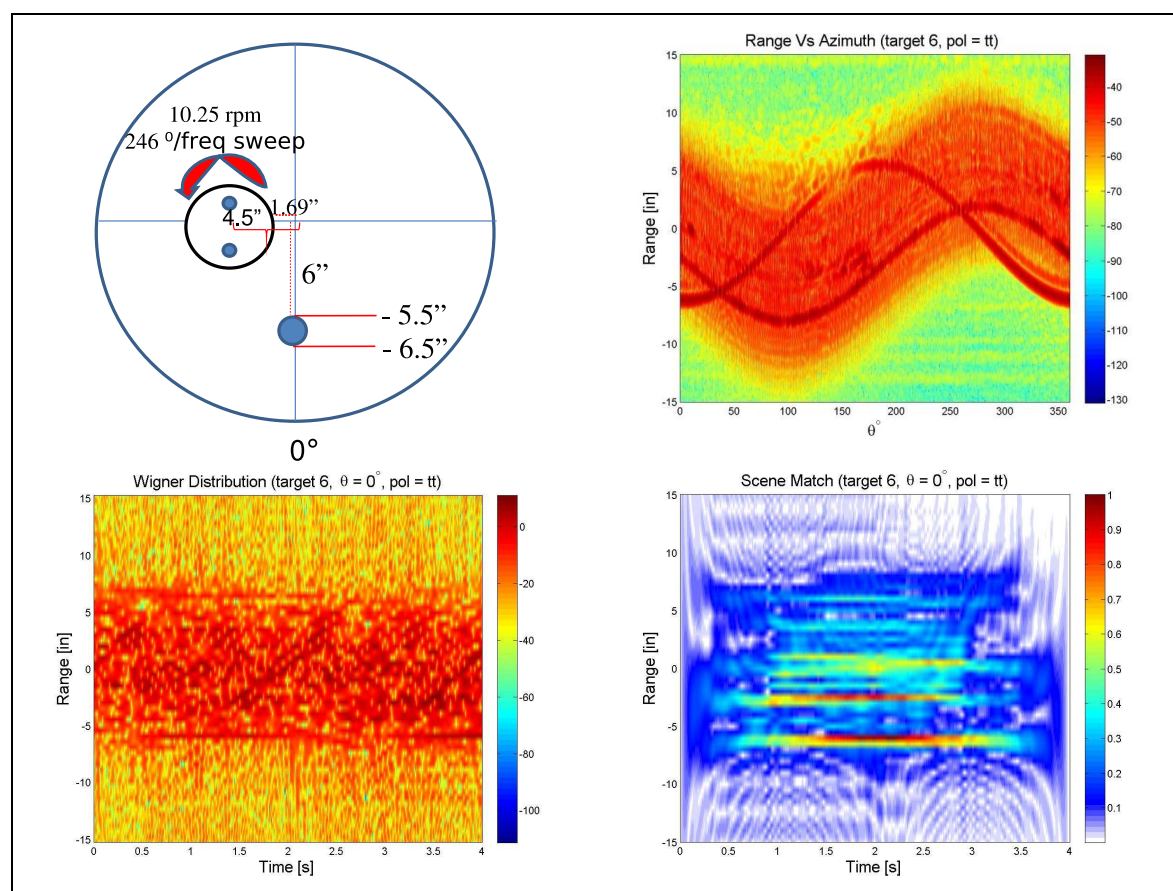
Figure H.16:   Target 6: Pol=TT, $\theta = 0°$, TFR's a.
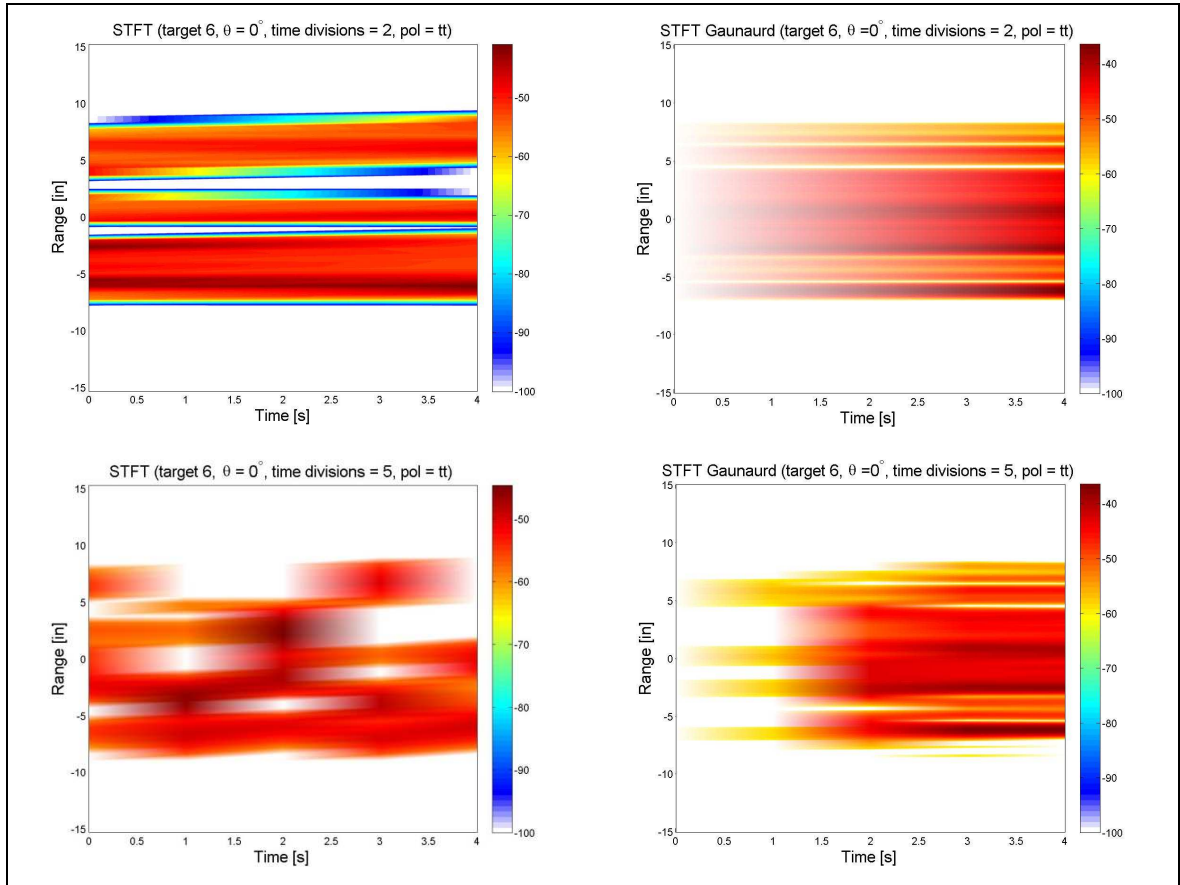
Figure H.17:   Target 6: Pol=TT, $\theta = 0°$, TFR's b.
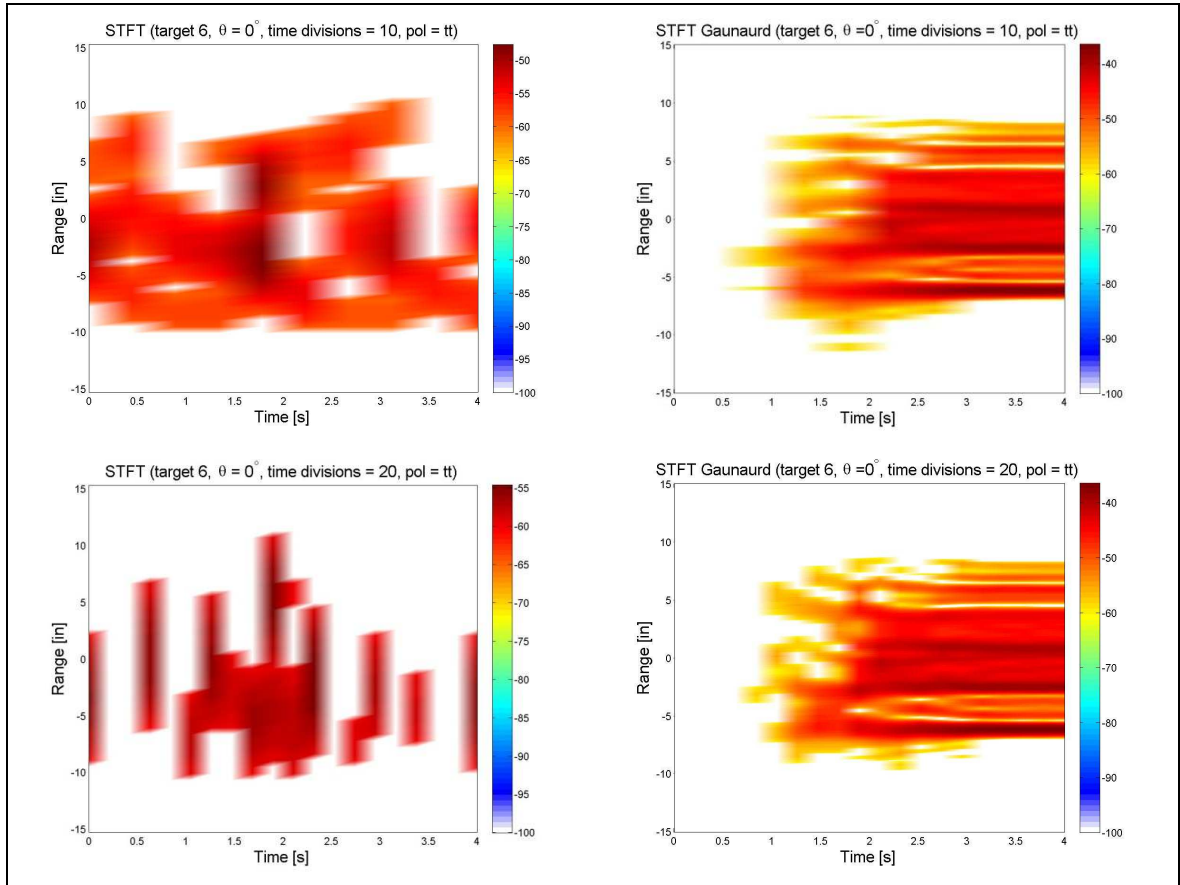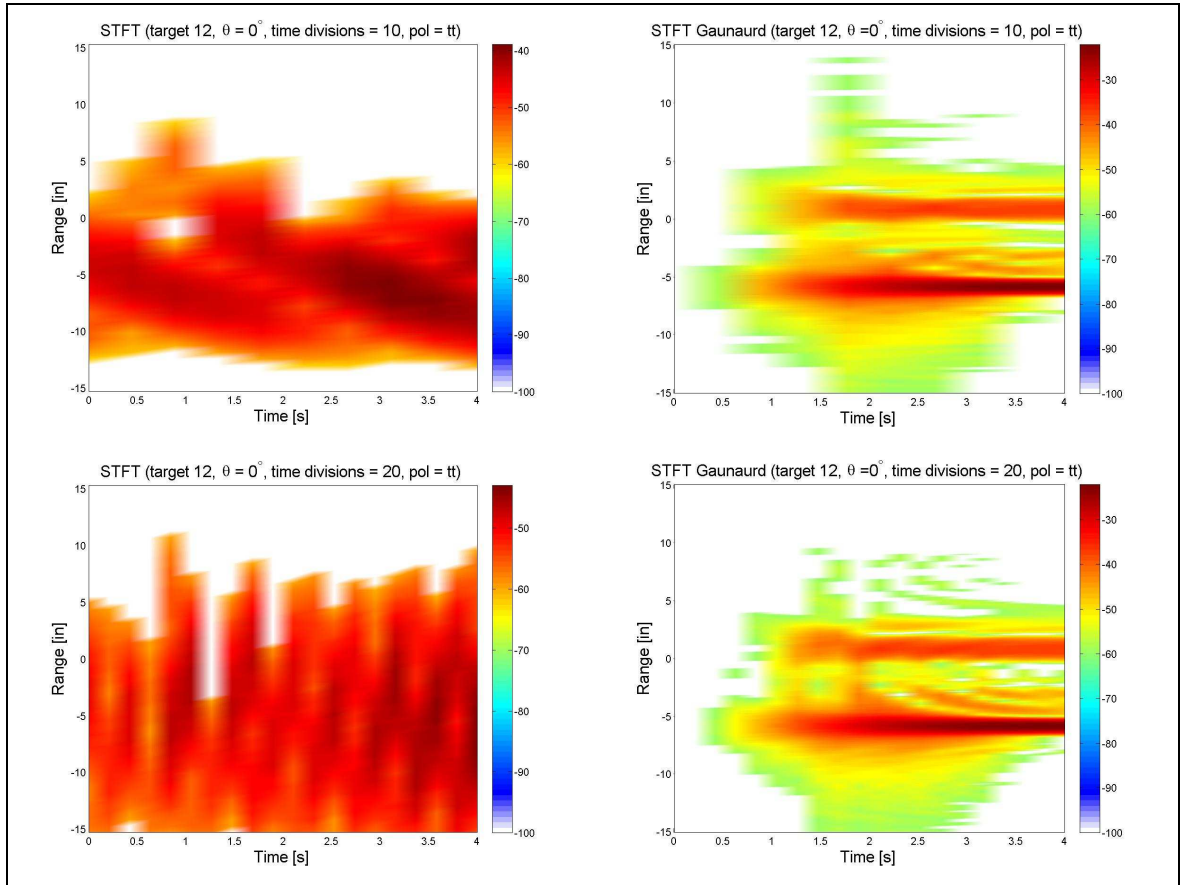
Figure H.18:   Target 6: Pol=TT, $\theta = 0°$, TFR's c.

8.6 Target 6 PP Results
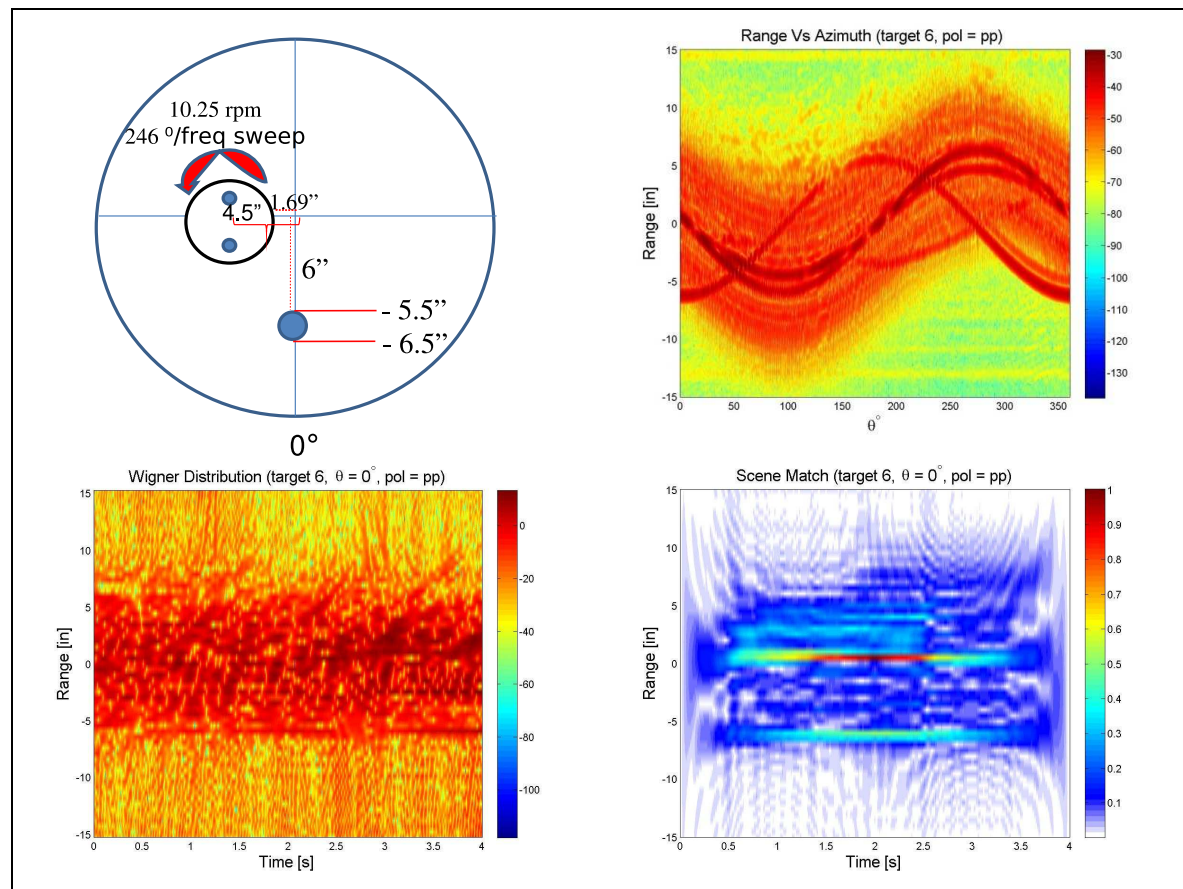
Figure H.19:   Target 6: Pol=PP, $\theta = 0°$, TFR's a.
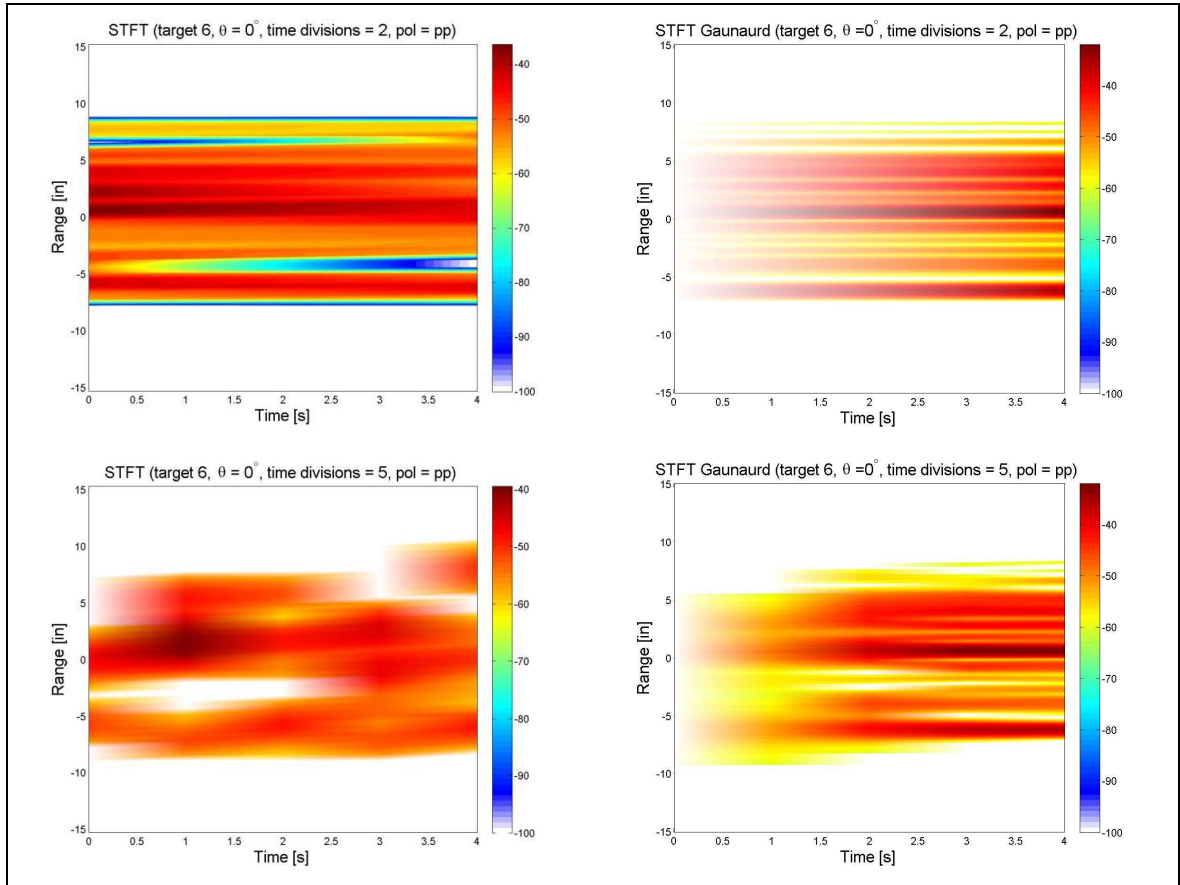
Figure H.20:   Target 6: Pol=PP, $\theta = 0°$, TFR's b.
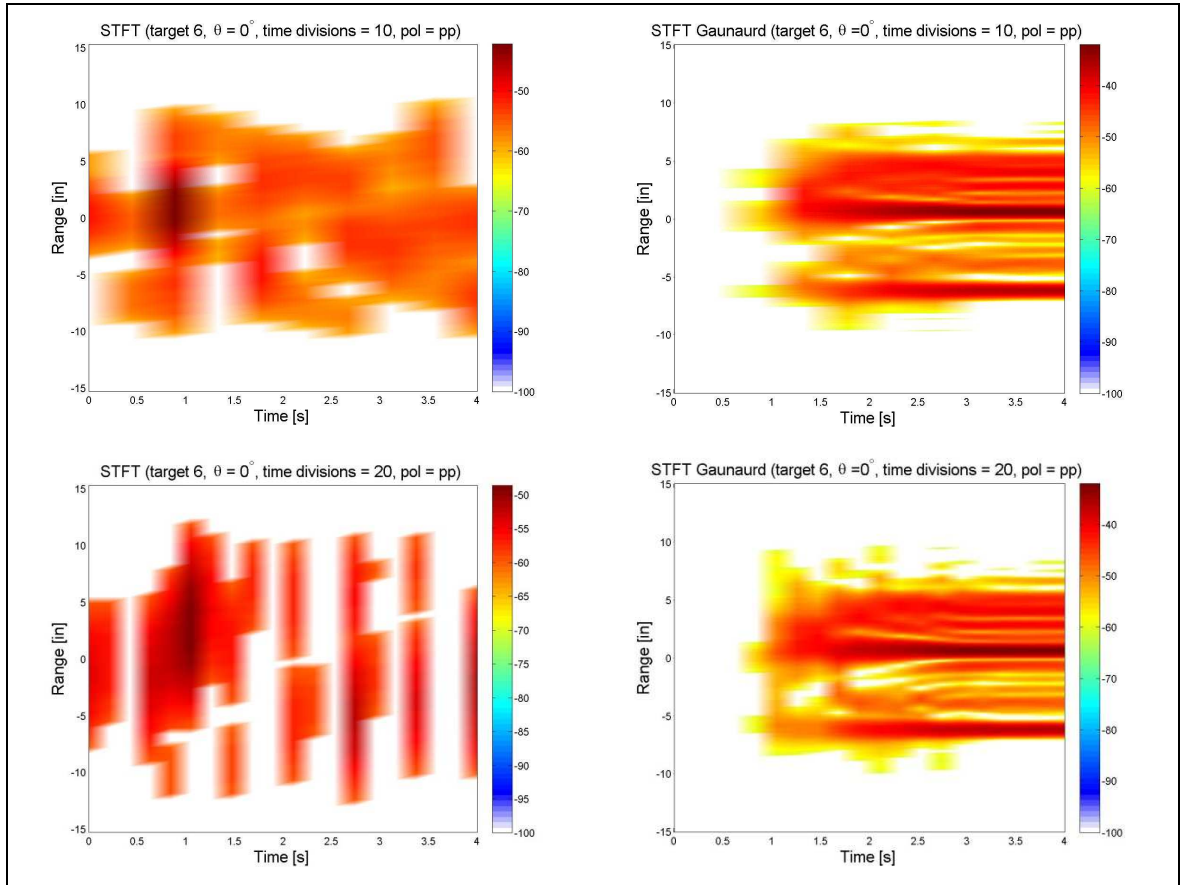
Figure H.21:   Target 6: Pol=PP, $\theta = 0°$, TFR's c.

8.7 Target 7 TT Results
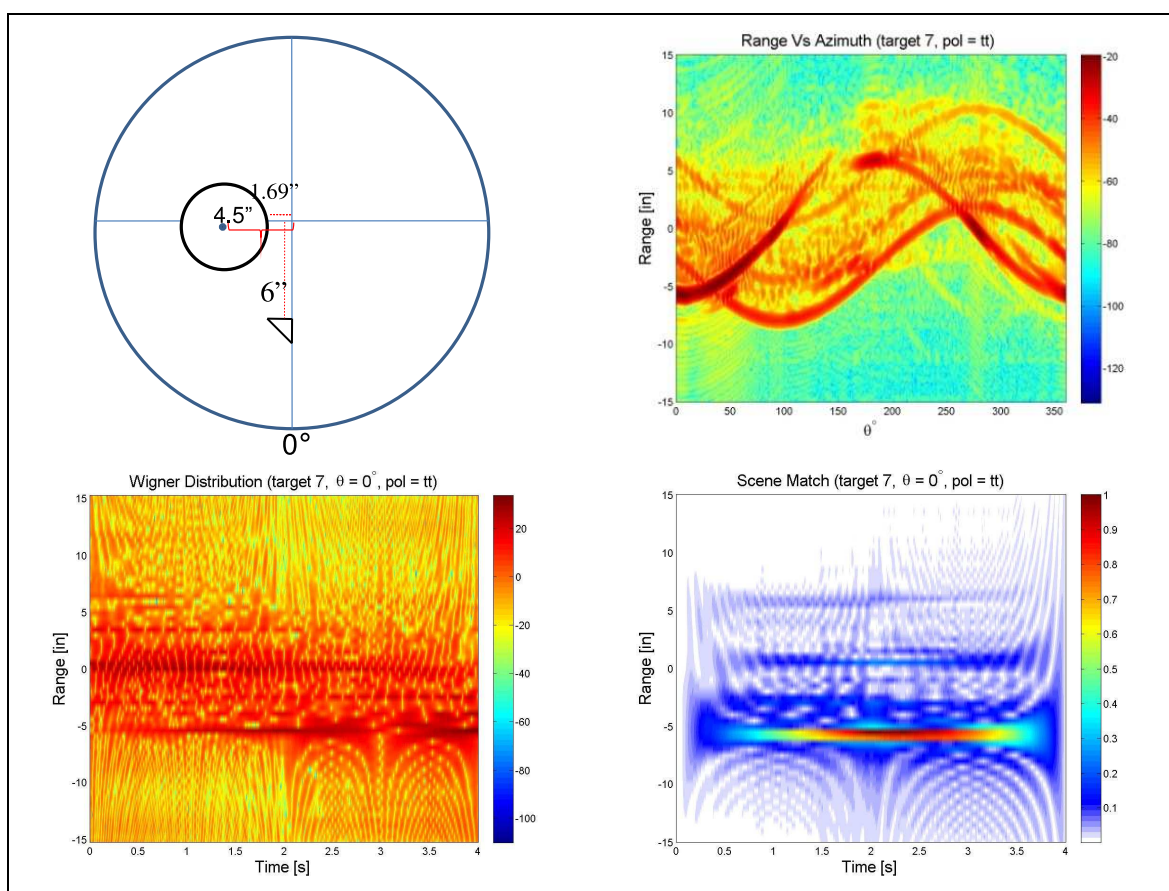
Figure H.22:   Target 7: Pol=TT, $\theta = 0°$, TFR's a.
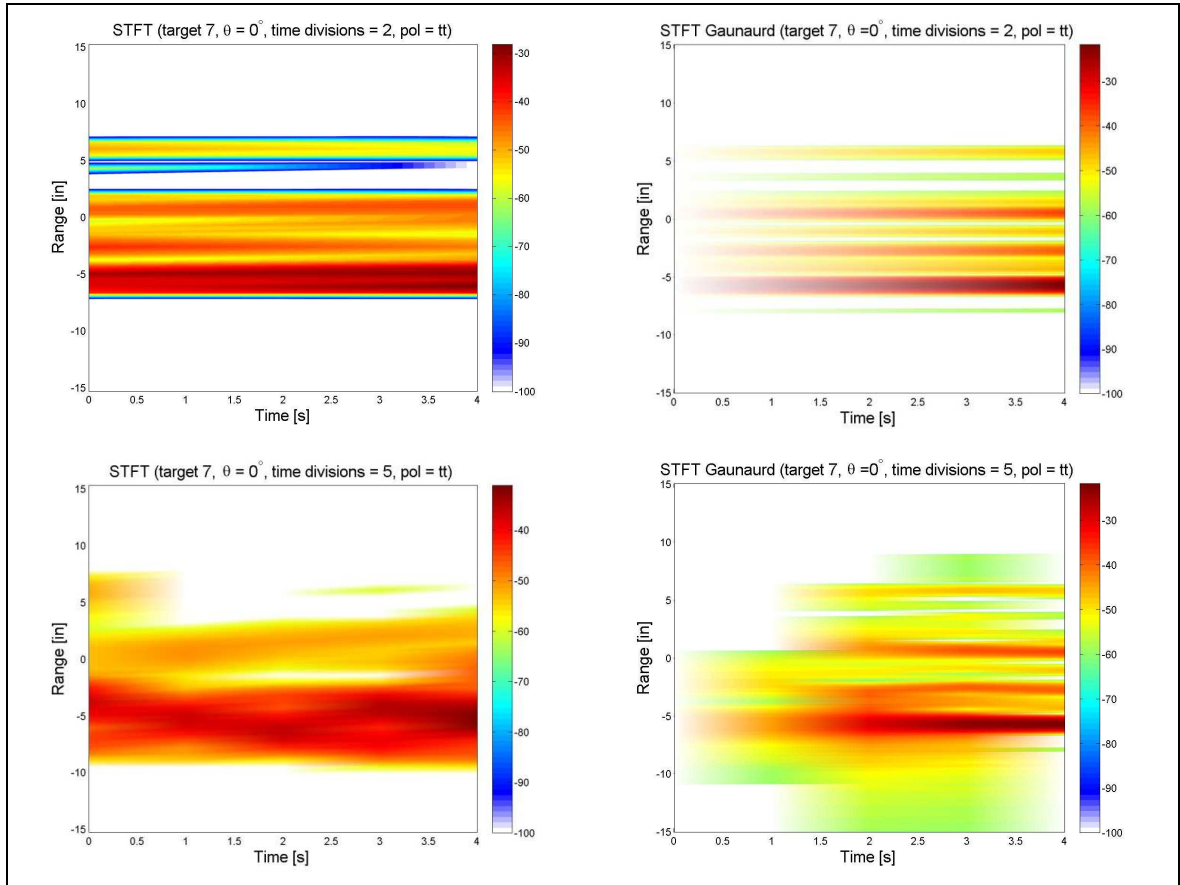
Figure H.23:   Target 7: Pol=TT, $\theta = 0°$, TFR's b.
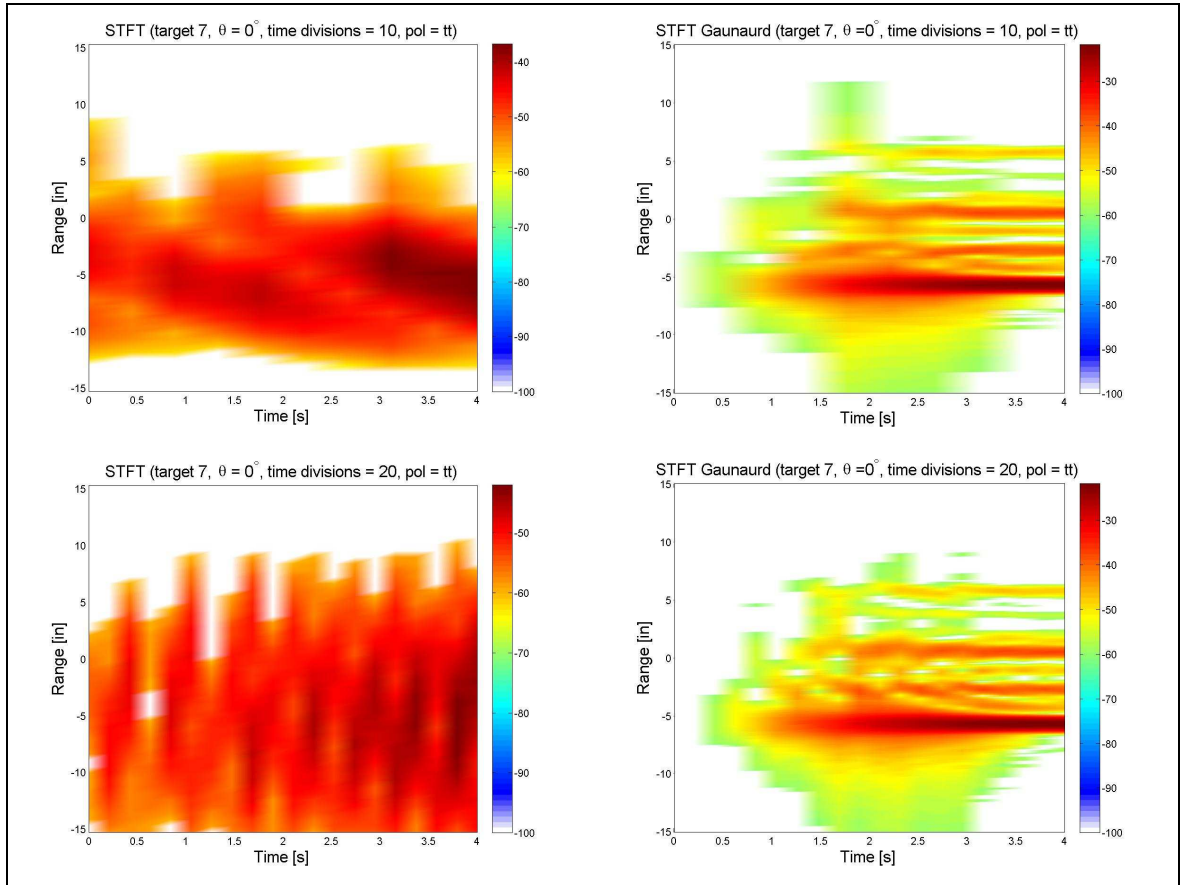
Figure H.24:   Target 7: Pol=TT, $\theta = 0°$, TFR's c.

8.8   Target 7 PP Results
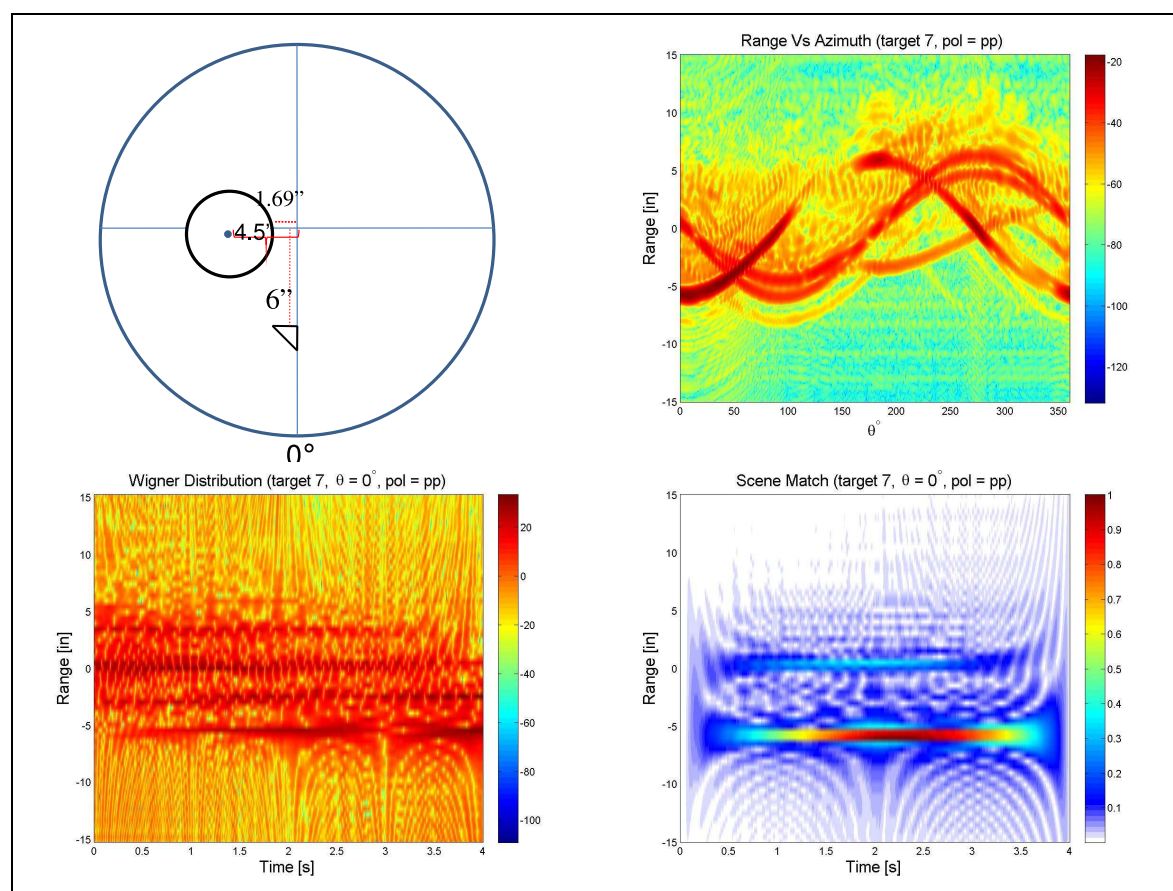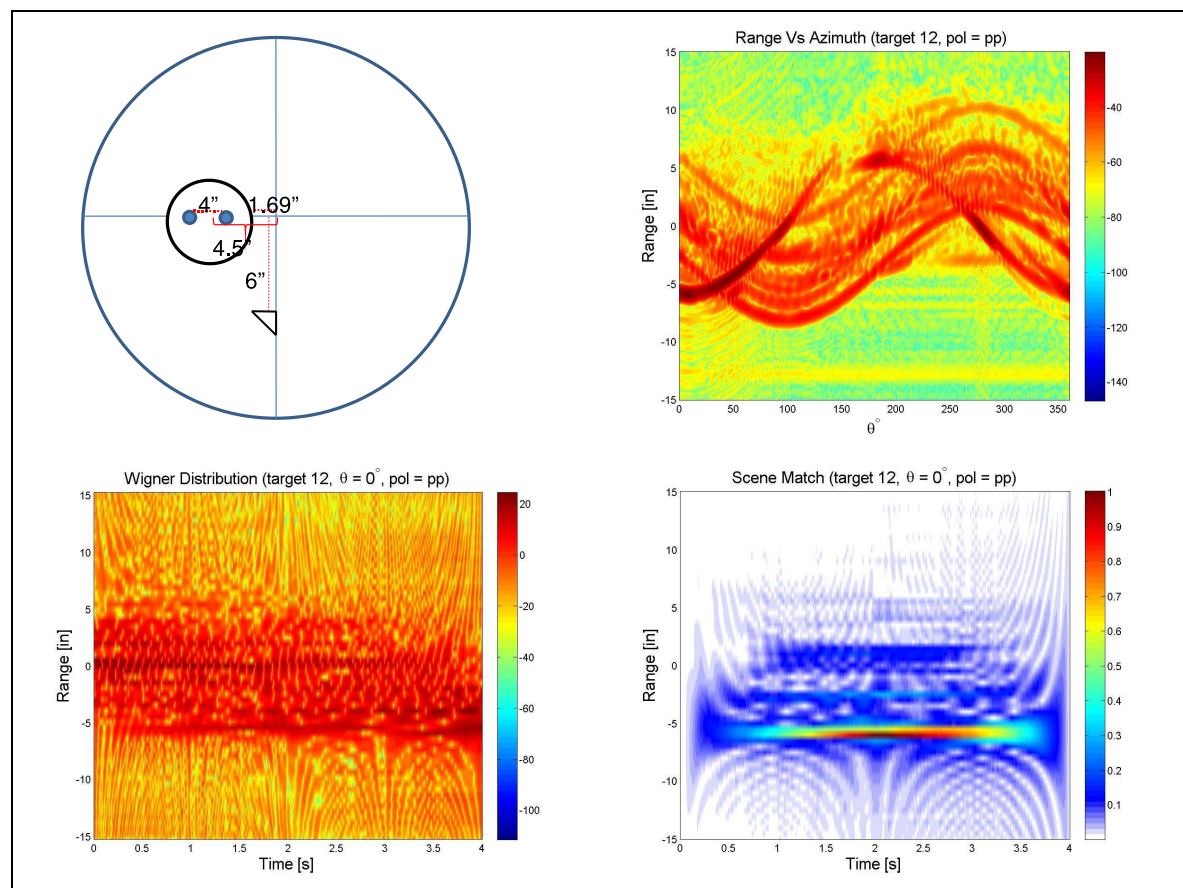

Figure H.25:   Target 7: Pol=PP, $\theta = 0°$, TFR's a.
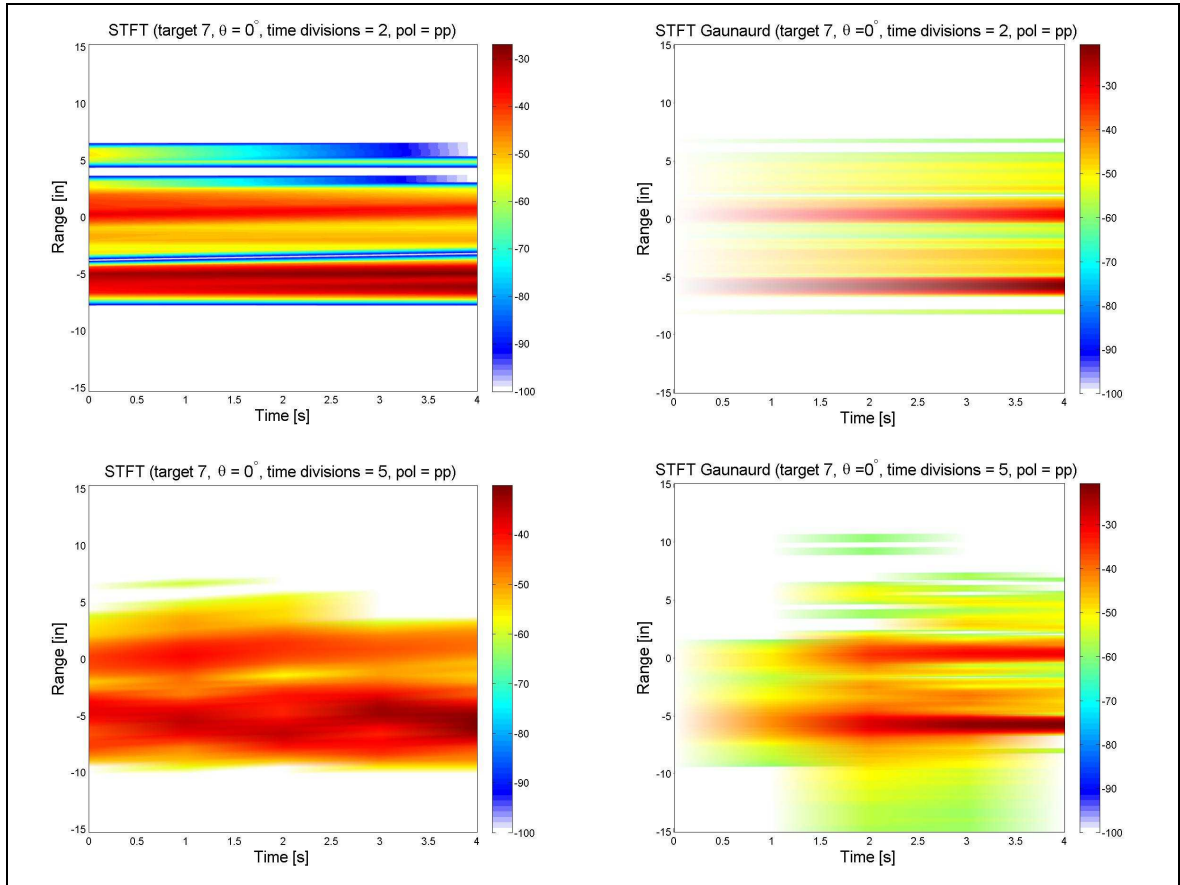
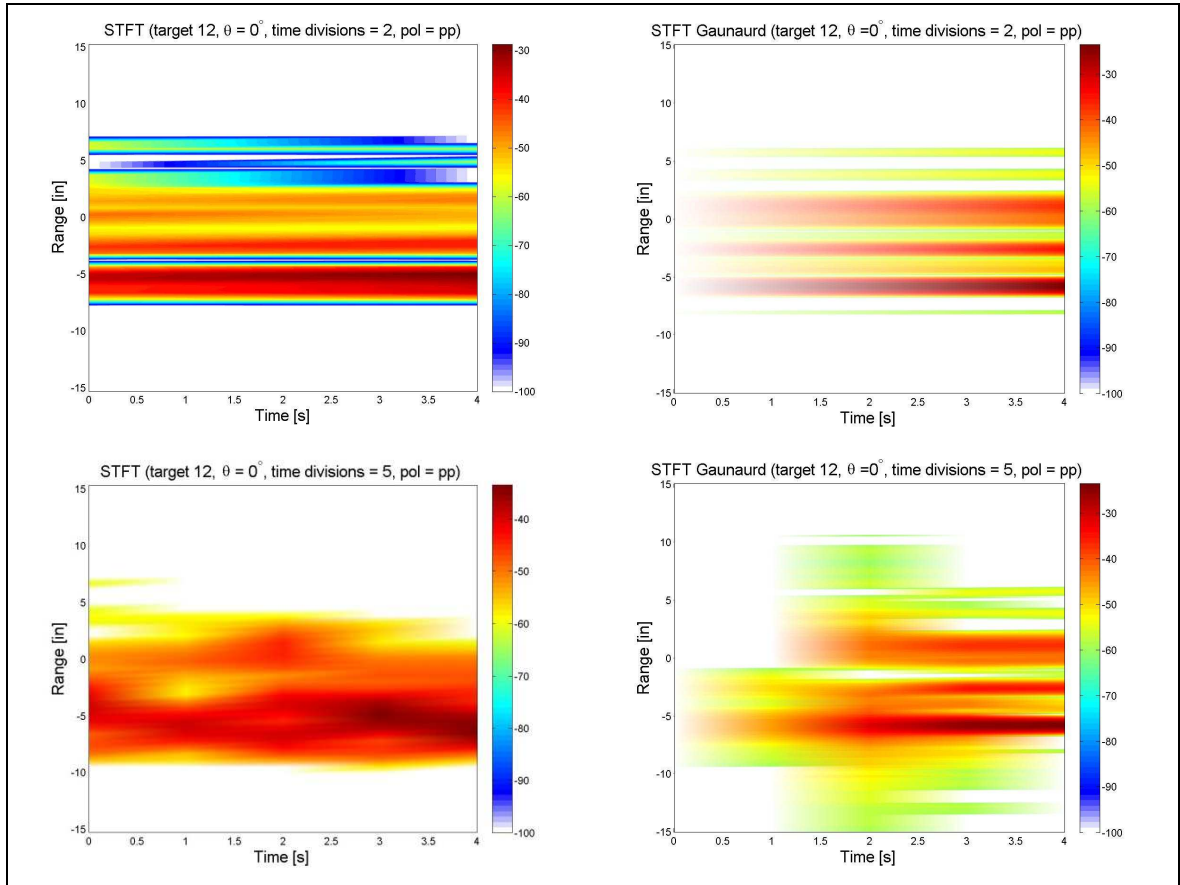Figure H.26:   Target 7: Pol=PP, $\theta = 0°$, TFR's b.
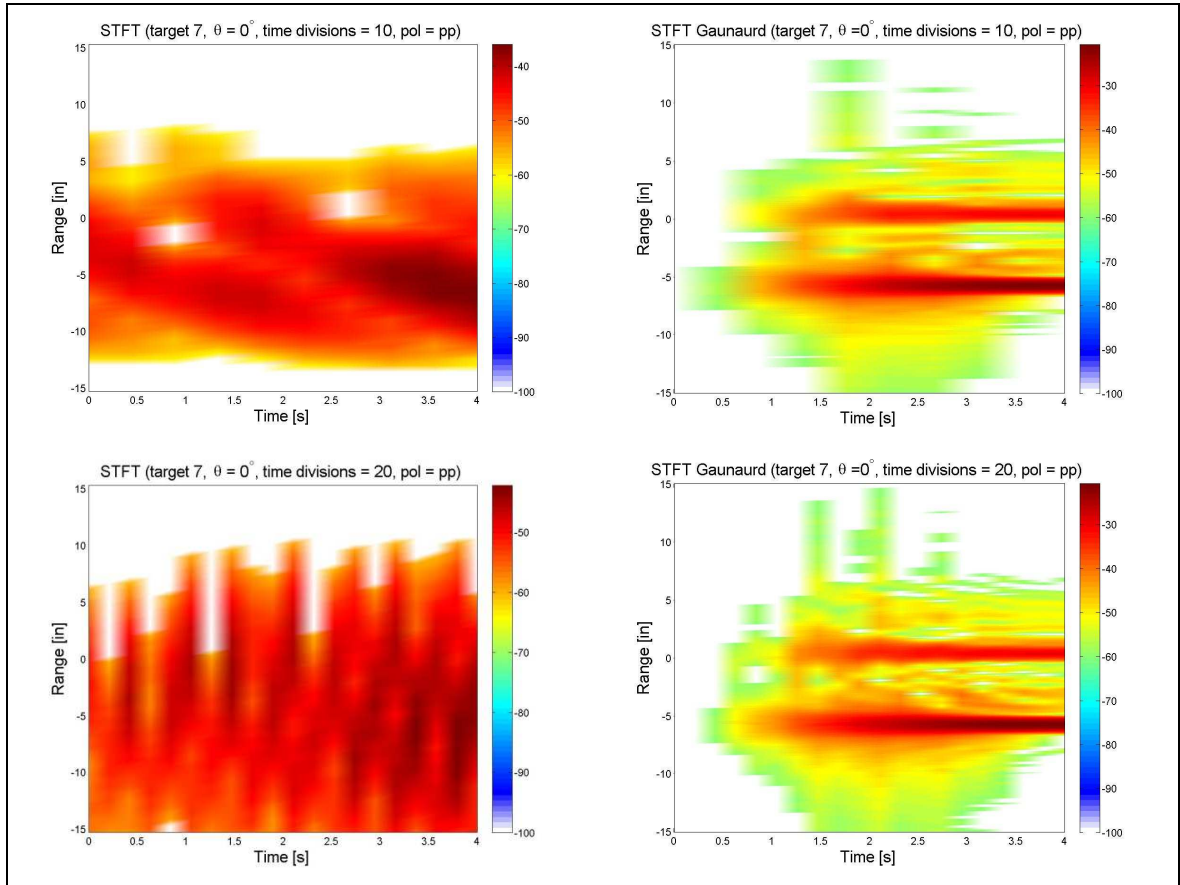
Figure H.27:   Target 7: Pol=PP, $\theta = 0°$, TFR's c.

8.9 Target 8 PP Results
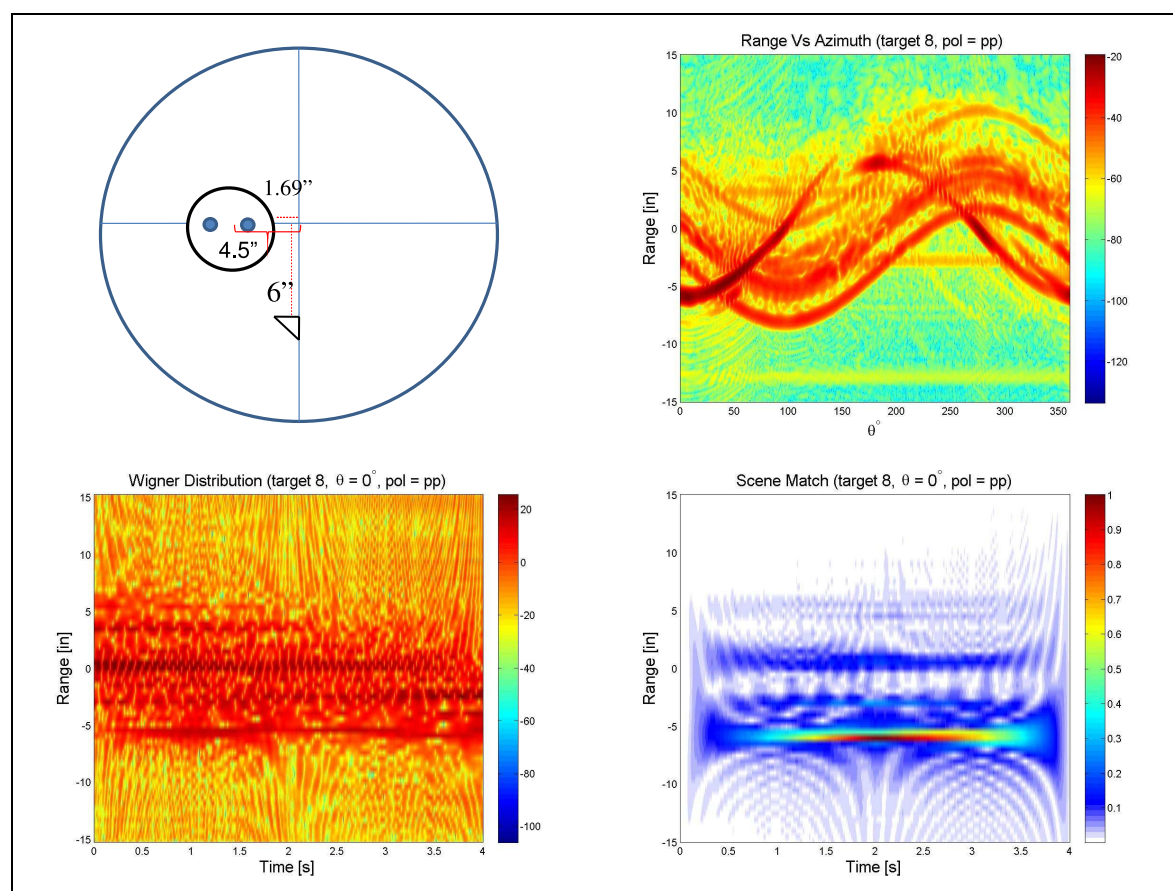
Figure H.28:   Target 8: Pol=PP, $\theta = 0°$, TFR's a.
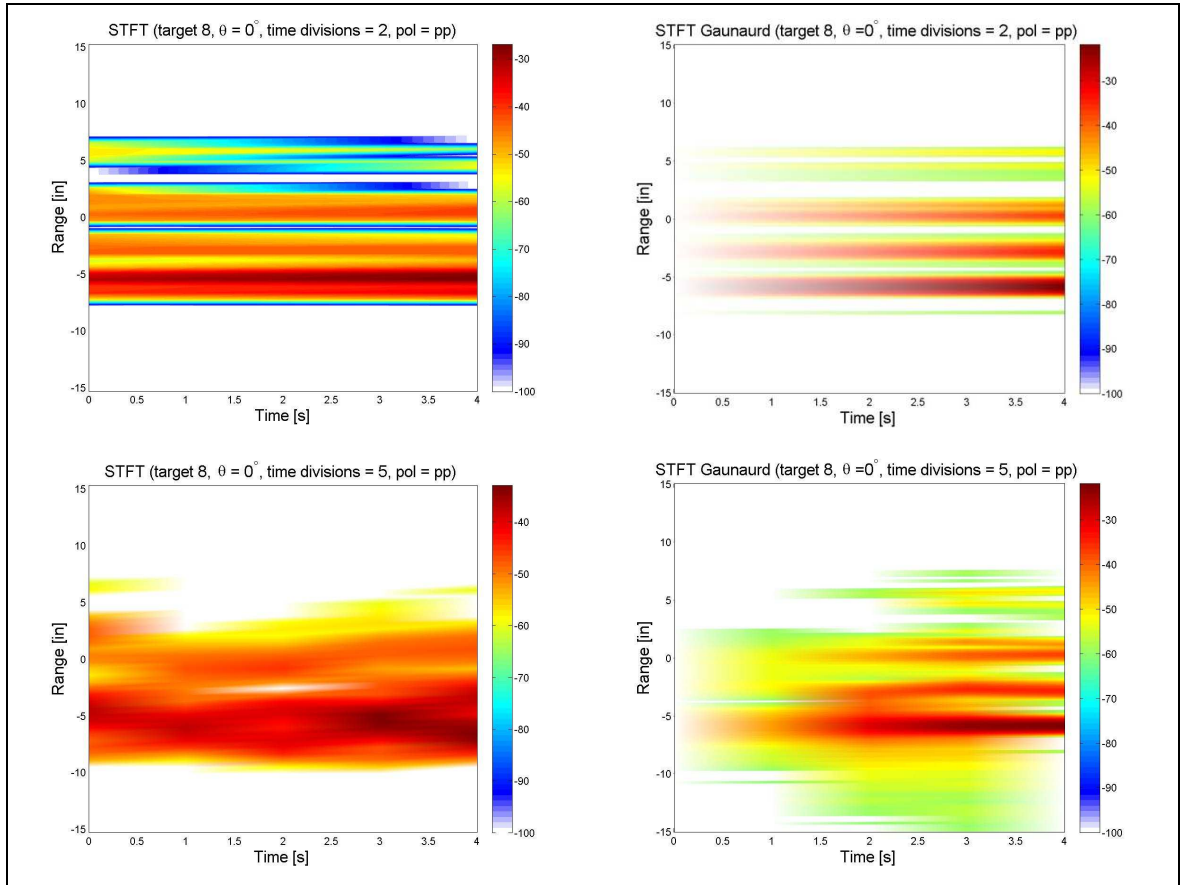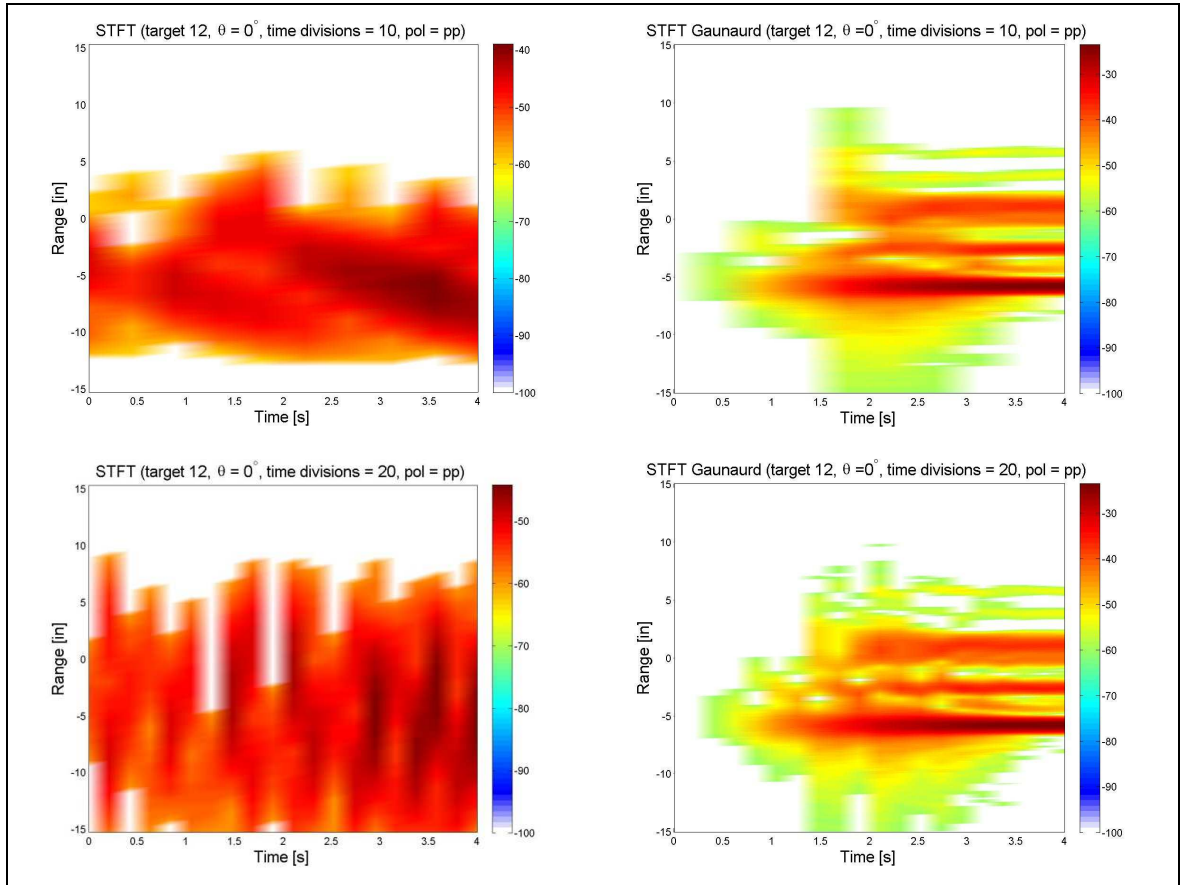
Figure H.29:   Target 8: Pol=PP, $\theta = 0°$, TFR's b.
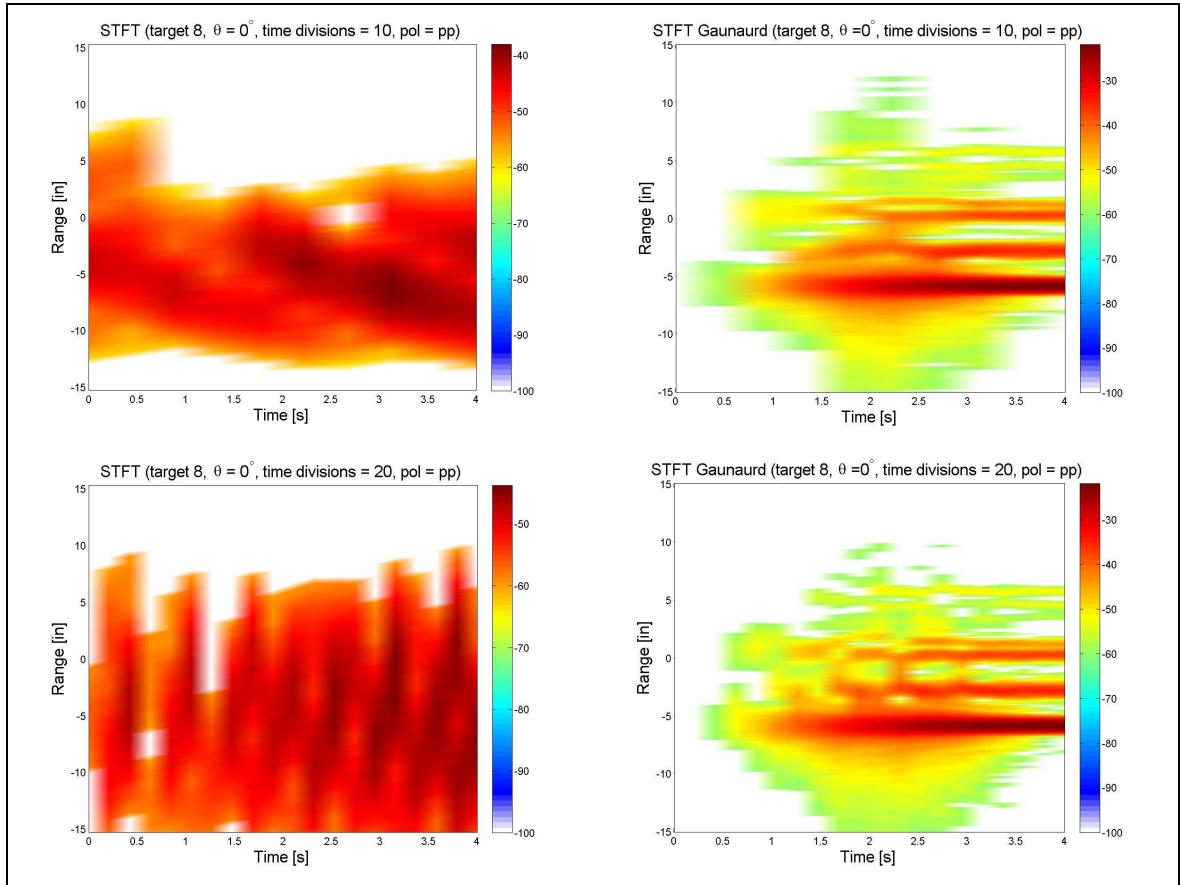
Figure H.30:   Target 8: Pol=PP, $\theta = 0°$, TFR's c.

8.10   Target 9 PP Results
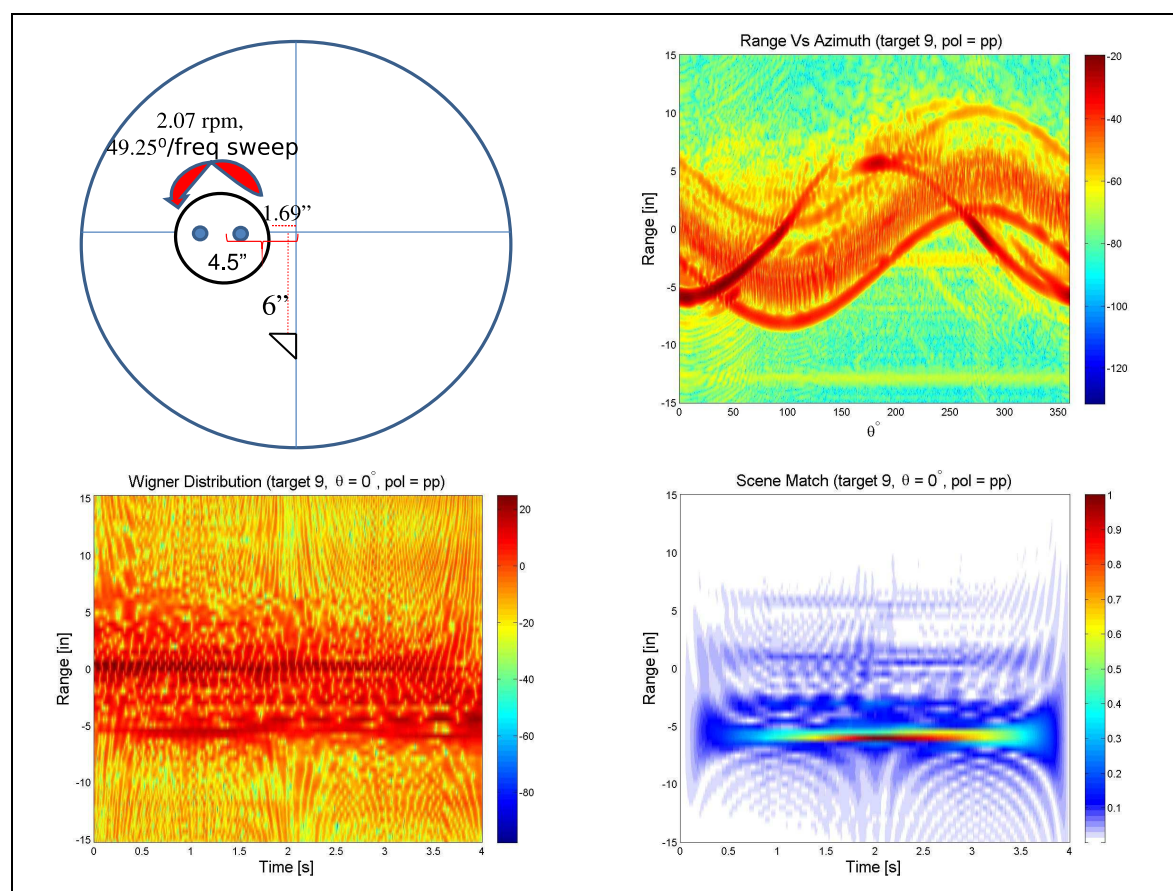
Figure H.31:   Target 9: Pol=PP, $\theta = 0°$, TFR's a.

8.11 Target 10 PP Results
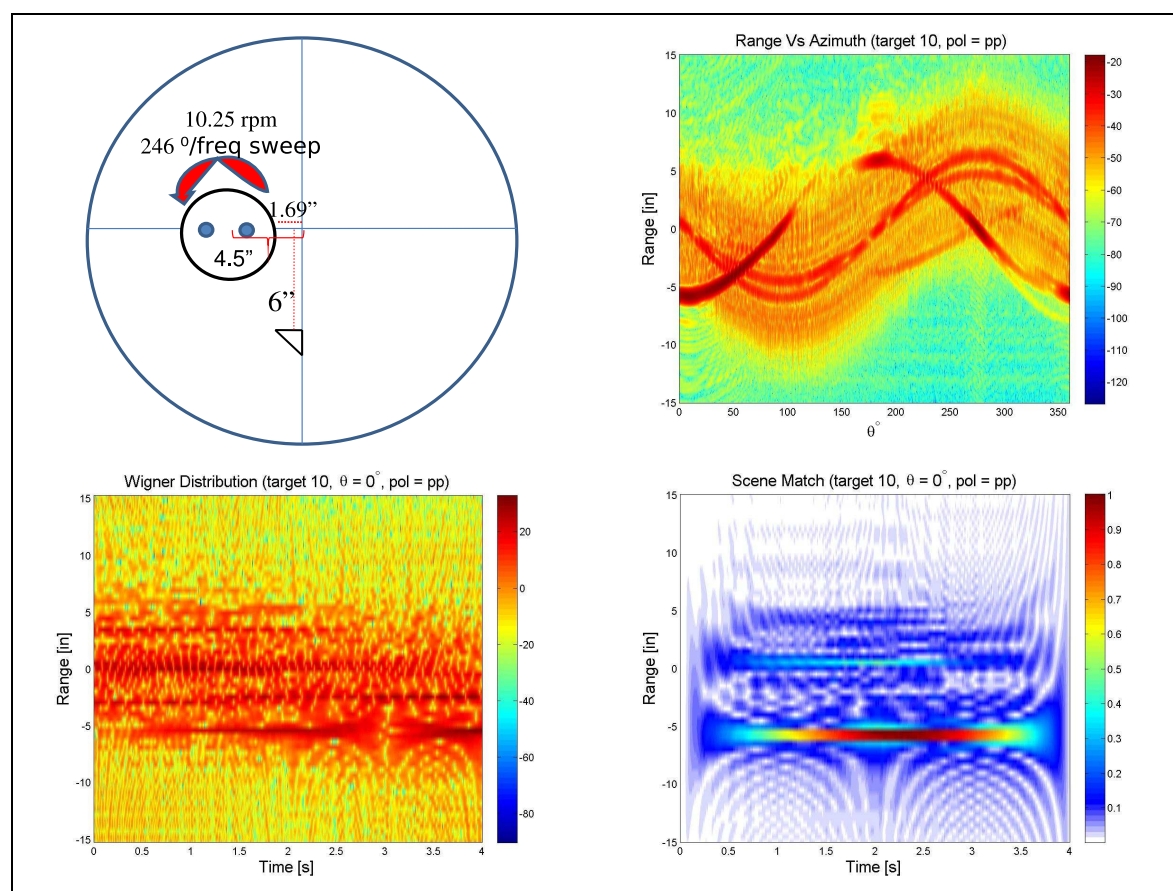
Figure H.32:   Target 10: Pol=PP, $\theta = 0°$, TFR's a.
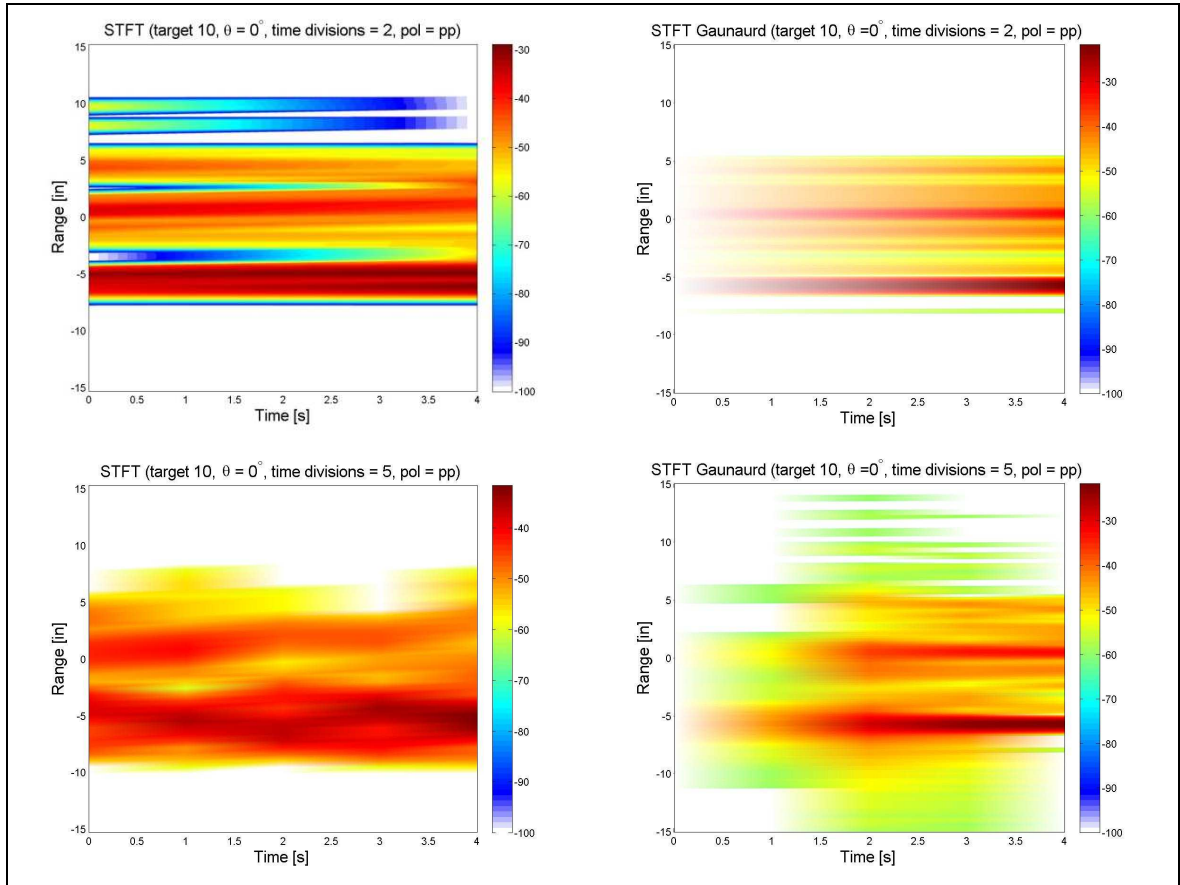
Figure H.33:   Target 10: Pol=PP, $\theta = 0°$, TFR's b.
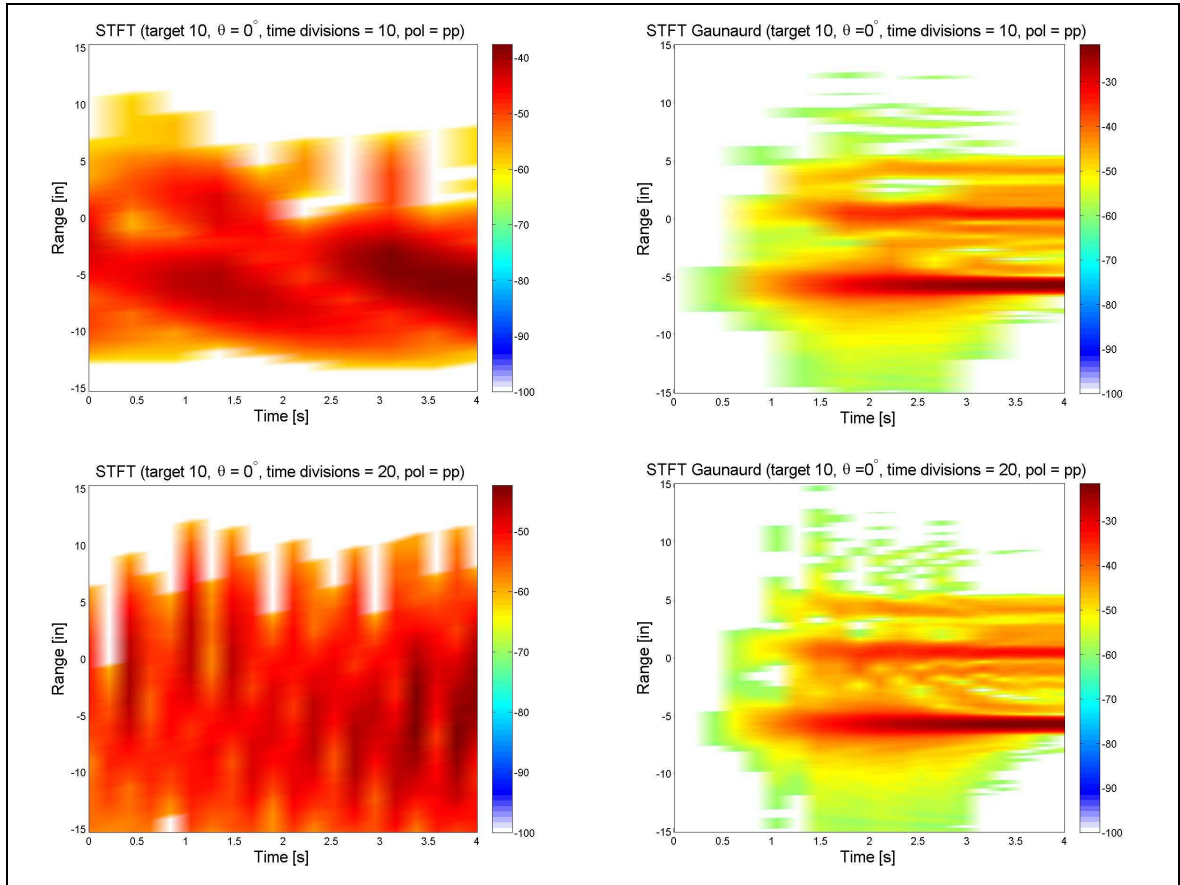
Figure H.34:　　Target 10: Pol=PP, $\theta = 0°$, TFR's c.

8.12 Target 11 PP Results
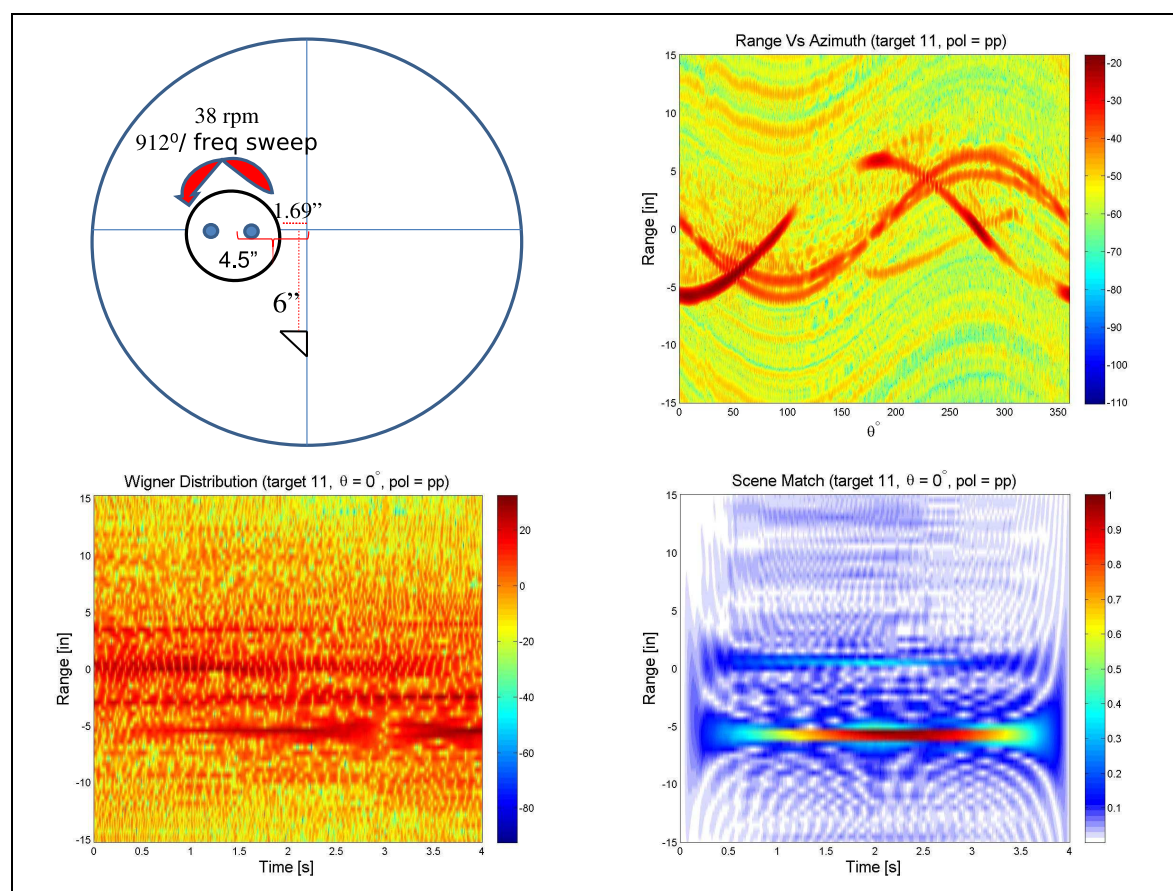
Figure H.35:   Target 11: Pol=PP, $\theta = 0°$, TFR's a.
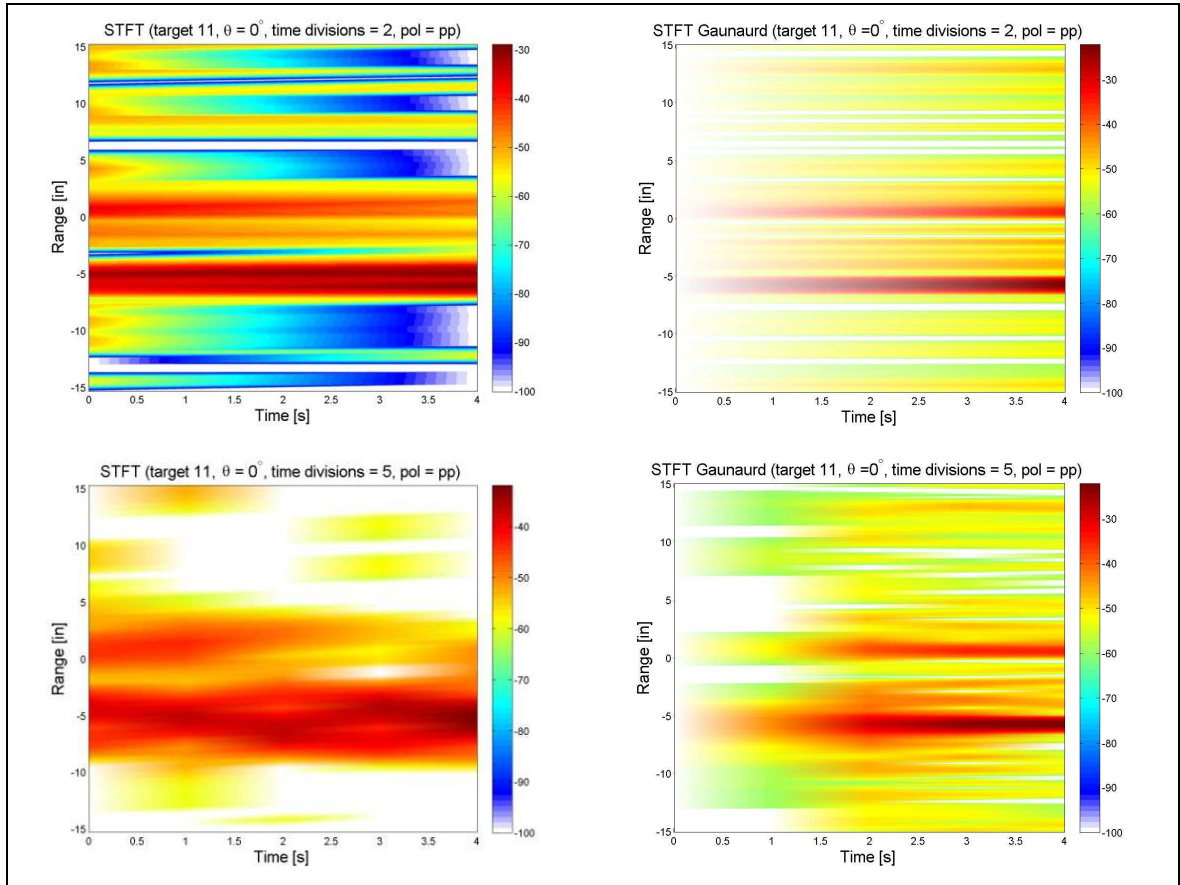
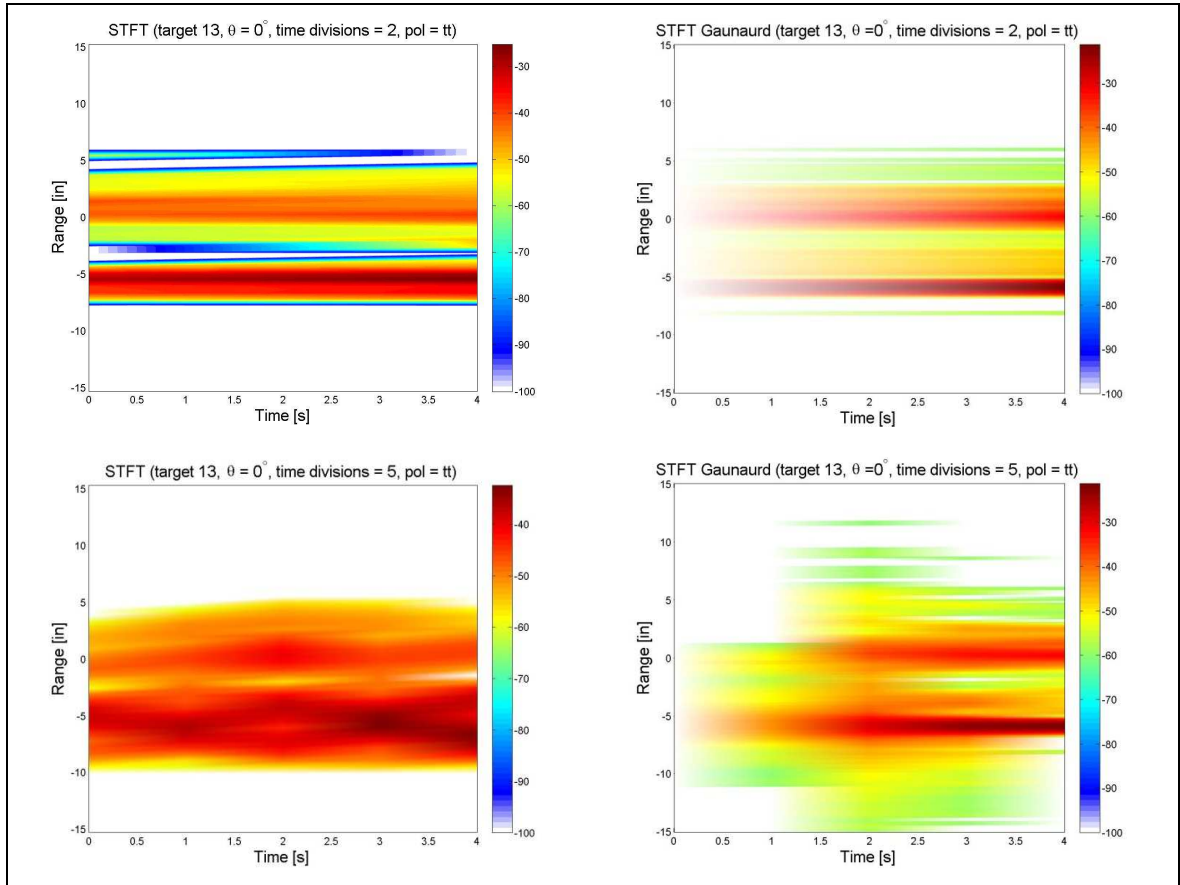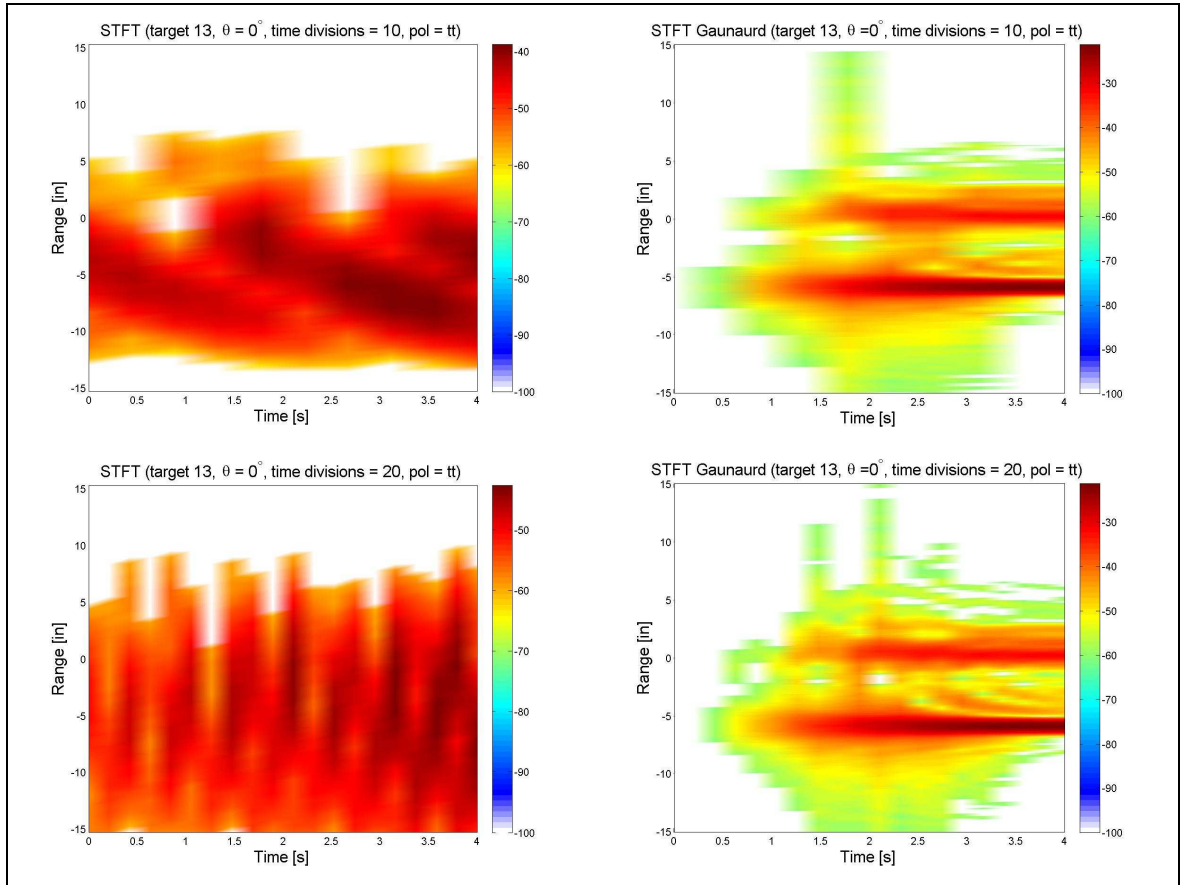Figure H.36:   Target 11: Pol=PP, $\theta = 0°$, TFR's b.

Figure H.37:   Target 11: Pol=PP, $\theta = 0°$, TFR's c.

Figure H.38:   Target 12: Pol=TT, $\theta = 0°$, TFR's a.
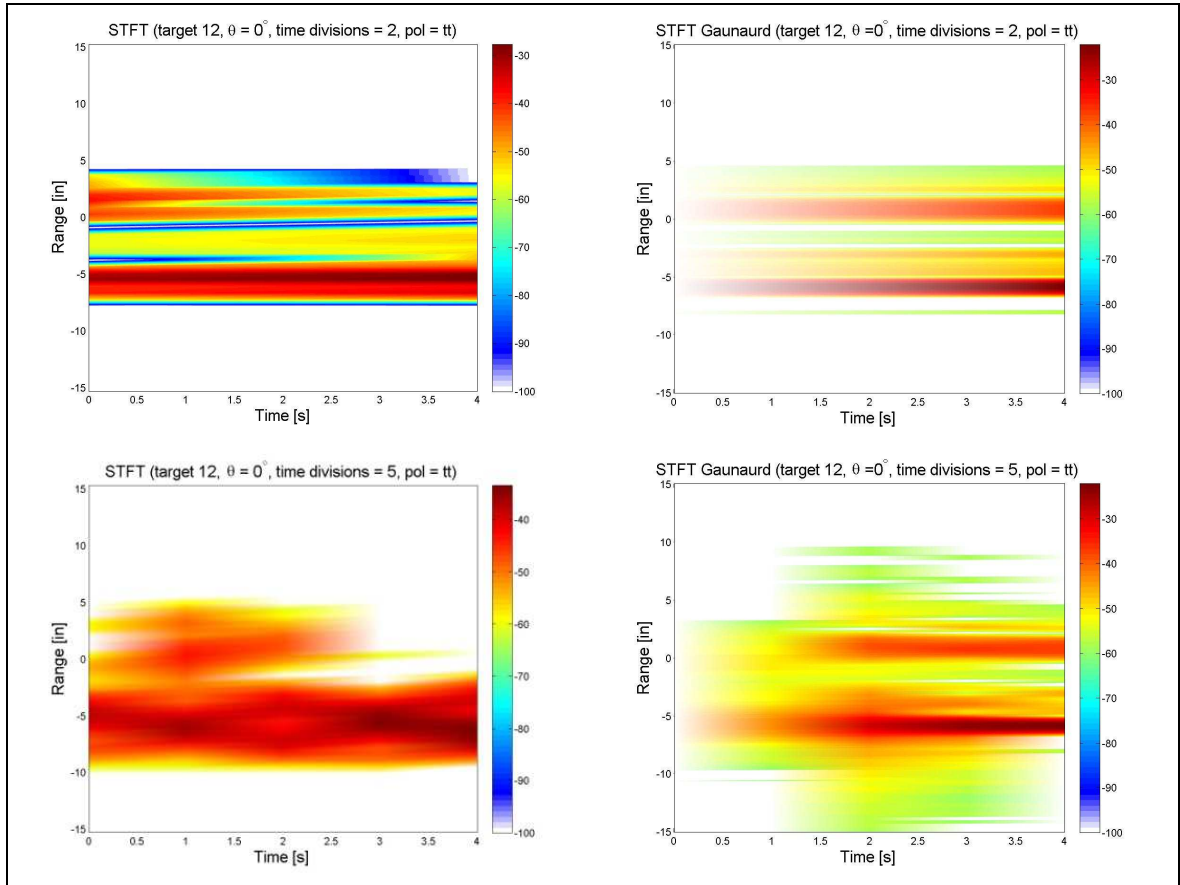
Figure H.39:   Target 12: Pol=TT, $\theta = 0°$, TFR's b.

Figure H.40:   Target 12: Pol=TT, $\theta = 0°$, TFR's c.

8.13 Target 12 PP Results
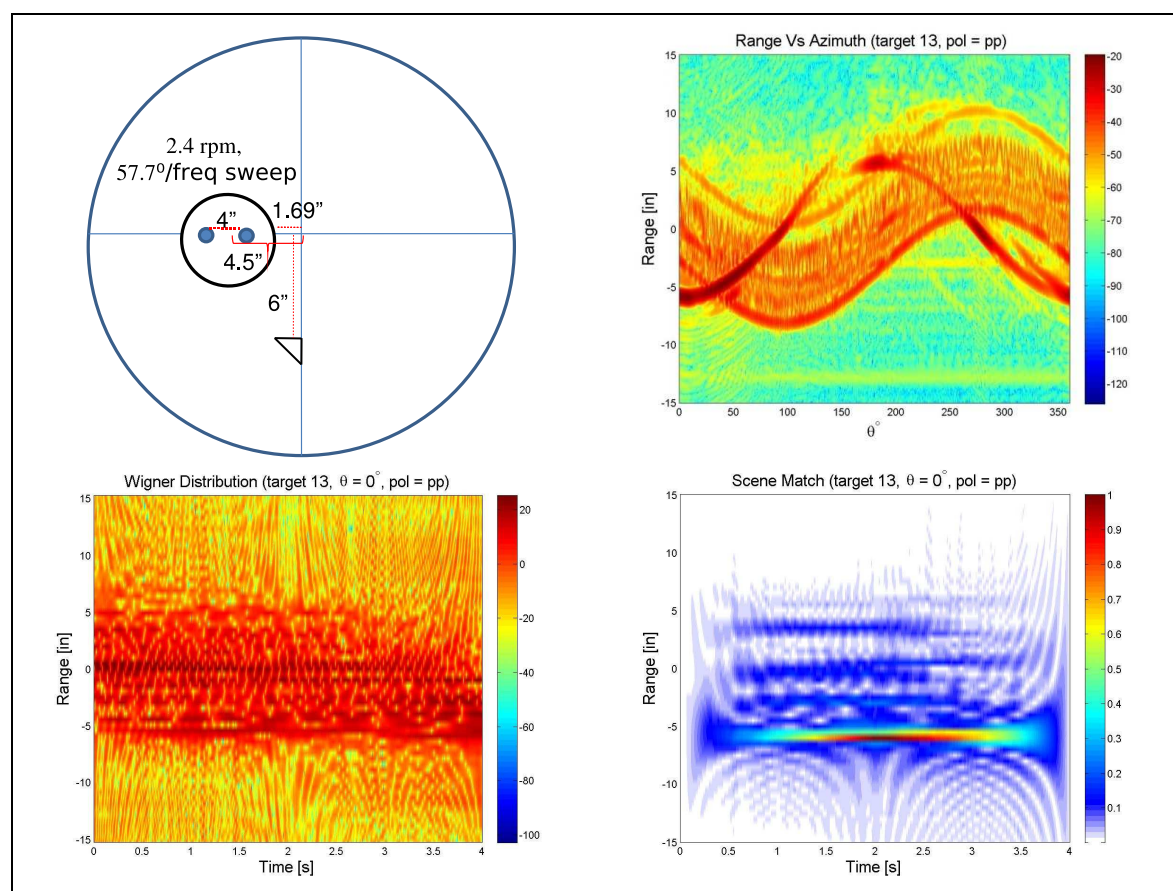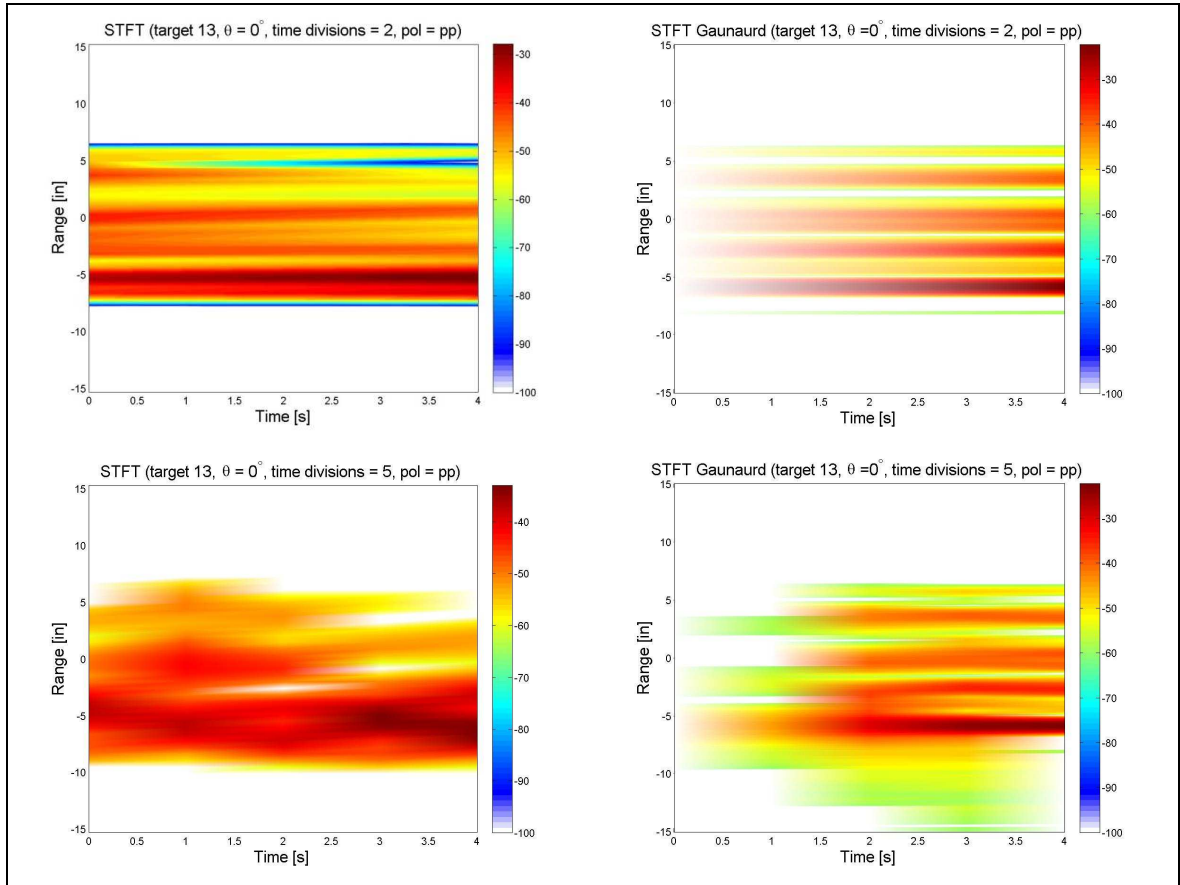

Figure H.41:   Target 12: Pol=PP, $\theta = 0°$, TFR's a.

Figure H.42:   Target 12: Pol=PP, $\theta = 0°$, TFR's b.

Figure H.43:　　Target 12: Pol=PP, $\theta = 0°$, TFR's c.

8.14 Target 13 TT Results
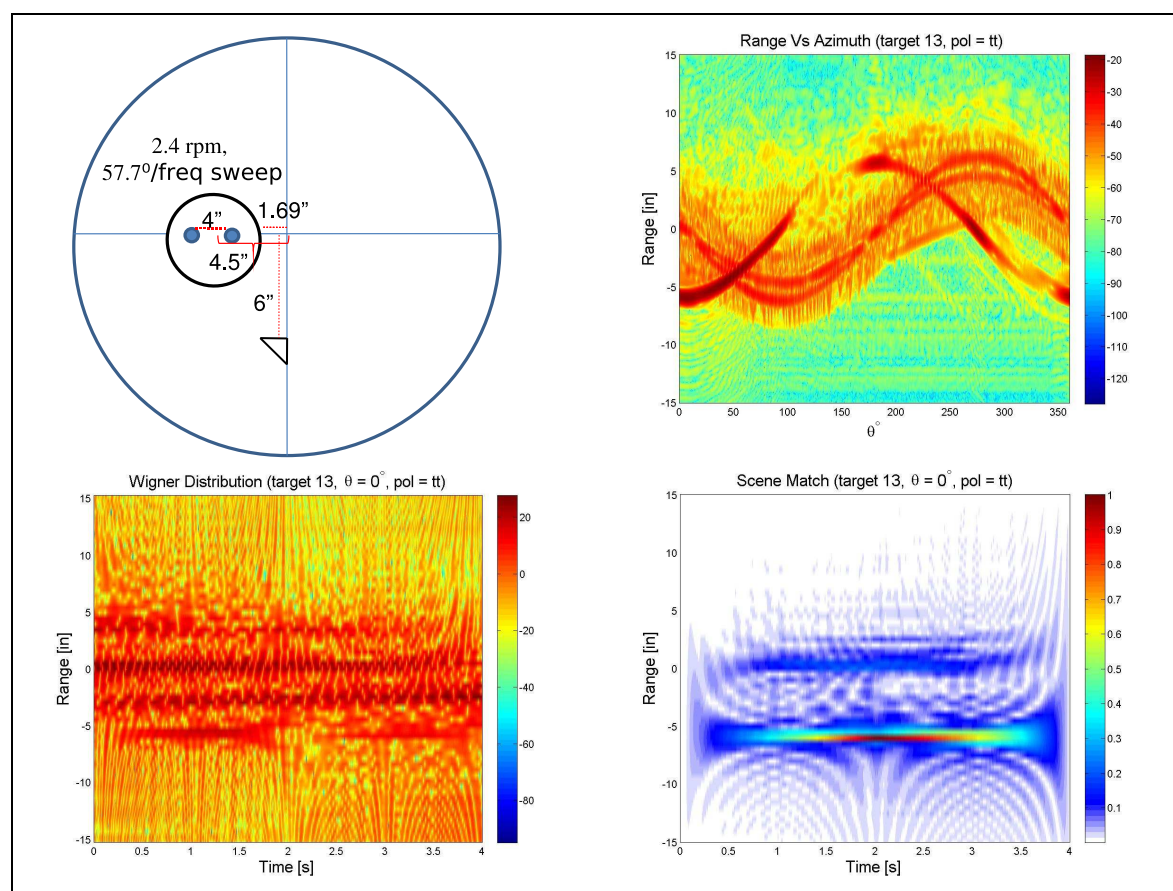
Figure H.44:   Target 13: Pol=TT, $\theta = 0°$, TFR's a.

Figure H.45:   Target 13: Pol=TT, $\theta = 0°$, TFR's b.

Figure H.46:   Target 13: Pol=TT, $\theta = 0°$, TFR's c.

8.15   Target 13 PP Results

Figure H.47:   Target 13: Pol=PP, $\theta = 0°$, TFR's a.
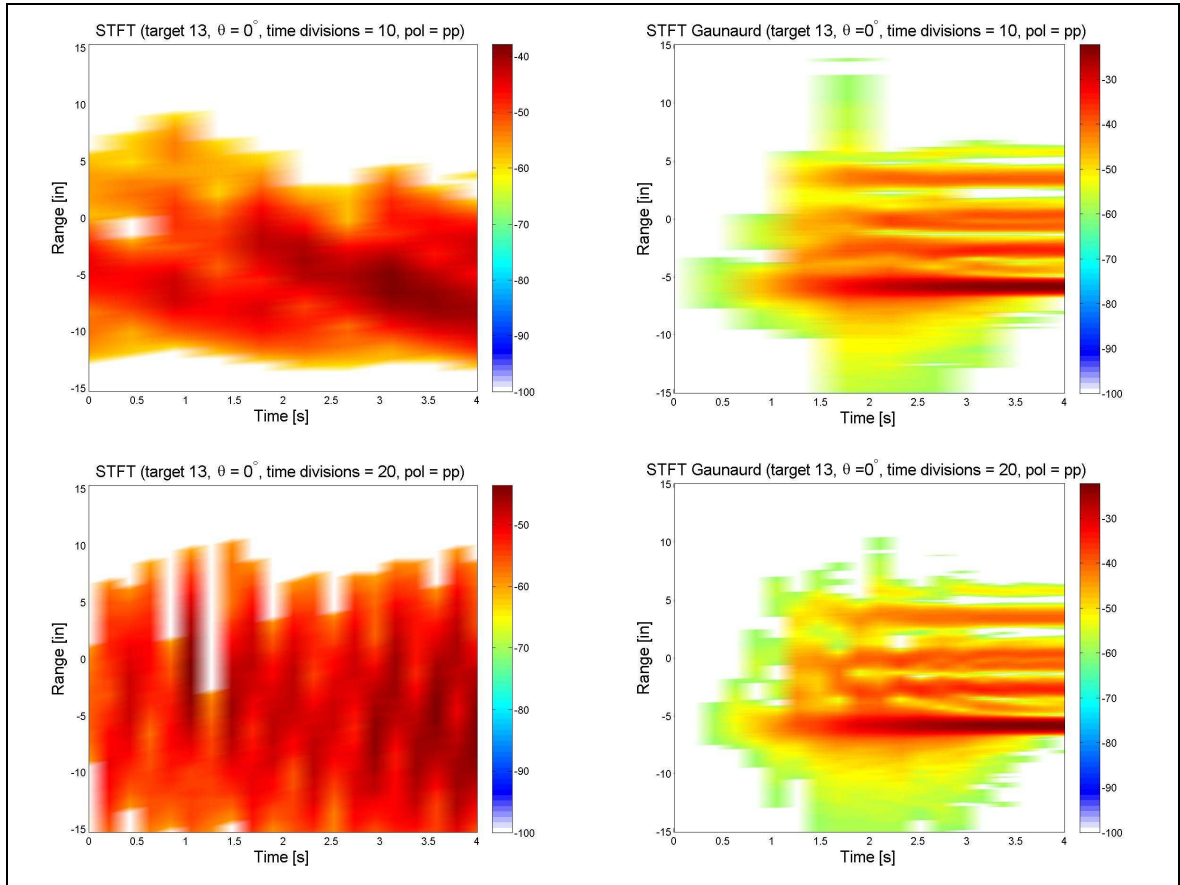
Figure H.48:   Target 13: Pol=PP, $\theta = 0°$, TFR's b.

Figure H.49:   Target 13: Pol=PP, $\theta = 0°$, TFR's c.

8.16   Target 14 TT Results
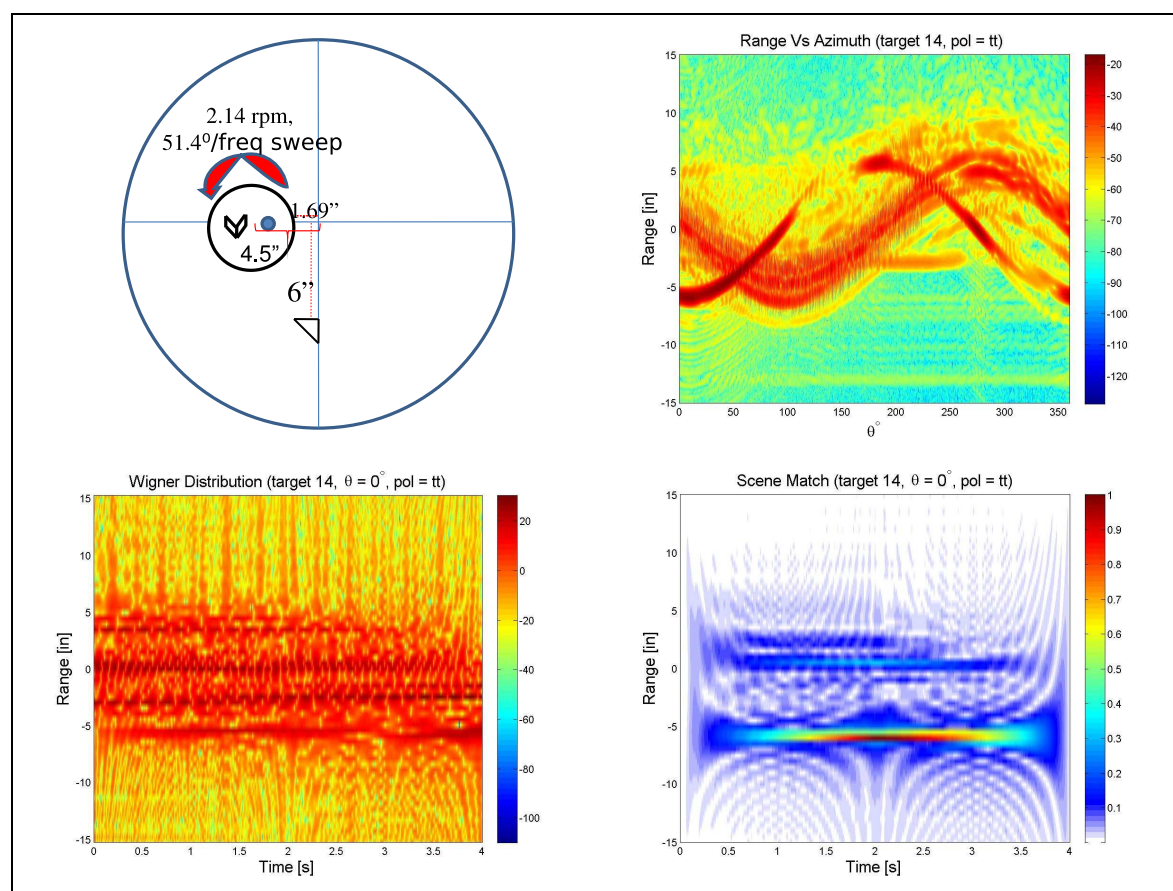

Figure H.50:   Target 14: Pol=TT, $\theta = 0°$, TFR's a.
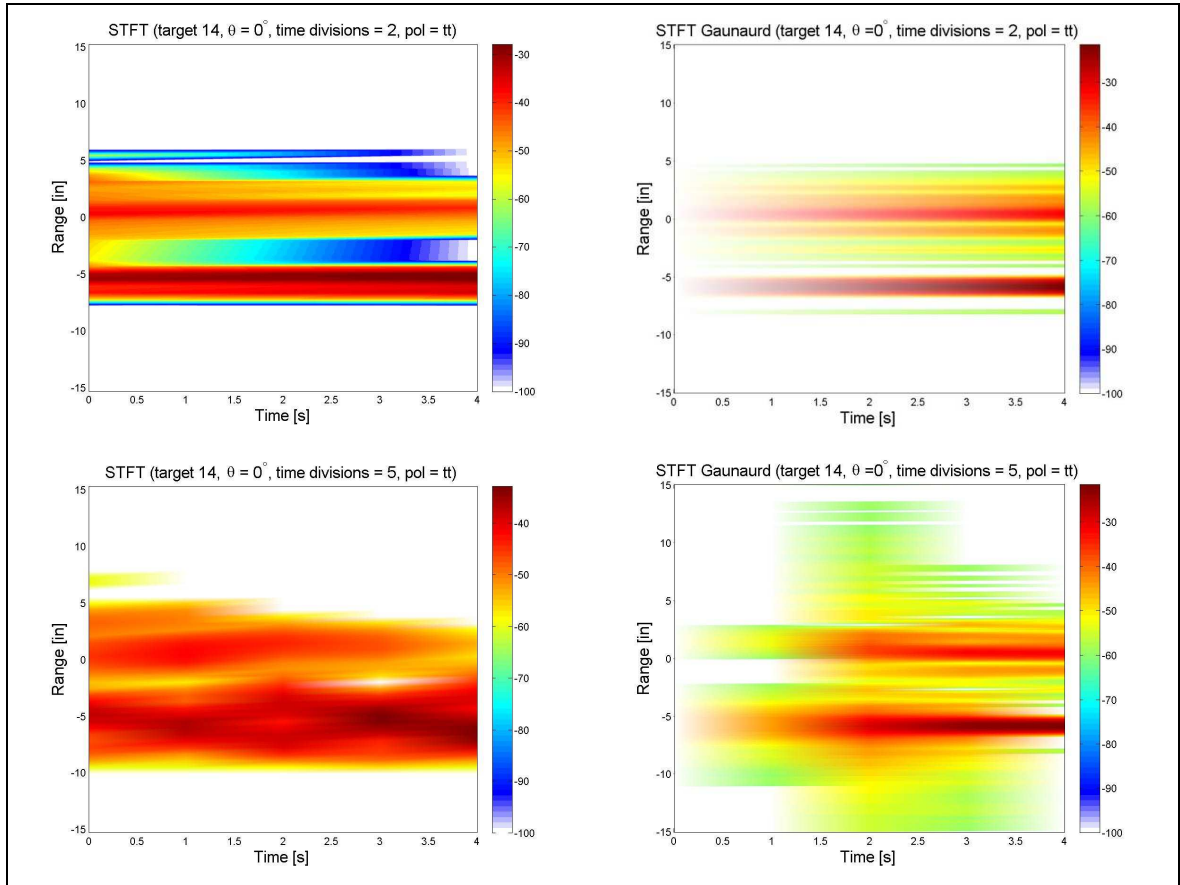
Figure H.51:   Target 14: Pol=TT, $\theta = 0°$, TFR's b.
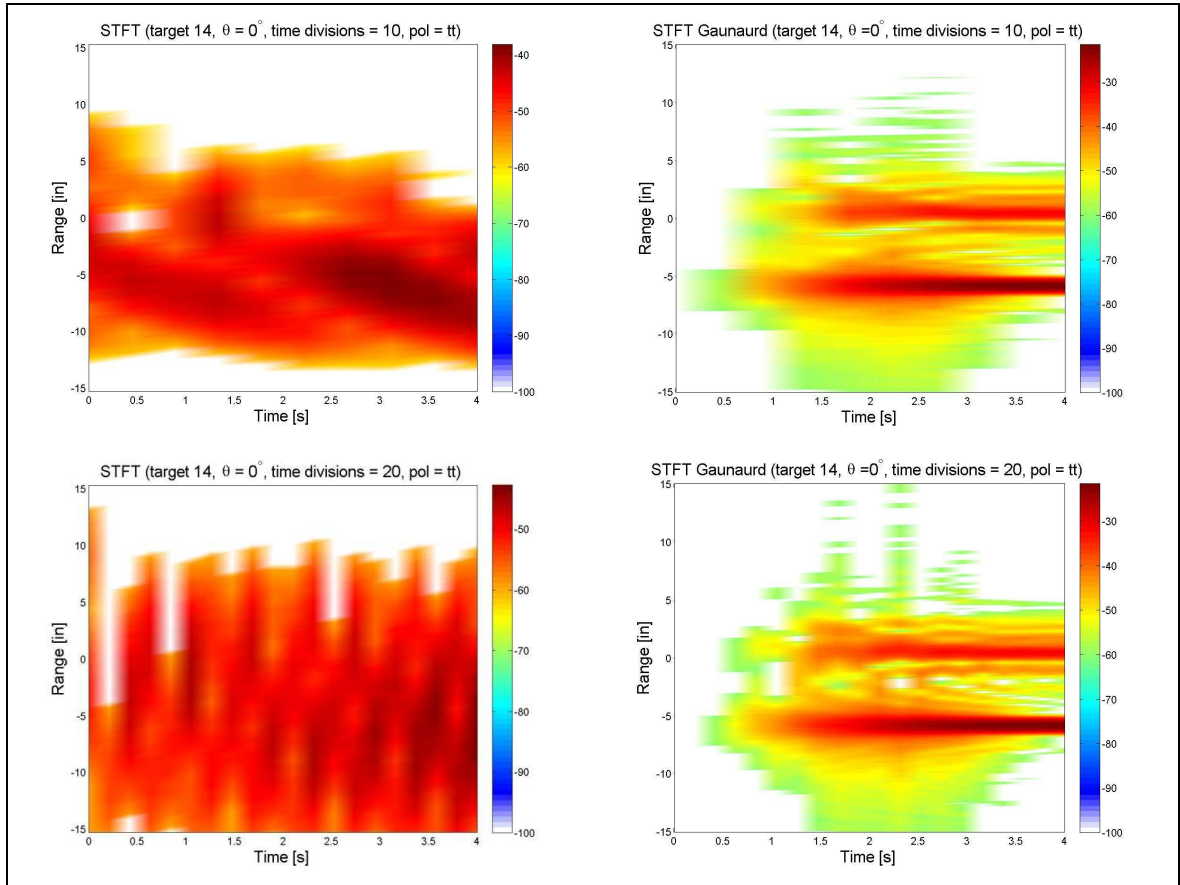
Figure H.52:   Target 14: Pol=TT, $\theta = 0°$, TFR's c.

8.17 Target 14 PP Results
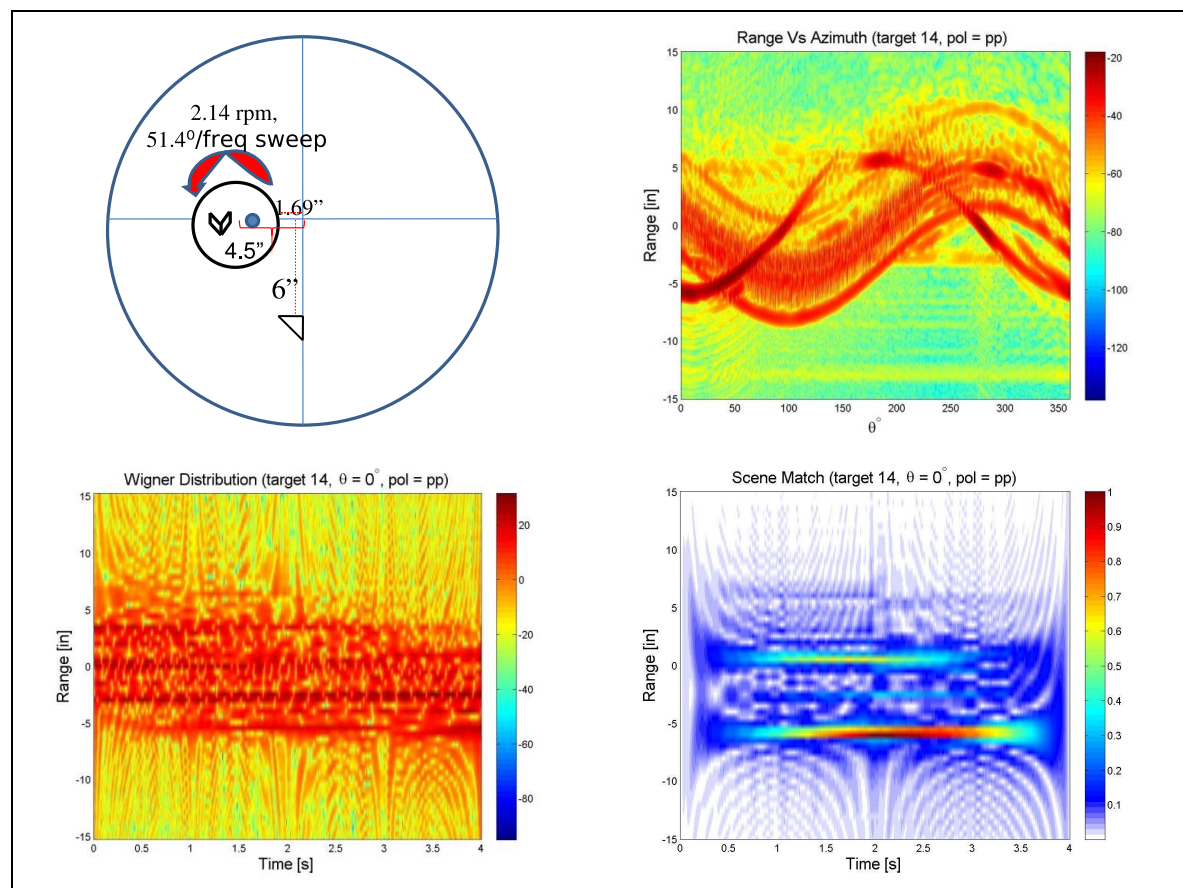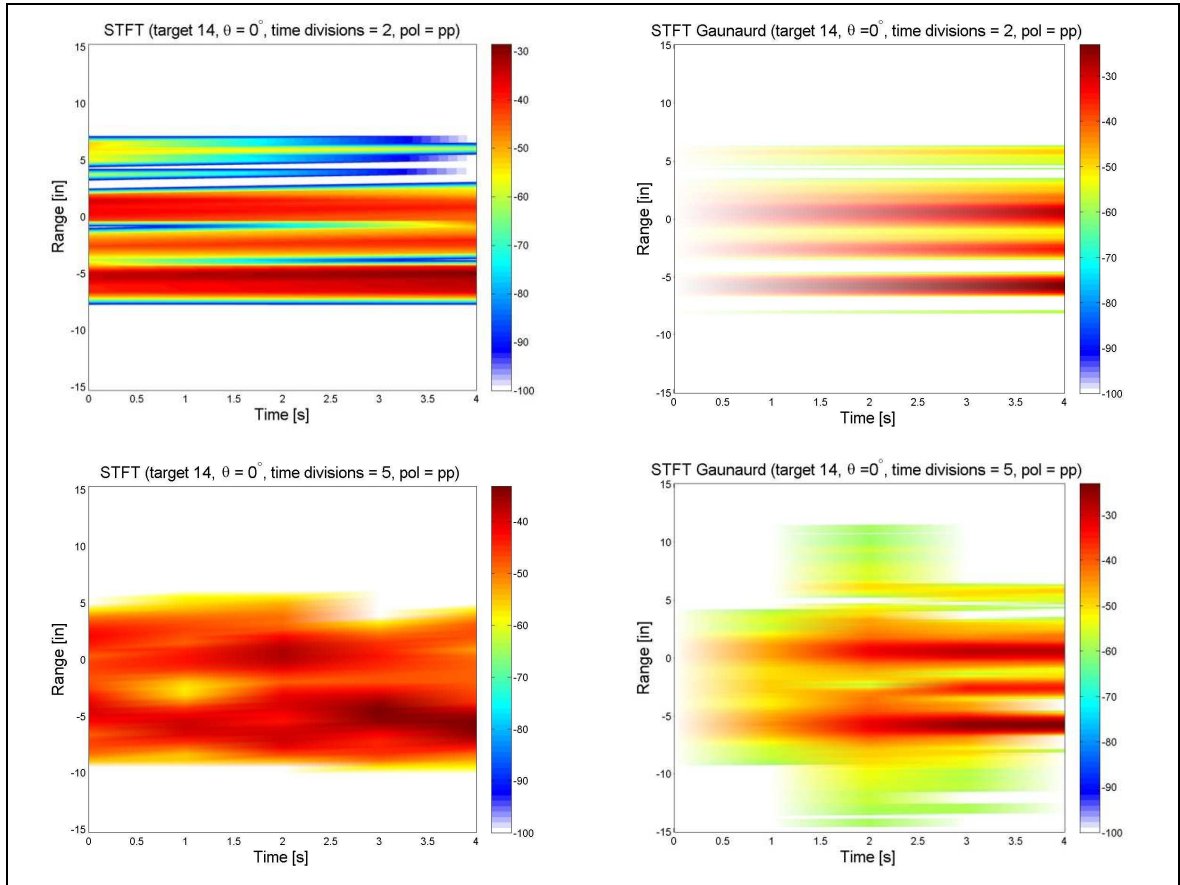

Figure H.53:   Target 14: Pol=PP, $\theta = 0°$, TFR's a.
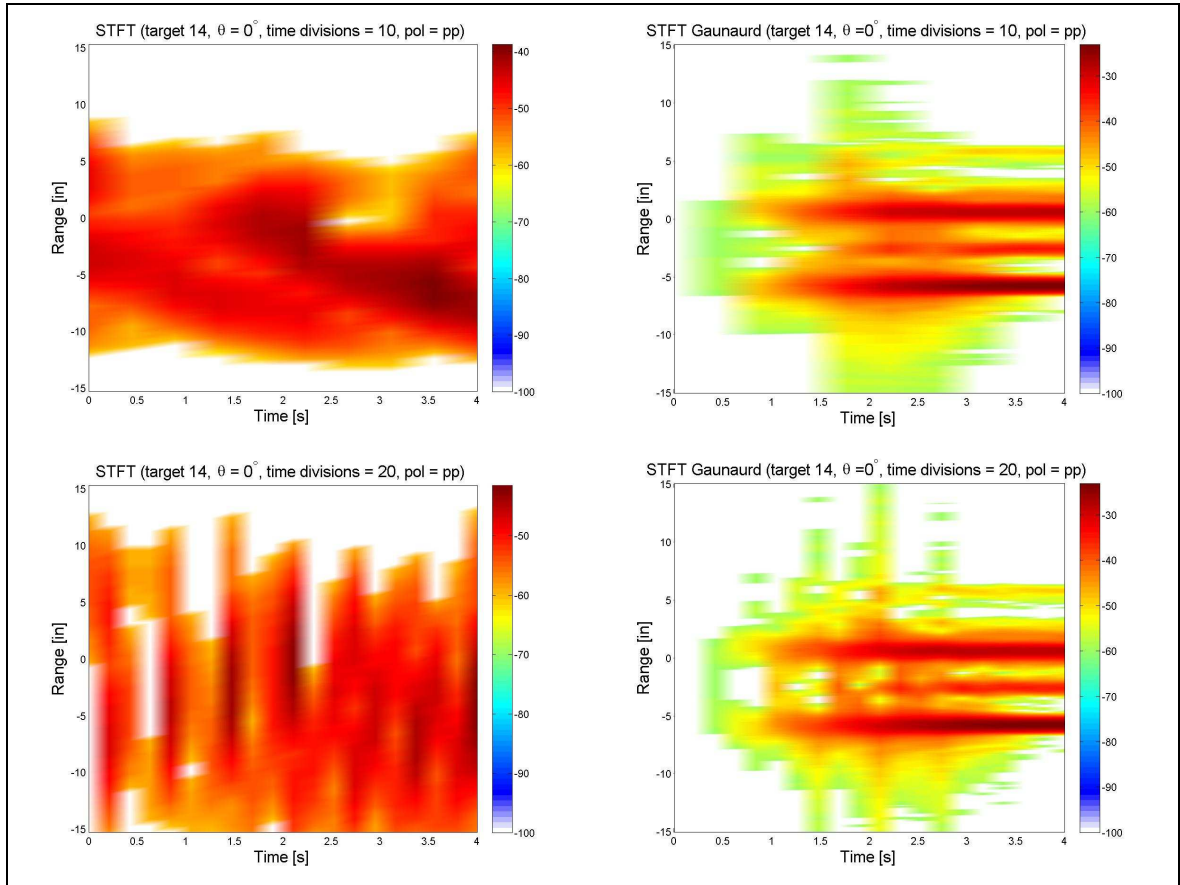
Figure H.54: Target 14: Pol=PP, $\theta = 0°$, TFR's b.

Figure H.55:   Target 14: Pol=PP, $\theta = 0°$, TFR's c.

Bibliography

1. *PNA Pulsed-RF S-Parameter Measurements using Wideband and Narrowband Detection*, November 2007. Application Note: 1408-12.

2. Atlas, L. E., G. D. Bernard, and S. B. Narayanan. "Applications of time-frequency analysis to signals from manufacturing and machine monitoring sensors". *Proceedings of the IEEE*, 84(9):1319–1329, 1996. ID: 1.

3. Bor, Jenn-Chyou and Chung-Yu Wu. "Analog electronic cochlea design using multiplexing switched-capacitor circuits". *Neural Networks, IEEE Transactions on*, 7(1):155–166, Jan 1996. ISSN 1045-9227.

4. Chunyan, Nie, Shi Yaowu, Yi Wensuo, and Cheng Fengqin. "Time-frequency analysis of chaos system based on Wigner distribution". *Signal Processing, 2004. Proceedings. ICSP '04. 2004 7th International Conference on*, 1:396–398 vol.1, Aug.-4 Sept. 2004.

5. Dragonette, L.R., D.M. Drumheller, C.F. Gaumond, D.H. Hughes, B.T. O'Connor, Nai-Chyuan Yen, and T.J. Yoder. "The application of two-dimensional signal transformations to the analysis and synthesis of structural excitations observed in acoustical scattering". *Proceedings of the IEEE*, 84(9):1249–1263, Sep 1996. ISSN 0018-9219.

6. Fanty, M., R. Cole, and M. Slaney. "A comparison of DFT, PLP and cochleagram for alphabet recognition". *Signals, Systems and Computers, 1991. 1991 Conference Record of the Twenty-Fifth Asilomar Conference on*, 326–329 vol.1, Nov 1991. ISSN 1058-6393.

7. Furlan, W.D., M. Martinez-Corral, B. Javidi, and G. Saavedra. "Analysis of 3-D integral imaging displays using the Wigner distribution". *Display Technology, Journal of*, 2(2):180–185, June 2006. ISSN 1551-319X.

8. Gaunaurd, G. C. and H. C. Strifors. "Signal analysis by means of time-frequency (Wigner-type) distributions-applications to sonar and radar echoes". *Proceedings of the IEEE*, 84(9):1231–1248, 1996. ID: 1.

9. Goncalves, P. and R. G. Baraniuk. "Pseudo affine Wigner distributions: definition and kernel formulation". *Signal Processing, IEEE Transactions on*, 46(6):1505–1516, 1998. ID: 1.

10. Johnston, J.A. "Wigner distribution and FM radar signal design". *Radar and Signal Processing, IEE Proceedings F*, 136(2):81–88, Apr 1989. ISSN 0956-375X.

11. Jones, D.L. and T.W. Parks. "A resolution comparison of several time-frequency representations". *Acoustics, Speech, and Signal Processing, 1989. ICASSP-89., 1989 International Conference on*, 2222–2225 vol.4, May 1989. ISSN 1520-6149.

12. Knott, E. F., J. F. Shaeffer, and M. T. Tuley. *Radar Cross Section.* The SciTech Radar and Defense Series. SciTech Publishing, Inc., Raleigh, NC 27613, 2nd edition, 2004. ISBN 1-891121-25-1. URL `www.scitechpub.com`.

13. Leong, M.P., C.T. Jin, and P.H.W. Leong. "Parameterized Module Generator for an FPGA-Based Electronic Cochlea". *Field-Programmable Custom Computing Machines, 2001. FCCM '01. The 9th Annual IEEE Symposium on*, 21–30, 2001.

14. Levanon, Nadav and Eli Mozeson. *Radar Signals.* John Wiley and Sons, Hoboken, New Jersey, 1st edition, 2004.

15. Mitra, Sanjit K. *Digital Signal Processing.* McGraw-Hill, 2nd edition, 2001.

16. Muthusamy, Y.K., R.A. Cole, and M. Slaney. "Speaker-independent vowel recognition: spectrograms versus cochleagrams". *Acoustics, Speech, and Signal Processing, 1990. ICASSP-90., 1990 International Conference on*, 533–536, Apr 1990. ISSN 1520-6149.

17. O'Neill, J. C., P. Flandrin, and W. J. Williams. "On the existence of discrete Wigner distributions". *Signal Processing Letters, IEEE*, 6(12):304–306, 1999. ID: 1.

18. Parks, T.W. and B.A. Weisburn. "Classification of whale and ice sounds with a cochlear model". *Acoustics, Speech, and Signal Processing, 1992. ICASSP-92., 1992 IEEE International Conference on*, 2:481–484 vol.2, Mar 1992. ISSN 1520-6149.

19. Pickles, James O. *An Introduction to the Physiology of Hearing.* Academic Press, 2nd edition, 1988.

20. Pitton, J. W., Kuansan Wang, and Biing-Hwang Juang. "Time-frequency analysis and auditory modeling for automatic recognition of speech". *Proceedings of the IEEE*, 84(9):1199–1215, 1996. ID: 1.

21. Santhi, S., V. Jayashankar, and V. Jagadeesh Kumar. "Time Frequency Analysis Method for the Detection of Winding Deformation in Transformer". *Instrumentation and Measurement Technology Conference Proceedings, 2008. IMTC 2008. IEEE*, 2126–2130, May 2008. ISSN 1091-5281.

22. Skolnik, Merrill I. *Introduction to Radar Systems.* McGraw-Hill, New York, NY, 3rd edition, 2001.

23. Skrapas, K., G. Boultadakis, A. Karakasiliotis, and P. Frangos. "Time - frequency analysis of radar signals for ISAR applications". *Recent Advances in Space Technologies, 2005. RAST 2005. Proceedings of 2nd International Conference on*, 699–703, June 2005.

24. Slaney, M. "Pattern playback from 1950 to 1995". *Systems, Man and Cybernetics, 1995. Intelligent Systems for the 21st Century., IEEE International Conference on*, 4:3519–3524 vol.4, Oct 1995.

25. Stergiopoulos, Stergios (editor). *Advanced Signal Processing Handbook*. CRC Press LLC, 2001.

26. Sun, Mingui, Shie Qian, Xiaopu Yan, S. B. Baumann, Xiang-Gen Xia, R. E. Dahl, N. D. Ryan, and R. J. Sclabassi. "Localizing functional activity in the brain through time-frequency analysis and synthesis of the EEG". *Proceedings of the IEEE*, 84(9):1302–1311, 1996. ID: 1.

27. Taylor, James D. (editor). *Ultra-Wideband Radar Technology*. CRC Press LLC, 2001.

28. Tsai, Yichang and C.J. Kuo. "An improved Wigner distribution synthesis method for separation of multiple nonstationary signals". *Circuits and Systems, 2004. ISCAS '04. Proceedings of the 2004 International Symposium on*, 3:III–577–80 Vol.3, May 2004.

29. Watts, L., D.A. Kerns, R.F. Lyon, and C.A. Mead. "Improved implementation of the silicon cochlea". *Solid-State Circuits, IEEE Journal of*, 27(5):692–700, May 1992. ISSN 0018-9200.

30. Williams, W. J. "Reduced interference distributions: biological applications and interpretations". *Proceedings of the IEEE*, 84(9):1264–1280, 1996. ID: 1.

IX. Vita

Capt. John D. McShane graduated from Riverside Brookfield High School in Riverside, Illinois in 2000. He then graduated from the United States Air Force Academy in Colorado Springs, Colorado with a Bachelor's of Science degree in Electrical Engineering in 2004.

He was commissioned into the United States Air Force through the United States Air Force Academy in June of 2004. His first assignment was to the 46th Test Squadron at Eglin AFB, where he was a Flight Test Engineer and Flight Element chief for the Electronics Warefare Flight. In August of 2007, he entered the Graduate School of Engineering at the Air Force Institute of Technology, where he studied Low Observables under the Electrical Engineering department. Upon graduation, he will be assigned to the Sensor's Directorate of AFRL at WPAFB.

1. REPORT DATE *(DD–MM–YYYY)*	2. REPORT TYPE	3. DATES COVERED *(From — To)*
26–03–2009	Master's Thesis	Aug 2007 — Mar 2009

4. TITLE AND SUBTITLE

Application of Time-Frequency Representations
To Non-Stationary
Radar Cross Section

5a. CONTRACT NUMBER

AFIT/GE/ENG/09-28

5b. GRANT NUMBER

5c. PROGRAM ELEMENT NUMBER

6. AUTHOR(S)

John D. McShane, Capt, USAF

5d. PROJECT NUMBER

08-141

5e. TASK NUMBER

5f. WORK UNIT NUMBER

7. PERFORMING ORGANIZATION NAME(S) AND ADDRESS(ES)

Air Force Institute of Technology
Graduate School of Engineering and Management (AFIT/ENG)
2950 Hobson Way
WPAFB OH 45433-7765

8. PERFORMING ORGANIZATION REPORT NUMBER

AFIT/GE/ENG/09-28

9. SPONSORING / MONITORING AGENCY NAME(S) AND ADDRESS(ES)

46TG/781TS (Lt Col Christopher Miller)
871 DeZonia Road
Holloman AFB, NM 88330
(DSN 349-3323, Christopher.miller@holloman.af.mil)

10. SPONSOR/MONITOR'S ACRONYM(S)

46TG/781TS

11. SPONSOR/MONITOR'S REPORT NUMBER(S)

12. DISTRIBUTION / AVAILABILITY STATEMENT

Approval for public release; distribution is unlimited.

13. SUPPLEMENTARY NOTES

14. ABSTRACT

Radar Cross Section imaging of a non-wide sense stationary signal poses significant problems in identifying scattering centers in the post processed radar-generated image. A non-wide sense stationary RCS is typically encountered when moving parts on the target impress a phase shift into the backscatter signal that is uncorrelated to the previous return pulse. When the Fourier transform of the phase shifted complex signal is taken, range and cross range information on scattering centers are misplaced. Time Frequency Representations must be used to help locate these scattering centers so they can be properly treated to reduce the target's RCS and increase its survivability. This thesis analyzes and compares various TFRs on non-wide sense stationary signals in hope of providing test centers with better methods for locating scattering centers under time variant conditions.

15. SUBJECT TERMS

Radar Cross Section, Time Frequency Representation, Wigner distribution, Ambiguity function, Cochleagram, Short Time Fourier Transform, Scene Match function

16. SECURITY CLASSIFICATION OF:			17. LIMITATION OF ABSTRACT	18. NUMBER OF PAGES	19a. NAME OF RESPONSIBLE PERSON
a. REPORT	b. ABSTRACT	c. THIS PAGE			Dr. Peter Collins
U	U	U	UU	227	19b. TELEPHONE NUMBER *(include area code)* (937) 255-3636, ext 7256; peter.collins afit.edu